Universidad de Navarra

Facultades de Medicina y Ciencias

Oncolytic adenovirus Delta-24-RGD engineered to express 4-1BBL or OX40L as therapeutic approach for diffuse intrinsic pontine gliomas

VIRGINIA LASPIDEA USTÉS

Pamplona, 2022

Universidad de Navarra

Facultades de Medicina y Ciencias

Oncolytic adenovirus Delta-24-RGD engineered to express 4-1BBL or OX40L as therapeutic approach for diffuse intrinsic pontine gliomas

Memoria presentada por Dª Virginia Laspidea Ustés para aspirar al Grado de Doctor por la Universidad de Navarra en el Programa de Doctorado de Medicina Aplicada y Biomedicina

El presente trabajo ha sido realizado bajo la Dirección de los siguientes Profesores en el Departamento de Pediatría de la Clínica Universidad de Navarra y Tumores Sólidos del CIMA y autorizamos su presentación ante el Tribunal que lo ha de juzgar.

Pamplona, 11 de octubre de 2022

Dra. Marta Alonso Roldán

Dra. Ana Patiño García

Este trabajo ha sido realizado gracias a la concesión de las ayudas predoctorales del Gobierno de Navarra (2019)

A mi familia

ACKNOWLEDGMENTS

En primer lugar, me gustaría agradecer a la Universidad de Navarra por darme la oportunidad de realizar la tesis doctoral y al Gobierno de Navarra, por concederme la beca predoctoral, así como la beca de movilidad para realizar una estancia en Houston.

Gracias a mis directoras de tesis Marta Alonso y Ana Patiño por darme la oportunidad de realizar tanto el trabajo de fin de master como el doctorado en su laboratorio. Marta, muchas gracias por dejarme ser parte de tu equipo, y por creer en mi incluso más que yo misma. Ha sido una suerte tenerte como jefa, gracias por tu apoyo tanto en lo profesional como en lo personal. Por mirar siempre por nuestro futuro, gracias por tus consejos y por las oportunidades que me has dado durante estos cuatro años; papers, congresos, estancia... Que suerte haber podido ser parte de este proyecto tan bonito. Ana, gracias por tu apoyo y ayuda durante estos años, y por brindarnos tu sabiduría y alegría cada vez que vienes al laboratorio. ¡Qué suerte tenerte como codirectora! Muchas gracias a Jaime por mostrarnos el otro lado, el de los pacientes, motivándonos a seguir con nuestro trabajo para que pueda llegar a ellos. También me gustaría agradecer a los miembros del tribunal de la defensa de tesis por querer formar parte del mismo.

A mis compis de laboratorio, por su apoyo y ayuda durante mi tesis y por el buen ambiente que tenemos trabajando. En especial a Marta Z. por estar siempre dispuesta a ayudarme desde el primer día, sin hacer falta que te lo pida. Me has ayudado muchísimo, incluso en esas excursiones que teníamos que hacer al CIFA. Has sido mi mayor apoyo, siempre preocupándote y preguntándome qué tal va todo. Marisol, la impulsora de que entrase en este laboratorio!! Gracias por estar siempre dispuesta a ayudar y a buscar soluciones cuando no salen las cosas. Luciluu desde el principio hemos congeniado, ha sido un placer trabajar contigo y hacer los planes fuera del lab, espero que todavía queden muchos más por hacer. A mis super compis Ausejo y de la Nava, gracias por vuestra ayuda, pero sobre todo por los momenticos en el despacho! Iker, gracias por apoyarme y animarme siempre. Compañero de estancia, no hubiera sido lo mismo visitar Texas sola. Has sido un apoyo importante durante mi tesis, nos vemos en los bares y en los montes! Dani, compi del team buterfly, gracias por tu ayuda, por preocuparte, y por tu alegría, no cambies nunca! Seguro que os va a ir todo genial, toméis el camino que toméis. A Sara y Marc, que suerte haber coincidido con vosotros durante esta etapa. Sara, desde que viniste has hecho que todos aumentemos nuestro conocimiento en la inmunología;) Me has ayudado muchísimo con mi proyecto, gracias por escucharme y por todos tus consejos. Que bueno que viniste! Marc fuiste mi primer mentor en el máster, gracias por toda tu ayuda desde entonces. Ha sido un placer trabajar contigo y aprender tanto de ti. Monsss, gracias por estar dispuesta a ayudar y por preocuparte por mí siempre.

Javi, Reyes, Andrea, Antonio, Sara N, Laasya e Irati gracias por vuestra ayuda y por estar pendientes de cómo me iba mientras escribía la tesis, aunque hayamos coincidido menos. Irati, tu sí que eres una persona vitamina! Nos contagias tu alegría y positividad. Finalmente, también me gustaría agradecer a Juan y a Cande por acogerme en Houston y por hacer que mi estancia ahí fuera mucho más fácil. Ha sido una suerte poder trabajar con vosotros y empaparme de todo

vuestro conocimiento. Gracias también por querer formar parte del tribunal de tesis, me hace especial ilusión.

Quiero dar las gracias a mi familia, en especial a mis padres y a mi hermana. Por preocuparse y estar siempre pendientes de mí, y por ayudarme a tomar las decisiones correctas. Os quiero mucho. Gracias por escucharme cuando os doy la tabarra cuando no salen las cosas, y por contar con orgullo lo que hago. Por apoyarme en todas mis decisiones y por querer que siempre esté ahí, con vuestros "cuando vienes?" A mi madre, por cuidarnos tanto a todos y estar siempre pendiente de que estemos bien. Porque eres la primera persona a la que acudo cuando me preocupa algo. A mi padre, por ser un ejemplo. No conozco a nadie que haya trabajado tanto y tan duro como tú. Nunca pierdas tu humor. Marina, gracias por preocuparte por mí, aunque seas la hermana pequeña. Por ser calma y alegría, porque contagias tu risa a cualquiera. Gracias al resto de mi familia, por preocuparse y estar pendientes de mis pasos. A mi abuelica por esos abrazos que dan vida.

Zuri ere maitia, nire bizitzako oinarria zarelako. Eskerrik asko ni entzuteagatik, beti lagundu, animatu eta beldurrak kentzeagatik, zuretzat egiten dudana onena delako. Baina batez ere, nire hurrengo etapan eskutik jarraitu nahi izateagatik. Hoberena zara, nire zoriontasunaren motore. Beti, denetan, nire partekide onena zarelako. Maite zaitut! Baita zure familiari ere, ni zaintzeagatik eta nire pausoengatik beti kezkatzen direlako.

También quiero dar las gracias a mi otra familia, a la que se elige. Siempre pendientes de cómo me va en el laboratorio, y por qué va a ser de mi futuro. Mis ratones también agradecen vuestra preocupación por ellos ;) Si me preguntan dónde iría para desconectar, lo tengo claro. Porque estoy deseando que llegue el viernes para poder ir a Burgui, a casa. Es calma, no solo por el sitio, sino por vosotrxs. "Y si la cosa se tuerce, pues nos cogemos y nos vamos pa´l pueblo!!" Por esos momenticos tomando Alhambras en el Zati, que son la mejor medicina, por los planes y las locuras que nos hacen llorar de risa. Sois desconexión, felicidad, un pilar fundamental en mi vida. En especial a mis txiks, por estar ahí siempre. Sois lo mejor, os quiero mucho.

A Maite, juntas empezamos la andadura en la ciencia. Mi inseparable durante la carrera, eres fuerza y alegría. Gracias por estar siempre ahí, me alegras las mañanas cuando te veo en el parking. Maite zaitut!!

Que suerte teneros!

Index

INDEX

List of abbreviations

A

$A_{2A}R$	Adenosine A2a receptor
ACK	Ammonium chloride potassium
ACVR1	Activin A receptor type 1
ADCC	Antibody-dependent cell-mediated cytotoxicity
AhR	Activator of aryl hydrocarbon receptor
ALP	Alkaline phosphatase
ALT	Alanine aminotransferase
ANOVA	Analysis of variance
APC	Antigen presenting cell
AST	Aspartate aminotransferase
AT/RT	Atypical teratoid/rhabdoid tumor
ATCC	American type culture collection
ATP	Adenosine triphosphate

B

BBB	Blood brain barrier
BHGpA	Bovine growth hormone polyadenylation signal
BMP	Bone morphogenetic protein
Bp	Base-pair
BSA	Bovine serum albumin

C

cAMP	Cyclic adenosine monophosphate
CAR T cell	Chimeric antigen receptor T cell
CAR	Coxsackie and adenovirus receptor
CCL	C-C motif chemokine ligand
CCR	C-C motif chemokine receptor
CD	Cluster of differentiation
cDNA	Complementary deoxyribonucleic acid
CEEA	Comité de ética para la experimentación animal
CNS	Central nervous system
CRT	Calreticulin

CTLA-4	Cytotoxic T-lymphocyte antigen 4

D

DAMP	Danger-associated molecular patterns
DAPI	4 ',6-diamidino-2-fenilindol
DBP	DNA-binding protein
DC	Dendritic cells
DIPG	Diffuse intrinsic pontine glioma
DMEM	Dulbecco´s modified eagle medium
DMG	Diffuse midline gliomas
DNA	Deoxyribonucleic acid
dNTP	Deoxynucleotide triphosphates
DNX-2401	Delta-24-RGD

E

E1A	Early region 1A
E1B	Early region 1B
E2	Early region 2
E2F	E2F Transcription Factor
E3	Early region 3
E4	Early region 4
EDTA	Ethylene diamine tetraacetic acid
ELISA	Enzyme-linked immunosorbent assay
ELISPOT	Enzyme-linked immunospot assay
EGFR	Epidermal growth factor receptor

F

FAP	Fibroblast activation protein
FBS	Fetal bovine serum
FDA	Food and drug administration
FFPE	Formalin-fixed, paraffin-embedded
FOXP3	Forkhead box protein P3

G

GAPDH	Glyceraldehyde-3-phosphate dehydrogenase
GBM	Glioblastoma
GD2	Disialoganglioside GD2
GITR	Glucocorticoid-induced TNFR-related protein
GM-CSF	Granulocyte-macrophage colony-stimulating factor
GO	Gene ontology
GRB2	Growth factor receptor-bound protein 2
GrzB	Granzyme B
Gy	Gray

H

HAdv	Human adenovirus
HEK293	Human embryonic kidney 293 cells
HLA-A	Human leukocyte antigen A
HMGB1	High mobility group box 1 protein
HSP70	70 Kilodalton heat sock protein
HSP90	90 Kilodalton heat sock protein
HSV-1	Herpes simplex virus 1
hTERT	Human telomerase reverse transcriptase

I

IC	Inhibitory concentration
ICAM-1	Intercellular Adhesion Molecule 1
ICD	Immunogenic cell death
IDO	Indoleamine 2,3-dioxygenase
IF	Immunofluorescence
IFN	Interferon
IgG	Immunoglobulin G
IHC	Immunohistochemistry
IL-	Interleukin
INK4ARF	Inhibitor of cyclin dependent kinase 4 alternative reading frame
IP	Intraperitoneal

IT Intratumoral

ITR Inverted terminal repetitions

iTreg Induced Treg

K

Kb Kilobase

L

L1 Late region 1

L2 Late region 2

L3 Late region 3

L4 Late region 4

L5 Late region 5

M

MFI Mean fluorescence intensity

MHC-I Major histocompatibility complex class I

MLP Major late promoter

MOI Multiplicity of infection

MRI Magnetic resonance imaging

mRNA Messenger ribonucleic acid

MSC Mesenchymal stem cell

MTS 3-(4,5-dimethylthiazol-2-yl)-5-(3-carboxymethoxyphenyl)-2-(4-sulfophenyl)-2H-tetrazolium

N

NK cell Natural killer cell

NSCLC Non-small cell lung cancer

nTreg Natural Treg

O

OS Overall survival

OV Oncolytic virotherapy

OX40L OX40 ligand

P

PAMP	Pathogen-associated molecular patterns
PBS	Phosphate buffer saline
pCMV	Cytomegalovirus promoter
PCR	Polymerase chain reaction
PD-1	Programed death 1
PDGF	Platelet derived growth factor
PDGFRA	Platelet derived growth factor receptor alpha
PD-L1	Programed death ligand 1
PFS	Progression-free survival
PFU	Plaque forming unit
pHGG	Pediatric high-grade glioma
PKR	Protein kinase R
PNET	Primitive neuroectodermal tumor
PRC2	Polycomb repressive complex 2
PSA	Prostate-specific antigen
pTreg	Peripheral Treg

Q

qPCR	Real time polymerase chain reaction

R

Rb	Retinoblastoma protein
RCAS	Replication-competent ASLV long terminal repeat with a splice acceptor
RGD	Arginine-glycine-aspartic acid
RNA	Ribonucleic acid
rpm	Revolutions per minute
RT	Room temperature
RT	Radiotherapy

S

S phase	Synthesis phase
SD	Standard deviation

SEM	Standard error of the mean

T

TCR	T cell receptor
Teff	Effector T cells
TGF-β	Tumor growth factor beta
Th3	T helper 3 cells
TIL	Tumor-infiltrating lymphocytes
TLR	Toll-like receptor
TME	Tumor microenvironment
TNF	Tumor necrosis factor
TNFRSF4	Tumor necrosis factor receptor superfamily member 4
TNFRSF9	Tumor necrosis factor receptor superfamily member 9
TP	Terminal protein
TP53	Tumor protein P53
Tr1	Type 1 regulatory cells
Treg	Regulatory T cells
TRM	Tissue-resident macrophage
TSA	Tyramide signal amplification
tTreg	Thymus Treg
T-VEC	Talimogene laherparepvec

V

VP	Viral particles

W

WHO	World health organization

4-1BBL	4-1BB ligand

Introduction

1. Pediatric tumors

Pediatric tumors appear during childhood and adolescence and are diagnosed from 0 to 19 years old.[1] The WHO estimates that 400,000 cases are diagnosed every year globally, which account for about 1% of all cancer diagnoses.[2] Pediatric tumors differ substantially from tumors occurring in adults. While adult cancer occurs due to the accumulation of genetic mutations and cell damage with age, pediatric tumors are usually caused by a blockage in the maturation of immature developing cell types. Therefore, the latter show much lower genetic aberrations.[3,4] The most frequently diagnosed tumors during childhood are hematological malignancies (including leukemia and lymphoma), followed by tumors of the central nervous system (CNS). Specifically, leukemia (24.7%), tumors of the central nervous system (17.2%), non-Hodgking lymphoma (7.5%), Hodgking lymphoma (6.5%), soft-tissue sarcoma (5.9%) and bone tumors (4-8%) are the most common groups[5] (Figure 1). In this work, we will focus on brain tumors, and specifically on diffuse midline gliomas (DMGs).

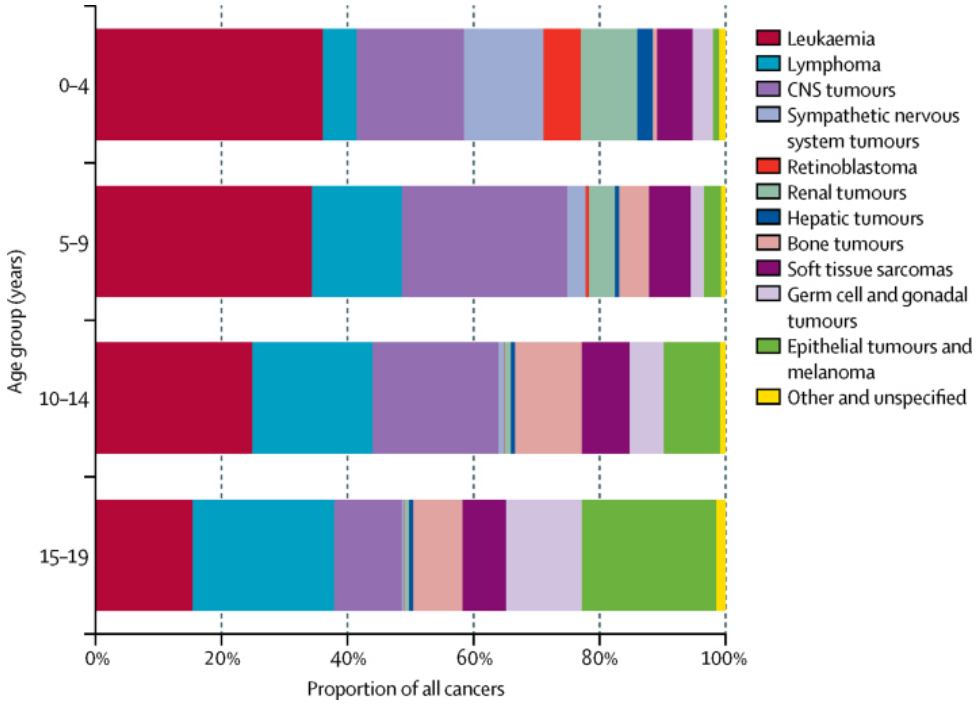

Figure 1. Proportion of all pediatric cancers divided by ages (0 to 19 years old). Image obtained from Steliarova-Foucher E. *et al.*, 2017.[1]

2. Pediatric brain tumors

Pediatric brain tumors comprise a diverse group of histologic subtypes that differ in epidemiology, molecular characteristics, location, treatments and outcomes. They are the most common solid tumors in children and adolescents and the leading cause of cancer-related deaths in childhood.[6]

The 4th edition of CNS tumors classification by the WHO, classifies these tumors in 4 grades (grade I to IV) depending on a "malignancy scale" that considers characteristics such as proliferation, invasive patterns, tumor aggressiveness and prognosis. Grades I and II are less aggressive and are denominate as low-grade, whereas grades III and IV include the most aggressive tumors and the ones with worst outcome, named high-grade tumors[7] (Table 1).

Table 1. Characteristics of WHO brain tumor grades stablished in 2007.

Grade	Characteristics
I	Low proliferative, non invasive and curable with surgical resection
II	Slow growing, can infiltrate and recur to a higher grade
III	Fast growing, can infiltrate into nearby tissues and recur as a higher grade
IV	Very fast growing and aggressive, widely infiltrative, and recurs rapidly.

However, thanks to advances in molecular and histological techniques in recent times, a new classification emerged in 2016 taking into account genetic and histological characteristics of tumors. The major restructuration occurred in diffuse gliomas, medulloblastoma and other embryonal tumors[8].

In 2021, the last edition of WHO brain tumor classification was published[5,9]. In this new classification, in addition to histological and genetic features, novel diagnostic technologies such as DNA methylation profiles were used to establish new tumor entities[9]. More importantly, for the first time, pediatric tumors were classified in a separate volume. Therefore, in addition to integrate histologic patterns and leading molecular diagnostic tools, they introduced "pediatric-type" and "adult-type" categories for both low-grade and high-grade gliomas to account for the age-specific biology[5] (Table 2).

Table 2. The WHO new classification of CNS tumors that are most frequent in children and adolescents. Changes with respect to WHO Classification of CNS Tumors 2016 are highlighted in red (new). Molecularly defined entities are marked in green. Table obtained from Pfister M. *et al*., 2021[5].

Gliomas, glioneuronal, and neuronal tumors
- *Pediatric-type diffuse low-grade gliomas*
  - Diffuse astrocytoma, *MYB* or *MYBL1*-altered new
  - Angiocentric glioma
  - Polymorphous low-grade neuroepithelial tumor of the young new
  - Diffuse low-grade glioma, MAPK pathway-altered new
- *Pediatric-type diffuse high-grade gliomas defined by H3 status*
  - Diffuse midline glioma, H3 K27-altered
  - Diffuse hemispheric glioma, H3 G34-mutant new
  - Diffuse pediatric-type high-grade glioma, H3-wild-type and IDH-wild-type new
  - Infant-type hemispheric glioma new
- *Circumscribed astrocytic gliomas*
  - Pilocytic astrocytoma
  - High-grade astrocytoma with piloid features new
  - Pleomorphic xanthoastrocytoma
  - Subependymal giant cell astrocytoma
  - Astroblastoma, *MN1*-altered
- *Glioneuronal and neuronal tumors*
  - Ganglioglioma
  - Desmoplastic infantile ganglioglioma/Desmoplastic infantile astrocytoma
  - Dysembryoplastic neuroepithelial tumor
  - Diffuse glioneuronal tumor with oligodendroglioma-like features and nuclear clusters (DGONC)[a] new
  - Diffuse leptomeningeal glioneuronal tumor
  - Multinodular and vacuolating neuronal tumor new
- *Ependymal tumors*
  - Supratentorial ependymoma
  - Supratentorial ependymoma, *ZFTA* fusion-positive
  - Supratentorial ependymoma, *YAP1* fusion-positive new
  - Posterior fossa ependymoma
  - Posterior fossa ependymoma, Group PFA new
  - Posterior fossa ependymoma, Group PFB new
  - Spinal ependymoma, *MYCN*-amplified new
  - Myxopapillary ependymoma

Choroid plexus tumors
- Choroid plexus papilloma
- Atypical choroid plexus papilloma
- Choroid plexus carcinoma

CNS embryonal tumors
- *Medulloblastomas, molecularly defined*
  - Medulloblastoma, WNT-activated
  - Medulloblastoma, SHH-activated & *TP53*-wild-type
  - Medulloblastoma, SHH-activated & *TP53*-mutant
  - Medulloblastoma, non-WNT/non-SHH
- *Medulloblastoma, histologically defined*
  - Medulloblastoma, histologically defined
- *Other CNS embryonal tumors*
  - Atypical teratoid/rhabdoid tumor
  - Cribriform neuroepithelial tumor[a] new
  - Embryonal tumor with multilayered rosettes
  - CNS neuroblastoma, *FOXR2*-activated new
  - CNS tumor with *BCOR* internal tandem duplication new
  - CNS embryonal tumor NEC/NOS

Pineal region tumors
- Pineoblastoma

Melanocytic tumors
Meningeal melanocytosis and melanomatosis
Tumors of the sellar region
Pituitary endocrine tumors
Pituitary adenoma/PitNET
Pituitary blastoma new
Craniopharyngiomas
Adamantinomatous craniopharyngioma

As mentioned above, in the new classification, pediatric diffuse gliomas are separated into low-grade and high-grade, the latter being more aggressive. High-grade entities are defined by histone 3 status. In this group are included the diffuse midline gliomas (DMG), in which we will focus.

2.1. Diffuse Midline Gliomas (DMG)

DMGs are infiltrative high-grade gliomas that arise in the brain midline, including brainstem, spinal cord, cerebellum and thalamus[10]. This group also includes tumors occurring in the pons, which were named Diffuse Intrinsic Pontine Gliomas (DIPG) until the new CNS tumor reclassification in 2016. However, due to the advances in molecular diagnostics, it was discovered that some tumors occurring in the midbrain share the same mutation; the substitution of one lysine for methionine in the aminoacid number 27 (K27M) in the histone 3 gene(s). Therefore, all these tumors were reclassified into a new tumor entity: diffuse midline glioma, H3K27-altered[5] (Table 2).

In this work we placed the focus on tumors occurring in the pons, previously named DIPG, and that account for 11% of brain tumors in children and adolescents, with a peak of incidence between 5-10 years old.[11] DIPG is the leading cause of pediatric death by brain tumors, with an overall survival (OS) of less than 1 year and a 5-year survival rate of less than 1%.[12]

2.1.1 Diagnosis

DIPGs are characterized by a rapid onset of symptoms. The symptoms depend on the localization of the tumor, but the classic triad of symptoms includes cerebellar signs such as ataxia or dysmetria, long-track signs like increased tone, motor deficit, hyperreflexia or Babinski sign, and cranial nerve palsies[13]. In addition to the previous symptoms, DIPG diagnosis is confirmed by magnetic resonance imaging (MRI) (Figure 2). The typical features of DIPG on MRI include[14]:

- Lesions involving >50% of the pons
- Hypointense T1 imaging
- Hyperintense T2 imaging
- Frequently involvement of the pons and encasement of the basilar artery

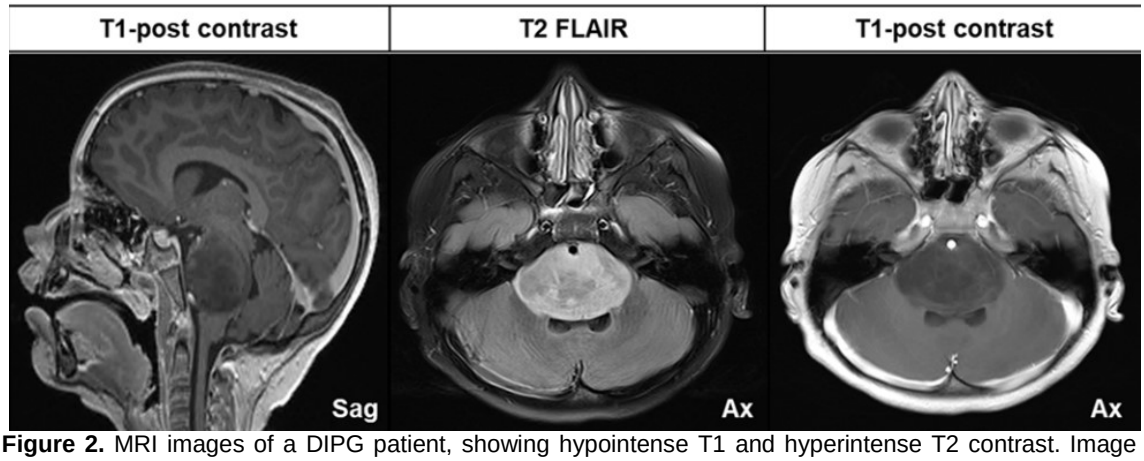

Figure 2. MRI images of a DIPG patient, showing hypointense T1 and hyperintense T2 contrast. Image obtained from Chiang J. *et al.*, 2020.

Although DIPG diagnosis is made by clinicopathology and MRI, there was a huge controversy about the feasibility and safety of tumor biopsies until several years ago. Due to the location of the tumor, a biopsy is a complicated procedure in which the risks and benefits have been weighed. In the last years, it has been demonstrated that DIPGs can be safely biopsied, which is instrumental to obtain a more accurate molecular and histological information for both tumor stratification and treatment.[10,11,13]

2.1.2 Genetic aberrations

In addition to the above-mentioned advantages for clinical management, the ability to obtain tumor biopsy led to an understanding of the genetic alterations prevalent in DIPG. In this way, the high prevalence of the H3K27M mutation in these tumors (80%) was discovered, in addition to other common mutations. Moreover, it made it possible for a more precise tumor reclassification, in the above mentioned tumor class: diffuse midline gliomas, H3K27-altered.[12]

Histone 3 (H3) is part of the nucleosomes, which compose the chromatin by packaging the DNA to a highly compact form. Each nucleosome consists of an octamer of two copies of H3, H4, H2A and H2B. Chromatin has a central role in multiple cellular processes such as transcriptional regulation, DNA repair or chromosome segregation. This makes chromatin biology highly regulated, where post-translational modifications such as histone methylation or acetylation play an important role.[15] Mutations in chromatin-associated proteins are very common in pediatric cancers.[16] There are three

H3 variants; H3.1 and H3.2 that are expressed only during the S-phase of the cell cycle and H3.3 which is constitutively expressed and encoded by the *H3F3A and H3F3B* genes.[17] It is known that the K27M mutation occurs predominantly in *H3F3A* (H3.3) gene (70%), and lesser in *HIST1H3B/C* (H3.1). In normal conditions, H3K27 can be mono-, di- or tri-methylated, or acetylated, being the Polycomb Repressive Complex 2 (PRC2) responsible of H3K27 methylation. H3K27 di- and tri-methylation is associated with transcriptional repression, whereas its acetylation is associated with active transcription.[18] Due to the high prevalence of the mutation, its possible role as a driver of oncogenesis has been extensively studied. However, the effect of this mutation on DIPG is still unclear. It seems to play a dominant role, producing global DNA hypomethylation, which results in genomic instability and transcriptional activation of normally silenced genes.[19]

Other frequent mutations include mutations in *TP53* (40-77%), amplification of *PDGFRA* (13-36%) and *ACVR1* mutation (20-32%).[11,20,21] *TP53* is a well-known tumor suppressor gene implicated in many tumors, where its mutation promotes tumorigenesis. In DIPG, it is frequently associated with H3.3K27M mutation.[11] Platelet-derived growth factor (PDGF) and its receptors are involved in many cellular processes including migration, survival and proliferation. *PDGFRA* aberrations were enough to form gliomas on an *in vivo* model, indicating that it could be an early event in the tumorigenesis process.[22] Finally, the *ACVR1* gene encodes for ALK2, a receptor in the bone morphogenetic protein (BMP) pathway, which is important in embryogenesis and development, and it also regulates adult tissue homeostasis.[23] *ACVR1* mutation was described to activate BMP pathway. In DIPG, even though its role in tumorigenesis is still unknown, *ACVR1* mutation promotes proliferation and survival of tumor cells and it is usually accompanied by H3.1K27M mutation[20] (Figure 3).

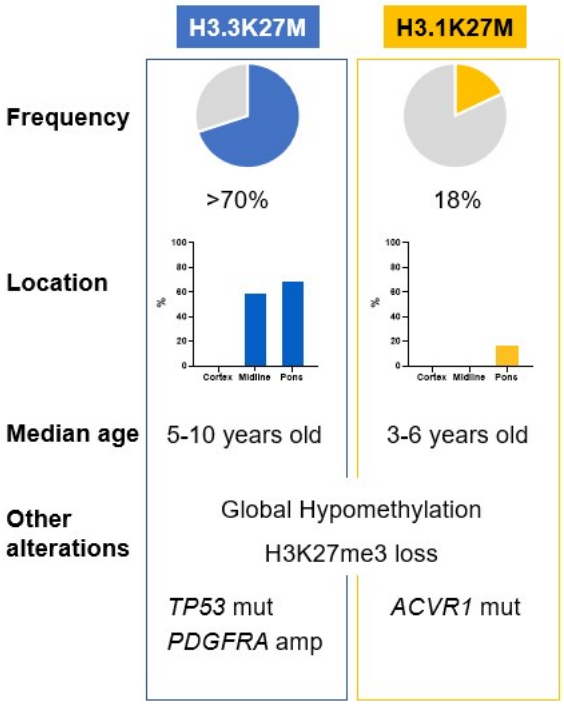

Figure 3. Frequency, location and epidemiology of tumors harboring H3.3K27M and H3.1K27M mutations in DIPG patients. Figure adapted from Pollack I. *et al.,* 2019.[24]

2.1.3 Treatment

Due to the infiltrative nature of the tumor and its pontine location, surgical resection is not an option. The current standard of care for DIPG is radiotherapy, which slightly improves the survival and quality of life of patients.[24] The radiation guidelines include hypofractionated focal radiation of 54-60 Gy given in fractions of 1,8-2 Gy once a day, for 5 days per week over a period of 6 weeks. About 80% of patients have an improvement, but just for 2-3 months.[13] Currently, in most of the cases re-irradiation (±20 Gy) is chosen as a second line treatment after relapse[10].

In contrast to adult glioblastoma (GBM), chemotherapy has not been shown to be effective in the treatment of DIPG. Different strategies have been tried, both alone and in combination with radiotherapy, but none of the cases has improved the effect obtained with radiotherapy.[25,26] One of the limitations is the impossibility of conventional chemotherapies to reach the tumor because in DIPG the blood brain barrier (BBB) is usually intact.[27] Some studies describe that radiotherapy increases the permeability of the BBB, but despite this, there is not an improvement of the efficacy of chemotherapy in combination with radiotherapy. [28]

2.1.4 Tumor microenvironment

Until recent years, it was thought that CNS was an immune privileged site, due to the lack of lymphatic system and the BBB that acts as a blockade to the blood system. However, it is known that immune cells can enter the CNS and mount an immune response.[29,30] Similarly to the lack of knowledge of genetic alterations, the absence of tumor biopsies has also made it difficult to analyze the composition of DIPGs tumor microenvironment (TME). Nevertheless, recent studies have uncovered that DIPGs TME is poorly infiltrated by the immune system and non-inflamatory.[31,32] Tumor-associated macrophages (conformed by resident microglia and peripheral macrophages) are the major immune component of glioma tumors, and in adult GBMs are correlated with overall survival.[33] Previous investigations described adult GBM tumor microenvironment as profoundly immunosuppressive. This is due to the presence of suppressor cells that favor tumor progression, like T regulatory cells and suppressor macrophages/microglia, as well as cytokines that promote the activation and proliferation of these populations.[34,35] DIPG samples have been compared with GBM tumors to evaluate whether their microenvironments were similar. However, both TMEs are very different. The largest population of immune cells in DIPG corresponds to microglia and macrophages, but unlike in GBM, these cells are not inflammatory, and they are not polarized to an immunosuppressive phenotype. On the other hand, the presence of T lymphocytes is minimal in both microenvironments, being almost absent in DIPG. Moreover, these T cells express significantly fewer checkpoint blockade targets, such as PD-1 or CTLA-4. The poor immune infiltration could be related to the low secretion of cytokines and chemokines in the DIPG microenvironment, since the recruitment of these populations is nearly absent.[31,32] All these data support that the TME of DIPG tumors is immunologically “cold”.

In order to increase the immune infiltration and its antitumor activity in DIPG, diverse immune-related therapies have been tested in recent years (Figure 4). Immune checkpoint inhibitors have shown effectivity in several cancers, especially those targeting PD-1/PD-L1 and CTLA-4.[36] Several clinical trials evaluated the effect of checkpoint inhibitors in DIPG, but for the moment they do not seem to improve the response obtained with the conventional standard of care.[37] This could be due to the low expression of PD-1/CTLA-4 and PD-L1 in T cells and DIPG tumor cells, respectively.[31] Another tested strategy is to boost the immune system by vaccination. Recently, an H3.3K27M-targeting peptide vaccination was tested on a clinical trial, since it was discovered an HLA-A*02:01-restricted epitope of the mutation. No adverse toxicities were observed and the 1-year OS for patients with DIPG was 44%, and 39% for other

DMG.[38] Antigen-loaded autologous or allogenic dendritic cells have been also tested as a vaccination strategy. The strategy has shown to induce antitumor response and no severe toxicities, but clinical benefits have to be shown yet.[39,40] The low T-cell infiltration suggests that adoptive cell transfer strategies may be a good option for DIPG. Therefore, some strategies are being used, such as CAR-T cell administration against GD2 disialoganglioside.[41] The results obtained in four patients treated with this CAR-T strategy were recently published. They showed no on-target off-tumor toxicities and they improved the survival of patients to 20 and 26 months.[42]

Finally, another emerging strategy for DIPG is the use of oncolytic viruses; currently there are several clinical trials to test their efficacy. Recently, our group published the results obtained in a phase I clinical trial with the oncolytic adenovirus DNX-2401, which will be later described. Briefly, viral administration was safe and do not cause severe toxicities, whereas the median survival was 17.8 months.[43]

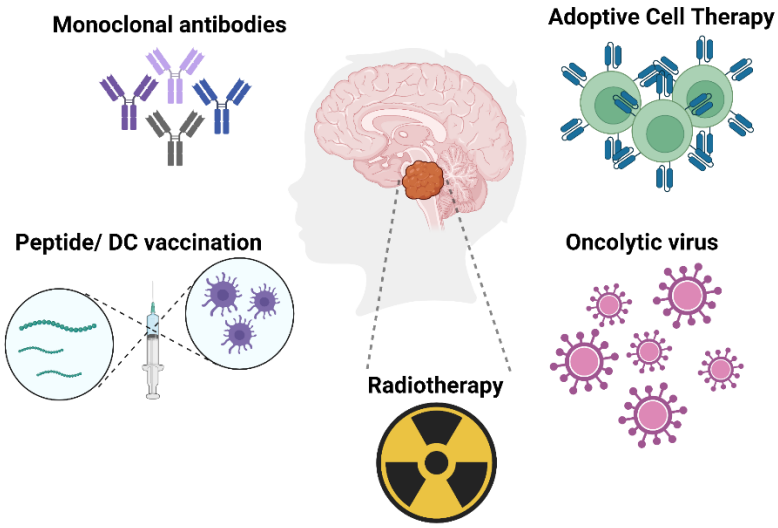

Figure 4. Emerging immunotherapies that are being evaluated in preclinical and clinical studies as a therapeutic strategy for patients with DIPG. At the bottom of the image is the conventional therapy, radiotherapy.

3. Oncolytic virotherapy

Oncolytic virotherapy (OV) is an emerging therapeutic approach that uses native or genetically modified viruses that specifically replicates in and kills tumor cells.[44] Their use emerged from the observation that patients with hematological malignancies underwent brief remissions after contracting an infectious disease.[45] Viruses started to be used as an anticancer therapy at the end of the 19th century, but there was not a real knowledge about the viral etiology at that time. In the 1950s and 1960s the understanding of virus

increased rapidly and oncolytic properties of viruses were also evaluated.[46] Alice Moore was the first to test oncolytic virotherapy in rodent models, using the Russian Far East encephalitis virus in five types of tumors.[47] Observations made in those studies showed that OV had antitumor effect, however they should be manipulated to make it more specific to cancer cells. The first hypotheses made by Moore and his colleagues were that if they made several passes of the virus through tumors, it would become more destructive as it would acquire mutations.[48] Interestingly, in 1968 it was shown that the virus genome could be modified, but it was not until the 1990s that the viral genome was finally modified.[49] The results obtained during these years using OV in several cancers prompted the approbation of the first oncolytic virus by the Food and Drug Administration (FDA); the herpes simplex virus, talimogene laherparepvec (T-VEC) for the treatment of advanced melanoma.[50]

3.1. Oncolytic properties

One of the problems of conventional therapies is the toxicity they generate because they also target and damage healthy tissue. Therefore, the ideal therapy would be the one that minimizes toxicity, especially in children, since they are still developing. Oncolytic viruses could be good candidates because they selectively target tumor cells without damaging normal cells, in addition to be easily modified to increase selectivity.

Tumor selectivity starts with the viral tropism for cell surface receptors, as viruses use cell receptors that are highly expressed in tumor cells to enter into the cells. For example, measles virus uses the CD46 receptor that is frequently expressed in tumor cells to avoid complement recognition[51], and coxsackievirus uses the adhesion molecule ICAM-1 which is highly expressed in breast cancer, multiple myeloma or melanoma. [52] This characteristic has also been considered when genetically modifying viruses to make them more selective. Additional examples include an oncolytic adenovirus that was modified by introducing an arginine-glycine-aspartic acid (RGD) motif in its fiber to bind $\alpha_v\beta_3$ and $\alpha_v\beta_5$ integrins that are frequently overexpressed in different malignancies.[53] Another feature of oncolytic viruses, that confers them with tumor selectivity, is that cancer cells are more permissive for viral replication. Cancer cells usually deregulate cellular signaling pathways involved in proliferation, survival, or immune system evasion, and viruses take advantage of this to replicate and spread. Often, cancer cells overexpress anti-apoptotic molecules that are targeted by some oncolytic viruses in order to have more time to infect, multiply and spread.[54,55] In relation to this, cancer cells also have less anti-viral response elements to detect and eliminate viral particles. These pathways can be activated by IFN release, which activates the PKR protein kinase that

recognizes viral components, promoting protein synthesis termination, cell death and viral clearance.[56] Sometimes, in cancer cells, the IFN pathway and PKR activity is abnormal, and thus, viral spread is not compromised.[57]

In addition to the above-mentioned tumor selective properties, other approaches have been used to genetically modify the viral genome.[44,58] One technique is to place viral genes under the control of tumor-specific promoters, frequently used to modify adenoviruses. The adenoviral E1A gene has been modified to be under the control of the prostate-specific antigen (PSA) promoter to direct viral activity into prostate cells[59], or coupled to the human telomerase reverse transcriptase (hTERT).[60] Using this approach, some adenoviruses have been also modified to deliver suicide genes with promoters that have increased activity in specific tumors. This is the case of the HSV-1 thymidine kinase, which has been placed under the control of the osteocalcin promoter that is overexpressed in patients with bone metastases.[61] Finally, other approaches focus in increasing the immune response generated due to the viral infection. Normally, infected cells release danger-associated molecular patterns (DAMPs) and pathogen-associated molecular patterns (PAMPs), which activate toll-like receptors (TLRs) that are key to activate antigen-presenting cells (APCs), natural killer cells (NK) and T cells.[58] In order to further increase the generated immune response, immunostimulatory molecules have been introduced into the viral backbone. This is the case of T-VEC that contains the human GM-CSF to recruit and activate APCs[62] or an adenovirus that overexpresses the heat sock protein 70 (HSP70) to improve antigen presentation.[63] Other strategies introduce cytokines, mostly interleukins, into the backbone of different oncolytic viruses, which have been tested for the treatment of different solid tumors such as brain tumors.[64] For example, an HSV[65] and vaccinia virus[66] expressing IL-12, or other vaccinia virus expressing IL-21 or IL-15. [67,68]

3.2. Mechanism of action

Oncolytic viruses have a double mechanism of action against tumors; they produce tumor cell lysis in addition to promote an antitumor immune response (Figure 5).

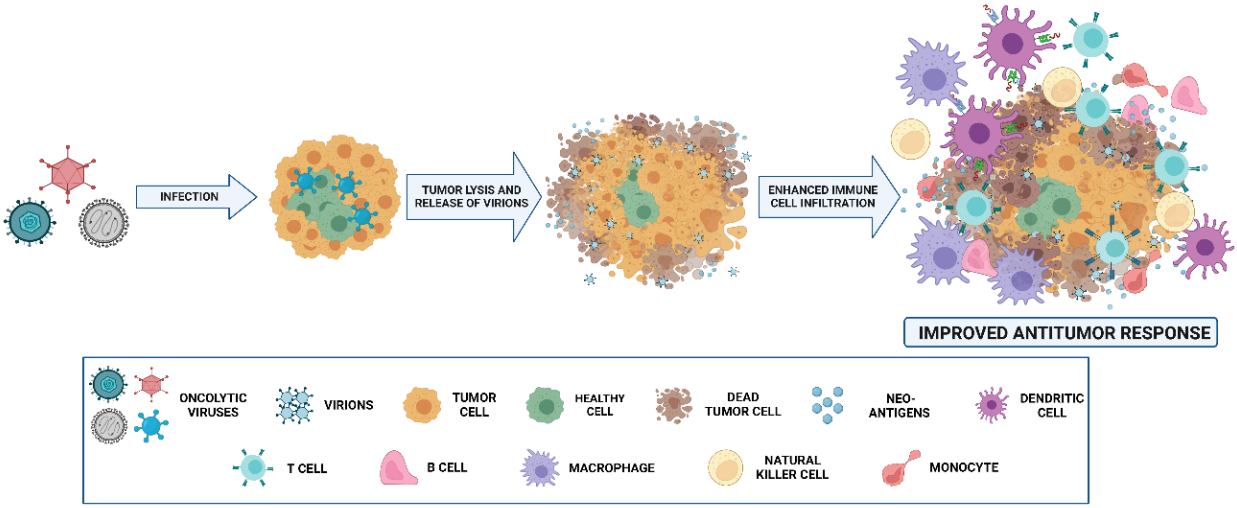

Figure 5. Mechanism of action of oncolytic viruses. Viruses replicate inside the tumor, producing the lysis of tumor cells and the release of new virions. Due to the release of new antigens, DAMPs and PAMPs, there is an increased immune infiltrate in the tumor that will attack the tumor. Figure obtained from de la Nava D *et al.*, 2022.[69]

Viruses need nucleic acids, amino acids and lipids to replicate. However, they are not able to produce them, and therefore, viruses sequester the cellular machinery to produce the biomolecules necessary for replication. Thus, the normal physiological processes of tumor cells are destroyed, causing cell death.[70,71] It was described that the type of cell death caused by oncolytic virus is a type of regulated death that activates the adaptive immune response, called immunogenic cell death (ICD). As infected tumor cells are dying, they release DAMPs (ATP, HSP70 and HSP90, HMGB1 or calreticulin exposure to the membrane) and cytokines (IFNγ, TNFα, IL-12), which activate the adaptive immune response by promoting the maturation of APCs.[72] Afterwards, APCs will present antigens to CD4 and CD8 T cells, and once activated, the latter will destroy tumor cells.[44] On the other hand, PAMPs, which include viral nucleic acids and proteins, will also be released, promoting the activation of the immune response through TLRs. Furthermore, cancer cell death will result in the release of tumor antigens that previously were hidden from the immune system.[44] Taking into account all of the above, it is clear that the immune system plays an important role in the antitumor action of OV.

In this work, an oncolytic adenovirus was tested as a therapeutic approach for DIPG.

3.3. Adenovirus

Adenoviruses are a non-enveloped double-stranded DNA viruses of 70-90nm size that belong to the *Adenoviridae* family. In normal conditions, they can cause mild infections in the respiratory tract, conjunctiva or gastrointestinal tract.[73] *Adenoviridae* family is

composed of up to 50 serotypes, named with consecutive numbers, which are classified within 7 species (HAdV-A through HAdV-G).[74]

The adenovirus genome is a linear double-stranded DNA of about 36 Kb long that is transcribed at different time points, generating transcripts that are classified into early (E), intermediate (I) and late (L) (Figure 6).[75] The early regions, E1A, E1B, E2, E3 and E4, are the first to be transcribed and function as activators of transcription of the rest of regions. The E1A gene induce the progression of the cell cycle to S phase and promotes the transcription of the other viral regions. E1B inhibits apoptosis though the inhibition of p53, and E2 proteins mediate viral DNA replication. E3 proteins protect the virus from the immune system clearance; they prevent T cell recognition by blocking antigen presentation though MHC-I and inhibit the apoptosis of infected cells downregulating membrane receptors involved in TNFα-mediated apoptosis. Finally, E4 is involved in different cell signaling that regulate apoptosis and inhibit DNA repair machinery.[76,77] Intermediate regions are composed by L4-22K and L4-33K that allow the expression of late genes by activating the major late promoter (MLP), and structural proteins pIX and IVa2 that help in viral packaging into virions.[76]

Finally, late genes correspond to L1, L2, L3, L4 and L5 and codify to proteins that compose the viral capsid and other elements for the correct assembly and virion maturation. These genes are expressed through alternative splicing from the MLP.[76] The adenoviral structure corresponds to an icosahedral capsid mainly composed by the structural proteins hexon, penton and fiber. The major component is the homotrimeric hexon, since the capsid contains 240 units on his faces. In each of the vertices there is a penton, from which the fiber protrudes.[78] The fiber protein is composed of 3 domains; a proximal tail that anchors to the penton, a distal knob that serves for receptor recognition and a shaft that separates both parts (Figure 6).[79]

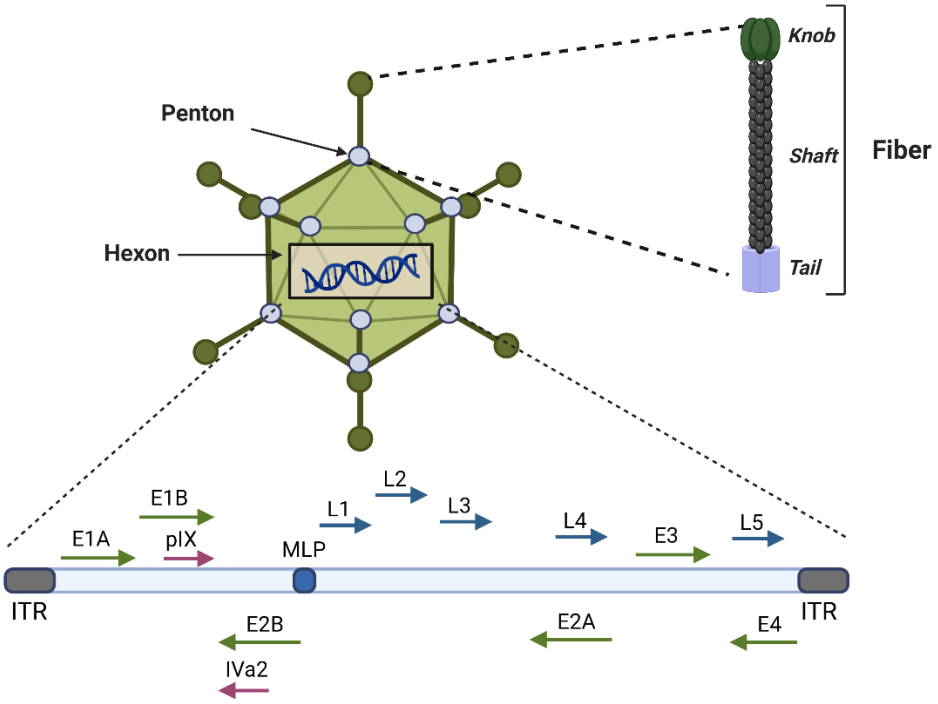

Figure 6. Adenovirus structure and genome. It is a double stranded DNA non-enveloped virus with an icosahedral capsid composed of hexon, penton and fiber. Its genome is transcribed at different time-points; early (green), intermediate (pink) and late (blue), depending on the replication, and it is flanked by two inverted terminal repetitions (ITR).

3.3.1 Adenovirus cycle

The adenovirus infection starts with the recognition of the cell surface receptor by the fiber. The knob of the fiber will bind to the receptor, usually the coxsackie and adenovirus receptor (CAR) or CD46 for adenovirus of serotype B, between others.[80] Afterwards, an arginine-glycine-aspartic acid (RGD) motif that is present on the penton base, will bind $\alpha_v\beta_3$ and $\alpha_v\beta_5$ integrins, facilitating the entry of the virus by endosome.[81] The endosome is then acidified, causing the dissociation of the capsid and the release of protein VI that will lysate the endosome.[82,83] The virus will now move to the nucleus through microtubules, and when it reaches the nuclear pores, the virus is disassembled and the genomic content enters the nucleus.[84]

Once inside the nucleus, the transcription starts. First, the early E1A gene is transcribed, which promotes the transcription of the rest of early genes. These early proteins have the function of activating the expression of cell proteins for DNA synthesis, activating other viral genes, and avoiding premature cell death by the host cell defenses.[76] Then, the viral DNA is replicated in a process in which more than three virus-encoded proteins are involved: terminal protein (TP) that acts as a primer, DNA-binding protein (DBP) and DNA polymerase. When the replication starts, the transcription moves from early to late regions, to obtain the structural proteins. This transcription is driven by the MLP, in a

complex process involving polyadenylation signals and splicing.[85] Finally, the DNA is encapsulated in the nucleus and new virions are released causing cell lysis (Figure 7).[86]

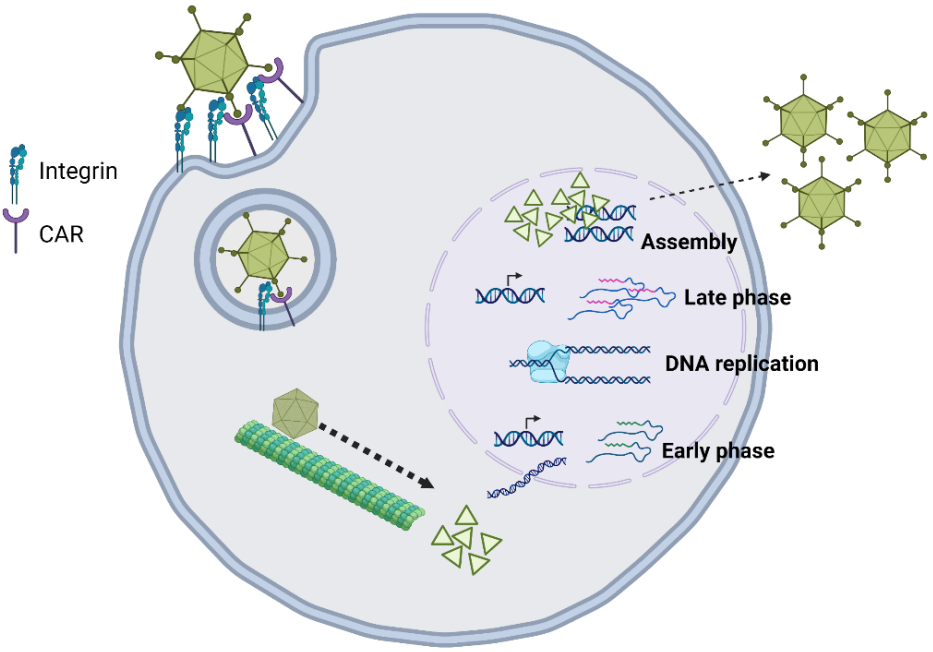

Figure 7. Adenovirus cycle. The virus enters the cells by endocytosis after the recognition of cell surface receptors. It goes to the nucleus through microtubules and once inside the nucleus, transcription of early proteins, DNA replication, transcription of late proteins, and viral assembly happen. Finally new virions are released, causing cell lysis. Figure adapted from Garcia-Moure M. *et al*., 2017.[79]

3.3.2 Adenovirus as anticancer tool

Adenoviruses are among the most used oncolytic viruses as therapeutic tools. This is due to their safety, since they do not produce dangerous diseases and do not integrate into the host genome. Additionally, the size of their genome allows the introduction of foreign products into the virus making this virus a versatile biotherapeutic tool. The most commonly used adenovirus serotypes are 2 and 5. In this work, we have used the oncolytic adenovirus Delta-24-RGD, which will be explained below.

3.3.3 Delta-24-RGD

Delta-24-RGD is an oncolytic adenovirus of serotype 5 that contains two genetic modifications. The first confers tumor-selectivity, and it is the 24bp deletion of the E1A gene, in the region of the binding to Rb protein. In normal conditions, the mutated E1A cannot bind to pRb and therefore, there will not be viral replication. However, tumor cells usually have mutated Rb protein or altered pathway that at the end, promote the release of the transcription factor E2F, which initiates viral replication (Figure 8).[87]

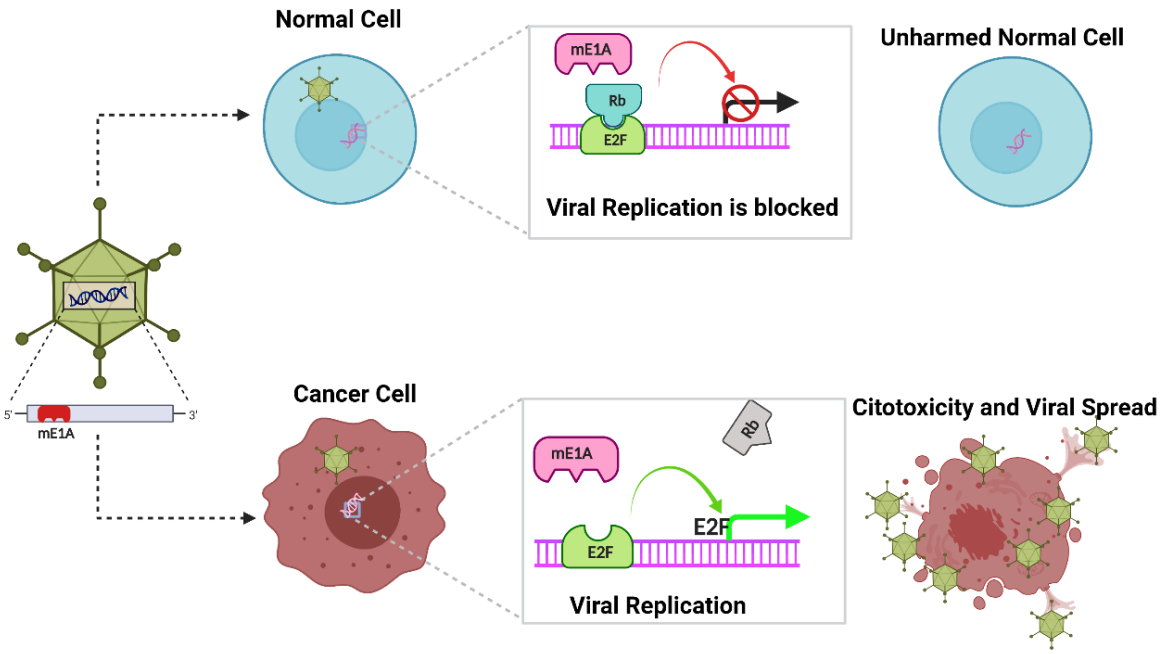

Figure 8. The deletion of 24bp of E1A gene impedes its union to Rb protein, which protects normal cell from viral replication. However, it does not alter the normal cycle in tumor cells, producing cell lysis and viral spread.

The second modification was added to the original Delta-24 adenovirus in order to increase infectivity. The natural receptor for the adenovirus is the CAR, which is not always broadly expressed and the tumor cells downregulate its expression as a mechanism of defense.[88,89] Thus, an arginine-glycine-aspartic acid (RGD) motif that normally is present in the penton has been introduced into the fiber knob, making possible the recognition of the cell through integrins, which are highly expressed by a variety of tumor cells (Figure 9).[90]

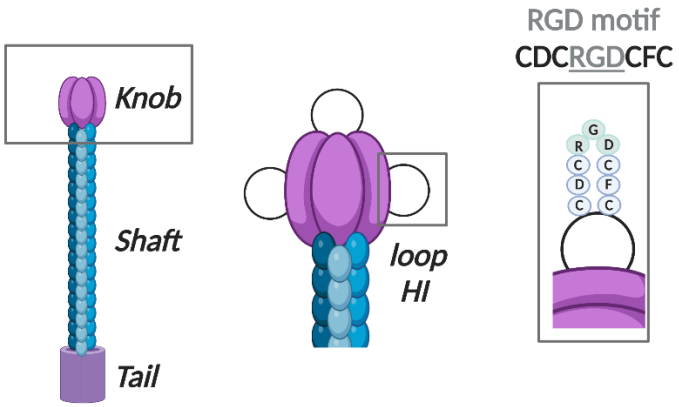

Figure 9. Illustration of RGD motif into the fiber knob.

In the area of brain tumors, Delta-24-RGD was first tested in adult GBM, in which an increase in median survival and a higher immune infiltration in immunocompetent mouse models were observed.[91] The good results obtained in preclinical studies encouraged the translation of Delta-24-RGD (DNX-2401) into the clinic, in a phase I study for adult patients with recurrent GBM. A dose-escalation of the virus was evaluated, no dose-limiting toxicities were observed and a reduction of tumor mass accompanied with an increased immune infiltration were obtained. Moreover, 20% of patients survived more than 3 years, 3 of them showing >95% of tumor reduction.[92]

Afterwards, our group evaluated the effect of Delta-24-RGD in orthotopic murine models of DIPG and pediatric high-grade gliomas (pHGG). After confirming that CAR and integrins were expressed in cell lines and tumors, the viral effect was evaluated both *in vitro* and *in vivo*. Delta-24-RGD was able to infect and replicate in human cell lines, in addition to significantly increasing the survival of treated mice in both tumor models. Besides, a higher T cell infiltration was observed in DIPG tumors, which showed an active phenotype by IFN measurement.[93] Since the standard of care of DIPG patients is radiotherapy, the combination with Delta-24-RGD was evaluated, and a potent synergistic effect was observed.[94]

Continuing with preclinical studies, our group has also evaluated the effect of Delta-24-RGD on tumors of embryonal origin AT/RT and PNET. We have demonstrated that *in vitro,* the virus can infect and kill cells in an immunogenic manner. Furthermore, *in vivo*, the virus significantly prolonged the survival of mice resulting in long-term survivors. More interestingly, humanized models were used, in which the virus significantly increased survival in addition to increase immune infiltration.[95]

The encouraging results obtained in the preclinical field, prompted the transition of the virus to the clinic in a phase I, dose-escalation study for newly diagnosed DIPG patients. Despite that the primary objective was to evaluate the safety of the administration, the survival benefit was also evaluated. A total of 12 patients (3-18 years old) were enrolled and received a single dose of DNX-2401. Four patients received a dose of 10^{10} viral particles and the subsequent eight patients $5x10^{10}$ viral particles, with subsequent radiotherapy in 11 of 12 patients (median of 54 Gy, in a median interval of 17 days after viral administration). The most frequent adverse effects were headache, vomiting, neurological deterioration, fatigue and fever and no grade 4 and 5 adverse effects were observed. Regarding the clinical response, 3 patients (25%) had a partial response (>25% of tumor reduction for ≥8 weeks), with durations of 3.5, 7.6 and 10.3 months. Stable disease was observed in eight patients (67%). Therefore, disease control, which

includes complete response, partial response and stable disease, was obtained in 11 patients; 92% of patients benefit from DNX-2401 administration. Although progression free survival (PFS) was difficult to determine due to pseudoprogression, the clinicians determined a PFS of 10.7 months. The median OS was 17.8 months, and three patients were still alive 19.3, 31.4 and 33.5 months after DNX-2401 administration. Finally, the samples obtained in one patient allowed the analyses of immune infiltration by multiplexed immunofluorescence (IF) and single-cell RNA sequencing. Results showed that after viral administration, there was an increase of T cell and myeloid cells in the tumor, while macrophages had an increment of pathways associated with virus processes and immune response.[43]

3.3.4 Delta-24-ACT

Due to the impressive results obtained with the Delta-24-RGD virus in both preclinical and clinical studies, we decided to continue with this approach. As discussed above, Delta-24-RGD virus was shown to promote an increased immune infiltrate in the tumor. However, we believe that the functionality of this infiltrate was not sufficient for a complete antitumor response, and that we can further promote a more active phenotype of immune cells. For that purpose, we created a new adenovirus, Delta-24-ACT that incorporates 4-1BBL. Delta-24-ACT contains the same genetic modifications of Delta-24-RGD (24bp deletion of E1A and RGD insertion), but incorporates 4-1BBL in the place of E3 (Figure 10).[96,97]

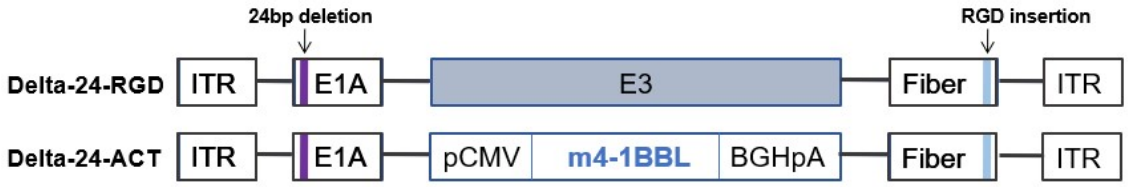

Figure 10. Delta-24-ACT structure. It contains the same genetic modifications as Delta-24-RGD but mouse 4-1BBL has been placed on the E3 place, flanked by cytomegalovirus promoter (pCMV) and bovine growth factor polyadenylation signal (BHGpA).

4-1BB (CD137, TNFRSF9) is a co-stimulatory receptor of the TNF superfamily.[98] It is expressed on T cells, and its expression is induced by antigen-recognition and potentiated by CD28 signaling. It is also expressed on regulatory T cells (Treg), dendritic cells (DC) and NK cells. The only known ligand is 4-1BBL, which is expressed on APCs such as macrophages, DCs and B cells and also have an inducible expression.[99] 4-1BB co-stimulation works in both CD4 and CD8, but preferentially in CD8 T cells, promoting the cytolytic effect, cell proliferation and survival, and cytokine secretion. It also plays a role in generation and maintenance of CD8 memory cell and in activating NK cells.[100]

Agonist antibodies targeting 4-1BB have been evaluated in clinical trials for different tumors like melanoma, hematological malignancies, and several solid tumors. This is the case of Urelumab, an anti-41BB antibody that was clinically tested with promising antitumor results. However, it was withdrawn for causing two deaths due to hepatotoxicity. Therefore, another antibody, Utomilumab, was developed, which decreased liver toxicity but with less clinical benefit. In order to improve this issue, new strategies have emerged to target 4-1BB into the tumor and thus, avoid toxicity. [101,102]

One strategy is the use of bispecific antibodies, which were developed to target both 4-1BB and a tumoral antigen. In this way, the 4-1BB agonism will be strictly dependent on the presence of tumoral antigens. This is the case of 4-1BB-EGFR[103], 4-1BB-Her2[102] or 4-1BB-FAP[104] bispecific antibodies, which demonstrate a therapeutic effect comparable to that obtained with the anti-41BB antibody, but without causing hepatotoxicity. Other bispecific antibodies include 4-1BB-OX40[105] or 4-1BB-PDL1[106], which are also effective and safe. Another described strategy is "masked" antibodies, such as an anti-41BB antibody prodrug called Probody therapeutic. This antibody has a linker attached to a "masking" peptide that binds to the antigen-binding site. The linker will be cleaved only by proteases of the tumor microenvironment, producing the release of the peptide and leaving the antigen-binding site free for its function.[107] In our case, we targeted 4-1BB agonism into the tumor by introducing it into the Delta-24-RGD virus (Delta-24-ACT), being intratumorally administered.

3.3.5 Delta-24-RGDOX

With the same rationale as above, to boost the immune system, in Dr. Fueyo´s lab, with whom we frequently collaborate, they engineered a Delta-24-RGD virus armed with the OX40 ligand (OX40L). Delta-24-RGDOX also contains deletion in E1A as well as the introduction of RGD motif on the fiber, and incorporates OX40L in the place of E3 (Figure 11).[108]

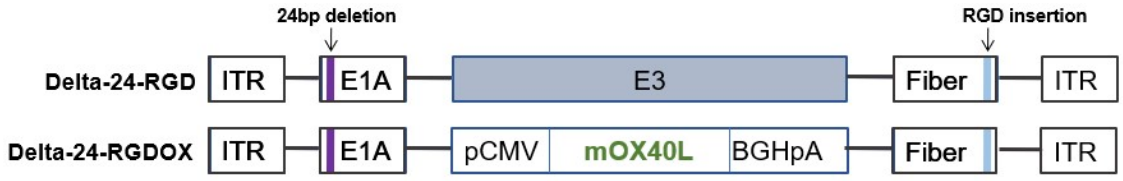

Figure 11. Delta-24-RGDOX structure. It contains the same genetic modifications as Delta-24-RGD but mouse OX40-L has been placed on the E3 place, flanked by cytomegalovirus promoter (pCMV) and bovine growth factor polyadenylation signal (BHGpA).

OX40 (CD134, TNFRSF4) is a co-stimulatory receptor of TNF superfamily.[98] It is transiently expressed on CD4 and CD8 T cells and NK cells, induced through TCR signaling. It is also expressed constitutively on Treg cells. Its ligand, OX40L, is transiently expressed in APCs as well.[109] OX40 signaling promotes CD8 and CD4 T cell proliferation and survival of effector and memory phenotypes, having more effect on CD4 cells. It also promotes NK cell activation and function. In all these populations OX40-OX40L co-stimulation promotes cell division, survival, differentiation and cytokine production.[110]

Delta-24-RGDOX has been evaluated by Dr. Fueyo´s and Dr. Gomez-Manzano´s lab, in several studies in adult GBM. They showed that Delta-24-RGDOX increases survival and tumor-specific immune response. In addition, the combination of the virus with an anti-PDL1 antibody had a synergistic effect.[108] They also demonstrated that Delta-24-RGDOX has a systemic effect that could be used for metastasis. Because when treating intracranial GBM tumors with Delta-24-RGDOX, they also observed tumor reduction of distal subcutaneous tumors.[111] Recently, a study has shown that the virus causes a change in the TME by increasing immunosuppressive mechanisms such as the Indoleamine 2,3-dioxygenase (IDO) pathway. IDO produces the catabolism of tryptophan to kynurenine, an activator of aryl hydrocarbon receptor (AhR), promoting robust immunosuppression. Therefore, they use an IDO inhibitor to potentiate the effect of the virus, and observe a significant increase of survival and infiltration.[112]

The objective of using Delta-24-ACT or Delta-24-RGDOX adenoviruses is to increase the antitumor immune response, since the tumor cells will express 4-1BBL and OX40L, respectively, in their membranes, promoting the activation of immune cells (Figure 12).

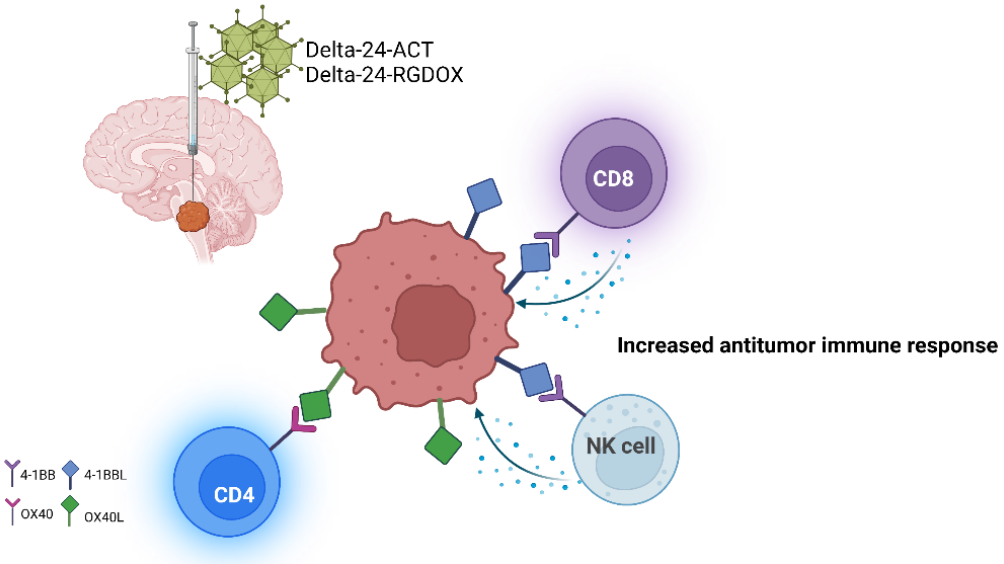

Figure 12. Intratumoral administration of Delta-24-ACT and Delta-24-RGDOX will promote the expression of 4-1BBL and OX40L on the membrane of infected cells, producing the increment of the antitumor immune response.

4. T regulatory cells (Treg)

In 1995 Sakaguchi *et al.* described a unique $CD4^+$ population that expressed CD25 and had regulatory functions and called it T regulatory cells. It was not until 2003 when the *Forkhead Box Protein P3* (*FOXP3*) was discovered, which was described to be fundamental for Treg development, function and homeostasis. In regards to their phenotype, Tregs can be described as $CD4^+CD25^+Foxp3^+$.[113] Tregs are regulatory cells whose main functions are to maintain immune homeostasis, prevent autoimmune disorders through the mediation of peripheral tolerance (lack of response to self-antigens) and moderate the inflammation caused by pathogens or other insults.[114]

4.1. Treg development

Two different Treg subtypes are differentiated depending on the developmental origin; thymus Treg (tTreg) or natural Treg (nTreg) and peripheral Treg (pTreg) or induced Treg (iTreg).[113]

nTreg develop in the thymus during the negative and positive processes. The thymic selection process guarantees that T cells react against foreign antigens without reacting against self-antigens. First, positive selection occurs, by which those cells that are able to recognize their own MHC molecules will continue their development, while those that do not will die by apoptosis. Next, self-antigens are presented to the surviving cells. Those that recognize antigens with high affinity are eliminated by negative selection, only those that recognize them with low affinity will continue. Treg develop from T cells that recognize self-antigens with intermediate affinity.[115]

On the other hand, iTreg develop in the periphery from CD4 conventional T cells that recognize exogenous antigens in presence of cytokines such as IL-2 or TGF-β. Other cytokines like IL-4 and IL-13 can also induce iTreg. Within the iTreg we differentiate 2 subtypes; the Tr1 that differentiate in the presence of IL-10 and Th3 that differentiate in the presence of TGF- β. These cells secrete large quantities of the cytokines with which they develop.[113]

4.2. Suppression mechanisms

Treg have the ability of suppressing the function of other immune cell populations through different mechanisms (Figure 13).

Cytokine release: Treg secrete immunosuppressor cytokines like IL-10, TGF- β and IL-35 that inhibit the function of T effector cells, or potentiate the immunosuppressive phenotype of macrophages.[116,117]

Cell cytolysis: They can secrete granzyme and perforin that cause the direct cytolysis of T effector cells and NK cells. [118,119]

Metabolic disruption: Tregs constitutively express CD25 and require high levels of IL-2 to survive and proliferate. Effector T cells also need IL-2 to proliferate, so by deprivation of this cytokine due to its high uptake, it causes the death of effector T cells.[120,121] On the other hand, Tregs express CD39 and CD73 on their membrane. The generated adenosine causes the suppression of T effector cells through its binding to $A_{2A}R$ receptor. In addition, Tregs directly transfer the potent inhibitory cAMP to effector T cells through gap junctions.[122,123]

Targeting dendritic cells: Tregs constitutively express CTLA-4, which binds to CD80/86 in dendritic cells, promoting IDO expression. IDO produces the catabolism of tryptophan to kynurenine, an activator of AhR, resulting in the suppression of effector T cells.[124,125]

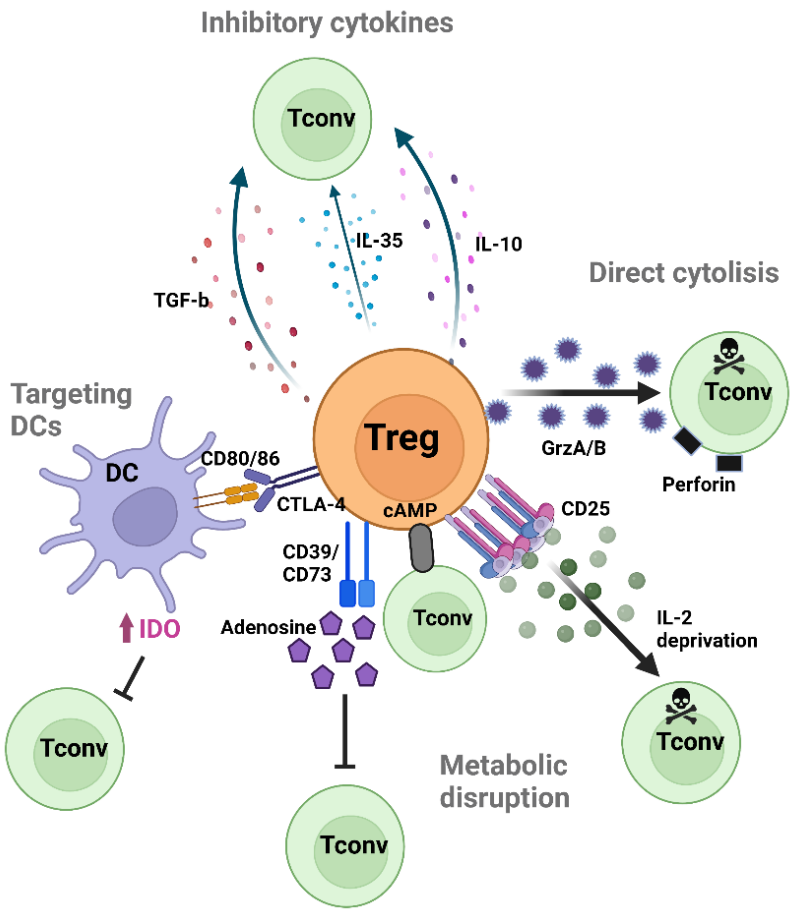

Figure 13. Treg suppression mechanisms. Adapted from Workman CJ *et al,* 2009 with Biorender.[113]

4.3. Treg in disease

Due to their important role in maintaining self-tolerance, Tregs prevent from autoimmune diseases. Therefore, when Tregs do not function properly, the activity of effector cells that will recognize their own antigens as foreign is not blocked, resulting in an exacerbated immune response that leads to disease. This occurs in autoimmune diseases such as inflammatory bowel disease, allergy and asthma, multiple sclerosis or type I diabetes.[113]

However, in cancer it happens just the opposite, Tregs are usually upregulated as a mechanism of tumor-escape, avoiding the correct antitumor immune response.[113] Treg can be induced inside the tumor due to a suppressive microenvironment from CD4 conventional cells. Moreover, they can be attracted through chemokines expressed by inflammatory cells inside the tumors. Tregs express multiple chemokine receptors; CCR4, CCR5, CCR8 or CCR10, whose ligands are CCL17/22, CCL5, CCL1 and CCL28, respectively.[126] Furthermore, Tregs have a high metabolic adaptation into the TME.

Usually, tumors change to a lactate-rich, hypoxic environment that is unfavorable for effector cells but favors Tregs.[127] It was described that FOXP3 promotes OXPHOS and NAD^+ oxidation, which allows Tregs to use lactate as a source of energy.[128]

For all of the above, different strategies have been evaluated to eliminate the suppressive function of Tregs. The most widely used approach is the use of depleting antibodies, such as anti-CTLA4 and anti-CD25 antibodies that deplete Tregs by antibody-dependent cell-mediated cytotoxicity (ADCC), because those molecules are highly expressed on Tregs.[129,130] More recently, antibodies against CD39 and CD73 have been evaluated, or an antisense oligonucleotide (AZD8701) specific against FOXP3, which is in clinical trials.[131]

Regarding the role of 4-1BB and OX40 in Tregs functionality and development, it is known that OX40 is constitutively expressed whereas 4-1BB is expressed at low levels in naïve cells and increases when Tregs activate. Both receptors are overexpressed on tumoral Treg.[132] It was described both 4-1BB and OX40 co-stimulation promote Treg survival and proliferation but there is huge controversy about their role in the suppressive effect; since it depends on the cytokine milieu.[133–135]

Hypothesis and objectives

HYPOTHESIS

Diffuse pontine gliomas (DIPGs) are very aggressive brain tumors that affect children, with a median overall survival of less than one year. Therefore, it is necessary to search for new therapeutic strategies for this tumor. The promising results obtained with the adenovirus Delta-24-RGD both in preclinical models and in a phase I trial in children with DIPG, prompted us to continue along this line. However, we believe that there is still room for improvement regarding the antitumor effect of the virus. Delta-24-RGD promotes an increase of immune infiltration into the tumor, but we could further improve the activation of the infiltration in order to improve survival. Therefore, we have used two adenoviruses containing 4-1BBL (Delta-24-ACT) and OX40L (Delta-24-RGDOX) for the treatment of DIPG orthotopic models. 4-1BBL and OX40L are costimulatory ligands expressed by antigen presenting cells (APCs). The stimulation of 4-1BB and OX40 receptors by its ligands, promote the activation and maturation of T lymphocytes and NK cells, as well as maturation of $CD8^+$ and $CD4^+$ memory T cells.

Our hypothesis is that the treatment of DIPG tumors with Delta-24-ACT and Delta-24-RGDOX viruses will enhance the effect of the Delta-24-RGD adenovirus since, in addition to the oncolytic effect of the virus, the co-stimulatory ligands will potentiate the activation of the immune infiltrate generated by the viral action.

OBJECTIVES

1. To characterize the antitumor effect of Delta-24-ACT and Delta-24-RGDOX oncolytic adenoviruses in *in vitro* and *in vivo* DIPG models.
2. To analyze the changes in the DIPG tumor microenvironment after Delta-24-ACT and Delta-24-RGDOX administration.
3. To elucidate the mechanisms of resistance developed by the tumor in common for both Delta-24-ACT and Delta-24-RGDOX, due to the presence of 4-1BB and OX40 ligands.

Materials and methods

1. Cell lines

The murine NP53 and XFM cell lines were provided by Dr. Becher (Mount Sinai, New York, USA). Both cell lines were obtained from DIPG tumors generated in genetically modified mice. NP53 was generated from a DIPG tumor driven by PDGF-β signaling, *TP53* loss and an H3.3K27M mutation,[136] whereas XFM was generated from a tumor induced by PDGF-β signaling and INK4A/ ARF loss.[137] Both cell lines were maintained in Dulbecco´s Modified Eagle Medium (DMEM) supplemented with 10% fetal bovine serum and 1% antibiotics (streptomycin, penicillin).

The SU-DIPG IV cell line was kindly provided by Dr. Michelle Monje (Standford, California, USA), and TP54 was kindly provided by Marie-Pierre Junier and Hervé Chneiweiss (INSERM Institute, Paris, France). Both human cell lines were maintained as neurospheres in serum-free specialized media. TP54 cells were cultured in medium supplemented with a human neural stem cell proliferation supplement (NeuroCultTM NS-A Proliferation Kit, 05751, STEMCELL Technologies), basic fibroblast growth factor and epidermal growth factor (20 ng/mL Sigma-Aldrich), while SU-DIPG IV cells were cultured in DMEM/F12 supplemented with B27 (17504-044, Gibco), heparin and basic fibroblast growth factor and epidermal growth factor (20 ng/mL). HEK293 (ATCC®CRL-1573™) and A549 (ATCC® CCL-185™) cell lines were used for viral construction. All cell lines were maintained in a humidified atmosphere at 37°C and 5% CO_2.

2. Delta-24-ACT construction

Delta-24-ACT was constructed by preserving the Delta-24-RGD modifications of a 24-base pair deletion and introduction of RGD. To this end, the expendable adenoviral locus E3 was replaced by an expression cassette encoding mouse 4-1BBL gene (Figure 10). Briefly, murine 4-1BBL was first cloned into a pCDNA3.1 plasmid using the *KpnI* and *XhoI* restriction enzymes (New England Biolabs). Then, m4-1BBL flanked with the cytomegalovirus promoter (CMV) and bovine growth hormone polyadenylation signal (BGH polyA) were subcloned into the pAB26-RGD shuttle plasmid[87] at the *ClaI*/*BamHI* restriction sites. Finally, the m4-1BBL expression cassette was cloned into the pVK-500C-Δ24 plasmid, which contains the full Delta-24-RGD genome, and the Delta-24 plasmid was generated by homologous recombination. pVK-500C-Δ24 and pAB26-m4-1BBL were linearized with *SwaI* and *EcoRV* restriction enzymes, respectively, and electroporated in the recombinase positive E.coli strain BJ5183. Individual clones were screened by Sanger sequencing to confirm the positive cloning. To allow viral production, pVK-500C-m41BBL was linearized with *Pac I* and transfected into HEK293 cells with

Lipofectamine® 2000 (Invitrogen). Once cytopathic effect was observed, infected cultures were harvested and subjected to three freeze/thaw cycles to release the viral particles. Then, after confirmation of genetic modifications by PCR and sequencing, Delta-24-ACT was amplified in A549 cells, purified and stored at -80°C (Figure 14).

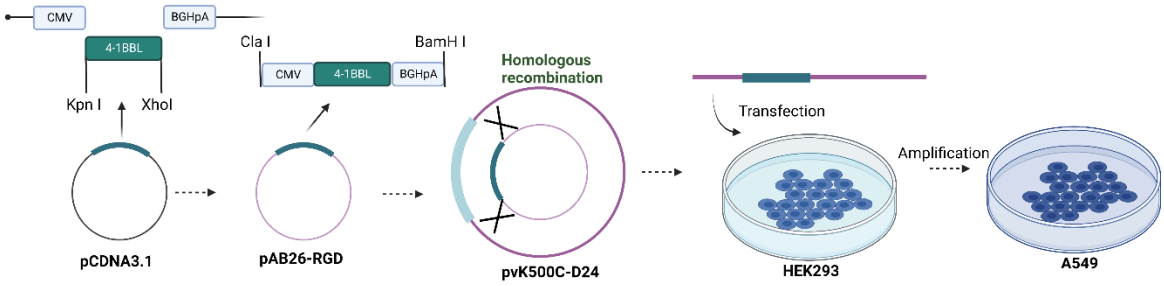

Figure 14. Schematic representation of Delta-24-ACT construction and production.

3. Expression of viral ligands

3.1. Gene expression

3.1.1 RNA extraction

Total RNA from infected cells was extracted using TRIzol™ reagent (Life technologies), which is a lysis solution composed of phenol isothiocyanate and guanidine. Briefly, pellets were resuspended in 1 mL of cold TRIzol for 5 min at room temperature (RT). Then, 0.2 mL of chloroform were added for 3 min at RT, and centrifuged at 12,000g for 15 min at 4ºC. Chloroform promotes the generation of two phases: an aqueous phase containing RNA and an organic phase containing DNA and proteins. Therefore, the aqueous phase was collected to which 1 µl of glycogen and 0.5 mL of isopropanol were added for 10 min at RT. After, it was centrifuged at 12,000g for 10 min at 4°C. 1 mL of 75% ethanol was added to the pellet and after homogenization, it was centrifuged at 7,500g for 5 min at 4°C. Finally, once the pellet was dry, it was resuspended in 20-50 µl of RNAse-free water and the quality and quantity of RNA measured using NanoDrop 1000 spectrophotometer (Thermo Fisher Scientific).

For RNA extraction from tumors, tumors were first mechanically disaggregated and then, the same procedure as in cells was performed.

3.1.2 Reverse Transcription

1 µg of RNA was retro-transcribed to obtain cDNA, using the High-Capacity cDNA Reverse Transcription Kit (4368813 Applied Biosystems). The reverse transcription was

performed on a *GeneAmp PCR System 2400* thermocycler (Perkin Elmer), on a two-step reaction: 10 min at 25ºC and 2h at 37ºC.

3.1.3 Real time PCR (qPCR)

Quantitative real time PCR was performed to quantify the expression of 4-1BBL in cells infected with Delta-24-ACT and expression of OX40L in cells infected with Delta-24-RGDOX. Fast SYBR Green PCR Master Mix (Applied Biosystems) was used, which is a non-specific DNA intercalating agent. Samples were run in triplicates, and GAPDH (Glyceraldehyde-3-phosphate dehydrogenase) was used as endogenous control gene. Samples were subjected to 50ºC 2 min, 95ºC 10 min and 40 cycles of 95ºC 15 s and 60ºC 1 min, on a QuantStudio3 thermocycler (Applied Biosystems). Sequences of primers are listed on table 3.

Table 3. List of primers used for real time PCR. Murine *Gapdh* was used as endogenous control gene in murine cells and human *GAPDH* for human cell lines.

Gene	Forward	Reverse
Tnfsf9 **(4-1BBL)**	CTGTGTTCGCCAAGCTACTG	GGGACTGTCTACCACCAACT
Tnfsf4 **(OX40L)**	AATCTGGAAAACGGATCAAG	CAGGCAGACATAGATGAAGC
Gapdh **(mouse)**	GGGAAATTCAACGGCACAGT	AGATGGTGATGGGCTTCCC
GAPDH **(human)**	AGCCACATCGCTCAGACAC	GCCCAATACGACCAAATCC

3.2. Protein expression

3.2.1 Western Blot

Protein isolation

Proteins were extracted from infected cells using a lysis buffer composed of phosphate buffer saline (PBS), 0.1% Triton X-100 and protease inhibitor for 30 min on ice. Then, samples were centrifuged at 12,000 rpm for 20 min at 4ºC. The supernatants were collected since this is where the proteins are found.

Protein quantification

Proteins were quantified using the Protein Assay Dye Reagent Concentrate (Bio-Rad) colorimetric assay, diluted 1:5 on water. In order to know the protein concentration, we made a standard curve with increasing concentrations of bovine serum albumin (BSA), ranging between 0 and 10 µg/µl. Both the standard and samples were quantified in duplicates on a 96-well plate. 200 µl of the diluted reagent were added to each well and

absorbance measured at 595 nm using the Spectrostar^{Nano} reader (BMG Labtech). Finally, the concentration of protein present in each sample was obtained from the extrapolation of the absorbance in the equation of the standard curve.

Western blot

To analyze the expression of 4-1BBL after Delta-24-ACT infection, we prepared 30 µg of protein with 4X NuPAGE LDS Sample loading buffer (Invitrogen) to get reduction conditions. Samples were then subjected to sodium dodecyl sulfate-tris-glycine gel electrophoresis, and transferred into a nitrocellulose membrane for 1h at 110 V. Once confirmed that the transference was correct by staining the membrane with Ponceau S (Sigma-Aldrich), it was blocked with 5% non-fat dried milk diluted in PBS + 0.1% Tween for 1h at RT. After cutting the membranes depending on the molecular weight of the proteins, they were incubated with the different primary antibodies overnight at 4ºC (Table 5). The next day, membranes were incubated with the corresponding secondary antibodies for 1h at RT (Table 4). GRB2 was used as a protein-loading control. Finally, proteins were detected by enhanced chemiluminescence using the Lumi-light PLUS Western blotting substrate (Roche), on the Chemidoc MP imaging system (Bio-Rad).

Table 4. Primary and secondary antibodies used for western blot.

Antibody	Specie	Dilution	Company	Reference
4-1BBL	Goat	1:1000	R&D systmens	AF1246
GRB2	Mouse	1:1000	BD transduction laboratories	610112
Anti-goat IgG	Donkey	1:2000	Abcam	AB97110
Anti-mouse IgG	Horse	1:2000	Sigma-Aldrich	A9044

3.2.2 Flow cytometry

For 4-1BBL and OX40L expression analysis, cells were infected with Delta-24-ACT and Delta-24-RGDOX, respectively (MOIs of 25 and 50 for murine cells and 5 and 10 for human cells). Cells were harvested 48 h later for staining with a PE-coupled anti-4-1BBL antibody (1:200, 107105 Biolegend) or anti-OX40L PE-coupled antibody (1:200, 12-5905-81 Invitrogen). Dead cells were removed by Zombie NIR staining (1:1000, Biolegend, 423105), and the remaining samples were then analyzed using the FACSCanto^{TM} II system (BD Biosciences).

3.2.3 Immunofluorescence

NP53 or XFM cells ($5x10^5$) were seeded on glass slides and infected with Delta-24-ACT at a MOI of 50 24h after (1 condition was not infected as a control). Forty-eight hours after infection, the cells were fixed with 4% formaldehyde/methanol-free (28906; Thermo Fisher Scientific) and blocked for 1h at RT (S0809; Dako). Finally, the cells were stained with a PE-coupled anti-4-1BBL antibody (1:200, 107105 Biolegend) for 2h at RT, and nuclei were stained with DAPI (40009 Biohum).

4. Viral assays

4.1. Cell viability assay

All the cell lines were seeded in 96-well plates (NP53 and XFM at a density of 500 cell/well and SU-DIPG IV and TP54 at $1x10^4$ cell/well). Then, the cells were infected with Delta-24-ACT or Delta-24-RGDOX at MOIs ranging from 5 to 100. Five days after infection, cell viability was assessed using the CellTiter 96® Aqueous One Solution Cell Proliferation Assay (Promega, Fitchburg, WI, USA; G3581). The reagent contains a tetrazolium compound [GR, inner salt; MTS] that is broken by the metabolically active cells, producing a colored solution. Five days later, cell viability was analyzed by measuring the absorbance at a wavelength of 490 nm and 650 nm (reference) using the Spectrostar^{Nano} reader (BMG Labtech). Viability curves were analyzed using GraphPad Prism 9 (Statistical Software for Sciences) to determine the half-maximal inhibitory concentration (IC_{50}) values of Delta-24-ACT/ Delta-24-RGDOX in the tested cell lines (IC_{50} is the viral dose at which 50% of cells are affected, i.e., 50% survival).

4.2. Viral replication assay

NP53 and XFM cells were seeded in 6-well plates at a density of $5x10^4$ cells/well and infected with Delta-24-ACT or Delta-24-RGDOX at a MOI of 100. Human SU-DIPG IV and TP54 cells were infected with the virus at a MOI of 10. Sixteen and 72 h after viral infection, the cells and supernatants were collected and viral replication was assessed in HEK293 cells by an anti-hexon staining-based method. Briefly, cells were lysed after three freeze-thaw cycles and centrifuged to 1,500rpm for 5 min at 4ºC. Then, serial dilutions (1:10) of the virus were performed in 96-well plates, and 100,000 HEK293 cells were added to every well. 36h after, the hexon staining, which involves the use of a primary antibody against hexon and a secondary antibody Alexa 488 (A21202 Life Technologies), was performed on cells. Finally, the FITC positive cells were manually

counted under a fluorescent microscopy (Zeiss Imager MP). For each viral dilution, triplicates were made, and the experiment was performed three times. The amount of viral particles per mL (VP/mL) was calculated using the formula:

$$VP/mL = \text{average of } FITC^{+} \text{ cells} \times \text{dilution factor} \times 10$$

4.3. Viral protein expression

The early E1A and the late fiber protein expression was analyzed by western blot, using the same procedure as described before, in the section on ligand expression by western blot. The used primary and corresponding secondary antibodies are listed on table 5. GRB2 was used as protein-loading control.

Table 5. List of the primary and secondary antibodies used for western blot.

Antibody	Specie	Dilution	Company	Reference
E1A	Rabbit	1:1000	Santa Cruz Biotechnology	Sc-430
Fiber	Mouse	1:1000	Novus Biologicals	NB600-541
GRB2	Mouse	1:1000	BD transduction laboratories	610112
Anti-rabbit IgG	Goat	1:2000	Cell Signaling Technology	7074
Anti-mouse IgG	Horse	1:2000	Sigma-Aldrich	A9044

4.4. Study of Immunogenic Cell Death (ICD)

In order to evaluate the DAMPs produced by cells after the viral infection, each cell line was seeded at a density of $2x10^5$ cells per well (on 6-well plates) and infected with Delta-24-ACT at its corresponding IC_{50}. 72h after viral infection, supernatants were collected for posterior analyses.

ATP measurement. To quantify the amount of ATP in the supernatants, we used the ENLITEN® ATP detection kit (Promega), following manufacturer´s instructions. The reagent contains recombinant luciferase that catalyzes the following reaction:

$$ATP + D\text{-}Luciferin + O2 \rightarrow Oxyluciferin + AMP + PPi + CO2 + Light\ (560\ nm)$$

Therefore, the intensity of light is directly proportional to the ATP concentration, which was measured using the luminometer FLUOstar OPTIMA (BMG Labtech).

HMGB1 measurement. HMGB1 concentration was measured using an ELISA kit (ST51011, IBL International), following manufacturer´s protocol. The absorbance was measured at 450 nm using the Spectrostar^{Nano} reader (BMG Labtech).

Calreticulin (CRT) detection on the membrane. The translocation of calreticulin from the endoplasmic reticulum to the membrane is a feature of immunogenic cell death. For measuring CRT translocation after viral infection, flow cytometry and immunofluorescence were performed.

For flow cytometry, 150,000 cell/well were seeded on 6-well plates and infected with 150 PFU/cell of Delta-24-ACT. Four hours after infection, cells were collected and stained with the primary antibody anti-calreticulin (ab2907, Abcam) (1:100 in BSA 5%) for 30 minutes. The secondary antibody Alexa Fluor® 488 (Life Technologies) (1:200 dilution in BSA 5%) was added for 30 minutes. All the process was carried out at 4 ºC. Finally, CRT expression on cell membranes was evaluated using a FACSCanto II cytometer (BD Biosciences) and results were analyzed using FlowJo® software.

In the case of immunofluorescence, cells were seeded into glass slides and infected with Delta-24-ACT. 4h after, cells were fixed with 4% methanol-free formaldehyde (Thermo Fisher Scientific) for 15 min at 37ºC and permeabilized with 0.1% Triton X-100. Then, samples were incubated with the primary anti-calreticulin antibody (ab2907, Abcam) at 1:250 dilution for 1h at RT. The secondary antibody was Alexa Fluor® 488 (Life Technologies) (1:200 dilution), that was incubated for 1h at room temperature. Nuclei were stained with DAPI (40009 Biohum). Finally, immunofluorescence images were obtained with the Zeiss Image MP (Oberkochen) microscope.

5. Costimulation assay

$CD8^+$ cells from B6.CgThy1a-Tg(TcraTcrb)Rest/J (PMEL) mice were isolated under sterile conditions with a $CD8a^+$ T cell isolation kit (130-104-075, Miltenyi Biotec) according to the manufacturer's instructions and seeded with CD3 (clone 145-2C11, 100314 Biolegend) and CD28 (clone 37.51, 102112 Biolegend) antibodies for 24h. NP53 cells were infected with Delta-24-RGD, Delta-24-ACT, Delta-24-RGDOX or a mock control at a MOI of 100 for 48 h and then incubated with 1 µg/mL hgp100 (RP20344, GenScript) for 2h (mock NP53 and NP53-ACT cells without hgp100 served as controls). Finally, $CD8^+$ cells and target cells were cocultured for 48h, and the cells and supernatants were then collected. IFN-gamma expression was analyzed in the supernatants using a mouse IFN-gamma DuoSet ELISA kit (DY485, R&D Systems) according to the manufacturer's instructions. The absorbance was measured at 450 nm using the Spectrostar^{Nano} reader (BMG Labtech).

Cells were stained with the intracellular granzyme-B antibody (25-8898-80, Thermo Fisher) for flow cytometry assessment. Briefly, cells were first incubated with Golgi Stop (51-2092KZ BD Biosciences) and Golgi plug (51-2301KZ BD Biosciences) for 4h at 37ºC, which are protein transport inhibitors that block protein transport processes. Therefore, there is an accumulation of cytokines and proteins in the Golgi, in order to capture granzyme expression on cells. Then, the extracellular staining was made, with PE-CD45 (103105 Biolegend) and APC-CD8a (100712 Biolegend). After cell fixation with BD Cytofix® (BD Biosciences), intracellular staining for granzyme-B (PeCy7 25-8898-80, Thermo Fisher) was performed.

6. In vivo experiments

Every in vivo study was revised and approved by the Bioethics department of the Government of Navarra and the ethics department for the animal experimentation of the University of Navarra (CEEA). Ethical protocol 094-17.

6.1. Screw-guided system

All the orthotopic models were performed using the screw-guided system, developed by Dr. Fred Lang.[138] This model replaces stereotaxic procedures, allowing more than one mouse to be operated at a time.

The screw-guided system consists on the implantation of a bolt (screw) on the desired brain coordinates, through which cells are injected to create the tumors. After, the desired treatment can be administrated in the same place, in this case oncolytic adenovirus.

The bolt (C212SG) is 2.5 mm long and has a central hole of 0.5 mm, which permits the introduction of a Hamilton syringe (87900 Thermo Fisher Scientific). The syringe has a needle of 26G/51mm/pst2 to which we have added a stopper sleeve to control the depth of the implantation. For both cell implantation and virus administration, an infusion pump was used, with a constant speed of 0.25 µl/min. We use the PHD 2000 *Infusion syringe pump multiple syringe holder* (Harvard Apparatus), which permits to inject 10 mice at the same time (Figure 15).

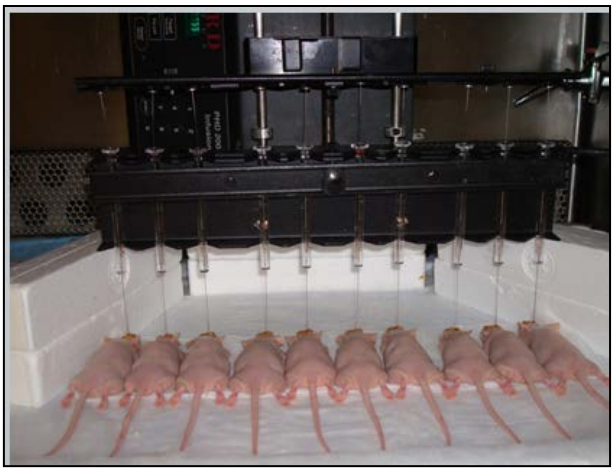

Figure 15. Image showing the cell implantation procedure, in which cells are injected in a constant speed using an infusion pump. It permits to inject 10 mice at the same time.

6.2. Bolt implantation

Animals were first anesthetized with an intraperitoneal injection of ketamine (Imalgene) / Xylacine (2% Rompun Bayer), in a dose of 100 mg ketamine and 10 mg Xylacine per mouse Kg. Then, the surgery takes place. A dose of buprenorphine (961425 Buprex) was administered as analgesia, before and 24h after the surgery.

Povidone iodine was applied to the head of the mouse to disinfect the area, followed by an excision of about 5 mm with a scalpel. Once the coordinates are localized using a ruler, a small hole is drilled in the skull with a 1mm diameter drill bit (8J60, Plastics One Drill HSS). The bolt is then screwed with a special screwdriver (Plastics One Screwdriver SD#1) (Figure 16). The screw remains implanted until the end of the experiment, and the scission is closed with a special glue for this purpose (Hystoacryl, 10520010 B-Braun).

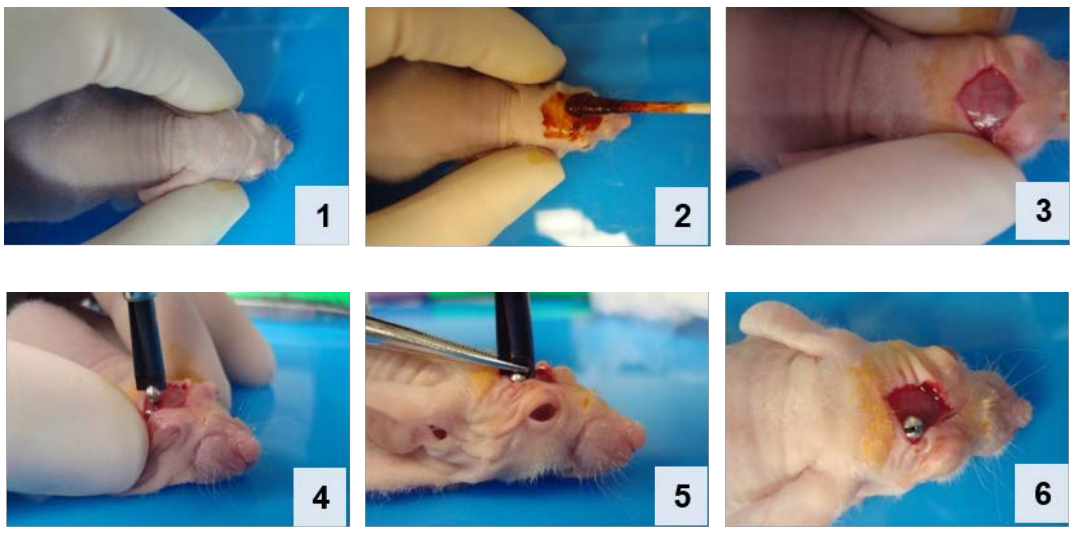

Figure 16. Image series showing the process in which the bolt is implanted into the mouse's screw. The skin is disinfected with povidone iodine (2) and a scission made with a scalpel (3). Finally, the bolt is screwed with a special screwdriver (4-6).

6.3. DIPG orthotopic model

The model for the orthotopic implantation of DIPG tumors was developed and described by Miguel Marigil *et al*.[139] They adapted the method previously described by Fred Lang, with the specific coordinates to implant the cells into the pons. They define the definitive coordinates to reach the pons: 1 mm right to and 0.8 mm posterior to lambda as well as 6.5 mm depth insertion of the needle (Figure 17).

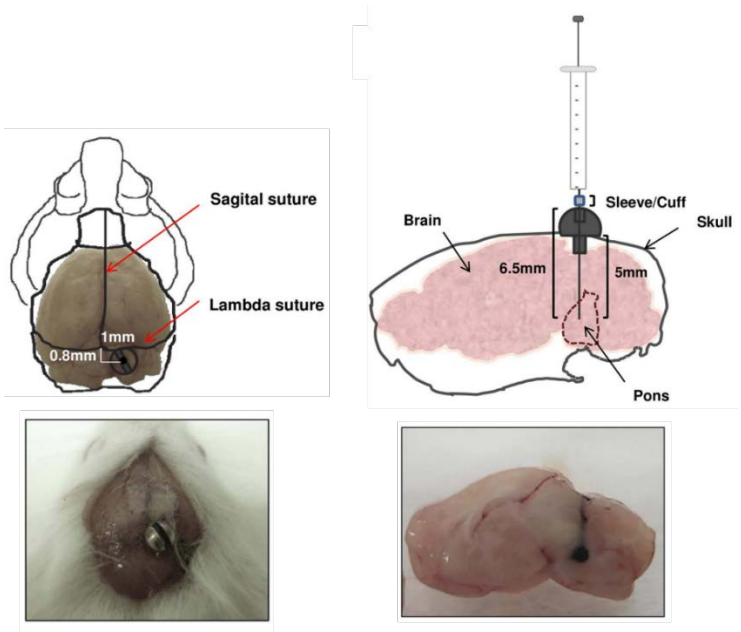

Figure 17. Description of DIPG orthotopic model. The coordenates to implant tumors into the pons are 1 mm right to and 0.8 mm posterior to lambda as well as 6.5 mm depth. Obtained from Marigil M *et al.*, 2017.[139]

The 5 mm scission was made to expose both the sagittal and lambdoid sutures. Afterwards, the screw was introduced by applying slight pressure through the previously made hole, until it was flushed with the cranial surface. Finally, cells were introduced using a Hamilton syringe into the pons. Due to the small size of the pons, no more than 3 µl can be injected.

- **NP53**: 10,000 cells in 2 µl of uncomplemented DMEM in transgenic mice kindly provided by Dr. Oren Becher. NP53 cell line was obtained from tumors generated using the RCAS (Replication-Competent ASLV long terminal repeat (LTR) with a Splice acceptor) system in NP53$^{fl/fl}$ mice, obtained from crossing Nestin tv-a (Ntv-a) and p53 floxed (p53$^{fl/fl}$, C57BL/6 background) mice. Nestin Tv-a mice contain the TVA receptor (receptor for RCAS to infect) under the Nestin promoter.[137] The cells that express Nestin are the glial progenitor cells, so the virus will infect the

Nestin^{+} cells, producing the PDGF and H3.3K27M mutations in those cells. So, Dr. Becher *et al*,[136] derived the NP53 cell line from tumors generated using this system and therefore, we implant the cell line in the same mice it was created.

- **XFM**: 1,000 cells in 2 µl of uncomplemented DMEM in BALB/c mice.

Three days after cell injection, 2 µL of PBS or adenovirus (10^6 PFUs/mouse) was administered intratumorally (Figure 18). Animals that showed obvious symptoms of disease were sacrificed, and survival curves were plotted according to the Kaplan-Meier method with GraphPad Prism 9.

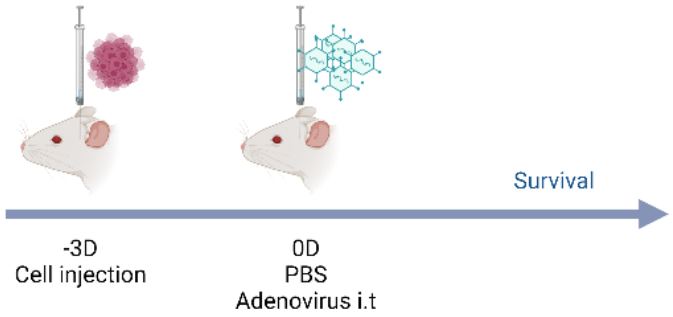

Figure 18. Schedule used for survival experiments. NP53 or XFM cell lines were implanted and 3 days later, adenovirus or PBS as control-group are injected intratumorally. Mice are then monitored for survival analyses.

7. Analysis of the tumor microenvironment

7.1. Flow cytometry

For tumor-infiltrating lymphocyte (TIL) analysis, brains were collected, and tumor samples were disaggregated to obtain a cell suspension. Briefly, the tumor samples were disaggregated mechanically and then chemically with collagenase/DNase I (Gibco) using gentleMACS™ Dissociator (Miltenyi Biotec). Afterwards, tumor suspensions were passed through a 40-µm cell strainer and then subjected to 30% Percoll treatment to obtain TILs. Finally, TILs were pelleted for posterior cell staining.

First, dead cells were removed by PromoFluor-840 staining (1:10,000, PK-PF840-3-01, PromoCell) for 15 min at 4ºC. Then, extracellular staining was made by incubating cells with 50 µL of the antibodies resuspended in PBS 1X + 0.5% FBS + 0.5% EDTA. The antibodies used are listed in Table 6. For intracellular staining, cells were first fixated and permeabilizated with the Foxp3 Transcription Factor Fixation/Permeabilization kit (00-5521-00 Invitrogen). Finally, samples were analyzed using CytoFLEX (Beckman Coulter)

and CytExpert software (Beckman Coulter) and results were analyzed using FlowJo® software.

Table 6. List of the antibodies used for the analysis of the TME by flow cytometry.

ANTIBODY	CLONE	DILUTION	COMPANY	REFERENCE
CD4 FITC	RM4-5	1:800	Biolegend	100510
CD4 BUV496	GK1.5	1:200	Biolegend	612952
CD8a BV510	53-6.7	1:400	Biolegend	100752
CD11b BV510	M1/70	1:400	Biolegend	101263
CD11c PECy7	N418	1:160	Biolegend	117318
CD19 BV421	6D5	1:400	Biolegend	115538
CD45 APC/Fire750	30-F11	1:400	Biolegend	103154
CD69 PECy7	H1.2F3	1:100	Biolegend	104511
CD73 PE	TY/11.8	1:100	Biolegend	127205
CD134 (OX40) PE	OX-86	1:200	Biolegend	119409
CD137 (4-1BB) PE	17B5	1:200	Biolegend	106105
F4/80 APC	BM8	1:200	Biolegend	123116
FOXP3 PE-eFluor610	FJK-16s	1:100	Invitrogen	61-5773-82
GITR PerCP/Cy5.5	DTA-1	1:200	Biolegend	126316
Granzyme B PeCy7	NGZB	1:80	Thermo Fisher	25-8898-80
IA/IE BV605	M5/114.15.2	1:300	Biolegend	107641
IL-10 APC	JES5-16E3	1:100	Biolegend	505009
Ki67 FITC	11F6	1:100	Biolegend	151204
Ly6C FITC	HK1.4	1:400	Biolegend	128006
Ly6G PerCP/Cy5.5	1A8	1:400	Biolegend	127616
NK1.1 BV605	PK136	1:100	Biolegend	108710
NKp46 BV605	29A1.4	1:100	Biolegend	137619
PD-1 BV421	29F.1A12	1:160	Biolegend	135218
TCRb BV785	H57-597	1:100	Biolegend	109249

7.2. Immunohistochemical analysis

Brains obtained from sacrificed mice were fixed with formol for 24h and dehydrated with absolute ethanol. Then, brains were embedded in paraffin blocks and sections of 3 µm were obtained using the Microm HM 340E (Thermo Fisher Technologies). Paraffin-embedded mouse brain sections were first stained with hematoxylin-eosin for tumor analysis. Once tumor status was confirmed, the remaining staining experiments were performed with antibodies against adenovirus rabbit E1A, (1:1000; Santa Cruz Biotechnology, Santa Cruz, CA), CD3 (1:300; clone SP7, NeoMarkers, Fremont, CA), CD4 (1:1000; EPR19514, ab183685 Abcam, Cambridge, MA), CD8a (1:1000, (D4W2Z) #98941 Cell Signaling, Danvers, MA) and FoxP3 (1:400; clone JFK-16s, ref. 14–5773, eBiosciences, Thermo Fisher, Waltham, MA). For immunohistochemical staining, Vectastain ABC kits (Vector Laboratories Inc., Burlingame, CA) were used according to

the manufacturer's instructions. Finally, the selected preparations were scanned with Aperio C52 image capture device (Leica Microsystems). The number of positively stained cells per mm^2 was quantified using the Fiji platform.

7.3. Multiplexed immunofluorescence

A multiplex immunolabeling protocol based on tyramide signal amplification (TSA) and Opal fluorophores was developed and validated as previously described.[140] Briefly, paraffin-embedded sections of mouse brains were deparaffinized, hydrated and treated with peroxidase. Then, each section was subjected to sequential rounds of antibody staining, each including heat-induced antigen retrieval at pH 6 and protein blocking with 20% normal goat serum (Dako) in PBS. Finally, the sections were incubated with a primary antibody and secondary antibody HRP conjugate (Dako), followed by TSA visualization with fluorophores Opal 520, Opal 540, Opal 570, Opal 620, Opal 650, and Opal 690 (Akoya Biosciences).

The primary antibodies included CD8 (rabbit monoclonal; Cell Signaling Technology; 98941; 1:500), CD4 (rabbit monoclonal; Cell Signaling Technology; 25229; 1:400), CD31 (rabbit monoclonal; Cell Signaling Technology; 77699; 1:400), FOXP3 (rabbit monoclonal; Cell Signaling Technology; 12653; 1:600), GFAP (rabbit monoclonal; Cell Signaling Technology; 80788; 1:100), and F4/80 (rabbit monoclonal; Cell Signaling Technology; 70076; 1:400). After six sequential reactions, nuclei were counterstained with spectral DAPI (Akoya Biosciences), and sections were mounted with Diamond antifade mountant (Life Technologies).

Multiplexed immunofluorescence slides were scanned on a Vectra-Polaris Automated Quantitative Pathology Imaging System (Akoya Biosciences) as previously described.[140,141] The whole tissue present in a single FFPE tissue section was imaged, spectrally unmixed and exported as a component TIF image tile using Akoya Biosciences Inform software (version 2.4.8). Component TIF image tiles were then imported into the open-source digital pathology software QuPath version 0.2.0-m9 and stitched together using the x-y coordinates to create a new pyramidal TIF file.

7.4. NanoString analysis

RNA was isolated from formalin-fixed, paraffin-embedded (FFPE) tumor sections by dewaxing using deparaffinization solution (QIAGEN). Total RNA was extracted using the RecoverAll Total Nucleic Acid Isolation Kit (Ambion) according to the manufacturer's instructions. RNA purity was assessed on an ND NanoDrop 1000 spectrometer (Thermo

Fisher Scientific). For the NanoString platform, 100 ng of RNA was used to detect immune gene expression using the nCounterPanCancer Immune Profiling Panel along with custom CodeSet. Counts of the reporter probes were tabulated for each sample by the nCounter Digital Analyzer, and the raw data output was imported into R/Bioconductor.[142] First, gene expression data were normalized with the NACHO[143] R package. After quality assessment and outlier detection using R/Bioconductor, a filtering process was performed. Genes without read counts in more than 50% of the samples of all the studied conditions were considered not expressed in the experiment under study. LIMMA (Linear Models for Microarray Data)[144] was used to identify the genes with significant differential expression between experimental conditions. Genes were selected as differentially expressed using a p value cut off $p<0.01$. Further functional and clustering analyses were performed and graphical representations were generated using clusterProfiler[145] and R/Bioconductor.

8. IFN-γ ELISPOT

The enzyme-linked immunospot assay (ELISPOT) was performed to assay the systemic immune response after viral administration. This assay permits the quantification of cells producing IFN-γ. Three mice of each group (PBS- and Delta-24-RGDOX- treated) were sacrificed and spleens were obtained, for splenocyte isolation. Briefly, spleens were dissociated through a 70 µm cell strainer, and after centrifugation, erythrocytes were lysed with ACK for 3 min. Mouse IFN-γ ELISPOT set (551083 BD Biosciences) was performed following manufacturer's instructions. In previously coated 96-well plates, 400,000 splenocytes and 40,000 tumor cells (adenovirus- or mock-infected) were cocultured for 24h. The staining protocol was followed and finally, IFNγ -producing cells were counted using IMMUNOSPOT (Cellular Technology Limited).

9. Serum biochemistry

Serum samples from NP53-bearing mice were obtained 3 days after Delta-24-ACT administration (or PBS in the control group), to assess the possibility of the adenovirus to produce hepatic toxicity. Hepatocyte damage was assessed by alanine aminotransferase and aspartate aminotransferase, and cholestatic damage by alkaline

phosphatase. Finally, liver function was evaluated with bilirubin and albumin. The measurement was made using a Cobas C311 Autoanalyzer (Roche).

10. Treg experiments

10.1. Treg isolation

Treg cells were isolated from spleens of naïve mice using the $CD4^+CD25^+$ Regulatory T Cell Isolation Kit (130-091-041 Miltenyi Biotec). Once we had the spleens (through the same process explained in section 8), the specific isolation of Treg was made in a two-step procedure. First, a negative selection of $CD4^+$ cells was performed. Non- $CD4^+$ cells were magnetically labeled and depleted by separation through a MACS® Column, placed in a magnetic field of a MACS® Separator. In parallel, cells were labelled with CD25-PE. In the second step, the $CD25^+$ cells labeled with PE were magnetically labeled with anti-PE microbeads, and isolated by positive selection. In this way, the $CD4^+CD25^+$ cells were obtained (Figure 19). Finally, the number of cells were counted and resuspended in the desired concentration for seeding.

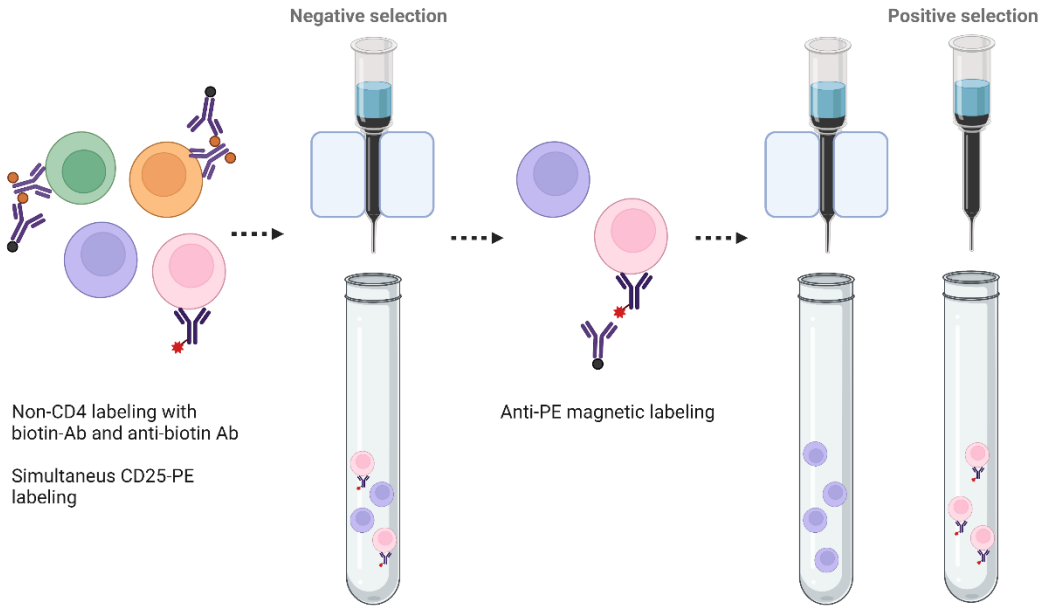

Figure 19. Schematic representation of $CD4^+CD25^+$ Treg cell isolation using a specific kit, based on the magnetic separation of labelled cells.

10.2. In vitro assays

10.2.1 Treg proliferation assay

The effect of 4-1BBL and OX40L, present on Delta-24-ACT and Delta-24-RGDOX respectively, in Treg proliferation was assessed *in vitro*. For that purpose, tumor cells

were mock-, Delta-24-RGD, Delta-24-ACT- or Delta-24-RGDOX- infected for 48h. Then, tumor cells were irradiated and cocultivated with Tregs in a 5:1 ratio (Treg: tumor cells). Tregs were activated with anti-CD3 (100340 Biolegend) and anti-CD28 (102116 Biolegend) antibodies. 48h later, cells were stained for flow cytometry analysis. Dead cells were eliminated with Zombie NIR Fixable Viability kit (423105 Biolegend) and antibody against CD3 was used to differentiate tumor cells from Treg cells (1:100, PE-CD3 100206 Biolegend). After cell fixation/permeabilization with the Foxp3 Transcription Factor Fixation/Permeabilization kit (00-5521-00 Invitrogen), intracellular staining with Ki67 (1:100 FITC-Ki67, 151204 Biolegend) was performed for proliferation assessment. Finally, samples were analyzed using CytoFLEX (Beckman Coulter) and CytExpert software (Beckman Coulter) and results were analyzed using FlowJo® software.

10.2.2 CD4 conversion to Tregs

The effect of the ligands on the conversion of CD4 cells to Tregs was also analyzed. First, $CD4^+$ cells were isolated from spleens using the $CD4^+$ isolation kit (130-095-248, Miltenyi Biotec) according to manufacturer´s instructions. $CD4^+$ T cells were seeded with 1µg/mL of anti-CD3 (100340 Biolegend) and anti-CD28 (102116 Biolegend), 50U/mL of IL-2 (11340023 InmunoTools) and 10ng/mL of TGF-β (11343160 ImmunoTools), because these conditions have been described as aiding in conversion. Finally, irradiated tumor cells in the same conditions as mentioned above were seeded with $CD4^+$ T cells (Figure 20). 72h after, the percentage of Treg was analyzed by flow cytometry. First, dead cells were removed with PromoFluor-840 staining (1:10,000, PK-PF840-3-01, PromoCell). Then, extracellular staining was made with BUV496 anti-CD4 (1:200 612952, Biolegend) and APC anti-CD25 (1:200 102008, Biolegend). After cell fixation/permeabilization with the Foxp3 Transcription Factor Fixation/Permeabilization kit (00-5521-00 Invitrogen), intracellular staining with PE-efluor610 Foxp3 antibody (1:100 61-5773-82, Invitrogen) was made. Finally, samples were analyzed using CytoFLEX (Beckman Coulter) and CytExpert software (Beckman Coulter) and results were analyzed using FlowJo® software.

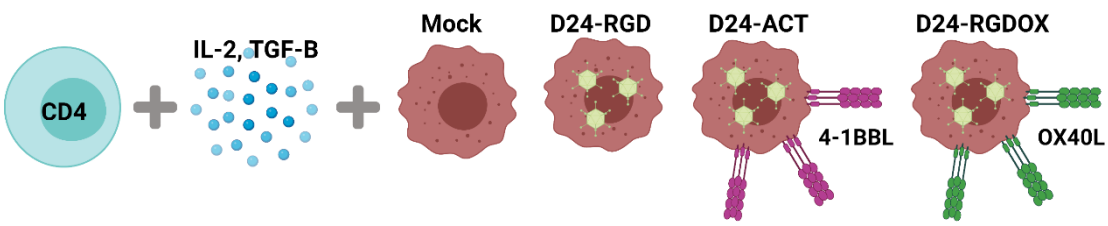

Figure 20. CD4 conversion assay. CD4 conversion to Treg was assessed by culturing CD4 cells with tumor cells in presence of IL-2 and TGF-β.

10.2.3 Treg suppression assay

The effect of ligands on the Treg suppressive function was also evaluated, through the suppression on $CD8^+$ T cells. Tumor cells were infected with Delta-24-RGD, Delta-24-ACT or Delta-24-RGDOX for 48h and then cocultured with Treg cells (isolated from spleens as previously described) at 5:1 ratio (Treg:tumor). Treg cells were activated with anti-CD3 (100340 Biolegend) and anti-CD28 (102116 Biolegend) antibodies. 48h after, Tregs were cocultured with $CD8^+$ cells, which were isolated from naïve spleens with the $CD8a^+$ T cell isolation kit (130-104-075, Miltenyi Biotec), and stained with the Proliferation Dye 450 (65-0842-85 Invitrogen). CD8 were activated with anti-CD3 and anti-CD28 antibodies as well. Tregs and CD8+ cells were cocultured at different ratios (1:1, 1:0.5, 1:0.25; CD8: Treg) (Figure 21). 72h after, CD8 proliferation was analyzed by flow cytometry. PromoFluor-840 staining (1:10,000, PK-PF840-3-01, PromoCell) was used to eliminate dead cells, CD8 were selected by APC-CD8 antibody (344722 Biolegend) and their proliferation was assessed using a proliferation dye staining.

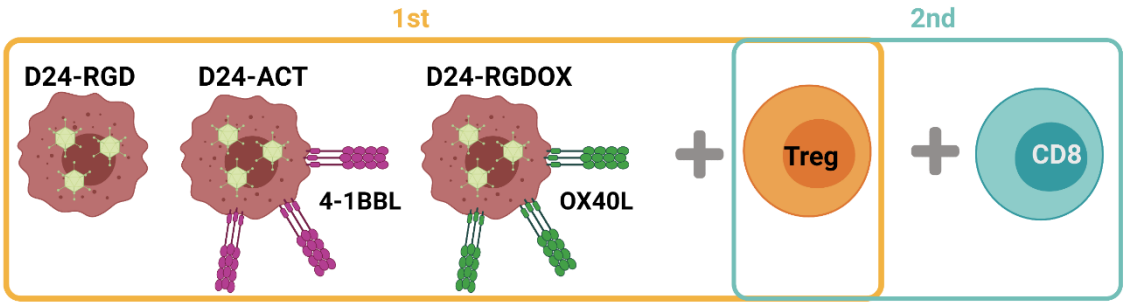

Figure 21. Suppression assay. The effect of the ligands on Treg suppressor function was evaluated by measuring CD8 proliferation.

11. Statistical analysis

The *in vitro* experiments were repeated at least 3 times. Dose–response curves for viral cytotoxicity were obtained by nonlinear regression. Data with normal distributions were assessed by Shapiro–Wilk tests, and comparisons among groups were performed with two-tailed nonparametric tests with 95% confidence intervals (CIs) for nonnormally distributed datasets or parametric tests when normality was confirmed (Student's t test or one/two-way ANOVA). For the comparison of groups in survival experiments, a log-rank test (Mantel–Cox) was used. GraphPad Prism 9 (Statistical Software for Sciences) was used for the statistical analyses. P values less than 0.05 were considered significant.

Results

1. Delta-24-ACT characterization in vitro and in vivo in orthotopic murine models of DIPG

1.1. Delta-24-ACT efficiently expresses functional 4-1BBL on the membrane of cell lines

The objective of generating Delta-24-ACT was to increase the antitumor immune response of Delta-24-RGD. Therefore, we incorporated the murine 4-1BBL into the backbone of Delta-24-RGD, maintaining the genetic modifications of 24bp-deletion of E1A and RGD motif introduction (Figure 10). After the generation of the virus, we first determined its ability to express the ligand in DIPG murine (NP53 and XFM) and human (SU-DIPG IV and TP54) cell lines after infection. We infected the cell lines with increasing doses of Delta-24-ACT and obtained both RNA and protein 48h later, to assess 4-1BBL expression. We readily detected the expression of 4-1BBL mRNA and protein in infected murine and human cell lines in a dose-dependent manner (Figure 22A and 22B), indicating that Delta-24-ACT efficiently expresses the ligand.

A

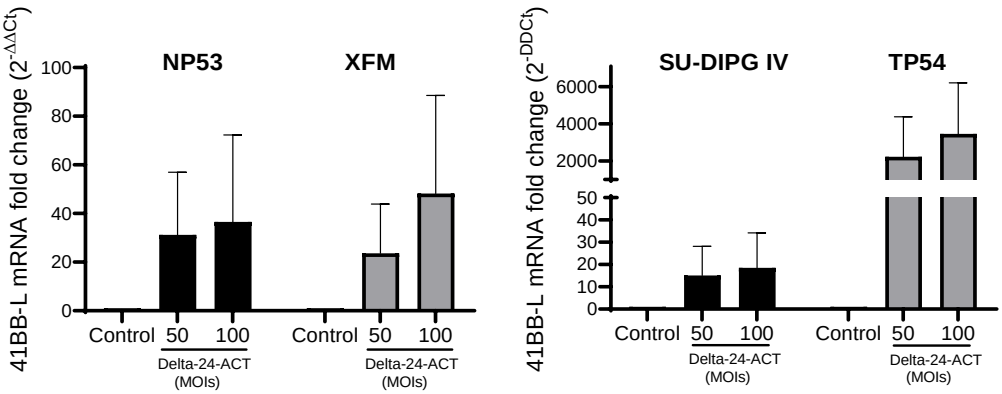

B

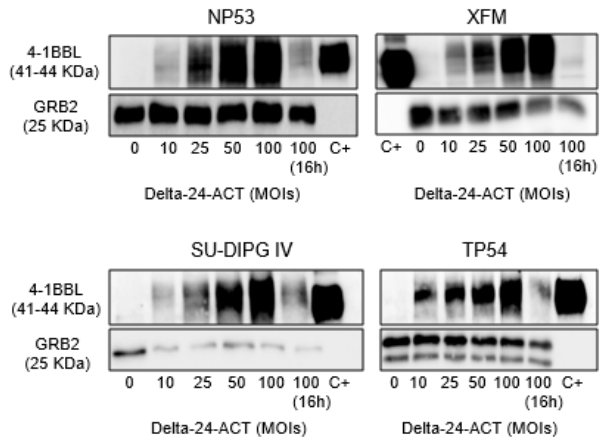

Figure 22. 4-1BBL expression in murine and human DIPG cell lines. A) 4-1BBL RNA expression as determined by qPCR in NP53 and XFM murine cell lines and SU-DIPG IV and TP54 human cell lines after Delta-24-ACT infection at the indicated MOIs (N=3). **B)** 4-1BBL protein expression in NP53, XFM, SU-DIPG IV and TP54 cells infected with Delta-24-ACT at the indicated MOIs as determined by Western blotting. C+: 4-1BBL recombinant protein.

However, it is necessary that 4-1BBL is expressed on the membrane of infected cells for its correct function. Thus, we analyzed 4-1BBL protein expression on the membrane of infected cells 48h after infection, by flow cytometry and immunofluorescence. For flow cytometry, we infected murine NP53 and XFM cell lines with 25 and 50 PFU, and human SU-DIPG IV and TP54 with 5 and 10 PFU. In all the cases, we observed an excellent expression of 4-1BBL on the cell membrane in a dose-dependent manner. In fact, 4-1BBL expression was detected in around 80% of infected mouse cell membranes at a multiplicity of infection (MOI) of 50, whereas this percentage was reached at an MOI of 10 on the surface of human cell membranes ($NP53_{50MOI}$= 76.4%±4.1; XFM_{50MOI}=94.7%±3.8; SU-DIPG IV_{10MOI}= 77.7%±4.5; $TP54_{10MOI}$= 69.4%±7.1) (Figure 23A). 4-1BBL expression was also confirmed by immunofluorescence in the membrane of NP53 and XFM cells (Figure 23B).

Of importance, we also observed a significant increase in the expression of the ligand in mouse DIPG tumors treated with Delta-24-ACT *in vivo*. For that purpose, Delta-24-ACT was intratumorally administered and 6 days after, tumors were obtained for RNA extraction and analysis of 4-1BBL expression (Figure 23C).

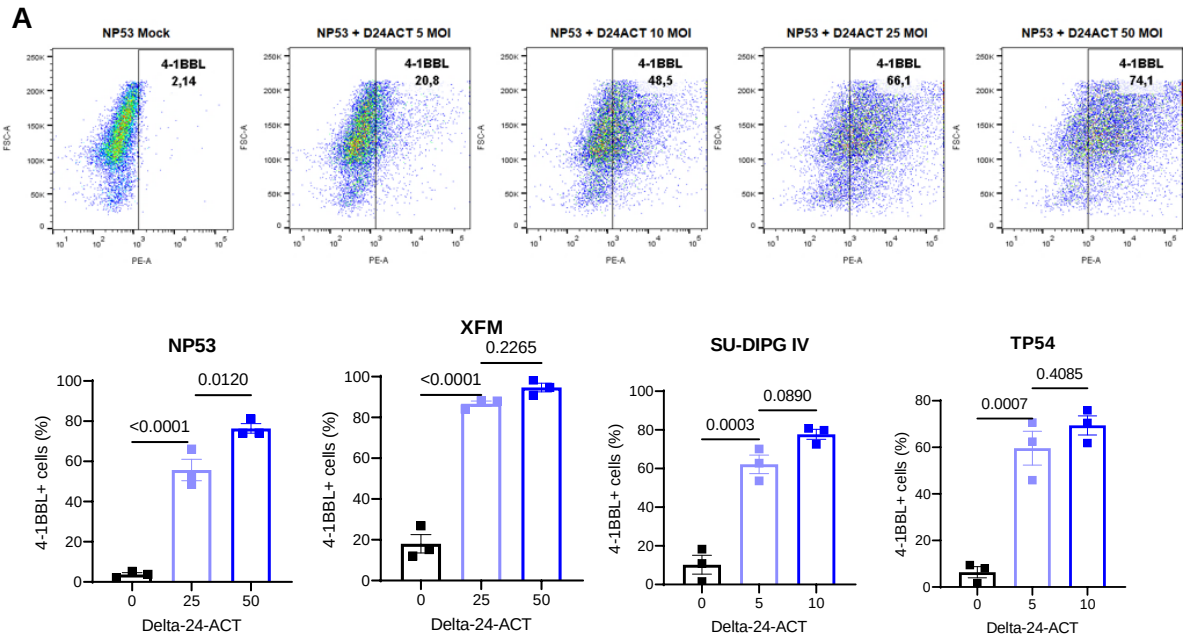

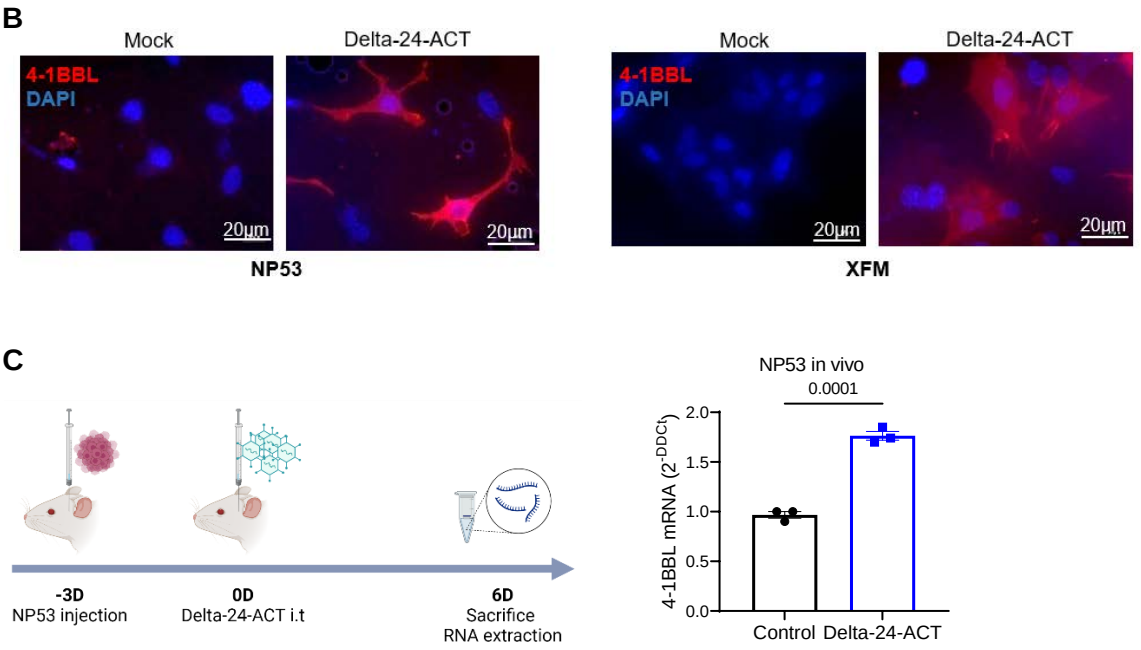

Figure 23. Delta-24-ACT expresses 4-1BBL on the membrane of infected cells. A) ***Upper panel,*** Representative images showing the 4-1BBL expression in the membranes of NP53 cells infected with Delta-24-ACT at different MOIs for 48h as determined by flow cytometry. ***Lower panel***, 4-1BBL protein expression in the membranes of murine and human cells infected with Delta-24-ACT at the indicated MOIs as determined by flow cytometry. The percentage of 4-1BBL-positive cells is shown. One-way ANOVA was performed (N=3, each group). Bar graphs indicate the mean ± SEM. **B)** Representative immunofluorescence images (scale bar 20 µm) of 4-1BBL expression in NP53- and XFM-infected cells compared with mock-infected cells. **C)** ***Left panel,*** Schedule of the experiment for the *in vivo* determination of 4-1BBL expression. ***Right panel,*** 4-1BBL protein expression was evaluated in NP53 tumors from control or Delta-24-ACT-treated mice (N=3) and determined by qPCR. Bar graphs indicate the mean ± SEM (Student´s t test).

Moreover, functional studies *in vitro* demonstrated that the 4-1BBL expressed by the virus was functional and capable of stimulating $CD8^+$ lymphocytes. We performed an experiment in which gp100-specific $CD8^+$ T cells from PMEL mice were cocultured with mock-, Delta-24-RGD- or Delta-24-ACT-infected NP53 cells (that were previously pulsed with the gp100 peptide) for 48 h. Afterward supernatants and cells were collected for further analyses of $CD8^+$ T cell activation. IFN-γ was measured on the supernatants and granzyme B expression in cells. We observed a significant increase in IFN-γ and granzyme B expression in T lymphocytes cocultured with NP53 cells infected with Delta-24-ACT compared to those cocultured in the presence of noninfected or Delta-24-RGD-infected NP53 cells (Figure 24A). In fact, activated $CD8^+$ T lymphocytes cocultured with Delta-24-ACT-infected NP53 cells acquired a more blastic morphology and formed more clusters in vitro (Figure 24B), indicative of CD8 activation. These results indicate that Delta-24-ACT expresses a functional 4-1BBL on the membrane of infected cells.

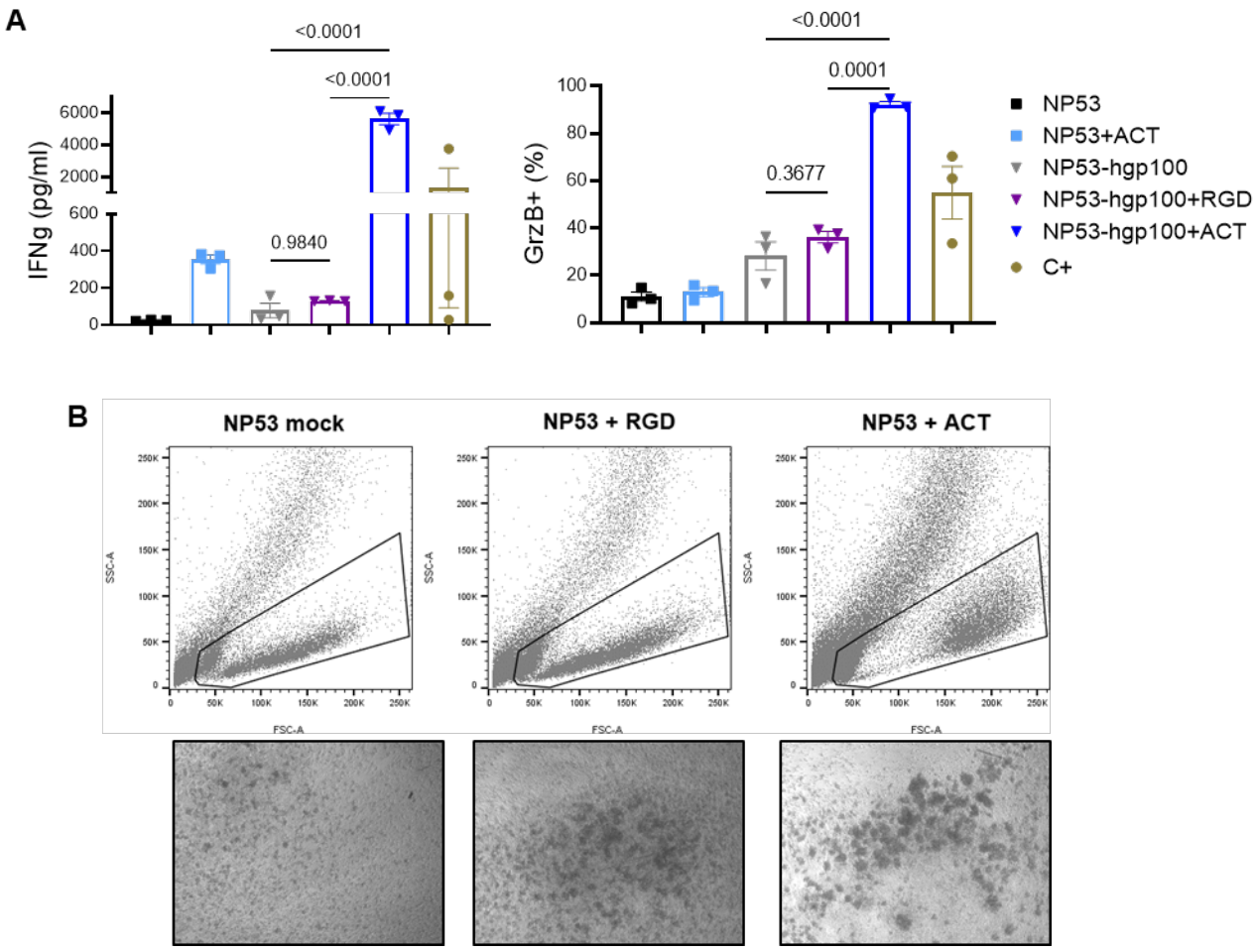

Figure 24. The 4-1BBL expressed by Delta-24-ACT is functional as it activated CD8 cells. A) IFN-gamma and granzyme B production by $CD8^+$ lymphocytes. $CD8^+$ T cells from PMEL mice were cocultured with NP53 cells infected with Delta-24-RGD, Delta-24-ACT (MOI 100) or the mock control. $CD8^+$ lymphocytes activated with CD3, CD28 and 4-1BB antibody were used as positive control for the experiment (C+). One-way ANOVA was performed (N=3, each group)**.** Bar graphs indicate the mean ± SEM. **B)** ***Upper panel***, representative flow cytometry image of $CD8^+$ lymphocytes cocultured with NP53 and NP53 cells infected with Delta-24-RGD or Delta-24-ACT (100 MOI). ***Lower panel***, representative images of $CD8^+$ clusters acquired on an inverted microscope.

1.2. Delta-24-ACT maintains the oncolytic features of Delta-24-RGD

Once we confirmed that 4-1BBL was functional, we next characterized the oncolytic effect of Delta-24-ACT in mouse and human DIPG cell lines. Western blot was used to analyze E1A and fiber expression, which are indicative of infection and viral replication, respectively, and we observed dose-dependent changes in viral protein expression in all the cell lines tested (Figure 25A). Moreover, we administered Delta-24-ACT into mice bearing NP53- or XFM-tumors and obtained brains 4 days after for viral protein staining. We observed E1A expression in treated tumors, what indicates that the virus can infect tumors *in vivo* as well (Figure 25B).

As already explained in the introduction, the expression of late viral proteins is activated after viral replication. Therefore, despite observing fiber expression on western blot, we wanted to study viral replication in infected lines. We performed an experiment to evaluate replication based on a hexon late protein detection method. So, we infected murine cells with 100 PFU of virus and human cells with 10 PFU, and collected the supernatants 16h and 72h later. The difference in labeling between the two times determines whether the virus has replicated, since at 72h more staining would be observed. However, as previously observed, Delta-24-ACT is unable to replicate in murine cells, whereas it does replicate in human cells. In human cells, there was a significant increase in the number of viral particles at 72h compared to 16h, but this does not occur in murine cells (Figure 25C).

Next, we tested the cytotoxic effect of Delta-24-ACT 5 days after viral infection. For that purpose, we infected cells with increasing amounts of Delta-24-ACT (MOIs ranging from 5 to 100) and measured viability by MTS. We observed a dose-dependent effect, as the percentage of viable cells decreased as the viral input increased. Delta-24-ACT displayed a half-maximal inhibitory concentration (IC_{50}) ranging from an MOI of 16.1 to an MOI of 0.2, and the values were lower in the human DIPG cell lines than in mouse cell lines as a result of effective replication (NP53: 16.1±1.1, SU-DIPG IV: 6.9±1.1, XFM: 2.5±1.5 and TP54: 0.2±1.6) (Figure 25D).

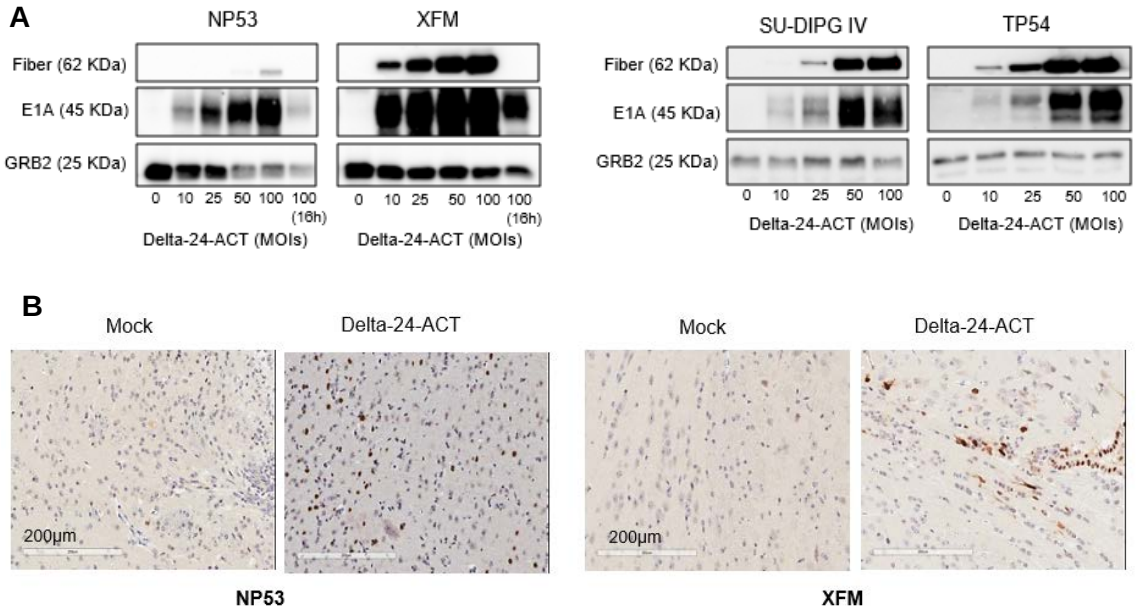

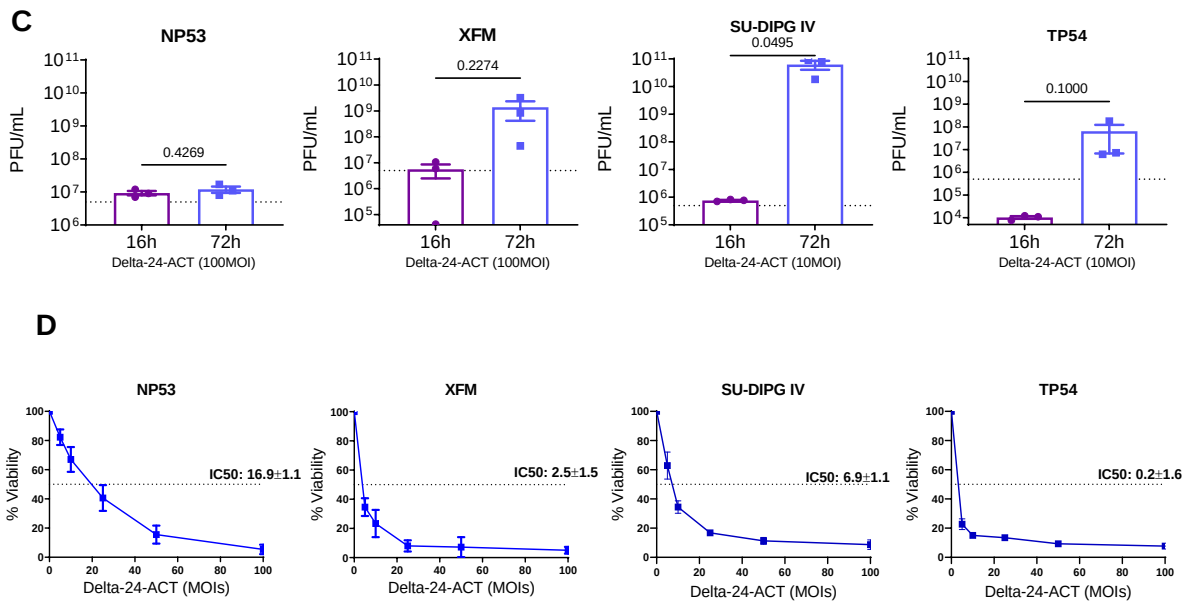

Figure 25. Delta-24-ACT produces an oncolytic effect in a dose-dependent manner. A) Assessment of viral protein expression (fiber and E1A) by western blot. Cells were infected with Delta-24-ACT at the indicated MOIs, and whole-cell lysates were collected 48 h later. GRB2 was used as a protein-loading control. **B)** Evaluation of the E1A viral protein *in vivo*, in mice bearing either XFM or NP53 cells three days after mock or Delta-24-ACT treatment. Representative micrographs are shown. **C)** Viral replication assay. Cell lines were infected at the indicated MOIs and supernatants obtained 16h and 72h after, to assess hexon staining. Bar graphs indicate the mean ± SEM (Student´s t test). **D)** Oncolytic effects of Delta-24-ACT on murine and human DIPG cells. Cells were infected at the indicated MOIs, and viability was evaluated five days later by MTS assays. The values indicate the percentages of viable cells in infected cultures compared to noninfected cultures (mean ± SD, N= 3 each group).

Once it was confirmed that the Delta-24-ACT virus maintained the cytolytic effect, we wanted to analyze whether the type of death it produces is immunogenic cell death (ICD). Therefore, we analyzed the secretion of ATP and HMGB1, as well as the exposure of calreticulin in the cell membrane, which have been described to be involved in ICD.[72] ATP and HMGB1 were measured in the supernatants of infected NP53 and XFM cell lines. In the case of ATP, cells infected with Delta-24-ACT secreted significantly higher levels compared to mock-infected cells; infected NP53 and XFM cells showed 18-fold higher and 44-fold higher ATP secretion, respectively (Figure 26A). Regarding HMGB1, supernatants were obtained 24h and 72h after cell infection and the amount of HMGB1 assessed by ELISA. In this case, cells infected for 72h secreted significantly higher levels than those infected 24h, secreting 26.9±3.6ng/mL and 13.6±2.7ng/mL in the case of NP53 and XFM, respectively (Figure 26B). Finally, we analyzed the location of calreticulin (CRT) on infected cells. We observed by immunofluorescence, that there was a translocation from the endoplasmic reticulum in mock-infected cells to the cell membrane in infected cells. We also confirmed that a higher percentage of cells expressed CRT on their membrane after Delta-24-ACT infection (NP53= 16.5% ±3.3; XFM= 53.5% ±7.6) (Figure 26C).

All these results indicate that Delta-24-ACT efficiently infect cells and produce oncolytic effect in an immunogenic manner.

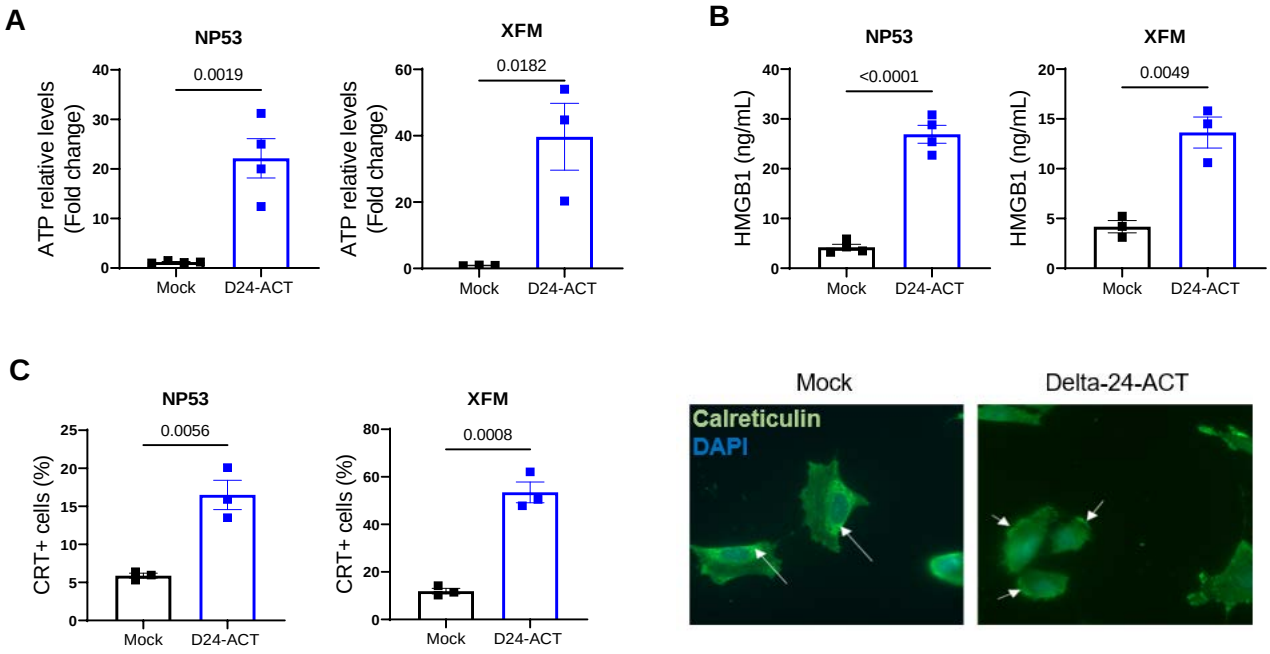

Figure 26. Delta-24-ACT promotes ICD on infected cells. A) ATP measurement in supernatants obtained from NP53 and XFM cultures at 72 h after Delta-24-ACT (N=3,4) or mock (N=3,4) infection. Data are shown as fold change and bar graphs indicate the mean ± SD (Student´s t test). **B)** Concentration of HMGB1 24h and 72h after Delta-24-ACT infection (N=3,4). Bar graphs indicate the mean ± SD (Student´s t test). **C)** ***Left panel***, Flow cytometric quantification of membrane calreticulin+ cells after Delta-24-ACT infection. The bar graphs show the mean ± SD values (N=3; Student´s t test). ***Right panel*****,** Representative fluorescence microscopy images of NP53 cells at 4 h after infection with Delta-24-ACT or mock infection. CRT at the cell surface was detected by immunofluorescence (green). Nuclei were stained with DAPI (blue).

1.3. Delta-24-ACT is safe and does not cause toxicity in vivo

Before starting to evaluate the efficacy of Delta-24-ACT in DIPG orthotopic models, we evaluated the safety profile of its administration *in vivo*. This is because the administration of an oncolytic virus with the capacity to unleash a potent immune response could result in lethal inflammation of the brainstem. In addition, 4-1BB agonist antibody administration in the clinic has been associated with liver toxicity.[101] We first assessed whether the virus had any effect in healthy tissue before viral administration into tumor-bearing mice. Therefore, we administered different doses of the virus (10^6 and 10^7 PFUs/mouse) or PBS as a control into the pons of two tumor-free immunocompetent mouse strains ($NP53^{fl/fl}$ and Balb/c). We weighed the animals every 2-3 days to assess weight variability as a sign of toxicity, as well as monitoring of mice to assess the impact on survival. We did not observe significant weight loss at any of the viral concentrations evaluated, nor differences between the control group and the group of the virus (Figure 27A). Moreover, we observed no deaths among any of the $NP53^{fl/fl}$ strain groups (Figure

27B). However, among Balb/c mice, there was one death each in the PBS and 10^6 PFU groups within the first 7 days of treatment (Figure 27C). The absence of a gross loss of body weight suggested that the viral injection was well tolerated, and we believe that these deaths were due to the procedure itself.

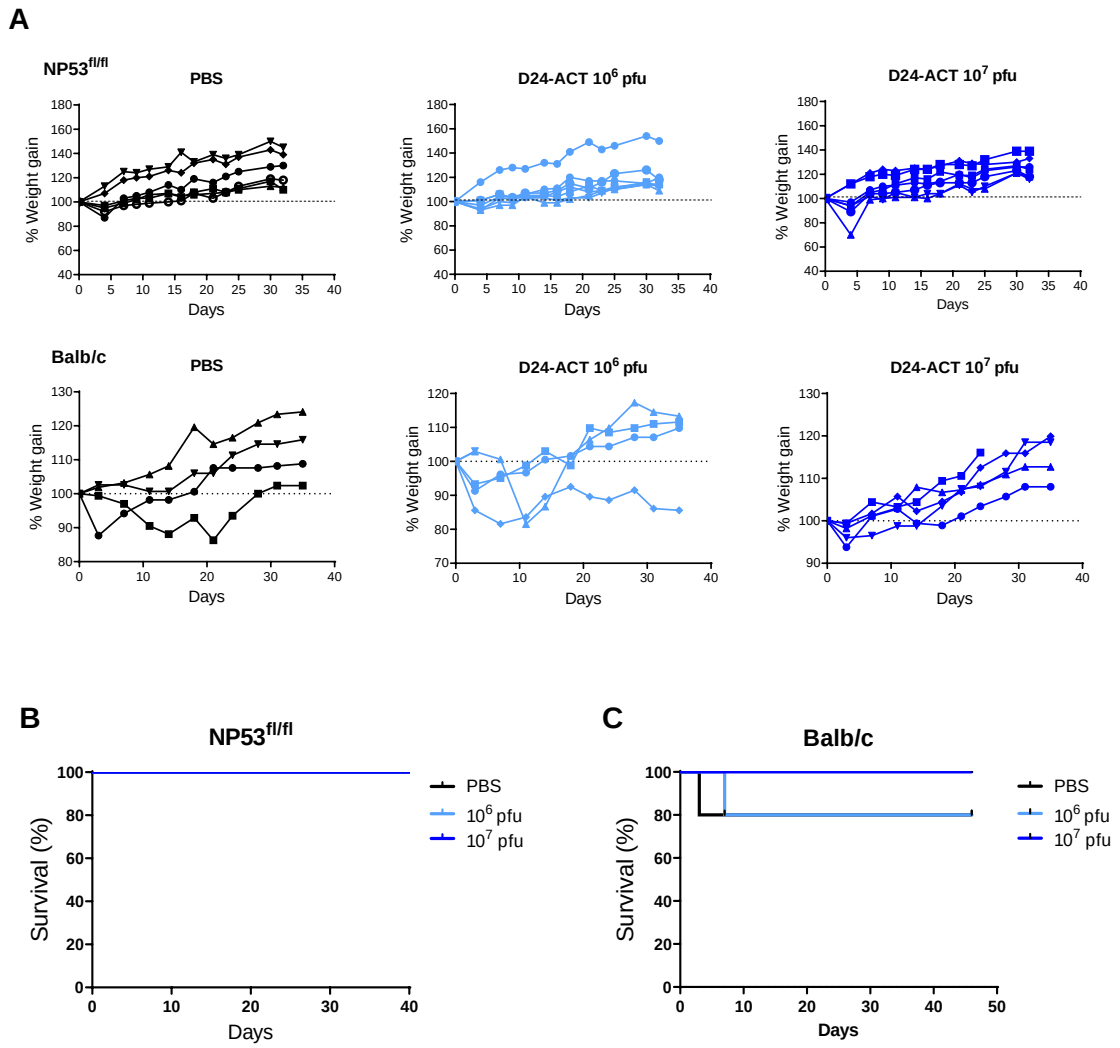

Figure 27. Safety evaluation of Delta-24-ACT administration. A) NP53$^{fl/fl}$ and Balb/c mice were treated intraparenchymally with mock (PBS) (N=6; 4) or Delta-24-ACT (N=7; 5) at the indicated doses. Mice from the different groups were weighed every 3-4 days until the end of the treatment (35 days). **B)** Kaplan–Meier survival plot of NP53$^{fl/fl}$ mice treated with PBS (control group) and 10^6 PFUs or 10^7 PFUs of Delta-24-ACT in the pons. **C)** Kaplan–Meier survival plot of Balb/c mice treated with PBS (control group) and 10^6 PFUs or 10^7 PFUs of Delta-24-ACT in the pons.

In a separate experiment, we obtained sera from mice bearing NP53 cells treated with either Delta-24-ACT or PBS (mock control) and measured several parameters indicative of hepatotoxicity. Thus, to analyze hepatocyte damage, we measured alanine aminotransferase (ALT) and aspartate aminotransferase (AST). The increase of ALT indicates inflammation and liver necrosis, and its elevation is proportional to the damage.

Likewise, AST increment shows complete lysis of the hepatocytes. On the other hand, we assessed alkaline phosphatase (ALP) levels since it is a good marker for cholestasis (any condition in which the flow of bile from the liver is reduced or obstructed). Finally, in order to analyze the hepatic function, we measured bilirubin and albumin levels. The liver produces albumin, and therefore, its decrease indicates a liver failure. On the contrary, an increase of bilirubin suggests bile duct obstruction.

We observed no significant differences between the virus-treated and PBS-treated mice in the measured parameters, except for AST and ALP levels, which were significantly increased in control (PBS-treated) mice. However, the obtained values were within the range of normal values in mice (AST=50-100 U/L, ALP=35-100 U/L) (Figure 28A).

To further analyze hepatic toxicity, we conducted anatomopathological analyses of mouse livers 15 days after viral administration to detect histological changes in this organ induced by Delta-24-ACT. Importantly, none of the analyzed livers showed signs of hepatic injury (Figure 28B).

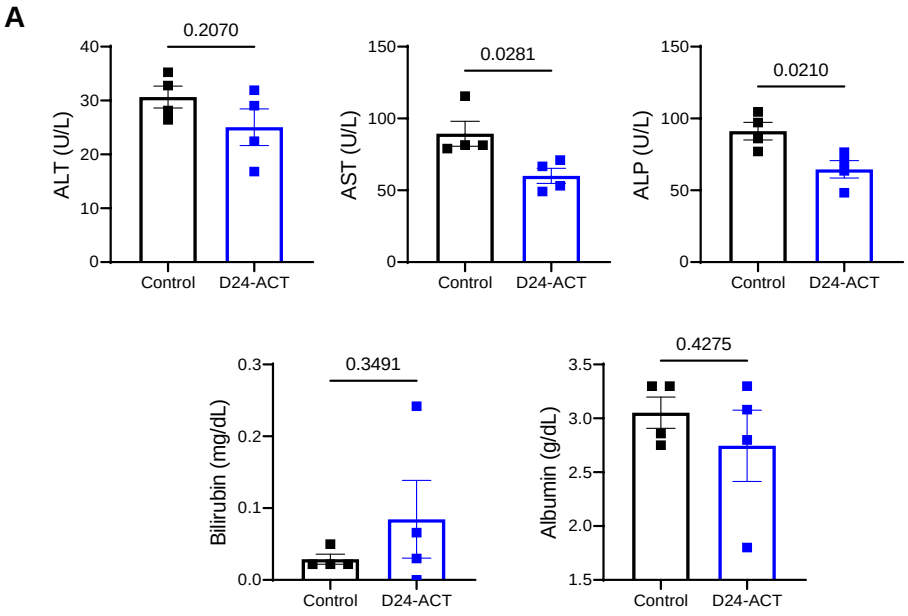

B

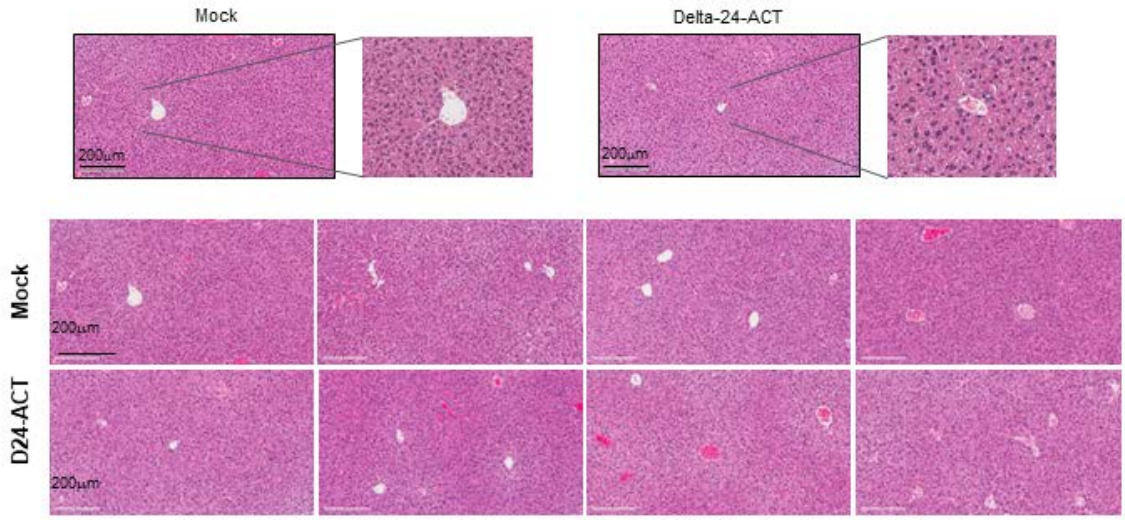

Figure 28. Evaluation of hepatotoxicity after Delta-24-ACT administration. A) Evaluation of biochemical parameters related to hepatic toxicity after intratumoral injection of Delta-24-ACT. The mice were treated with the mock or virus, and serum samples were collected 3 days later. Several parameters were measured, including alanine aminotransferase (ALT, U/L), aspartate aminotransferase (AST, U/L) and alkaline phosphatase (ALP, U/L) levels, to monitor hepatic injury and bilirubin (mg/dL) and albumin (g/dL) levels to assess hepatic function. Student's t test was performed. Bar graphs indicate the mean ± SEM. **B)** Histologic analysis of mouse livers bearing orthotopic DIPGs and treated locally with Delta-24-ACT at 10^8 PFUs. Representative micrographs of H&E staining (scale bar at 200 µm) of mouse livers from the indicated groups of DIPG models. The images show no viral presence in mouse livers and no signs of hepatotoxicity.

Moreover, we did not observe significant weight loss in NP53-bearing mice the following days after the administration of different doses of the virus (10^6 and 10^7 PFU/mouse) or PBS (Figure 29). These results highlight the safety of Delta-24-ACT and the fact that intratumoral injection of 4-1BBL does not induce hepatic toxicity.

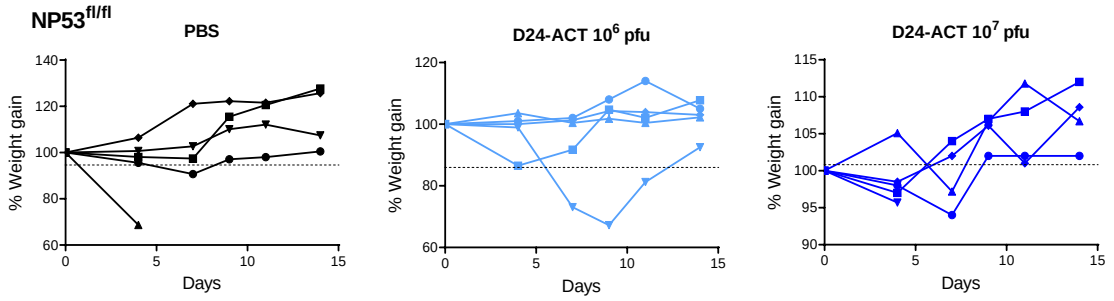

Figure 29. Percentage of weight change in $NP53^{fl/fl}$ mice-bearing NP53 tumors treated with 10^6 or 10^7 PFUs/mouse Delta-24-ACT or PBS as a control group.

1.4. Delta-24-ACT increases survival and promote immunological memory in orthotopic DIPG models

Once we confirmed Delta-24-ACT administration was safe, we evaluated the anti-DIPG effect of Delta-24-ACT *in vivo*. Using the above-mentioned screw-guided system, DIPG tumors were developed by the intracranial injection of NP53 or XFM cells into the pons of immunocompetent mice. Three days after cell injections, mice were treated with PBS (control group) or Delta-24-ACT (10^6 PFUs/mouse) and were monitored for survival (Figure 30A). We observed a significant increase in the median survival of mice treated with the virus in comparison to the control groups in both models (log-rank test; P=0.014 for NP53 cells, log-rank test; P<0.001 for XFM cells). The median survival time of the virus-treated mice injected with NP53 cells was 48.5 days, in comparison with 28 days for the controls (Figure 30B). In addition, 25% (2 out of 8) of the NP53-bearing mice were long-term survivors (Figure 30B). We also evaluated the antitumor efficacy of Delta-24-ACT in the XFM DIPG model using the same schedule (Figure 30C). The survival time was 30 days for the treated group of mice injected with XFM cells compared with 9 days for the controls. Importantly, 50% (5 of 10) of the XFM-bearing mice were long-term survivors (Figure 30C).

Since DIPGs are known to recur after treatment and the goal of this project was to not only show local efficacy but also to achieve protective immunological memory, we performed a rechallenge experiment with long-term survivors of the NP53 experiment. All of the naïve mice used as controls (4/4) developed tumors, while Delta-24-ACT-treated mice showed 100% protection against rechallenge with NP53 cells (2/2; Figure 30D). To demonstrate that the antitumor response observed was due to the immune response, we performed an experiment in immunodeficient mice (Balb/cA-Rag2$^{-/-}$γc$^{-/-}$) bearing NP53 murine cells, as the replication of the virus is highly attenuated in murine cell lines. Treatment with the virus did not present a survival benefit in this model (P = 0.622; Figure 30E).

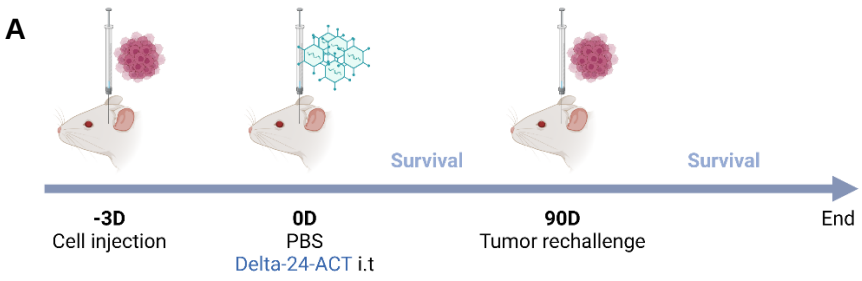

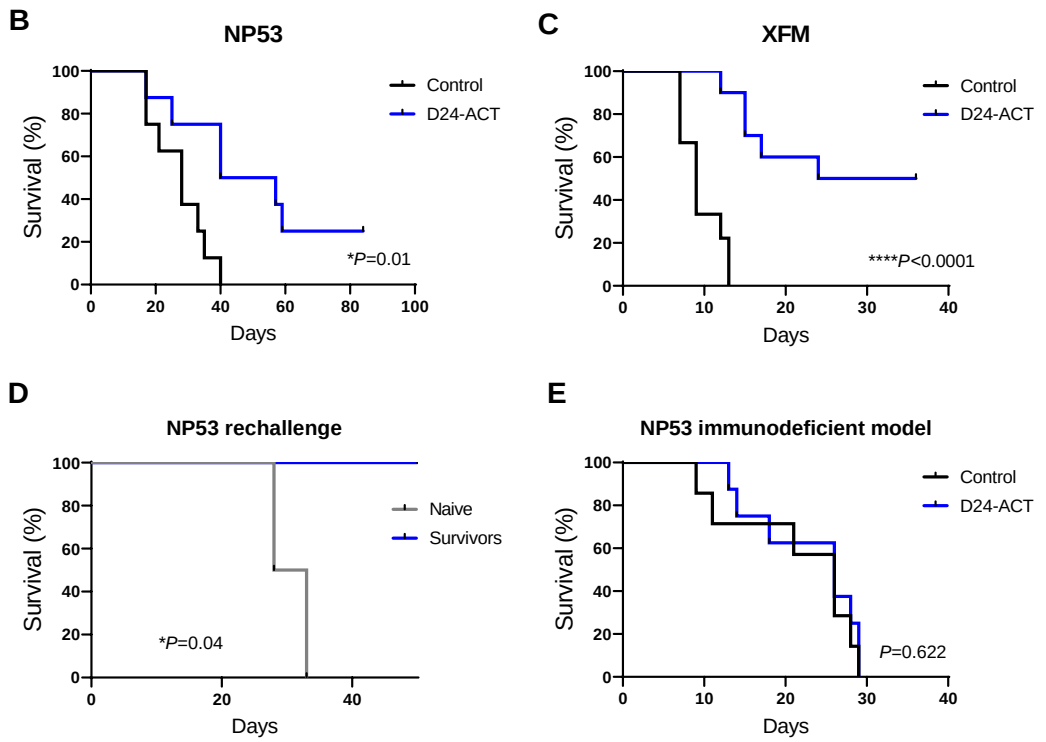

Figure 30. Evaluation of the anti-DIPG effect of Delta-24-ACT. A) Schedule of survival experiments performed with NP53 cells. **B)** Kaplan–Meier survival plot of mice bearing NP53 cells treated with 10^6 PFUs of Delta-24-ACT or a mock PBS control 3 days after cell administration (log-rank; P=0.01, N=8 each group). **C)** Kaplan–Meier survival plot of mice bearing XFM cells that were treated with 10^6 PFUs of Delta-24-ACT (N=10) or the mock PBS control 3 days after cell administration (N=9) (log-rank; P<0.0001). **D)** The long-term survivors from the Delta-24-ACT-treated group (N=2) were subjected to rechallenge with NP53 and compared with control naïve mice (N=4) (log-rank; P=0.04). **E)** Kaplan–Meier survival plot of immunodeficient mice (Balb/cA-Rag2$^{-/-}$γc$^{-/-}$) bearing NP53 cells treated with 10^6 PFUs of Delta-24-ACT (N=8) or a mock PBS control (N=7) 3 days after cell administration (log-rank; P=0.622).

Next, we assessed the antitumor effect of viral treatment in already established XFM tumors, and we postponed viral treatment until 7 days after cell injection instead of 3 days (Figure 31A). Delta-24-ACT significantly increased the median survival of treated mice and led to a 30% long-term survival rate (3/10; P = 0.0093 Figure 31B). Moreover, 66% of the treated XFM tumor-bearing mice exhibited immunological memory (2/3; Figure 31C), and these mice were free of tumors (Figure 31D). Thus, Delta-24-ACT treatment is efficacious against DIPG murine models and induces protective immunological memory against local tumor rechallenge.

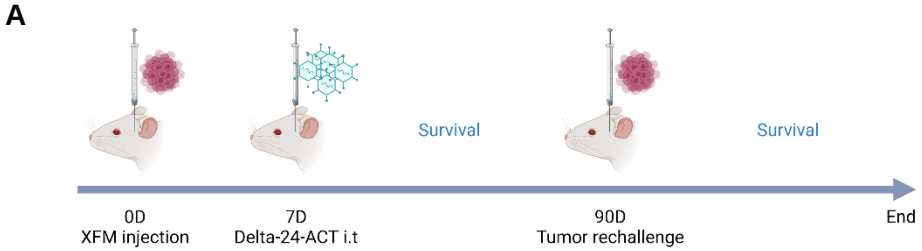

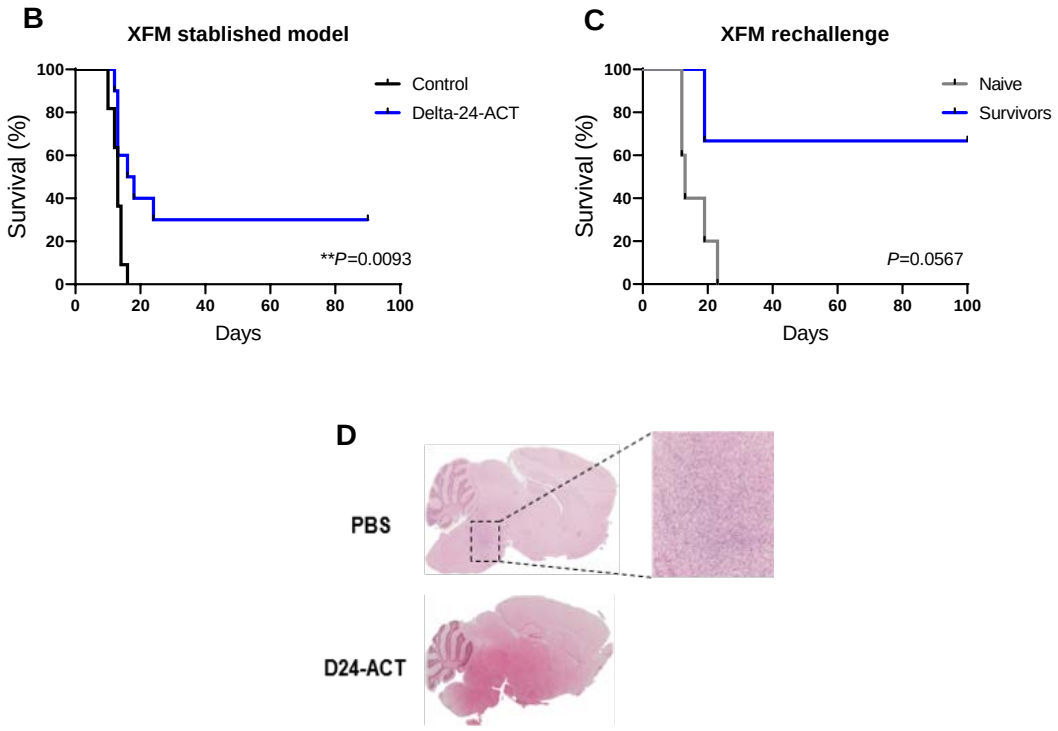

Figure 31. Delta-24-ACT prolongs survival of a stablished tumor model. A) Schedule of the survival experiment with the established XFM model; Delta-24-ACT was administered 7 days after cell injection. **B)** Kaplan–Meier survival plot of mice bearing XFM-established tumors treated with 10^6 PFUs of Delta-24-ACT (N=10) or a mock PBS control (N=11) 7 days after cell administration (log-rank; P=0.0093). **C)** The long-term survivors from the Delta-24-ACT-treated group (N=3) were subjected to rechallenge with XFM and compared with control naïve mice (N=5) (log-rank; P=0.02). **D)** Representative micrographs of XFM long-term survivors free of disease versus a naïve control (PBS) that presented a tumor.

1.5. Delta-24-ACT triggers a proinflammatory response in DIPG models

To better understand the mechanism underlying the therapeutic effect of Delta-24-ACT, we evaluated the triggered immune response. Thus, we intratumorally injected Delta-24-ACT or PBS (mock group) 3 days after NP53 cell implantation (0D). Then, tumor immune infiltrate was analyzed by NanoString and IHC multiplex (at 15 days) and flow cytometry at 3, 7 and 10 days after viral administration (Figure 32).

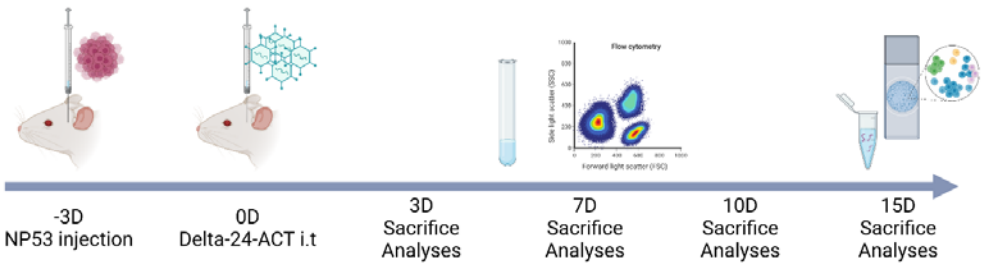

Figure 32. Schedule of mechanistic studies in the NP53 model. NP53 cells were engrafted (day -3), and animals were treated with a mock control or Delta-24-ACT (10^6 PFUs) three days later. Animals were sacrificed three (3D), seven (7D) or ten (10D) days later for flow cytometry and fifteen (15D) days later for NanoString and IHC multiplex analyses.

Regarding NanoString analyses, the 770-gene pancancer immunoprofile panel was performed. Gene set enrichment analysis of the control and Delta-24-ACT-treated tumors showed a clear separation between control and treated groups (Figure 33A) and revealed an increase in positive regulators of the immune response related to the activation and proliferation of lymphocytes (Figure 33B and 33C).

A

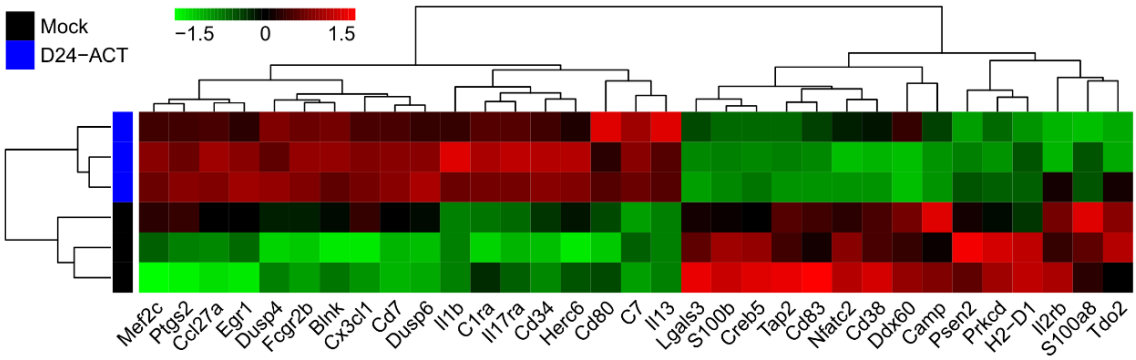

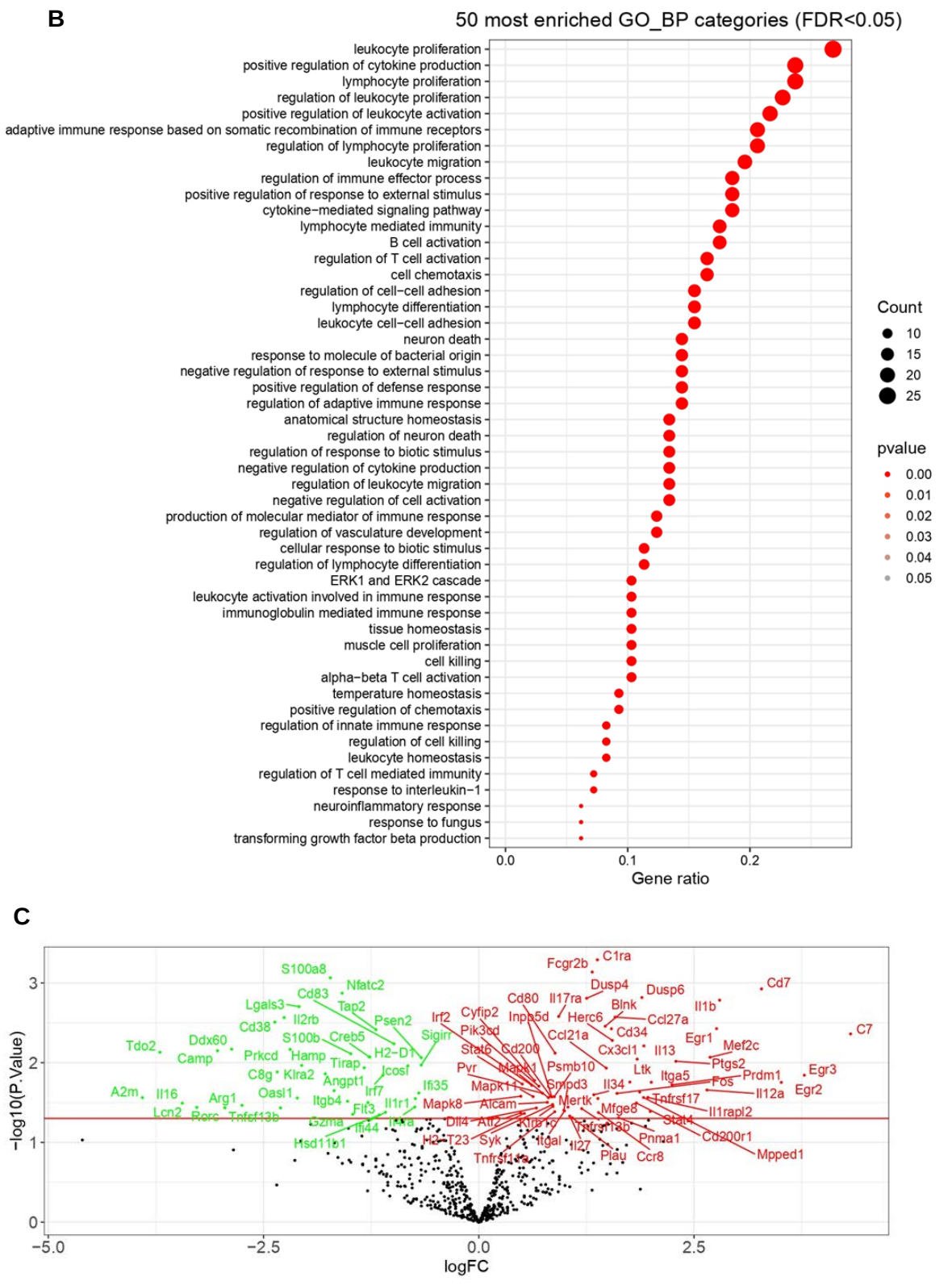

Figure 33. Analysis of tumor microenvironment by NanoString. A) Representative heatmap of transcriptome profiling using gene set enrichment analysis of murine DIPG tumors from mock-treated and Delta-24-ACT-treated mice (N =3) using the 770-gene pancancer immunoprofile panel in NanoString. **B)** Graph representing the 50 GO-biological processes enriched in Delta-24-ACT-treated animals versus control-treated. **C)** Volcano plot of statistical significance against fold-change between control-treated and Delta-24-ACT-treated, demonstrating the most significantly differentially expressed genes.

On the other hand, we analyzed the changes in the tumor microenvironment over the days by flow cytometry. Thus, we obtained the tumors 3, 7 and 10 days after viral administration. Similar to what we observed in the NanoString, flow cytometry analyses showed an increase over time in immune infiltration between the control and Delta-24-ACT-treated groups. By day 10 after viral treatment, tumors were significantly more infiltrated by nearly all the populations tested except for NK cells (CD45 *P*=0.0038; CD8 *P*=0.0056; CD4 *P*=0.0039; Treg cells *P*=0.0015; F4/80 *P*=0.0019; B cells *P*=0.0224; NK cells *P*=0.354; DCs *P*=0.0226) (Figure 34A). In addition, we analyzed the phenotype of $CD8^+$, $CD4^+$ T cells, and NK cells, by activation/exhaustion markers, such as GITR, OX40, PD-1, and CD69. We observed significantly upregulated expression of these markers in both populations at day 7 (Figure 34B) but not at day 10 (Figure 34C), indicating that the first boost of Delta-24-ACT promotes an immune-active state. More importantly, we also analyzed the expression of CD137 (4-1BB) on $CD8^+$ and $CD4^+$ T cells, Treg cells, and NK cells both at days 7 and 10. At day 7, the four tumor-infiltrating populations had higher surface CD137 expression in the Delta-24-ACT-treated tumors than in the controls (Figure 34D) (CD8 *P*=0.1889; CD4 *P*=0.0101; Treg cells *P*=0.0137; NK cells *P*<0.0001), indicating that they could directly interact with the cells expressing 4-1BBL in a Delta-24-ACT-dependent manner. This upregulation of CD137 expression was lost at day 10 (CD8 *P*=0.9254; CD4 *P*=0.5824; Treg cells *P*=0.0994; NK cells *P*=0.2188) (Figure 34E).

A

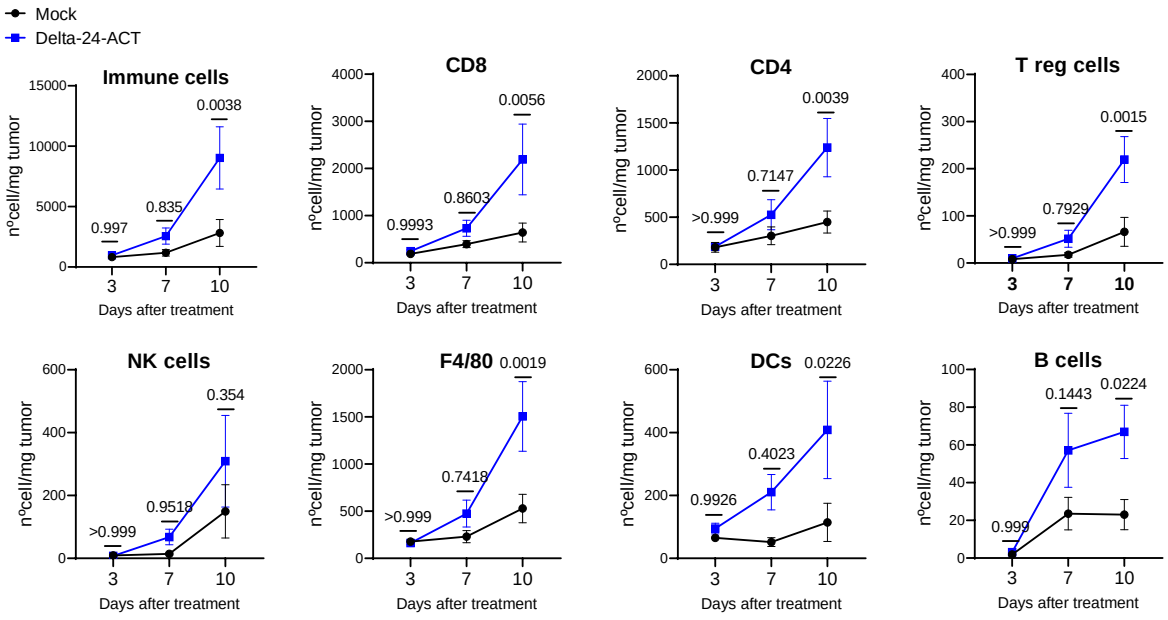

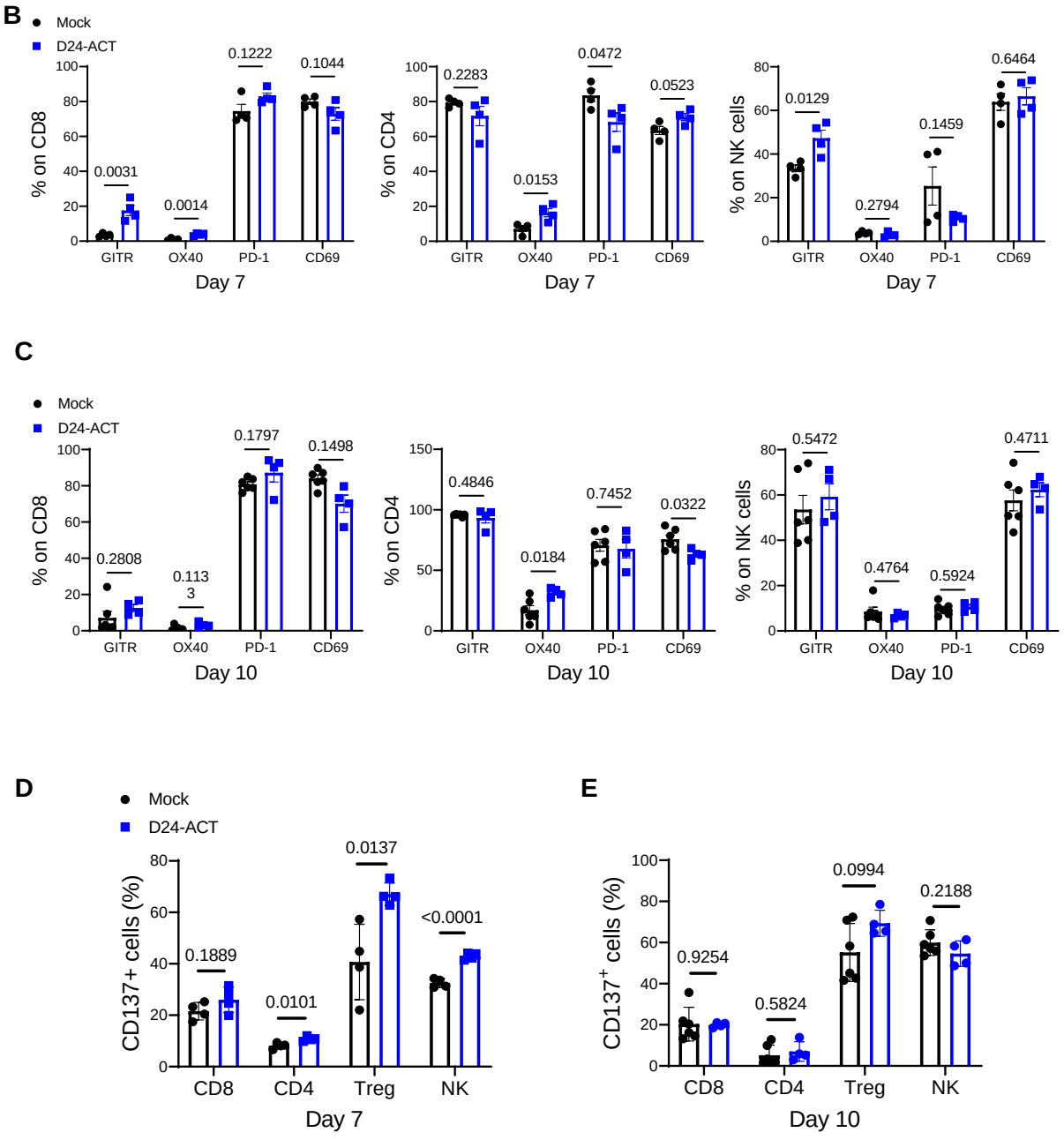

Figure 34. Analysis of the tumor microenvironment by flow cytometry 3, 7 and 10 days after treatment. A) Flow cytometry analyses of different immune cell populations in the brains of mice bearing NP53 tumors on the indicated days after treatment with Delta-24-ACT (blue) or PBS (black). Data are shown as number of cells/mg tumor (Immune cells: $CD45^+$; CD8 cells: $CD45^+/CD11b^-/TCR^+/CD8^+$; CD4 cells: $CD45^+/CD11b^-/TCR^+/CD4^+$; Treg cells: $CD45^+/CD11b^-/TCR^+/CD4^+/Foxp3^+$; NK cells: $CD45^+/CD11b^-/NKp46^+$; Macrophages(F4/80): $CD45^+/CD11b^+/F4/80^+$; DCs: $CD45^+/CD11b^+/MHC\text{-}II^+/CD11c^+$; B cells: $CD45^+/CD11b^-/CD19^+$). Two-way ANOVA was performed. **B)** Flow cytometry analyses of different activation (GITR, OX40, CD69) and exhaustion (PD-1) markers were performed in the $CD8^+$ and $CD4^+$ cell subsets at 7 and 10 days **(C)** after viral administration. Multiple comparison t-test was performed (N=4 each group). Bar graphs indicate the mean ± SEM. **D)** CD137 expression (%) in T cell populations and NK cells 7 and 10 **(E)** days after viral treatment. Multiple comparison t-test was performed (N=4 each group). Bar graphs indicate the mean ± SEM.

In addition, we analyzed tumor immune infiltration by immunohistochemistry 15 days after viral administration to NP53-bearing mice, to assess the viral effect at a later time. We performed serial brain sections and analyzed the presence of $CD8^+$, $CD4^+$ and Treg ($FOXP3^+$) lymphocyte populations. At this time point, we observed a significant increase in the $CD8^+$ subpopulation but no increase in $CD4^+$ cells (*P*=0.0168, *P*=0.5744, respectively). However, we also observed a significant increase in $FOXP3^+$ T regulatory cells after viral treatment (*P*=0.048) (Figure 35).

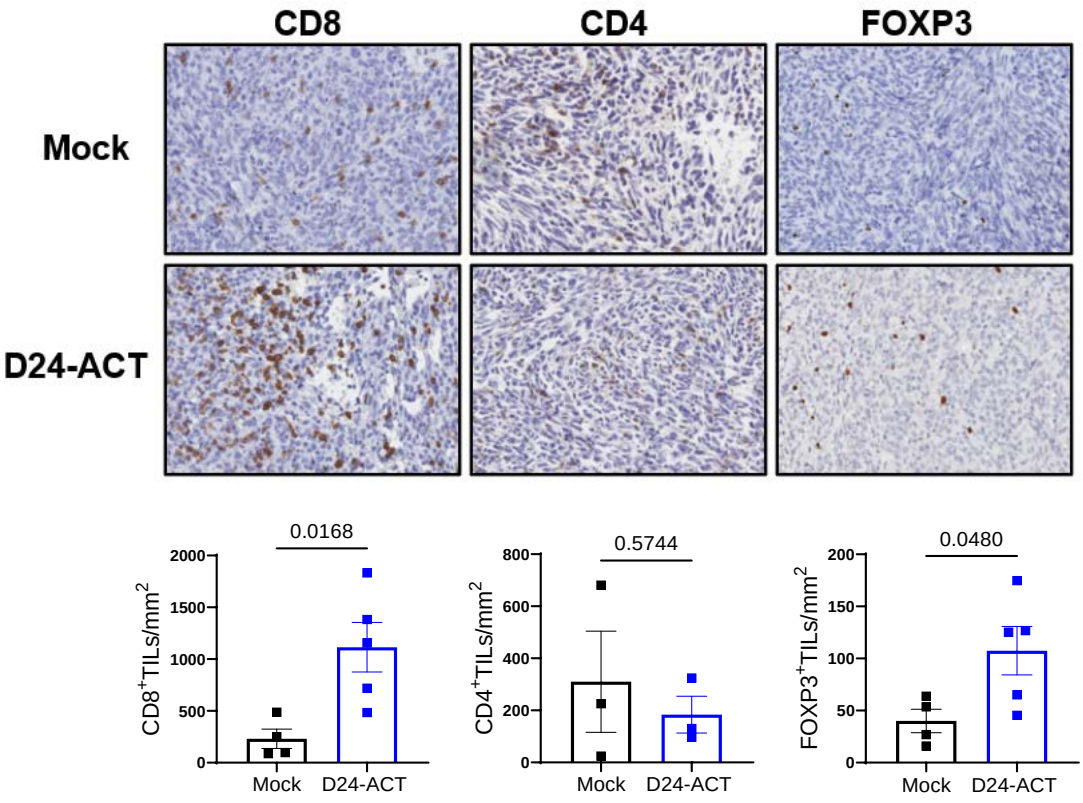

Figure 35. **Analysis of T lymphocytes by IHC 15 days after viral administration.** ***Upper panel***, representative images (scale bar, 100 µm) of CD4, CD8, and FOXP3 immunostaining of DIPG tumors from control and Delta-24-ACT-treated mice. ***Lower panel***, Graph showing the quantification of $CD8^+$, $CD4^+$ and $FOXP3^+$ cell infiltration at 15 days after cell implantation per mm^2 of tumors treated with either PBS or Delta-24-ACT (N =3-5). P values were calculated by Student's t-test.

Additionally, examination of long-term survivors from the rechallenge showed animals that were tumor free and lacking any kind of immune infiltration (Figure 36).

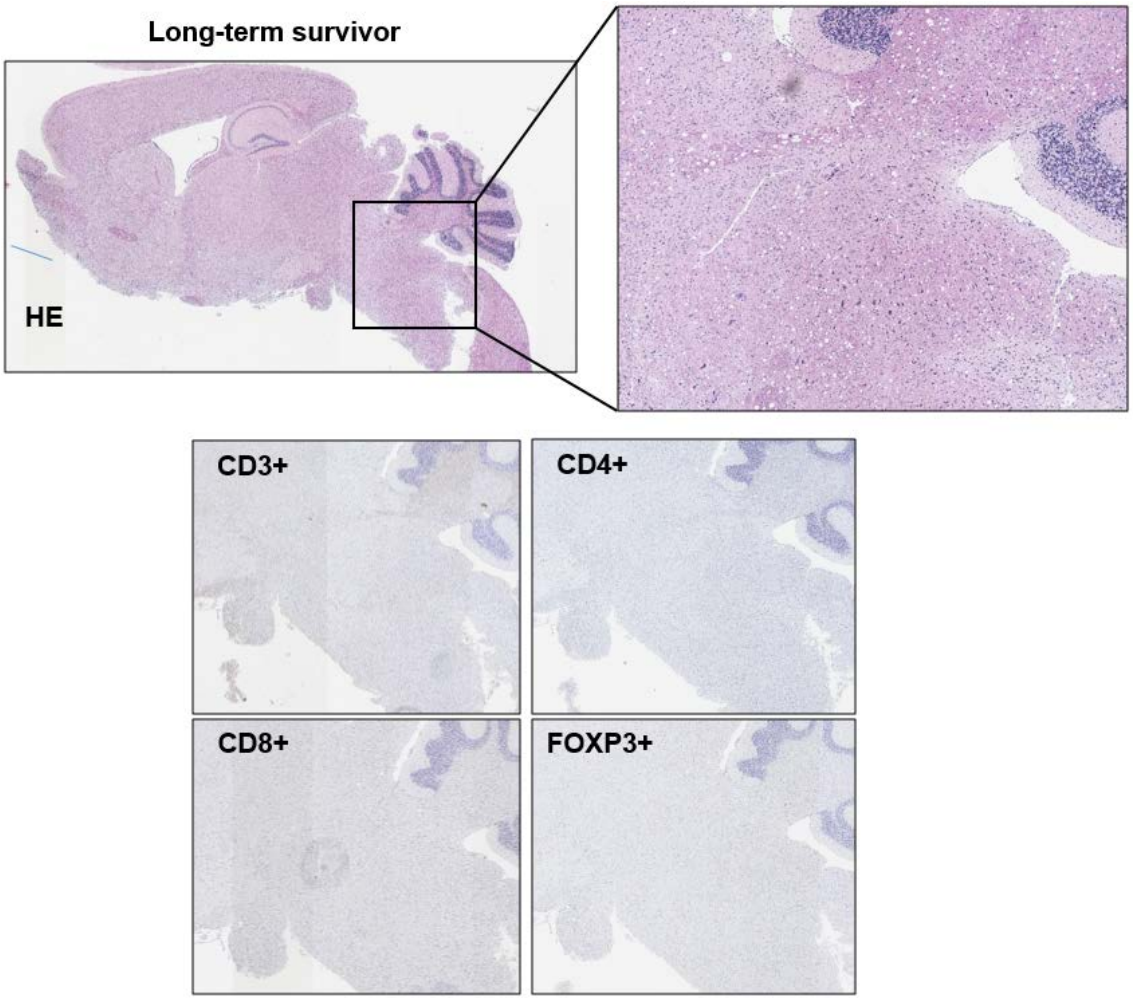

Figure 36. Representative image of the brain from a long-term survivor, which is tumor free and do not present immune infiltration, demonstrated by the absence of CD3, CD8, CD4 and FOXP3 staining.

In parallel, we used multispectral immunofluorescence to confirm the localization of the CD8, CD4, FOXP3, CD31, and F4/80-positive populations within the tumor 15 days after Delta-24-ACT treatment (Figure 37). We first confirmed that immune cells could infiltrate the tumor since the labeling was inside the tumor and not in the periphery (Figure 37A). In general, Delta-24-ACT treated group showed a more infiltrated tumor microenvironment (Figure 37B). Moreover, we observed an increase in T populations in the Delta-24-ACT group, which was significant for T regulatory cells ($CD8^+$ (%) P=0.1067; $CD4^+$ density P=0.5422; $Foxp3^+$ density P=0.0419). We also observed a decrease in the percentages of cells expressing the endothelial cell markers CD31 and F4/80 (which label microglia and macrophages), even though the differences were not significant (Figure 37B).

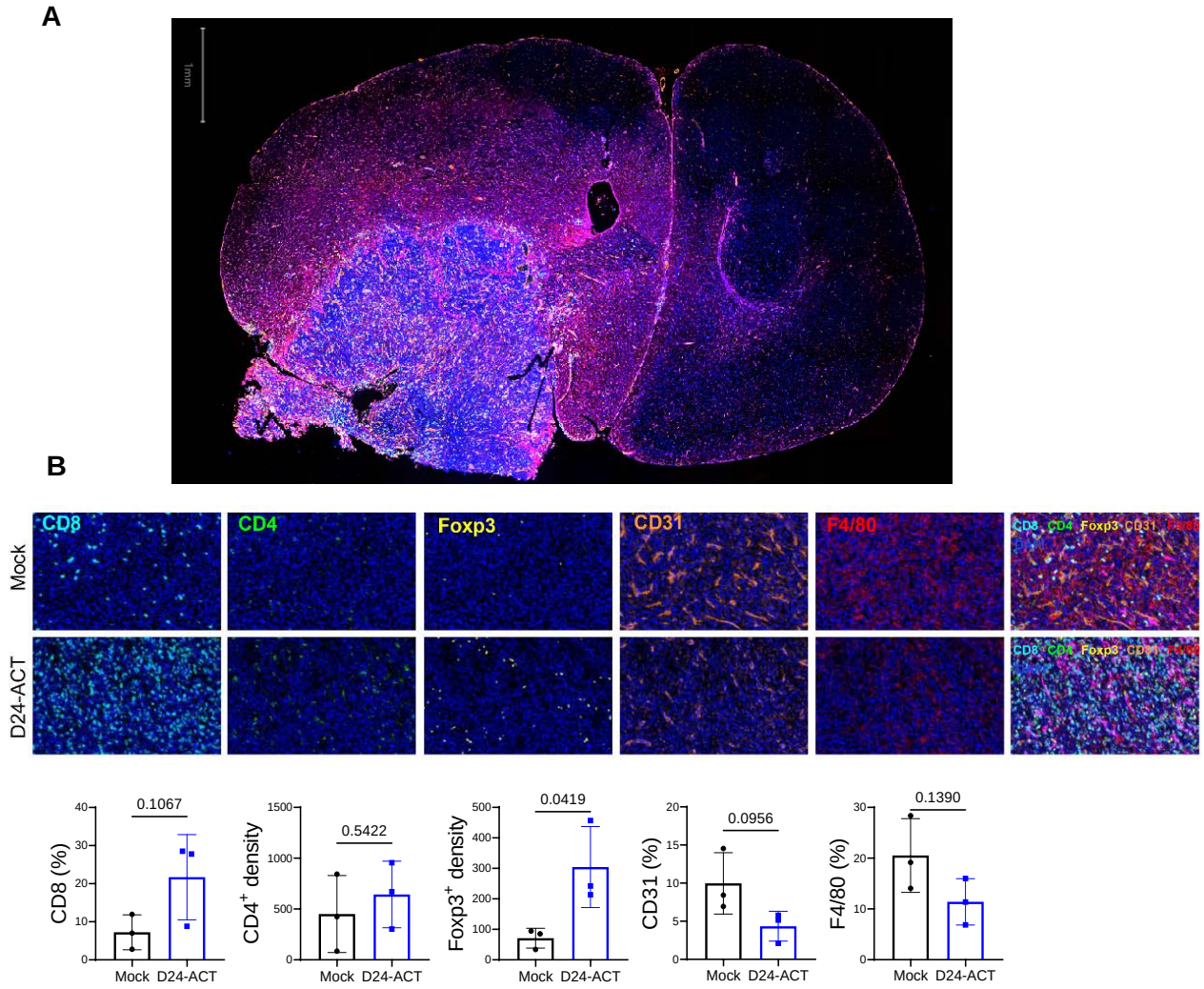

Figure 37. The brains of mice bearing NP53 cells were subjected to multiplexed immunofluorescence analysis to detect the following immune cell markers: CD8 (light blue), CD4 (green), Foxp3 (yellow), CD31 (orange), F4/80 (red), and GFAP (pink). The nuclei were counterstained with DAPI (blue). (N=3) **A)** Representative image of a brain section to show that immune infiltration can enter into the tumor. **B)** ***Upper panel,*** Representative micrographs of the staining of each population separately and all together. ***Lower panel,*** graphs showing the quantification of the different immune populations at 15 days after treatment (N=3). Percentages represent the percentage of positive cells respect to $DAPI^+$ cells, whereas the density shows the ratio of positive cells to nucleated ($DAPI^+$) cells.

Finally, we aimed to confirm these results in another DIPG tumor model (XFM), in this case adding Delta-24-RGD. We wanted to confirm that Delta-24-ACT was equally or more capable than Delta-24-RGD of increasing immune infiltration. Ten days after viral treatment (Figure 38A), tumor-infiltrating lymphocytes (TILs) from XFM tumors were analyzed by flow cytometry. Similar to the results for NP53 tumors, we observed significant increases in the immune infiltrates in the Delta-24-ACT treatment group versus the control group (Figure 38B). We observed major differences in the percentage of total immune cells ($CD45^+$), which was due to the increase in the percentage of T lymphocytes, more specifically in the $CD8^+$ cytotoxic population. Although the

proportions of CD4⁺ cells and Tregs tended to increase, their levels were not significantly different between the groups. We also did not observe any change in the percentage of NK cells between treatment groups (Figure 38B). However, we wanted to see if there were differences in proliferation (Ki67 labeling) in the CD8⁺, CD4⁺ and NK populations due to the presence of the ligand (when comparing Delta-24-ACT with Delta-24-RGD and the control) (Figure 38C). In fact, CD8⁺, CD4⁺ and NK cells present in Delta-24-ACT-treated tumors displayed significantly increased proliferation compared with Delta-24-RGD-treated or control tumors. Finally, we also observed that CD8⁺ and CD4⁺ lymphocytes expressed more PD-1 in the presence of Delta-24-ACT (Figure 38C).

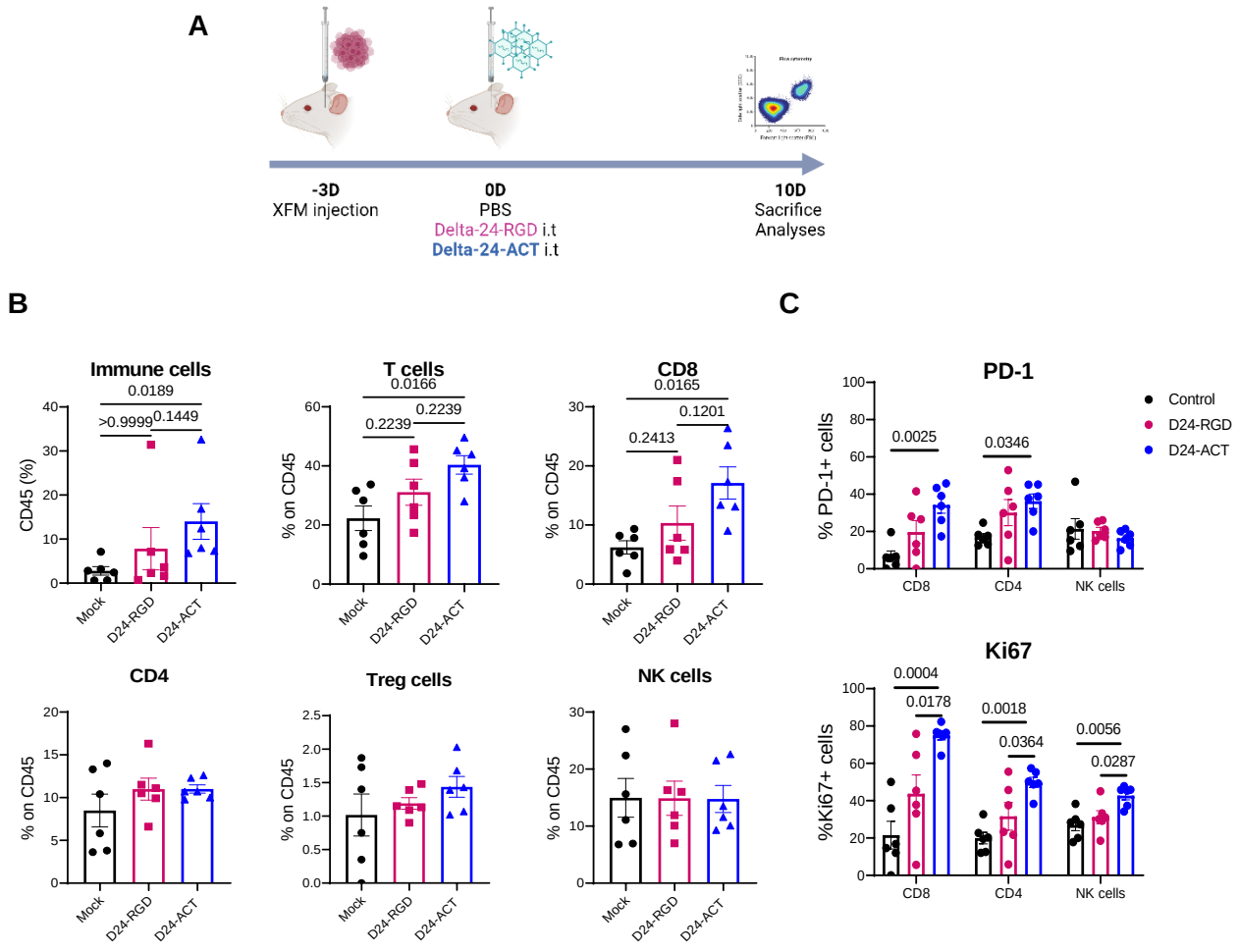

Figure 38. A) Schedule of mechanistic studies in the XFM model. XFM cells were engrafted (day -3), and the animals were treated with either a mock control, Delta-24-ACT or Delta-24-RGD (10^6 PFUs) three days later. The animals were sacrificed ten days (10D) later, and the different immune populations were assessed. **B)** Flow cytometry analyses of different immune cell populations in the brains of mice bearing XFM tumors 10 days after treatment with Delta-24-ACT (blue), Delta-24-RGD (magenta), or PBS (black). The bars indicate the mean ± SD (N=6), One-way ANOVA. **C)** Flow cytometry analyses of Ki67 proliferation and PD-1 markers were performed in the CD8, CD4, and NK cell subsets 10 days after viral administration. The bars indicate the mean ± SD (N=6).

All these results obtained with Delta-24-ACT adenovirus demonstrate that Delta-24-ACT, in addition to producing a cytolytic effect, is capable of efficiently expressing functional 4-1BBL. As a result, there is an increase of active immune infiltrate in the tumor microenvironment which translates into tumor shrinkage and thus, improved survival.

2. Delta-24-RGDOX characterization in vitro and in vivo in orthotopic models of DIPG

2.1. Delta-24-RGDOX efficiently expresses OX40L on the membrane of infected cell lines

Before starting with the *in vitro* characterization of Delta-24-RGDOX, we assessed whether the virus was able to produce OX40L on infected DIPG cells. For that purpose, we infected NP53 and XFM cell lines with increasing MOI of Delta-24-RGDOX (50, 100 and 300 PFU/cell) and obtained the RNA 48h after infection. We observed an increased expression of OX40L mRNA in a dose-dependent manner in both cell lines (Figure 39A).

In addition, we evaluated the expression of OX40L at the protein level. We first wanted to evaluate the general protein expression, regardless of cellular localization, by western blot. However, the existing antibodies on the market for this technique are not very efficient. We performed a test with an anti-OX40L antibody (R&D systems, MAB1236) using recombinant OX40L protein as a positive control. As shown in Figure 39B, the obtained staining was very unspecific, since we observed several bands, none of which coincided with the positive control. Therefore, we moved to assess OX40L expression by flow cytometry, which, in addition, allows us to analyze the expression in the cell membrane, necessary for the ligand to exert its function. We infected murine NP53 and XFM cells and human TP54 cells with 10 and 50 PFU/cell of Delta-24-RGDOX and analyzed OX40L expression 48h later. At an MOI of 10, more than 80% of XFM and TP54 cells expressed OX40L in their membrane (XFM= 90.8%± 4.1; TP54= 94.4%± 2.4), while 74.6%± 9.2 of NP53 cells expressed the ligand at the same dose (Figure 39C).

Finally, we wanted to elucidate the effect of the OX40L present on Delta-24-RGDOX on the activation of $CD8^+$ T cell using the same functional study explained above in the Delta-24-ACT section. Briefly, gp100-specific $CD8^+$ T cells from PMEL mice were cocultured with mock-, Delta-24-RGD- or Delta-24-RGDOX-infected NP53 cells (that were previously pulsed with the gp100 peptide) for 48h. Afterward, supernatants, and cells were collected to measure IFN-γ on the supernatants and granzyme B expression in the cells, as signs of CD8 activation. We observed a significant increase in the IFN-γ secretion by Delta-24-RGDOX infected cells in comparison with the control and Delta-24-RGD infected cells. We also observed a significant increase in granzyme B expression (Figure 39D).

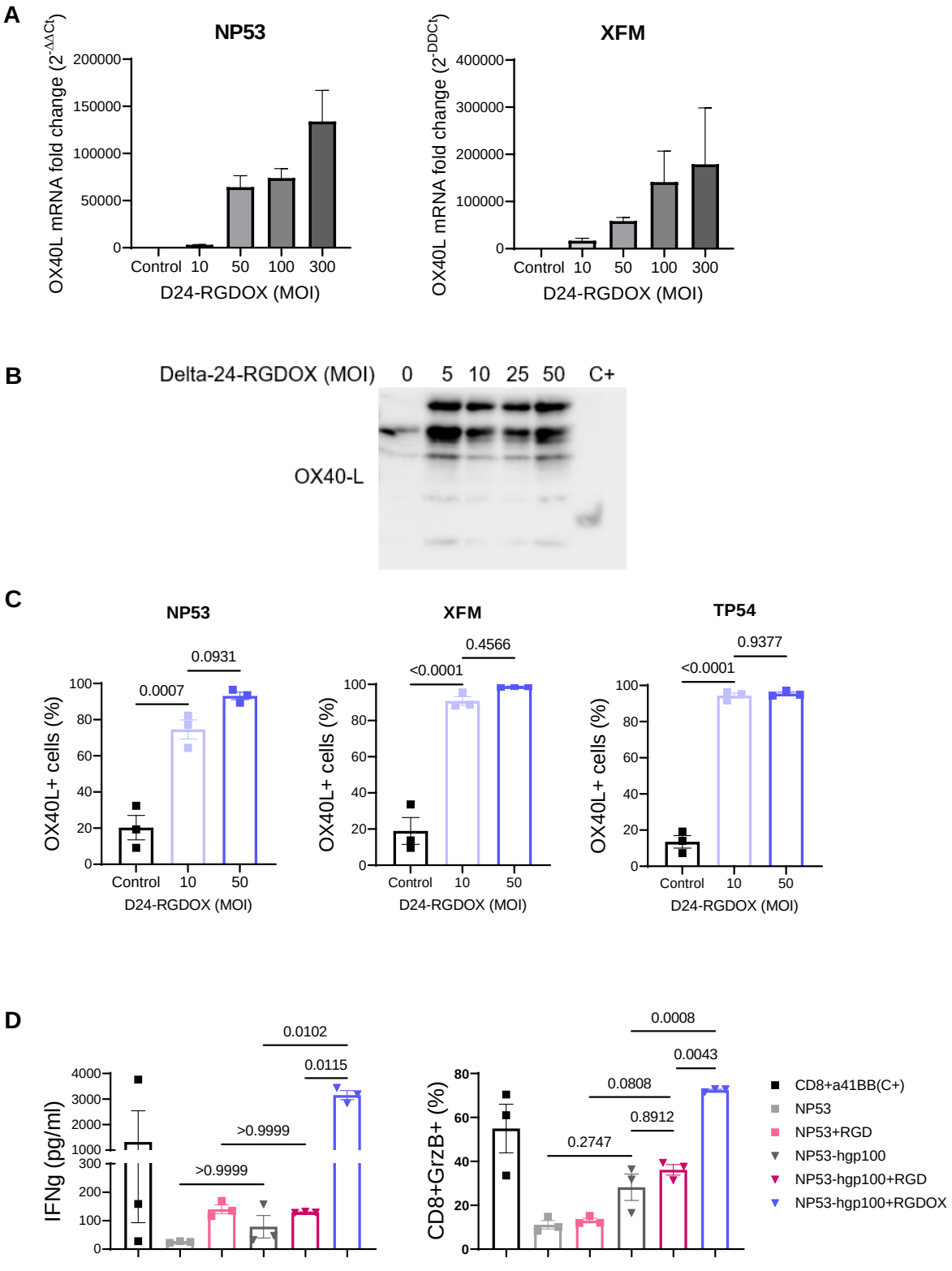

Figure 39. Delta-24-RGDOX express a functional OX40L on the membrane of infected cells. A) mRNA expression of OX40L on NP53 and XFM cell lines 48h after Delta-24-RGDOX infection at the indicated MOIs (N=3). **B)** OX40L protein expression in NP53 cells infected with Delta-24-RGDOX at the indicated MOIs as determined by western blotting. C+: OX40L recombinant protein. **C)** OX40-L expression on the membrane of infected cells 48h after infection by flow cytometry. The percentage of OX40L-positive cells is shown. One-way ANOVA was performed (N=3, each group). Bar graphs indicate the mean ± SEM. **D)** IFN-gamma and granzyme B production by $CD8^+$ lymphocytes. $CD8^+$ T cells from PMEL mice were cocultured with NP53 cells infected with Delta-24-RGD, Delta-24-RGDOX (MOI 100) or the mock control. $CD8^+$ lymphocytes

activated with CD3, CD28 and 4-1BB antibody were used as positive control for the experiment (C+). One-way ANOVA was performed (N=3, each group)**.** Bar graphs indicate the mean ± SEM.

These data demonstrate that Delta-24-RGDOX can express OX40L at both mRNA and protein levels. Moreover, OX40L on the membrane of infected cells is functional and had the capability to activate CD8 lymphocytes.

2.2. Delta-24-RGDOX infects, replicates in and kills murine and human DIPG cell lines

Once we confirmed that Delta-24-RGDOX expresses OX40L on the membrane of infected DIPG cells, we evaluated the oncolytic effect of the virus in murine and human cell lines. First, we evaluated E1A and fiber expression by western blot in cells infected for 48h. We observed E1A protein expression in a dose-dependent manner in all the lines tested, indicating that Delta-24-RGDOX efficiently infects tumor cells (Figure 40A). However, fiber was only expressed efficiently in human TP54 cells and at a lesser extent in XFM, while it was not expressed on NP53. Therefore, we performed a replication assay that allows us to analyze whether new virions were generated. In this experiment, we obtained the supernatant from previously infected cells and added it to other cells. Then, we detected the presence of hexon (viral capsid protein) in the new cells, indicating that new virions capable of infecting cells were produced. Murine cells were infected with 100 PFU/cell of Delta-24-RGDOX and human cells with 10 PFU/cell. Viral replication was compromised on NP53 cell line (*P*=0.113) and replicated efficiently in XFM (*P*=0.0094) and in the human cell line (*P*=0.0058) (Figure 40B), similar to what we obtained by western blot.

Finally, we evaluated the cytotoxic effect of Delta-24-RGDOX on DIPG cell lines 5 days after viral infection. For that purpose, we infected cells with increasing amounts of Delta-24-RGDOX (MOIs ranging from 5 to 100) and we measured the viability by MTS. We observed a dose-dependent effect, as the percentage of viable cells decreased as the viral input increased. Delta-24-RGDOX displayed a half-maximal inhibitory concentration (IC_{50}) ranging from an MOI of 36.9 to an MOI of 0.2, and the values were lower in the human DIPG cell lines than in mouse cell lines as a result of effective replication (NP53: 36.9±1.2, XFM: 14.1±1.3 and TP54: 0.1±20.9) (Figure 40C).

A

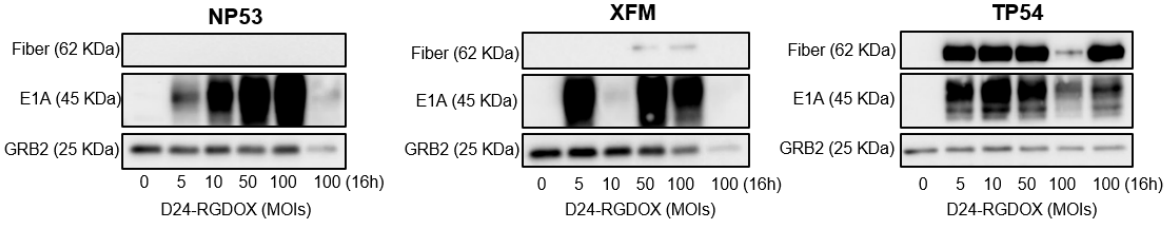

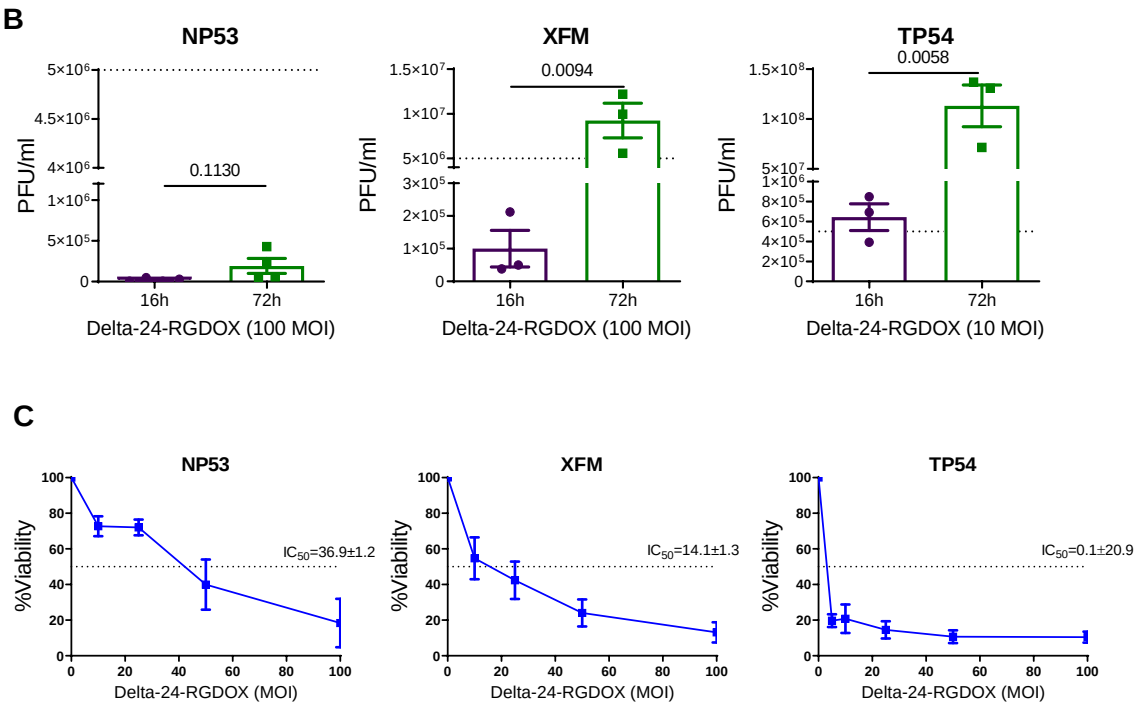

Figure 40. Delta-24-RGDOX produces oncolytic effect in DIPG cell lines. A) Assessment of viral protein expression (fiber and E1A) by western blot. Cells were infected with Delta-24-RGDOX at the indicated MOIs, and whole-cell lysates were collected 48 h later. GRB2 was used as a protein-loading control. **B)** Viral replication assay. Cell lines were infected at the indicated MOIs and supernatants obtained 16h and 72h after, to assess hexon staining. Bar graphs indicate the mean ± SEM (Student´s t test). **D)** Oncolytic effects of Delta-24-RGDOX on murine and human DIPG cells. Cells were infected at the indicated MOIs, and viability was evaluated five days later by MTS assays. The values indicate the percentages of viable cells in infected cultures compared to noninfected cultures (mean ± SD, N=3 each group).

In summary, Delta-24-RGDOX can infect, express viral protein, and efficiently replicate in DIPG human cell lines. Finally, the virus shows a cytotoxic effect in a dose-dependent manner.

2.3. Delta-24-RGDOX treatment displays a safe profile in DIPG orthotopic models

Before evaluating the anti-DIPG effect of Delta-24-RGDOX, we wanted to assure whether Delta-24-RGDOX administration into the pons was safe. For that purpose, we administered the virus into healthy mice, in both mice strains NP53$^{fl/fl}$ and Balb/c. Using the screw-guided system, we injected 10^6 or 10^7 PFU of Delta-24-RGDOX and PBS as a control group. We weighted animals every 2-3 days as a sign of toxicity. We did not observe significant decrease in weight, nor differences between the virus and control groups (Figure 44A and 44B). All Balb/c mice survived (Figure 41A), but one NP53$^{fl/fl}$ mouse containing 10^6 PFU of Delta-24-RGDOX died at day 20 (Figure 41B).

Finally, we also evaluated the potential viral toxicity in NP53-bearing mice. In this case, we administered tumor cells using the screw-guided system, and 3 days later, we injected Delta-24-RGDOX intratumorally. As a surrogate marker of toxicity, we weighted

mice every day for the first eight days. We did not observe significant differences in weight amongst the different treatment groups (Figure 41C).

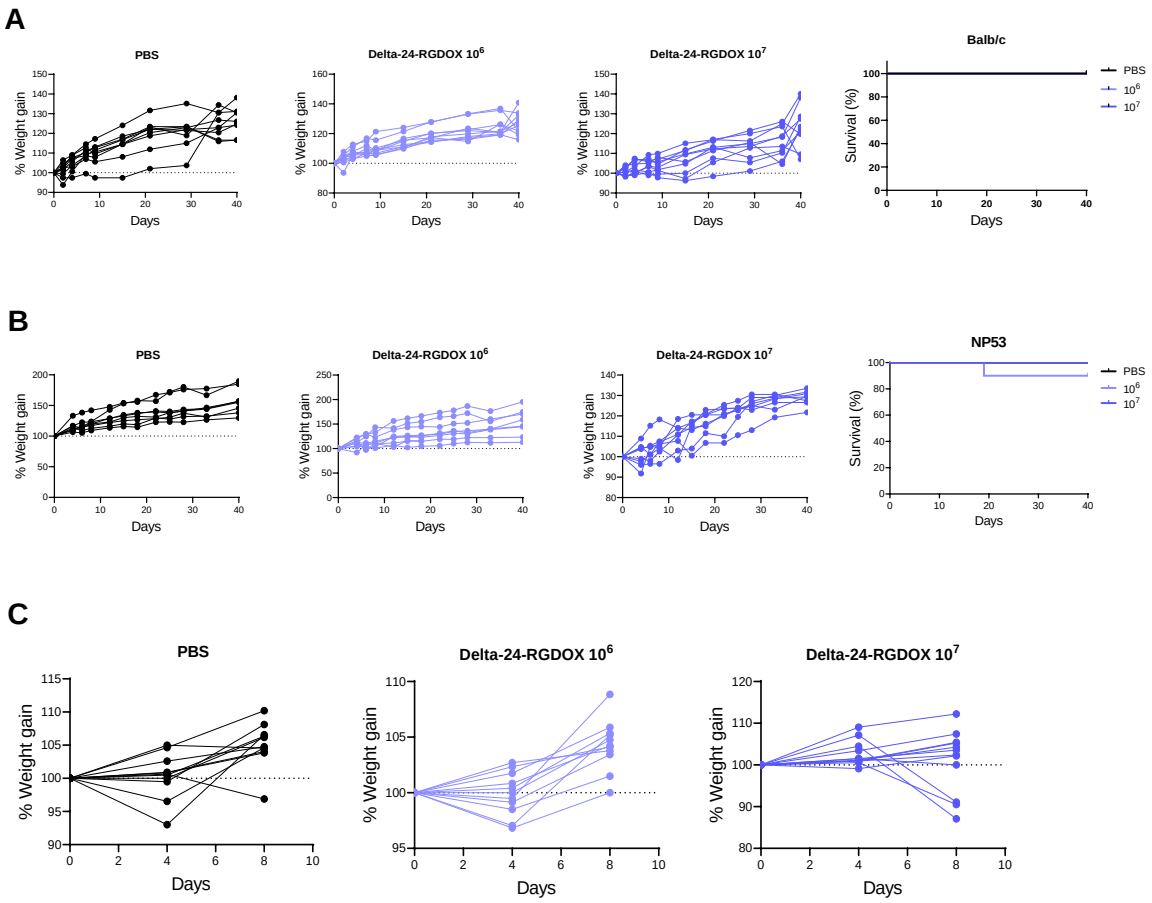

Figure 41. Evaluation of toxicity upon Delta-24-RGDOX administration. A) Balb/c and **B)** NP53$^{fl/fl}$ mice were treated intraparenchymally with mock (PBS) (N=8) or Delta-24-RGDOX (N=10) at the indicated doses. Mice from the different groups were weighed every 3-4 days until the end of the treatment (40 days). In addition, Kaplan–Meier survival plots of Balb/c and NP53$^{fl/fl}$ mice treated with PBS (control group) and 10^6 PFUs or 10^7 PFUs of Delta-24-RGDOX in the pons are shown. **C)** Mice bearing NP53 tumors treated with PBS (control) and 10^6 PFUs or 10^7 PFUs of Delta-24-RGDOX were weighted the first 8 days after viral administration.

2.4. Delta-24-RGDOX prolongs survival in orthotopic DIPG models

Once we confirmed that Delta-24-RGDOX administration into the pons of mice was safe and did not result in toxicity, we evaluated the antitumoral effect in orthotopic models of DIPG.

We generated tumors by the administration of murine DIPG cell lines (NP53 and XFM) using the screw-guided system. Three days later, we injected 10^6 PFU of Delta-24-RGDOX intratumorally, or PBS as a control group (Figure 42A). In the XFM model, we observed a significant increase in the survival of treated mice (P=0.0033), although there were not long-term survivors. The median overall survival was 9 days in the control group

and 12 days for the treated group (Figure 42B). Regarding the NP53 model, Delta-24-RGDOX prolonged the survival of treated mice, but the difference between groups were not significant (*P*=0.2190). However, we obtained 20% (2/10) of long-term survivors in the treated group (Figure 42C), and tumors were smaller than in the control group (Figure 42D). The overall survival of control groups was 25.5 days versus 28.5 days after Delta-24-RGDOX treatment.

On the other hand, we evaluated the effect of Delta-24-RGDOX in already established tumors. For that purpose, we changed the administration schedule and injected the virus 7 days after the cell implantation (Figure 42E). In this case, we observed a significant increase in the survival of treated mice, leading to a 10% (1/10) of long-term survivors (Figure 42E). The better response obtained in the XFM model with the established tumor could be due to the fact that the tumor volume is larger and therefore, the virus has more cells to attack.

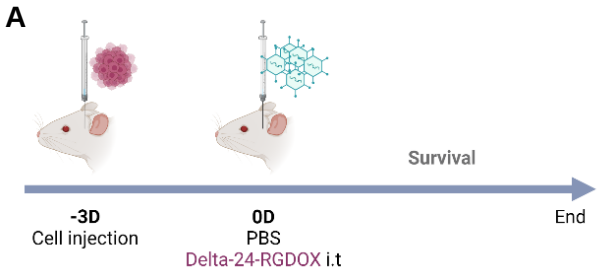

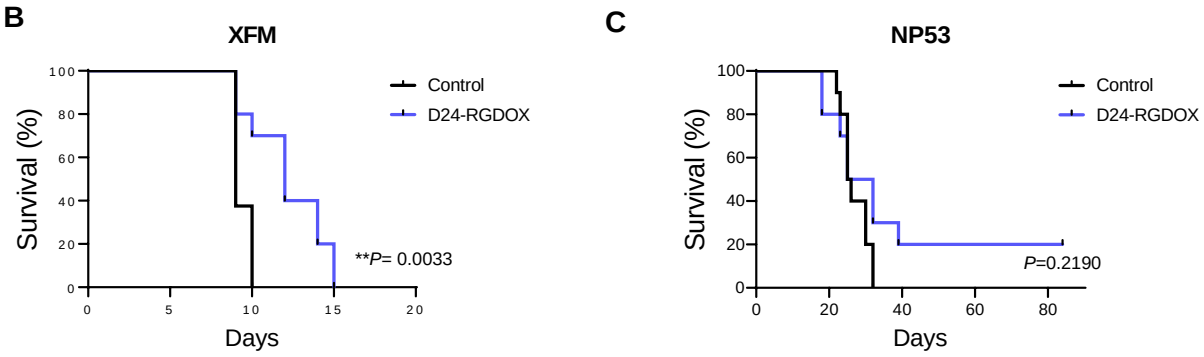

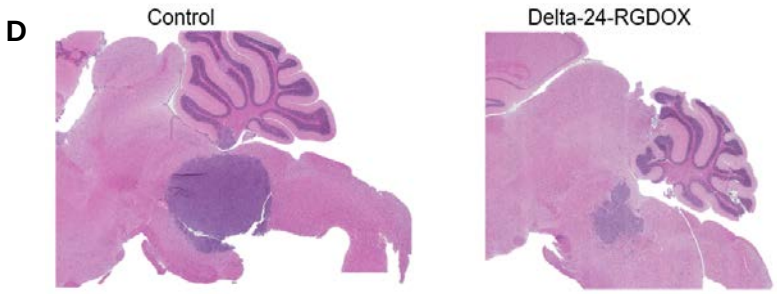

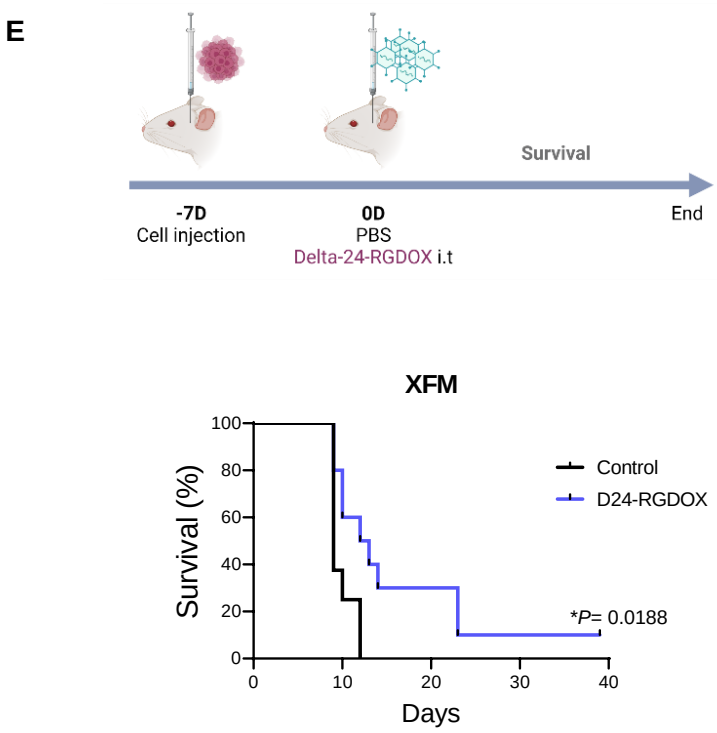

Figure 42. Evaluation of the anti-DIPG effect of Delta-24-RGDOX. A) Schedule of the survival experiment in XFM and NP53 models; Delta-24-RGDOX was administered 3 days after cell injection. **B)** Kaplan–Meier survival plot of mice bearing XFM tumors treated with 10^6 PFUs of Delta-24-RGDOX (N=10) or a mock PBS control (N=10) 3 days after cell administration (log-rank; P=0.0033). **C)** Kaplan–Meier survival plot of mice bearing NP53 tumors treated with 10^6 PFUs of Delta-24-RGDOX (N=10) or a mock PBS control (N=10) 3 days after cell administration (log-rank; P=0.2190). **D)** Representative micrographs of NP53 tumors in control (PBS) and treated (Delta-24-RGDOX) groups. **E)** ***Upper panel,*** schedule of the survival experiment in stablished XFM model; Delta-24-RGDOX was administered 7 days after cell injection. ***Lower panel,*** Kaplan–Meier survival plot of mice bearing XFM stablished tumors treated with 10^6 PFUs of Delta-24-RGDOX (N=10) or a mock PBS control (N=10) 3 days after cell administration (log-rank; P=0.0188).

2.5. Delta-24-RGDOX modulates the lymphoid compartment of DIPG tumors

The survival benefit obtained with Delta-24-RGDOX led us to elucidate the effect of the virus on the tumor microenvironment, especially on the lymphoid compartment. Therefore, we performed a mechanistic study to analyze the tumor microenvironment by flow cytometry. We injected XFM cells into the pons of Balb\c mice and 3 days later we injected Delta-24-RGDOX intratumorally. Then, we obtained tumors 3 and 7 days after the viral administration and analyzed CD8, CD4, Tregs and NK cells (Figure 43A). At day 3, we observed a tendency to increase on T cells, although it was not significant (CD8 *P*=0.4617, CD4 *P*=0.5010, Treg *P*=0.3095), while NK cells and total immune cells ($CD45^+$) were similar in both groups (NK *P*=0.2403, CD45 *P*=0.8793) (Figure 43B). However, at day 7, treated mice showed a significant increase of T cells into the tumor (CD8 *P*=0.0317, CD4 *P*=0.0234, Treg *P*=0.0188), as well as an increase on NK cells (*P*= 0.1775) (Figure 43C). We also analyzed the activation state of T cells through OX40

expression, but there were not differences between groups for this specific marker. The same occurred with PD-1 expression (Figure 43D). However, $CD4^+$ cells, and more markedly Tregs, were more proliferate in Delta-24-RGDOX group, measured by Ki67 expression (Figure 43D).

On a separate experiment, we analyzed the presence of T cells (CD3, CD8, CD4 and Treg) in the tumor by immunohistochemistry, 15 days after Delta-24-RGDOX administration. At this time, there was an increase of $CD3^+$ cells, which was mainly due to the $CD8^+$ compartment, although CD4 was also increased (CD3 *P*=0.0902, CD8 *P*=0.0803, CD4 *P*=0.3686) (Figure 43E).

All these data demonstrate that Delta-24-RGDOX increase the number of lymphoid populations inside the tumor and promotes the proliferation of CD4 subpopulation.

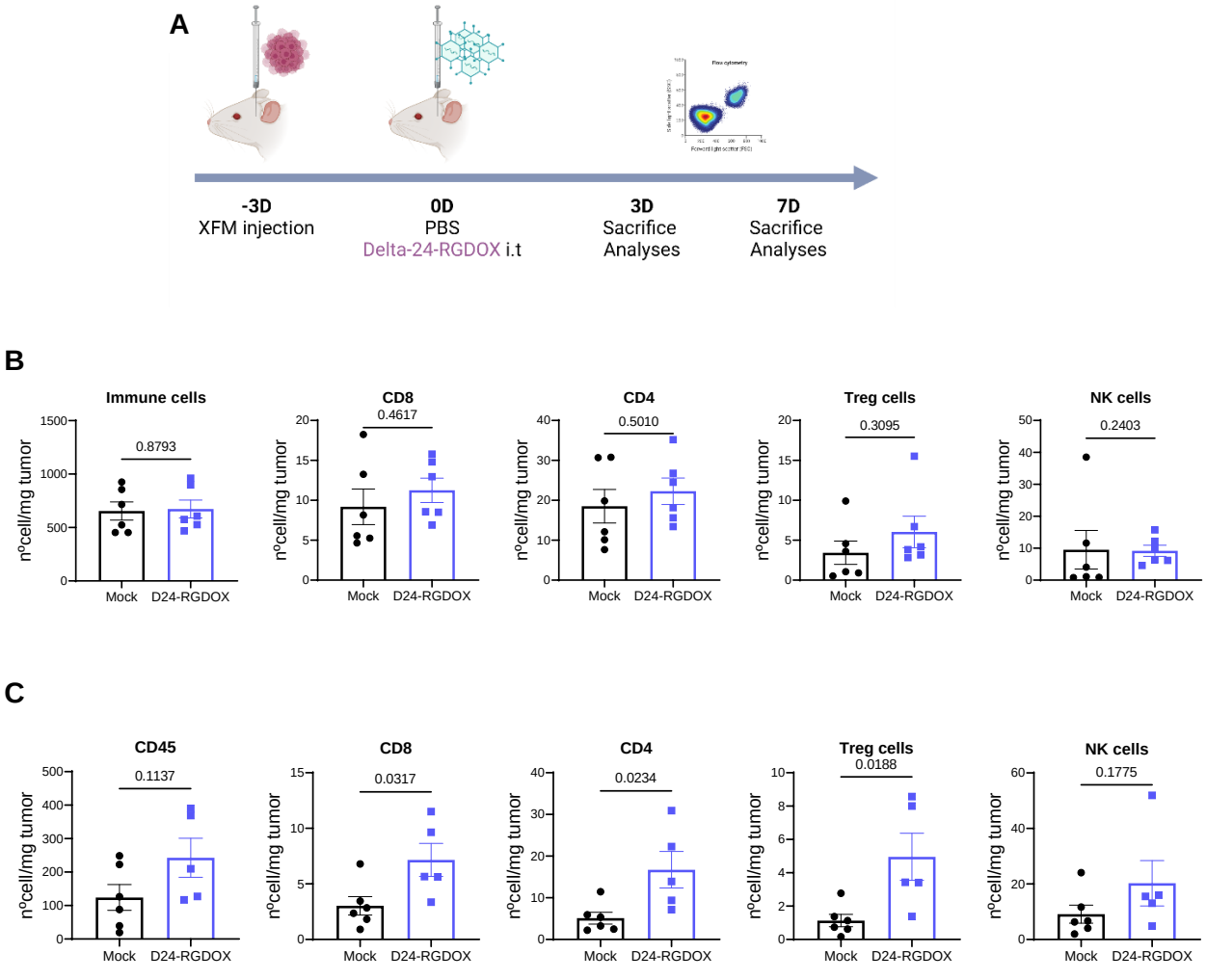

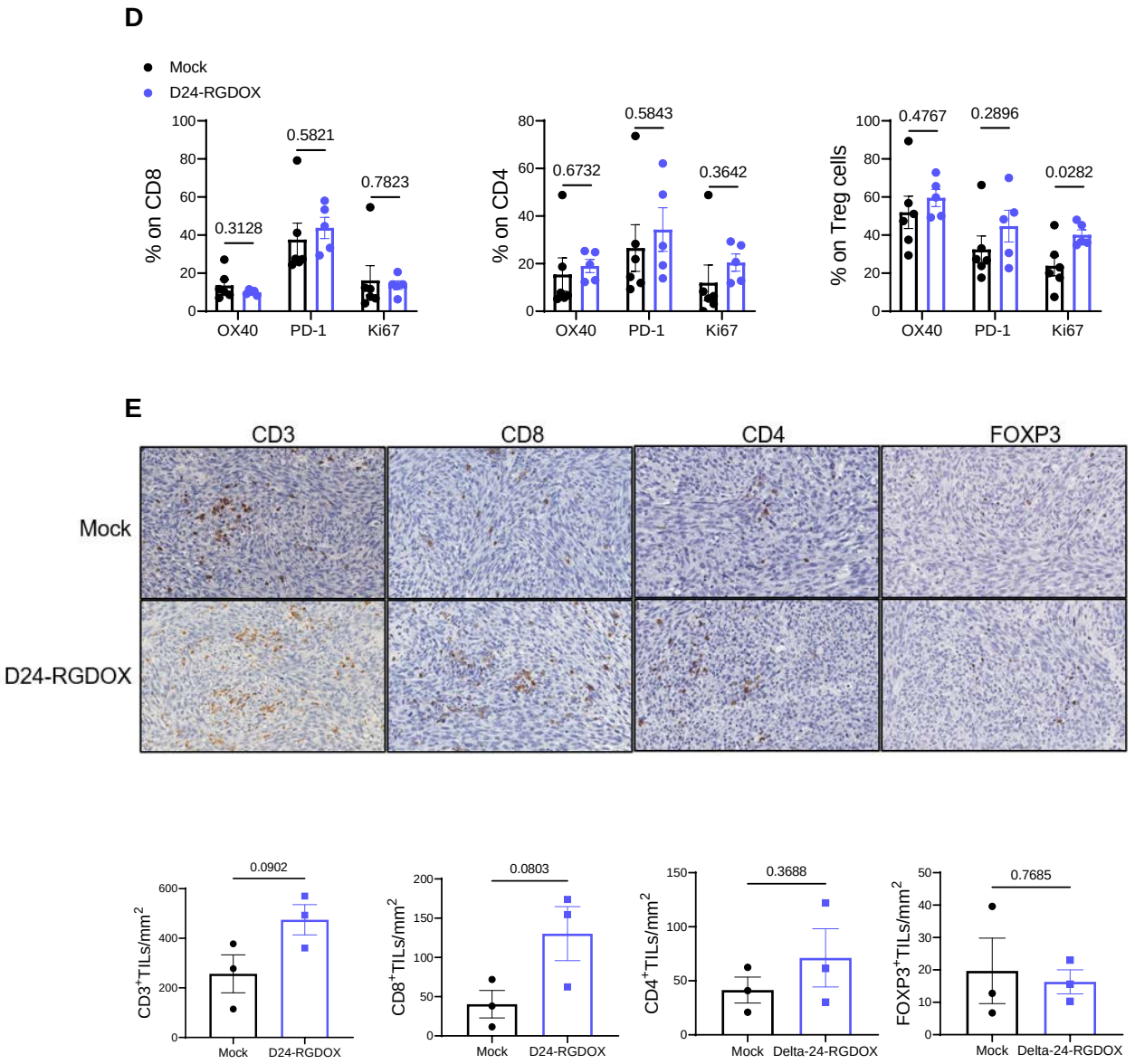

Figure 43. Evaluation of the tumor microenvironment after Delta-24-RGDOX treatment. A) Schedule for the mechanistic studies of the TME by flow cytometry, 3 and 7 days after Delta-24-RGDOX administration. **B)** Graphs showing the number of positive cells per mg of tumor in both control and Delta-24-RGDOX groups 3 days after viral administration (N=6). Bar graphs show mean±SEM. Student´s t test. **C)** Graphs showing the number of positive cells per mg of tumor in both control and Delta-24-RGDOX groups 7 days after viral administration (N=5,6). Bar graphs show mean±SEM. Student´s t test. **D)** Analysis of OX40, PD-1 and Ki67 markers on CD8, CD4 and Treg cells 7 days after the treatment (N=5,6). Bar graphs show mean±SEM. Multiple t test was performed. **E)** ***Upper panel,*** representative micrographs of XFM tumors stained for CD3, CD8, CD4 and FOXP3 markers. ***Lower panel,*** quantification of the positive cells per mm^2 of tumor (N=3). Bar graphs show mean±SEM. Student´s t test.

Afterwards, we also analyzed the effect of Delta-24-RGDOX on systemic immune response. We obtained splenocytes from treated and control groups and cocultured with XFM cell lines, mock- or Delta-24-RGDOX-infected. In addition to assess if the splenocytes from treated mice were more activated, these two conditions would allow us to evaluate whether the immune response is against the tumor or against the virus. In the case of antiviral response, we would only observe cell activation in splenocytes from treated mice cocultured with infected cells. We analyzed splenocyte activation through the detection of IFN-γ-producing cells by ELISPOT. Splenocytes from treated mice were significantly more active than those from control group, as shown by a higher number of cells producing IFN-γ, but there were not differences between mock-infected and virus-infected cells (Figure 44). This could indicate that the immune response generated by the virus is both against the tumor and the virus, and that the immune response generated by Delta-24-RGDOX is obtained both locally and systemically.

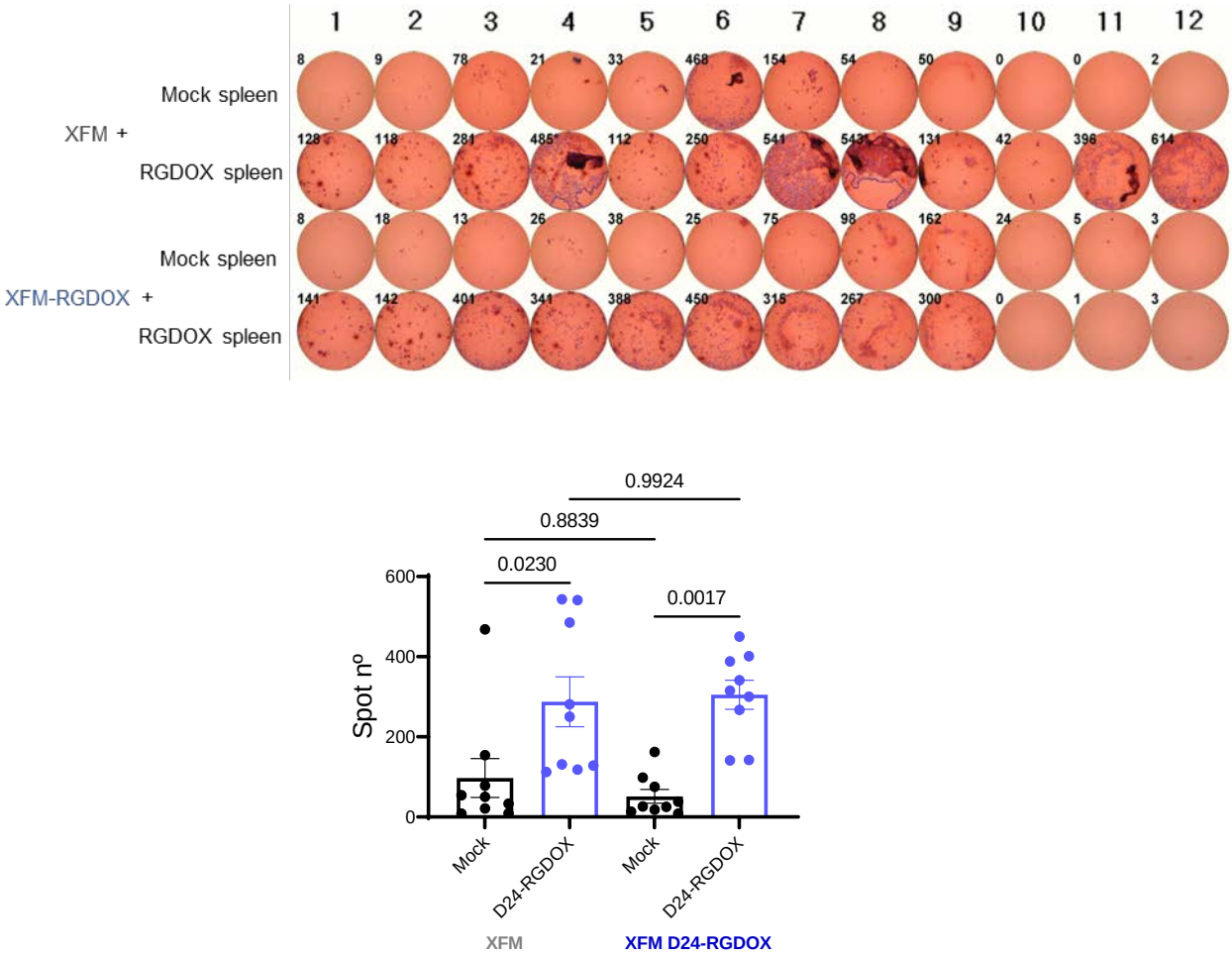

Figure 44. ELISPOT assay to assess the IFN-γ producing cells at 15 days after treatment. ***Upper panel***, picture of the spots obtained on the experiment, in which splenocytes from mock- or Delta-24-RGDOX-treated mice were cocultured with XFM cells, mock- or Delta-24-RGDOX-infected. ***Lower panel,*** quantification of the number of spots, each point corresponding to an IFN-γ producing cell. Bar graphs show mean±SEM, One-way ANOVA (N=9).

3. Evaluation of the role of Treg as a potential mechanism of resistance to 4-1BBL and OX40L-armed viruses

3.1. Delta-24-ACT and Delta-24-RGDOX viruses promote an increase of the Treg population

The results we obtained when analyzing the effect of Delta-24-ACT and Delta-24-RGDOX viruses in the tumor microenvironment, showed that both viruses produced a significant increase in Treg cells in the tumor. In the case of Delta-24-ACT, this was observed by flow cytometry (*P*=0.0015) as well as by immunohistochemistry (*P*=0.048) and multiplex immunofluorescence (*P*=0.0419) (Figure 45A). On the other hand, Delta-24-RGDOX-treated mice showed a significant increase in the number of Tregs at day 7, by flow cytometry (*P*=0.0188). Moreover, the CD8/Treg ratio at day 7 was significantly lower in treated mice compared to control mice (*P*=0.0313), which indicated that the inhibitory arm of the immune system overweighs the effector arm. Regarding the functional phenotype of these cells, Tregs showed a higher proliferative activity, measured by the expression of Ki67 (Figure 45B).

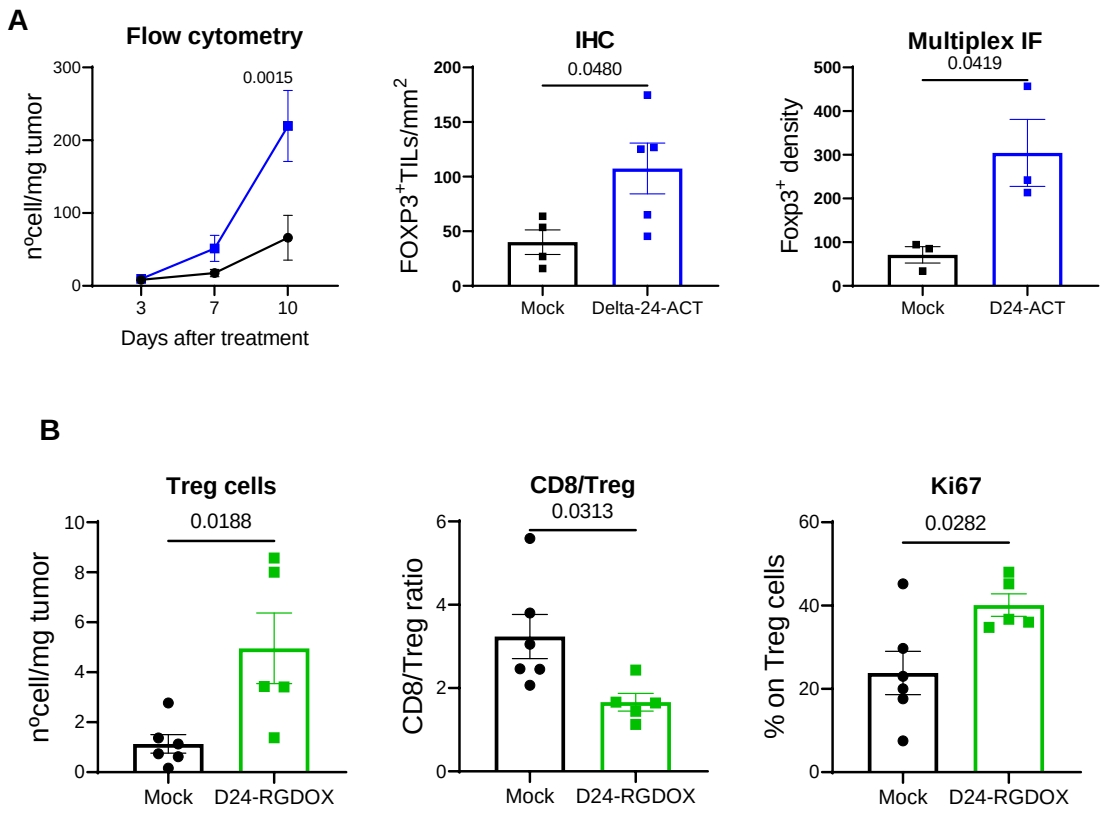

Figure 45. A) Quantification of Treg after Delta-24-ACT treatment by flow cytometry, IHC or multiplexed immunofluorescence. **B)** Analysis of Treg presence 7 days after Delta-24-RGDOX treatment by flow cytometry. Graphs showing number of cells per mg of tumor, CD8/Treg ratio and Treg proliferation by Ki67 staining (N=5,6). Student´s t test.

As discussed in the introduction, the receptors for 4-1BBL and OX40L are 4-1BB (CD137) and OX40 (CD134), which are expressed on lymphocytes and NK cells. Data obtained from the characterization of the TME after Delta-24-ACT and Delta-24-RGDOX, showed that these receptors were significantly more expressed on Treg cells than on effector cells, indicating that Tregs could be activated by the ligand of the virus (Figure 46).

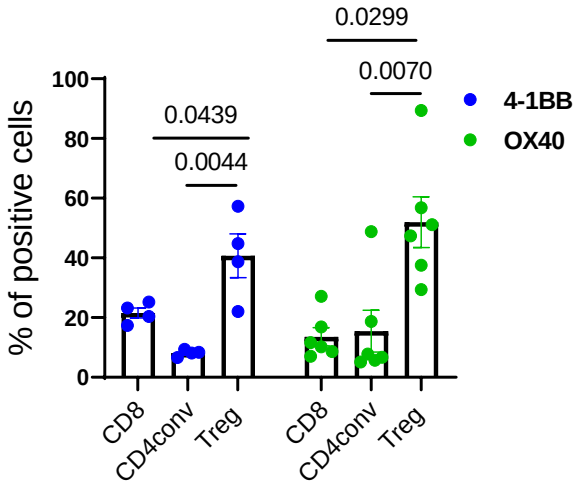

Figure 46. Expression of 4-1BB and OX40 receptors on tumoral CD8, CD4 and Treg cells by flow cytometry, 7 days after treatment (N=4,6). Multiple t test was performed. Bar graphs show mean±SEM.

These data are in concordance with results obtained by Dr. Fueyo's group using the Delta-24-RGDOX virus in GBM. In this work, RNA sequencing analysis demonstrated that Delta-24-RGDOX promoted an upregulation of IDO network, which is implied on the activation of Treg cells, as well as a significant increase of Treg cells after Delta-24-RGDOX administration.[112]

The results obtained on the effect of Treg during the characterizations of Delta-24-ACT and Delta-24-RGDOX and the fact that the survival obtained with Delta-24-RGDOX was not as satisfactory as expected, we set out to study the role of 4-1BBL and OX40L present in the viruses on the Treg population, as a resistance mechanism.

3.2. Intratumoral Tregs show a more suppressive phenotype after Delta-24-ACT and Delta-24-RGDOX treatment

To assess the specific effect of the ligands on Tregs, we started with the phenotypic characterization of intratumoral Tregs after Delta-24-ACT and Delta-24-RGDOX administration, and compared it with those from Delta-24-RGD treatment.

On a first experiment, we generated XFM tumors by the administration of cells using the screw-guided system. Three days after, we treated the tumors with Delta-24-RGD, Delta-24-ACT, Delta-24-RGDOX or PBS as control group, and obtained the tumors 7 days later (Figure 47A). We analyzed the Treg phenotype by flow cytometry, assessing the expression of 4-1BB, OX40, GITR and CD69. High expression of these markers has been associated with a more suppressive phenotype.[113] We observed a higher expression of 4-1BB, OX40, GITR and CD69 in Delta-24-ACT and Delta-24-RGDOX-treated tumors than in mock or Delta-24-RGD groups, being significant for all the cases in Delta-24-RGDOX (Figure 47B). In addition, we also obtained spleens and lymph nodes from the same mice to assess the phenotype of the systemic Tregs. In this case, we did not observe differences between groups, except for the case of GITR on spleen Tregs, which was lower in Delta-24-ACT and Delta-24-RGDOX-treated groups (Figure 47C).

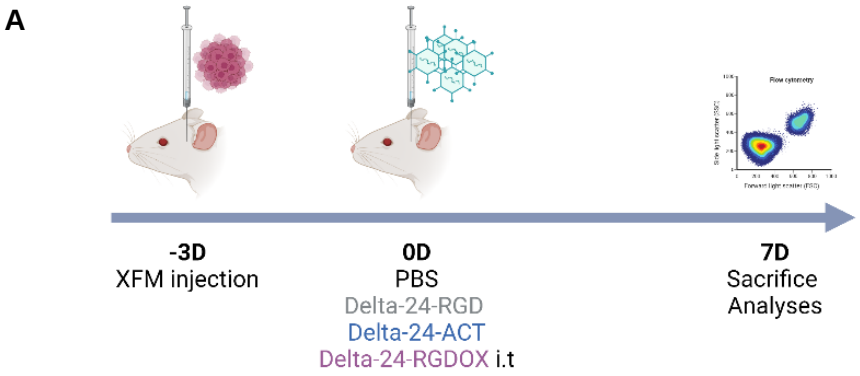

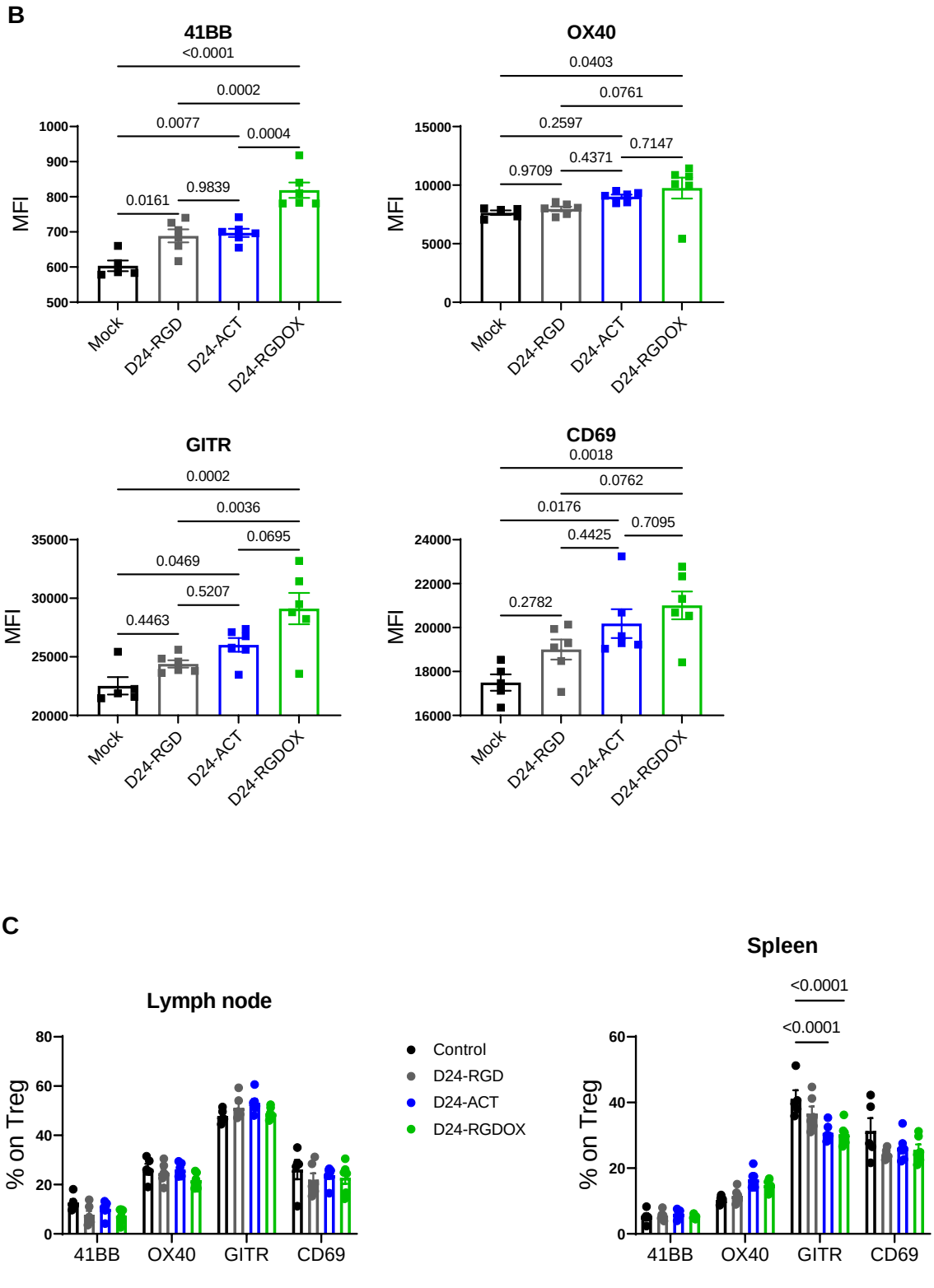

Figure 47. Treg phenotype 7 days after treatment with the different oncolytic adenoviruses. A) Schedule of the experiment for Treg phenotype on XFM model. Viruses were intratumorally injected 3 days after cell implantation, and tumors obtained 7 days after treatment. **B)** Expression of 4-1BB, OX40, GITR and CD69 markers on intratumoral Treg by flow cytometry. Data are shown as mean fluorescence intensity (MFI), and graphs show mean±SEM (N=6). One-way ANOVA. **C)** Expression of 4-1BB, OX40, GITR and CD69 markers on Treg of lymph node and spleen. Data are shown as the percentage of positive cells expressing the receptors. Graphs show mean±SEM (N=6). One-way ANOVA.

We performed a second experiment on the NP53 model to assess the expression of CD73 and IL-10, also well described in mediating Tregs suppressive functions.[114] We injected Delta-24-RGD, Delta-24-ACT, Delta-24-RGDOX or PBS (control group) 3 days after viral administration and obtained tumors 7 days after treatment (Figure 48A). We observed an increase of CD73 expression on Delta-24-ACT- treated group compared to the rest of groups, as well as an increase of IL-10 expression (Figure 48B). In the case of Delta-24-RGDOX, CD73 expression was at control levels, while IL-10 was also expressed as in the control, but more so than in the Delta-24-RGD group (Figure 48B).

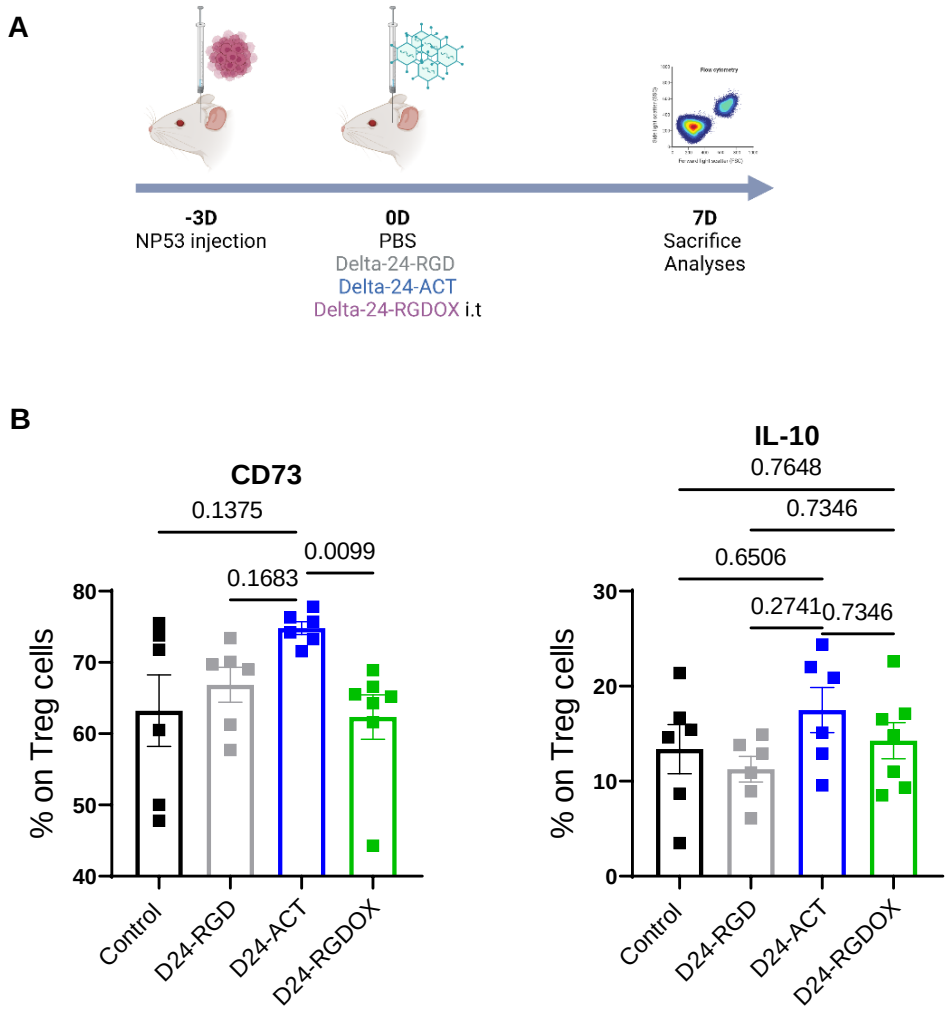

Figure 48. A) Schedule of the experiment for Treg phenotype on NP53 model. Viruses were intratumorally injected 3 days after cell implantation, and tumors obtained 7 days after treatment. **B)** Expression of CD73 and IL-10 markers on intratumoral Treg by flow cytometry. Data are shown as percentage of positive cells expressing the markers, and graphs show mean±SEM (N=6). One-way ANOVA.

All these data indicate that both Delta-24-ACT and Delta-24-RGDOX promote a suppressive phenotype in the intratumoral Treg cells by upregulating the expression of activator markers involved in their suppressive effect.

In order to validate these data, we assessed the suppressive effect of Tregs in the presence of 4-1BBL and OX40L on an *in vitro* suppression assay. Tumor cells were infected with Delta-24-RGD, Delta-24-ACT or Delta-24-RGDOX for 48h and then cocultured with Treg cells, previously isolated from naïve mice (Figure 49A). $CD8^+$ cells were stained with a proliferation dye that allowed us to assess the proliferation capacity of CD8 in the presence of Treg cells, and then seeded with Tregs (Figure 49A). We analyzed the proliferation capacity of CD8 by flow cytometry 72h later and observed that, CD8 cells in presence of Tregs cocultured with Delta-24-ACT and Delta-24-RGDOX, proliferated less than CD8 from Delta-24-RGD group (Figure 49B).

A

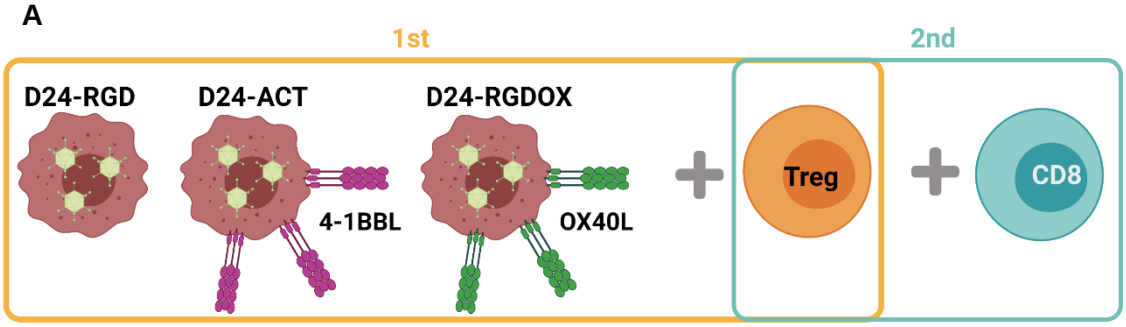

B

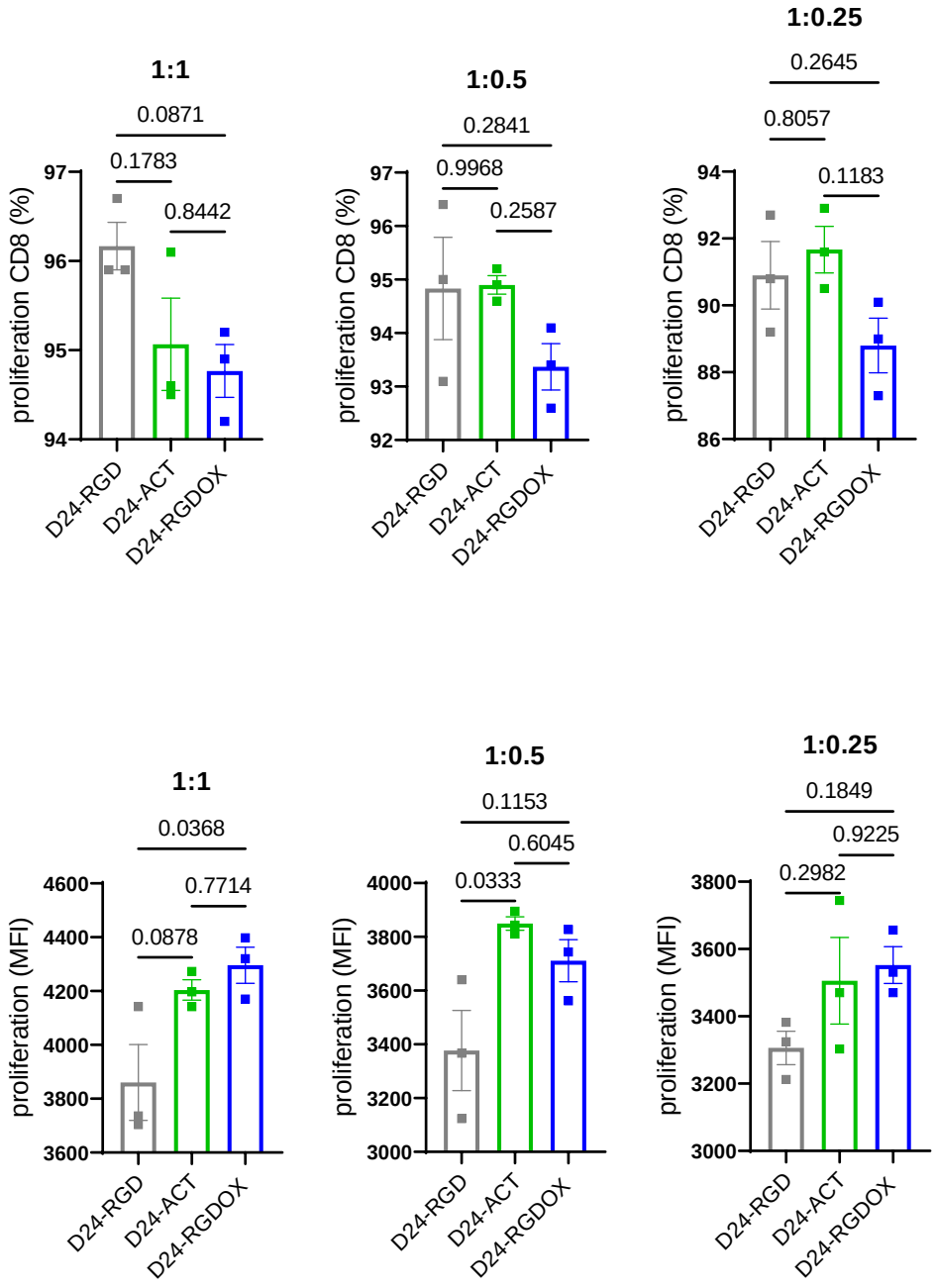
1:1
0.0871
0.1783
0.8442
proliferation CD8 (%)
97
96
95
94
D24-RGD
D24-ACT
D24-RGDOX
1:0.5
0.2841
0.9968
0.2587
proliferation CD8 (%)
97
96
95
94
93
92
D24-RGD
D24-ACT
D24-RGDOX
1:0.25
0.2645
0.8057
0.1183
proliferation CD8 (%)
94
92
90
88
86
D24-RGD
D24-ACT
D24-RGDOX
1:1
0.0368
0.7714
0.0878
proliferation (MFI)
4600
4400
4200
4000
3800
3600
D24-RGD
D24-ACT
D24-RGDOX
1:0.5
0.1153
0.6045
0.0333
proliferation (MFI)
4000
3800
3600
3400
3200
3000
D24-RGD
D24-ACT
D24-RGDOX
1:0.25
0.1849
0.9225
0.2982
proliferation (MFI)
3800
3600
3400
3200
3000
D24-RGD
D24-ACT
D24-RGDOX

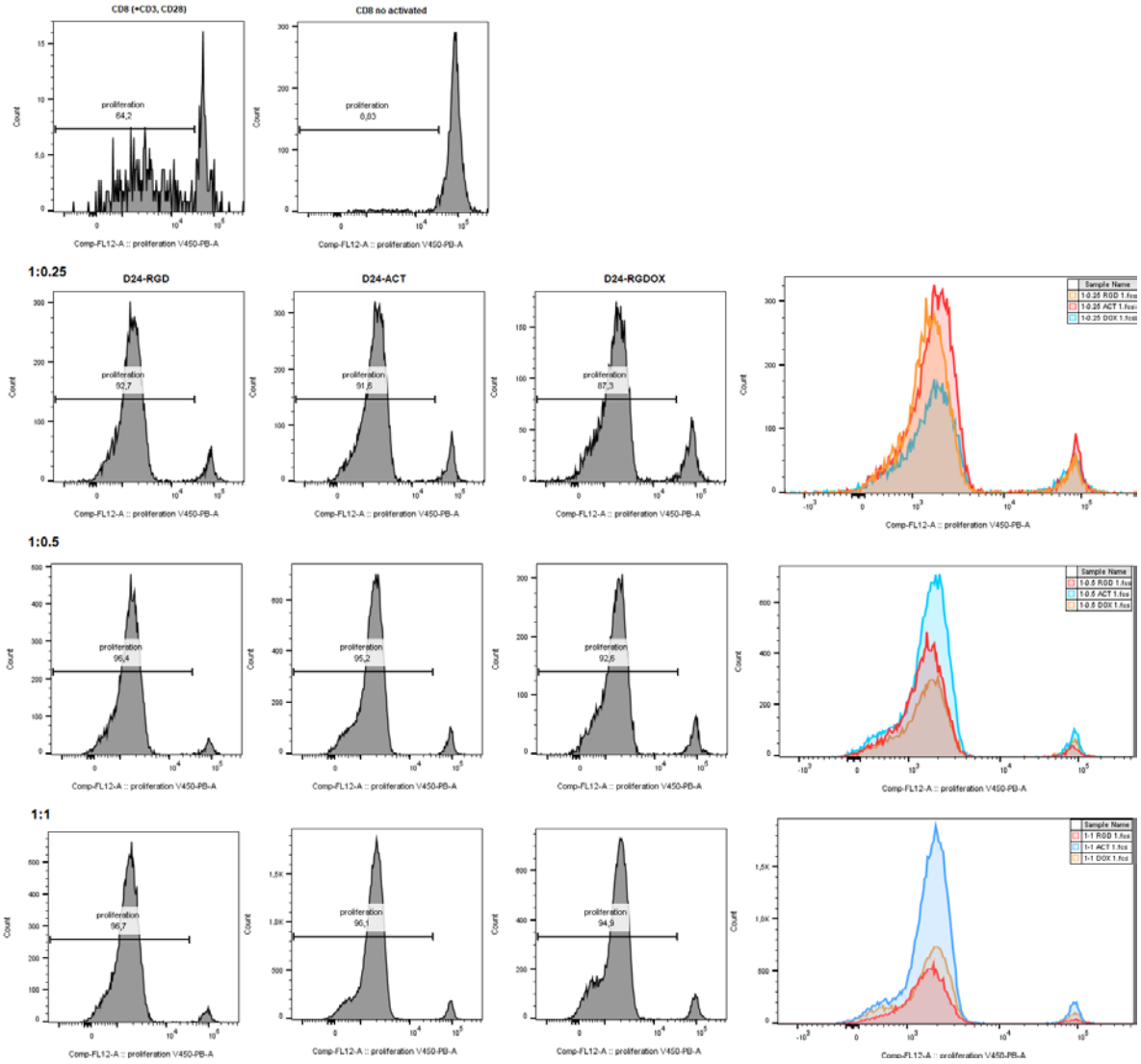

Figure 49. Assessment of Treg suppressive function in contact with 4-1BBL and OX40L. A) Schedule of suppression assay. Tregs were cocultured with Delta-24-RGD, Delta-24-ACT or Delta-24-RGDOX-infeceted NP53 cells and after with CD8 cells previously stained with a proliferation dye**. B)** ***Upper panel***, suppressive capacity of Treg was measured in vitro, by measuring their ability to decrease CD8 proliferation after being in contact with the ligands. Graphs show mean±SEM (N=3). Data are shown as the percentage of proliferative CD8 cells or MFI of the proliferation dye. One-way ANOVA. ***Lower panel,*** representative graphs proliferative CD8 on the different groups.

3.3. Delta-24-ACT and Delta-24-RGDOX promote Treg proliferation and CD4 conversion to Treg

We then wanted to evaluate the origin of the increase of Treg in the tumor, so we performed several *in vitro* experiments to assess whether it was due to an increase in Treg proliferation or a greater conversion from conventional CD4 to Treg.

To assess Treg proliferation in the presence of 4-1BBL and OX40L, we infected NP53 and XFM tumor cells with Delta-24-RGD, Delta-24-ACT, Delta-24-RGDOX or mock-infected for 48h and cocultured with Treg cells. We analyzed the Treg proliferation by

the measurement of Ki67 by flow cytometry. We observed a significant increase in proliferation of Treg cells in presence of both 4-1BBL and OX40L compared to the other groups (Figure 50A). Analyses of the Treg proliferation *in vivo* in NP53 and XFM tumors, showed an increase of Ki67^{+} intratumoral Tregs upon Delta-24-ACT and Delta-24-RGDOX treatments (Figure 50B).

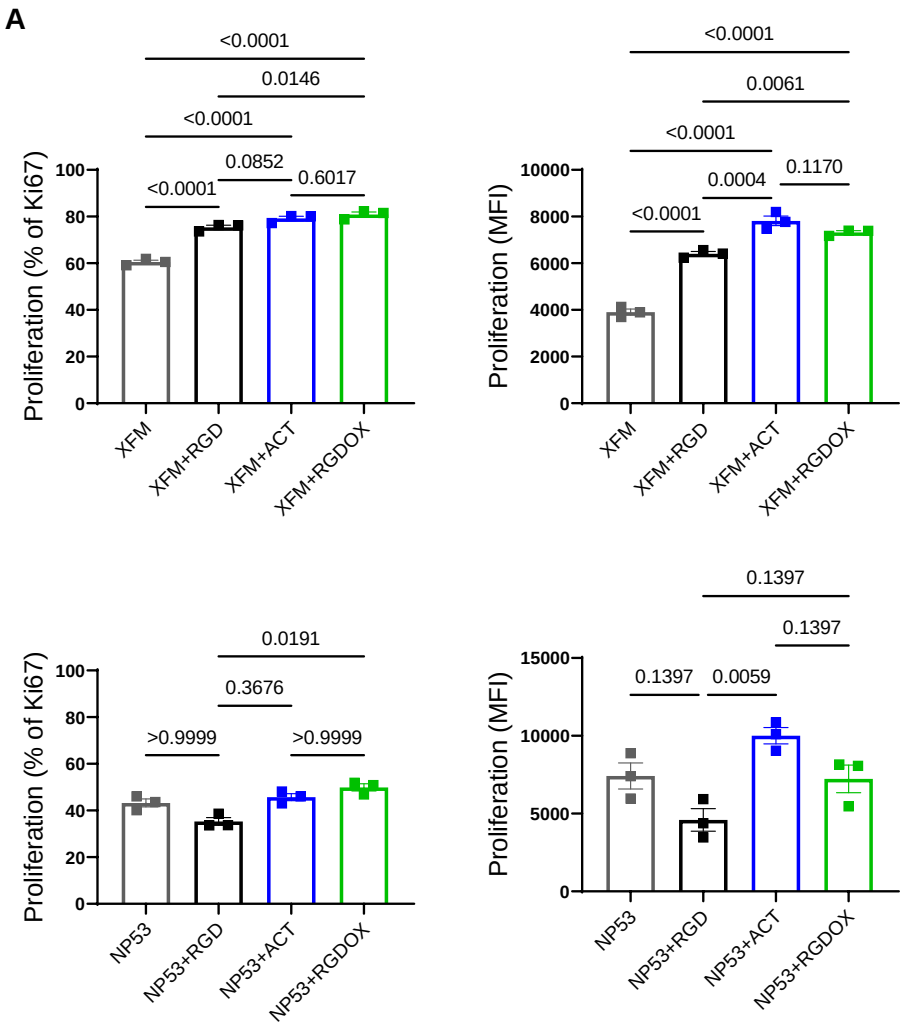

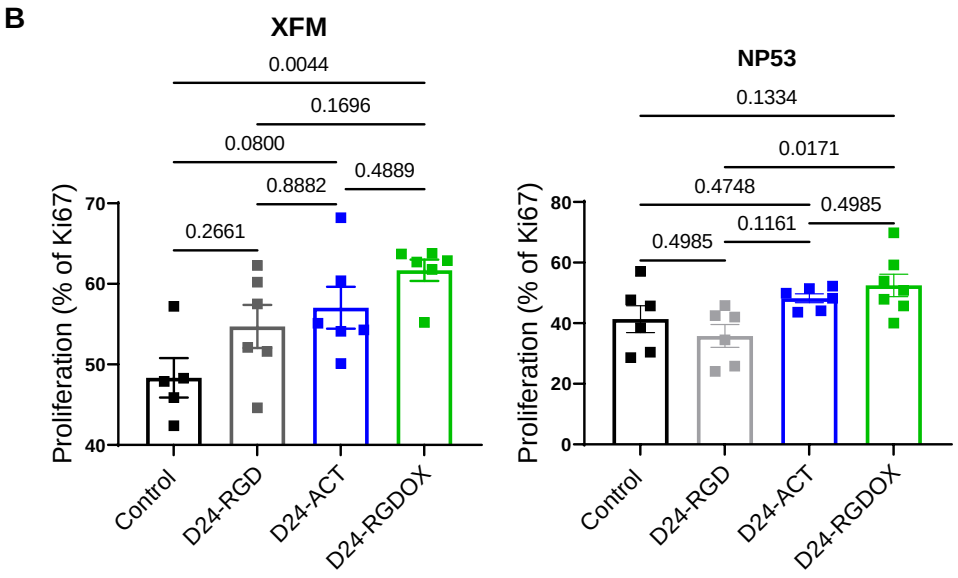

Figure 50. Analysis of Treg proliferation in presence of the oncolytic adenoviruses. A) *In vitro* measurement of Treg proliferation in contact with tumor cell lines mock-, Delta-24-RGD, Delta-24-ACT, or Delta-24-RGDOX-infected. Results are shown as percentage or MFI of Ki67 staining. Bar graphs show mean±SEM. One-way ANOVA. **B)** Proliferation of intratumoral Treg *in vivo*. Bar graphs show mean±SEM. One-way ANOVA.

On the other hand, we also evaluated the effect of 4-1BBL and OX40L present on Delta-24-ACT and Delta-24-RGDOX, respectively on the conversion of CD4 conventional cells to Treg cells. We cocultured infected cell lines with CD4 conventional cells, in presence of IL-2 and TGF-β, which are essential cytokines for this process (Figure 51A). We observed a significant increase of $CD25^{+}Foxp3^{+}$ CD4 cells on Delta-24-ACT and Delta-24-RGDOX conditions (Figure 51B).

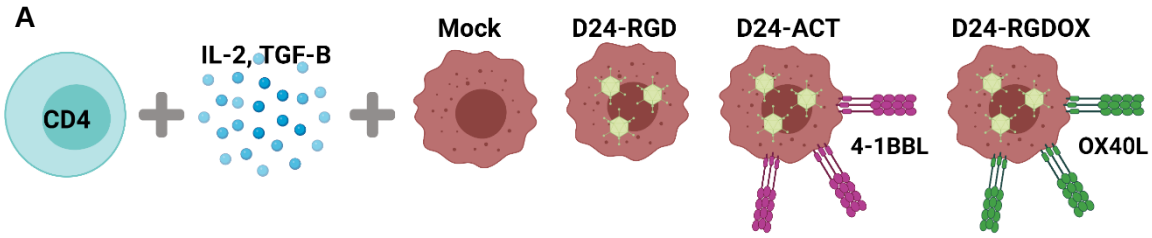

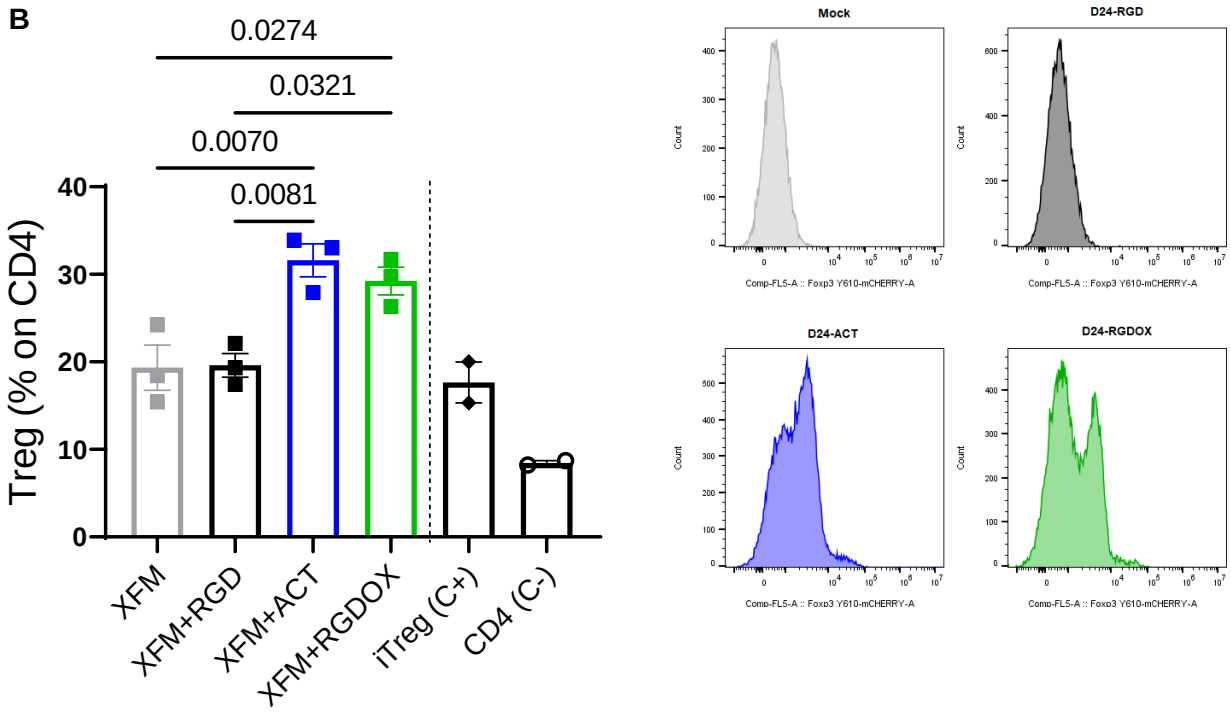

Figure 51. CD4 conversion assay. A) CD4 lymphocytes were cocultured with mock-, Delta-24-RGD, Delta-24-ACT or Delta-24-RGDOX-infected cells, in presence of IL-2 and TGF-β. **B)** Left panel, Percentage of Treg cells on CD4 subpopulation. Bar graphs show mean±SEM (N=6), one-way ANOVA. Right panel, representative histograms of Foxp3+ cells on the different groups.

The results demonstrate that 4-1BBL and OX40L present in the viruses promote the proliferation of Treg cells and the conversion from conventional CD4 to suppressor Treg. Both scenarios may be the response to increased Treg in the tumor, as they are not mutually exclusive.

Since it seems that 4-1BBL (Delta-24-ACT) and OX40L (Delta-24-RGDOX) favor Treg function, if we eliminate this population, we could improve the effector arm of the immune system. Therefore, our next goal would be to find a new strategy to deplete or modulate Treg cells.

Discussion

Pediatric brain tumors are considered rare diseases due to their low incidence. For this reason, until the last few years, there was a paucity of research solely focused on pediatric brain tumors. Although the knowledge of pediatric brain tumors has increased, the outcome for these patients is still dismal. This is the case for DIPGs, which have a five-year survival rate of less than 1%.[11] Clearly, there is an urgent need of finding efficacious therapeutic strategies for DIPG, to increase patient survival without causing severe toxicities.

The current standard of care for DIPG is radiotherapy, which slightly improves the survival and quality of life of patients, but it is not sufficient.[10] In recent years, novel strategies have been tried alone or in combination with the current standard of care (radiotherapy) to improve the outcome of DIPG patients. Different immunotherapy approaches have been tested, but few patients have benefited from these treatments. For example, antibodies against PD-1 and CTLA-4, approved by the FDA, and widely used in other cancers, [36,146,147] have failed to show efficacy in DIPG patients.[37] The lack of success of immune checkpoint inhibitors in DIPG may be due to the fact that immune infiltrate, specifically lymphocytes, is minimal and barely expresses checkpoint molecules.[31] On the other hand, it is critical to understand the composition of the tumor microenvironment, in order to correctly target the immunotherapy approach. In the context of DIPG, due to their anatomical location it has not until recent years that tumor biopsies have become the standard, allowing us to unravel the tumor microenvironment of this disease. Without tumor biopsies, the composition of the tumor microenvironment and the mutations present in DIPG would not have been known.[10,13,43] What we have learned from patient samples is that the immune infiltrate in DIPG is minimal,[31,32] so approaches aimed at increasing this infiltrate could be an interesting strategy. That would be the case of oncolytic viruses, so in our project we wanted to benefit from this feature and exploit the capacity of oncolytic viruses to trigger an immune response leading to an inflamed microenvironment. [44,148]

In fact, clinical and preclinical studies in brain tumors show that oncolytic viruses initiate targeted lysis of tumors and trigger a pro-inflammatory cascade that alters the balance of inhibitory and activating immune cells, thus rendering immunologically “cold” (poorly immune cell infiltrated) tumors “hot”.[44,148] Although oncolytic viruses have been extensively studied in the context of adult brain tumors, there is a paucity of studies that have addressed their suitability and efficacy for pediatric brain tumors and specifically for DIPGs. For example, besides Delta-24-RGD, another oncolytic adenovirus named CRAd.S.pK7, has been tested on preclinical models of DIPG. It was intranasally delivered on mesenchymal stem cells (MSCs), in order to avoid toxicities and ensure

that it reaches the tumor showing significant improved survival in combination with radiotherapy.[149] In addition to adenovirus, herpes simplex virus HSV1716 has been also tested in the preclinical setting of DIPG. The study showed that the virus could replicate in DIPG cells and decrease the typical infiltrative growing pattern of this tumor.[150]

Due to the importance of the immune system in the antitumor effect of oncolytic viruses, preclinical models that allow the accurate evaluation of the mechanism of action as a whole of these agents are of the utmost importance. Although in the last years several murine pediatric brain tumor models have been developed, there is still scarce pediatric brain tumor models for many tumor entities. In order to assess the effect of the immune system, the use of humanized mice will be a feasible option as it permits working with human cell lines in presence of the immune system.[95] However, these models are time-consuming, expensive and they have limitations when it comes to studying the mechanism of action underlying the effectiveness of immune therapeutic approaches. The use of orthotopic pediatric brain tumors is highly desirable since subcutaneous tumors do not properly recapitulate the tumor microenvironment. In the case of DIPG tumor generation, direct tumor implantation in the brain stem[138] or generation of tumors early during fetal development using transgenic mice or in utero electroporation[151] are being explored. However, in our strategy, that we administered the adenoviruses directly into the tumor, tumor formation by in utero electroporation would not be a valid strategy, since we would not know the precise location of the tumor. Therefore, the use of the screw-guided system is the perfect approach to generate the tumor,[139] as it allows us to implant the tumor in a precise location and the subsequent intratumoral treatment, which makes our strategies more easily translatable to the clinic. We are aware that with the screw-guided system, we are generating a local inflammation that would be amplifying the immune infiltrate produced by the viral action. However, we have the control groups in which we also place the screw, and inject PBS instead of the virus. Thus, they suffer the same surgery process and injections, with the inflammation that this procedure entails.

In parallel with the above-mentioned issue, the administration route of the virus is also a relevant matter for DIPG patients. It is known that the presence of neutralizing antibodies on patients' serum interferes with the capacity of the adenovirus to reach the tumor and thus with their effectivity.[152] The intratumoral administration of the virus, whenever it is possible, will avoid systemic toxicities and a higher viral amount in the tumor. However, the complicated location of DIPG tumors difficult the intratumoral administration, and therefore more sophisticated ways of delivery are being developed, for instance using stem cells as cellular carriers, such as neural stem cells[153] and bone marrow derived

mesenchymal stem cells[149,154] or nanoparticles.[155] Moreover, viruses are highly immunogenic and are rapidly erased by the humoral and complement systems. Shin DH *et al*. review the different strategies to develop selective tolerance against oncolytic viruses,[155] to delay viral clearance and increase the antitumor immune response. Thus, elucidating whether the generated immune response after oncolytic virus administration is against the virus or against the tumor and how to tip the scale to promote efficient epitope spreading is another area where we should focus our efforts.

In this work, we built upon our previous preclinical and clinical experience with Delta-24-RGD (DNX-2401) to engineer a virus with superior efficacy. Our clinical studies on adult gliomas and DIPGs uncovered the feasibility of oncolytic viruses and their efficacy in a subgroup of patients.[43,92] Because we previously observed that treatment of DIPG immunocompetent models with the oncolytic virus Delta-24-RGD resulted in increased tumor-infiltrating lymphocytes,[156] strategies aimed at activating these lymphocytes seemed to be the next logical step. Several positive actionable immune checkpoints exist, including 4-1BB, OX40, CD27, and GITR,[157] that could be introduced into the viral backbone to reach that objective. However, the broad spectrum of 4-1BB targets, including not only CD8 T lymphocytes but also other important populations, such as NK cells[158,159] prompted us to take advantage of its immune checkpoint ligands. More importantly, a 4-1BB agonist has been shown to exert antitumor effects in not only immunogenic tumor models but also nonimmunogenic models, which is very relevant for DIPGs since they are nearly devoid of infiltrating lymphocytes and present very few mutations.[31,32,160] One important feature exhibited by 4-1BB agonists in preclinical studies is their capacity to disrupt immunological ignorance[161] which seems very important for tumors such as DIPGs since their microenvironment is thought to be non-responsive. In our model, Delta-24-ACT administration led to the profound remodeling of the tumor microenvironment, leading to profuse tumor infiltration, which was most likely due to the virus itself, and to the presentation of functional T cells due to the 4-1BB ligand. In fact, preclinical studies on different tumor models showed that 4-1BB agonist treatment resulted in the restoration of T cell dysfunctionality in the tumor microenvironment[162] and increased persistence of tumor-specific T cells.[163] For example, 4-1BB costimulation further enhanced the anti-PD-1-mediated reinvigoration of exhausted $CD39^+$ $CD8^+$ T cells from the primary and metastatic sites of epithelial ovarian cancers.[164]

In our study, 4-1BB was efficient at triggering an effective antitumor immune response but, more importantly, at establishing immunological memory. Interestingly, these results were different from our study in glioma models, in which this virus was not able to trigger immune memory when subjected long-term survivors to rechallenge.[96] These results

suggest a different mechanism of action in DIPG models, which we know present a different microenvironment with less immunosuppression than adult gliomas.[31,32,160] Unfortunately, although 4-1BB agonists were very effective in preclinical models, clinical trials assessing the efficacy were hampered by high toxicity, specifically in the liver.[101] However, vectorizing 4-1BBL into a virus could circumvent all the toxicities associated with the systemic administration of 4-1BB agonists while maintaining a safe profile. Supporting this notion, we found no hepatic toxicity. Moreover, an Ankara virus armed with the 4-1BB ligand as well as tumor-associated antigens that was administered intratumorally was shown to be effective and safe for eradicating solid tumors.[165]

Interestingly, other adenovirus armed with OX40 ligand (Delta-24-RGDOX) showed promising results in preclinical models of adult glioblastoma[108,111,112]. More importantly, there is currently an open clinical trial at our institution with this virus (DNX-2440 in the clinic) in adult patients with glioblastoma (DNX-2440; NTC03714334). To date, 16 patients have enrolled, and it has proven to be safe, which prompted us to evaluate this virus for DIPG.

As well as 4-1BB, OX40 is a costimulatory receptor that could also promote lymphocyte activation. However, the effect of OX40 is mostly exerted on the CD4 compartment, both on the effector and memory cells.[109] Weinberg and colleagues demonstrated that an anti-OX40 antibody showed antitumor effect on mouse models of breast, colorectal, sarcoma, and melanoma cancers.[166] However, the effect of OX40 antibodies in monotherapy has been modest and thus, combination therapies are recomended.[109] In this line, some works have assessed the synergistic effect of an OX40 agonist with the blockage of inhibitory receptors such as CTLA-4 or PD-1. Redmon W. *et al.,* analyzed the effect of combining OX40 and CTLA-4 on pancreatic cancer and sarcoma, demonstrating that while the effect of the monotherapies was modest, the combination approach significantly increased tumor regression and survival in a T cell-dependent manner.[167] Similarly, the combination of OX40 and anti-PD1 in pancreatic adenocarcinoma increased the antitumor effect and promoted immunological memory. PD-1 blockade improved the OX40 agonistic effect by increasing T memory cells and downregulating both Tregs and exhausted T cells.[168] In addition, radiotherapy was added to OX40 and PD1 combination in a separate study on triple-negative breast cancer. Radiotherapy increased tumor immune infiltration and both OX40 and PD-1 effects augmented CD8 proliferation and functions, resulting in increased survival and decreased metastasis.[169] As with radiotherapy, the use of an oncolytic adenovirus will also generate an increased immune infiltrate in the tumor. As already mentioned, this was demonstrated with the Delta-24-RGD adenovirus.[43,156]

One limitation of our study is that murine models are not permissive to adenoviral replication;[156] consequently, the antitumor effect we observed is hampered by the fact that the virus expresses 4-1BBL and OX40L only once due to its inability to replicate in murine cells. Therefore, the effect we observed is somewhat suppressed at the therapeutic and safety levels. Nevertheless, our clinical study of DNX-2440 for recurrent gliomas has shown feasibility and safety, thus far supporting further translation to the clinic.

In our work, we have made an exhaustive analysis of the tumor microenvironment after the viral administration, especially Delta-24-ACT, demonstrating that it is able to significantly increase all the tested immune populations. The results obtained in the clinical trial with the Delta-24-RGD virus support our results as well.[43] This infiltration includes macrophages and Treg cells, which could be masking the complete viral effect. However, we have not analyzed in depth the role of macrophages in our DIPG models after Delta-24-ACT treatment. It is known that macrophages are the first line of defense against pathogens, and are activated by DAMPS, displaying a potent anti-viral activity through the production of IFN types I and III, which terminates on a rapid viral clearance.[170] In fact, macrophages and microglia can directly phagocyte the virus or infected cells, diminishing the antitumor effect of the virus, as observed in GBM tumors where vaccinia virus was phagocyted by microglia.[171] Therefore, different groups have depleted macrophages and microglia in brain tumors, to avoid viral clearance and to increase viral replication and delivery.[172,173]

Macrophages and microglia suppose the most frequent no-tumor population in brain tumor microenvironment.[31] When the virus is administered in the tumor, because it is a pathogen, it causes significant recruitment of macrophages, whose role is difficult to determine. It has been described that in GBM, oncolytic viruses polarize tumor-associated macrophages and microglia to an inflammatory phenotype ($CD68^+$, $iNOS^+$), which will attack the tumor.[174] This has been observed for HSV[175], adenovirus[176], parvovirus[177], or vaccinia virus[178]. However, these inflammatory macrophages are equally or more effective in viral clearance.[179] Therefore, further analysis of macrophages and microglia after administration of Delta-24-ACT and Delta-24-RGDOX viruses would be necessary in our models. In this way, we could determine the role of this population in the antitumor effect, as well as in the elimination of the virus. Thus, we could find new strategies to target macrophages and microglia to enhance the effect of the virus, since they are an important part of the tumor microenvironment of DIPG.

In our work we have focused on Treg cells as a possible mechanism of resistance to Delta-24-ACT and Delta-24-RGDOX viruses. In both cases, we observed a significant increase in this population and, the high expression of 4-1BB and OX40 receptors in Treg made them important candidates to be the targets of the viral ligands. There are several studies that have analyzed the role of 4-1BB and OX40 costimulation on Treg, both in cancer and autoimmune diseases. In the latter case, Treg have a crucial function, as they avoid an exacerbated immune response by blocking the activity of effector T cells. While in cancer, its function is counterproductive for antitumor treatments for the same reason.[113]

Freeman ZT *et al*., on an attempt to inhibit Tregs, performed RNA sequencing of Tregs in different cancers, including glioblastoma. Results showed 4-1BB as the most differentially expressed gene between cancer and normal tissue. In addition, tumoral Tregs expressed higher levels of 4-1BB than peripheral Tregs and was related to a more suppressive phenotype. In the same line, they described two different scenarios depending on the expression of 4-1BB. A high expression of 41BB in Treg and low in CD8 was related to a suppressive microenvironment, while a high expression in CD8 was related to an antitumor microenvironment.[180] It is known that 4-1BB costimulation promotes Treg proliferation and survival, but the effect on the suppressive function of Treg is controversial. For example, it was described that 4-1BB stimulation reduced the incidence and severity of multiple sclerosis and autoimmune encephalomyelitis, meaning that Tregs were more suppressive.[181] In a separate study, the effect of anti-41BB was improved when Tregs were depleted on a model of lymphoma, indicating that the treatment had an effect on Treg population somehow.[182] However, other studies defend that 4-1BB costimulation diminishes Treg suppressive functions.[180]

In the case of OX40 stimulation, as well as for 4-1BB, promotes Treg proliferation and survival, and it was described to be more expressed on tumoral Tregs than in peripheral Treg cells.[183,184] Regarding the effect on Treg suppressive function, the majority of studies describe that OX40 agonism does not have an effect on it or that it is decreased,[185] but Weinberg's study supported that it will depend on the cytokine milieu.[184] Following this line of thought, it is known that $OX40^{+}$ Tregs were more suppressive than those that do not express it, which leads us to think that their costimulation must play a role in their suppressive function. Supporting this, a study on chronic myeloid leukemia, showed that OX40 expressing Tregs block the cytotoxic function of CD8 cells, preventing them from killing the tumor.[186] On the opposite scenario, it was described that Tregs that do not express OX40 cannot control a model of colitis, which means that they lose their suppressive capacity leading to an exacerbated

autoimmune response.[187] In conclusion, both 41BB and OX40 promote the proliferation and increase of Tregs, but their effect on suppressive function will depend on the microenvironment of the disease.[188] In our work, treatment with either Delta-24-ACT or Delta-24-RGDOX resulted in an increase of tumoral Treg that were more proliferative and showed a more suppressor phenotype. Although we still have to find a way to inhibit Treg action, we think that depleting Treg cells after viral administration in our DIPG models could improve the antitumor efficacy of the virus, especially Delta-24-RGDOX.

Due to the high expression of 4-1BB and OX40 on the Treg surface, IgG2 antibodies against these molecules are used to promote the depletion of Treg through ADCC, improving the antitumor effect of CD8 T cells.[186,189] With the same rationale, anti-GITR or anti-CTLA4 antibodies have been tested for Treg depletion, as Tregs constitutively express these molecules in high amounts. Due to the high expression of CTLA-4 on Treg, antibodies against this marker have been explored as potential Treg depletion agent. However, the effectivity of those antibodies in Treg depletion is controversial, as they do not usually deplete Treg completely. Sergio Quezada's group described that the Fc effector function was contributing to the activity of human CTLA-4 on a humanized model, promoting Treg depletion and an increase of the CD8/Treg ratio.[190] GITR is another essential checkpoint for Tregs, as it is highly expressed and related to a superior suppression function. The DTA-1 IgG2b anti-GITR antibody has been used to deplete Treg.[191] And in the case of no-depleting, anti-GITR stimulation has shown to inhibit Treg proliferation and function and to increase CD8 and CD4 T effector cells (Teff).[192] In fact, anti-GITR antibody was used in glioblastoma in combination with anti-PD1, demonstrating that GITR stimulation improved anti-PD1 treatment by inhibiting Treg suppressive function and increasing Treg conversion to CD4 effector cells. However, in a separate work, Coe *et al*., observed that Treg suppressive function was not altered with the antibody. It just partially depleted Tregs but controlled tumor growth more efficiently than anti-CD25 (PC61 clone).[191] It was described that the PC61 clone of CD25 does not correctly deplete Treg cells, because the Fc cannot bind properly to the Fc receptors, impeding ADCC.[193] In addition, it also affects Teff cells because it blocks IL-2 signaling, so even if it does not deplete them, it avoids IL-2 signaling in these cells. Tregs need high amounts of IL-2 for survival and function, whereas Teff need it in lesser quantities for costimulation. Therefore, Quezada and colleagues developed a new antibody, $CD25^{NIB}$, which does not block IL-2, promoting Treg depletion without affecting effector T cells.[194]

The above-mentioned approaches are not so powerful in Treg depletion and affect Teff cells as well. Thus, strategies towards the specific targeting of Tregs should be explored.

FOXP3 is the transcription factor that differentiates Tregs from the rest of cell populations and is necessary for its development and function. Different methods have been employed to inhibit this transcription factor. For example, the use of an antisense oligonucleotide (AZD8701) that binds FOXP3, promoting the inhibition of FOXP3 expression and Treg suppressive capacity.[195] On the other hand, Lasarte *et al.,* developed a small peptide (P60) that enters the cells, binds FOXP3 and inhibits Treg functions. They have showed antitumor efficacy in models of breast, renal and pancreatic cancers.[196,197] This strategy is a good way to inhibit specifically the Treg population, but they should be intratumorally administered to avoid affecting peripheral Treg and in turn leading to autoimmune disorders.

Other strategies to inhibit Treg activity include the use of protein kinase inhibitors, which has shown to inhibit Tregs. This is the case of dasatinib, an inhibitor of SRC family kinase and BCR/ABL oncogenic fusion. Redin *et al*., showed on a model of non-small cell lung cancer (NSCLC), that the treatment with dasatinib decreased Treg in the tumor, inhibit CD4 conversion to Treg and Treg suppressive function, without changing Teff number.[198] Imatinib (Glivec®) as well, has shown to decrease Treg proliferation and function and to increase CD8 function.[199,200] Its combination with radiotherapy (RT) in glioblastoma has shown to increase RT sensitivity and tumor delay.[201] Interestingly, both drugs are inhibitors of PDGFRα and β, which is mutated in about 10-30% of DIPG patients. Therefore, it could be an interesting strategy for decreasing Treg in DIPG tumors.

However, we should deeply analyze which are the consequences of eliminating Treg activity, since they play an important role in brain homeostasis. A good example of this is the role played by Treg in brain repair. It has been described in several studies that Treg protect after ischemic stroke. In this case, their depletion prevents recovery from brain damage and increases astrogliosis.[202] In addition, Treg decrease on post-stroke recovery, decreases the number of oligodendrocytes in the damaged area, which leads to a decrease of myelinization. For this process, Treg interact with microglia, causing them to acquire a reparative microglia phenotype which promotes oligodendrocyte maturation and thus myelination.[203] This is not the unique case of Treg interaction with microglia or macrophages. In a model of NSCLC, it has been reported that Treg interact more with tissue resident macrophages (TRM) than with bone marrow-derived macrophages and that these TRMs promote the suppressive effect of Treg.[204] It was also described that in inflammation resolution after tissue injury, Tregs promote efferocytosis of macrophages, which is the phagocytosis of apoptotic cells in a noninflammatory manner. So, when Treg are depleted, efferocytosis is decreased, promoting an inflammatory response.[205] In this case, this could work in our favor to enhance the

antitumor response of the virus. For all these reasons, to have a reasonable success in the clinic, any therapy targeting Tregs will have to be exhaustively interrogated not only regarding its efficacy but taking all the Treg functions as a whole.

In summary, we have provided robust evidence that the intratumoral delivery of Delta-24-ACT is capable of disrupting DIPG microenvironment tolerance by inducing profound proinflammatory changes, leading to the activation of T cells and to the generation of immune memory and thus preventing tumor recurrence. The results of this study, along with the excellent safety profile of the Delta-24 platform, provide a strong rationale for exploring this approach in the clinic. In addition, we have seen that the viruses produce an increase in Treg suppressor cells that could be a mechanism of resistance to the proper functioning of the virus. This may be the first step to address this issue more deeply and generate new strategies based on Delta-24-ACT/RGDOX and Treg inhibition.

Conclusions

1. Delta-24-ACT expresses a functional 4-1BBL on the membrane of infected cells. It infects, exerts a cytotoxic effect in murine and human DIPG cell lines, and replicates in the latter *in vitro*. Moreover, the type of cell death it produces promotes the release of DAMPs that could activate the immune response.

2. *In vivo* administration of Delta-24-ACT is safe and does not cause toxicity. More importantly, Delta-24-ACT significantly improves the survival of treated mice, leading to long-term survivors, and induces protective immunological memory in orthotopic models of DIPG.

3. Delta-24-ACT administration into DIPG tumors promotes a significant increase of immune infiltration. It reshapes the immunologically "cold" microenvironment of DIPG to a "hot" one, highlighting the importance of the immune system in the antitumor effect of the virus.

4. Delta-24-RGDOX efficiently expresses OX40L on the membrane of infected cells, and exerts a potent oncolytic effect in a dose-dependent manner in murine and human DIPG cell lines *in vitro*.

5. *In vivo* administration of Delta-24-RGDOX adenovirus in orthotopic models of DIPG is safe and significantly increases survival of treated mice. This effect is also observed in established tumors.

6. Delta-24-RGDOX significantly increases T lymphocytes into the tumor seven days after its tumor administration. In addition, it has an effect on the systemic immune response as splenocytes from treated mice respond to tumor and viral antigens.

7. Both Delta-24-ACT and Delta-24-RGDOX adenoviruses produce a significant increase of regulatory T cells, which the tumor may be using as a mechanism of resistance to viruses.

8. 4-1BBL and OX40L present in Delta-24-ACT and Delta-24-RGDOX viruses promote the suppressor function of regulatory T cells. Moreover, they increase the proliferation of these cells and the conversion of conventional CD4 to regulatory T cells.

Bibliography

1. Steliarova-Foucher, E. *et al.* International incidence of childhood cancer, 2001-10: a population-based registry study. *Lancet Oncol* **18**, 719–731 (2017).

2. Pui, C. H., Gajjar, A. J., Kane, J. R., Qaddoumi, I. A. & Pappo, A. S. Challenging issues in pediatric oncology. *Nat Rev Clin Oncol* **8**, 540–549 (2011).

3. Behjati, S., Gilbertson, R. J. & Pfister, S. M. Maturation block in childhood cancer. *Cancer Discov* **11**, 542–544 (2021).

4. Filbin, M. & Monje, M. Developmental origins and emerging therapeutic opportunities for childhood cancer. *Nat Med* **25**, 367–376 (2019).

5. Pfister, S. M. *et al.* A Summary of the Inaugural WHO Classification of Pediatric Tumors: Transitioning from the Optical into the Molecular Era. *Cancer Discov* **12**, 331–355 (2022).

6. Miller, K. D. *et al.* Brain and other central nervous system tumor statistics, 2021. *CA Cancer J Clin* **71**, 381–406 (2021).

7. Louis, D. N. *et al.* The 2007 WHO classification of tumours of the central nervous system. *Acta Neuropathol* **114**, 97–109 (2007).

8. Louis, D. N. *et al.* The 2016 World Health Organization Classification of Tumors of the Central Nervous System: a summary. *Acta Neuropathol* **131**, 803–820 (2016).

9. Louis, D. N. *et al.* The 2021 WHO classification of tumors of the central nervous system: A summary. J *Neurooncol* **23**, 1231–1251 (2021).

10. El-Khouly, F. E. *et al.* Diagnostics and treatment of diffuse intrinsic pontine glioma: where do we stand? *J Neurooncol* **145**, 177–184 (2019).

11. Panditharatna, E., Yaeger, K., Kilburn, L. B., Packer, R. J. & Nazarian, J. Clinicopathology of diffuse intrinsic pontine glioma and its redefined genomic and epigenomic landscape. *Cancer Genet* **208**, 367–373 (2015).

12. Grasso, C. S. *et al.* Functionally defined therapeutic targets in diffuse intrinsic pontine glioma. *Nat Med* **21**, 555–559 (2015).

13. Vanan, M. I. & Eisenstat, D. D. DIPG in children - What can we learn from the past? *Front Oncol* **5**, (2015).

14. Kaye, E. C., Baker, J. N. & Broniscer, A. Management of diffuse intrinsic pontine glioma in children: current and future strategies for improving prognosis. *CNS Oncol* **3**, 421–431 (2014).

15. Tessarz, P. & Kouzarides, T. Histone core modifications regulating nucleosome structure and dynamics. *Nat Rev Mol Cell Biol* **15**, 703–708 (2014).

16. Huether, R. *et al.* The landscape of somatic mutations in epigenetic regulators across 1,000 paediatric cancer genomes. *Nat Commun* **5**, (2014).

17. Kumar, V. C. & Pai, R. Genes of the month: H3.3 histone genes: H3F3A and H3F3B. *J Clin Pathol* **74**, 753–758 (2021).

18. Ferrari, K. J. *et al.* Polycomb-Dependent H3K27me1 and H3K27me2 Regulate Active Transcription and Enhancer Fidelity. *Mol Cell* **53**, 49–62 (2014).

19. Lowe, B. R., Maxham, L. A., Hamey, J. J., Wilkins, M. R. & Partridge, J. F. Histone H3 mutations: An updated view of their role in chromatin deregulation and cancer. *Cancers (Basel)* **11**, 1–24 (2019).

20. Hoeman, C. M. *et al.* ACVR1 R206H cooperates with H3.1K27M in promoting diffuse intrinsic pontine glioma pathogenesis. *Nat Commun* **10**, (2019).

21. Cordero, F. J. *et al.* Histone H3.3K27M represses p16 to accelerate gliomagenesis in a murine model of DIPG. *Mol Cancer Res* **15**, 1243–1254 (2017).

22. Paugh, B. S. *et al.* Novel oncogenic PDGFRA mutations in pediatric high-grade gliomas. *Cancer Res* **73**, 6219–6229 (2013).

23. Wang, R. N. *et al.* Bone Morphogenetic Protein (BMP) signaling in development and human diseases. *Genes Dis* **1**, 87–105 (2014).

24. Pollack, I. F., Agnihotri, S. & Broniscer, A. Childhood brain tumors: Current management, biological insights, and future directions. *J Neurosurg Pediatr* **23**, 261–273 (2019).

25. Wolff, J. E. A. *et al.* Treatment of paediatric pontine glioma with oral trophosphamide and etoposide. *Br J Cancer* **87**, 945–9 (2002).

26. Chassot, A. *et al.* Radiotherapy with concurrent and adjuvant temozolomide in children with newly diagnosed diffuse intrinsic pontine glioma. *J Neurooncol* **106**, 399–407 (2012).

27. Veringa, S. J. E. *et al.* In vitro drug response and efflux transporters associated with drug resistance in pediatric high grade glioma and diffuse intrinsic pontine glioma. *PLoS One* **8**, e61512 (2013).

28. Teng, F., Tsien, C. I., Lawrence, T. S. & Cao, Y. Blood-tumor barrier opening changes in brain metastases from pre to one-month post radiation therapy. *Radiother Oncol* **125**, 89–93 (2017).

29. Ransohoff, R. M. & Engelhardt, B. The anatomical and cellular basis of immune surveillance in the central nervous system. *Nat Rev Immunol* **12**, 623–635 (2012).

30. Engelhardt, B. & Ransohoff, R. M. The ins and outs of T-lymphocyte trafficking to the CNS: anatomical sites and molecular mechanisms. *Trends Immunol* **26**, 485–95 (2005).

31. Lieberman, N. A. P. *et al.* Characterization of the immune microenvironment of diffuse intrinsic pontine glioma: Implications for development of immunotherapy. *J Neurooncol* **21**, 83–94 (2019).

32. Lin, G. L. *et al.* Non-inflammatory tumor microenvironment of diffuse intrinsic pontine glioma. *Acta Neuropathol Commun* **6**, 51 (2018).

33. Vauléon, E. *et al.* Immune genes are associated with human glioblastoma pathology and patient survival. *BMC Med Genomics* **5**, 41 (2012).

34. Chen, Z. & Hambardzumyan, D. Immune microenvironment in glioblastoma subtypes. *Front Immunol* **9** (2018).

35. Wilcox, J. A., Ramakrishna, R. & Magge, R. Immunotherapy in Glioblastoma. *World Neurosurg* **116**, 518–528 (2018).

36. Sun, H. *et al.* Specific TP53 subtype as biomarker for immune checkpoint inhibitors in lung adenocarcinoma. *EBioMedicine* **60**, 102990 (2020).

37. Cacciotti, C. *et al.* Immune checkpoint inhibition for pediatric patients with recurrent/refractory CNS tumors: a single institution experience. *J Neurooncol* **149**, 113–122 (2020).

38. Mueller, S. *et al.* Mass cytometry detects H3.3K27M-specific vaccine responses in diffuse midline glioma. *Journal of Clinical Investigation* **130**, 6325–6337 (2020).

39. Benitez-Ribas, D. *et al.* Immune Response Generated With the Administration of Autologous Dendritic Cells Pulsed With an Allogenic Tumoral Cell-Lines Lysate in Patients With Newly Diagnosed Diffuse Intrinsic Pontine Glioma. *Front Oncol* **8**, 127 (2018).

40. Sabado, R. L., Balan, S. & Bhardwaj, N. Dendritic cell-based immunotherapy. *Cell Res* **27**, 74–95 (2017).

41. Mount, C. W. *et al.* Potent antitumor efficacy of anti-GD2 CAR T cells in H3-K27M+ diffuse midline gliomas. *Nat Med* **24**, 572–579 (2018).

42. Majzner, R. G. *et al.* GD2-CAR T cell therapy for H3K27M-mutated diffuse midline gliomas. *Nature* **603**, 934–941 (2022).

43. Gállego Pérez-Larraya, J. *et al.* Oncolytic DNX-2401 Virus for Pediatric Diffuse Intrinsic Pontine Glioma. *N Engl J Med* **386**, 2471–2481 (2022).

44. Kaufman, H. L., Kohlhapp, F. J. & Zloza, A. Oncolytic viruses: A new class of immunotherapy drugs. *Nat Rev Drug Discov* **14**, 642–662 (2015).

45. PELNER, L., FOWLER, G. A. & NAUTS, H. C. Effects of concurrent infections and their toxins on the course of leukemia. *Acta Med Scand Suppl* **338**, 1–47 (1958).

46. WELLER, T. H., ROBBINS, F. C. & ENDERS, J. F. Cultivation of poliomyelitis virus in cultures of human foreskin and embryonic tissues. *Proc Soc Exp Biol Med* **72**, 153–5 (1949).

47. MOORE, A. E. & O'CONNOR, S. Further studies on the destructive effect of the virus of Russian Far East encephalitis on the transplantable mouse sarcoma 180. *Cancer* **3**, 886–90 (1950).

48. MOORE, A. E. Viruses with oncolytic properties and their adaptation to tumors. *Ann N Y Acad Sci* **54**, 945–52 (1952).

49. Rogers, S. & Pfuderer, P. Use of viruses as carriers of added genetic information. *Nature* **219**, 749–51 (1968).

50. Andtbacka, R. H. I. *et al.* Talimogene Laherparepvec Improves Durable Response Rate in Patients With Advanced Melanoma. *J Clin Oncol* **33**, 2780–8 (2015).

51. Dörig, R. E., Marcil, A., Chopra, A. & Richardson, C. D. The human CD46 molecule is a receptor for measles virus (Edmonston strain). *Cell* **75**, 295–305 (1993).

52. Guo, P. *et al.* ICAM-1 as a molecular target for triple negative breast cancer. *Proc Natl Acad Sci U S A* **111**, 14710–5 (2014).

53. Dmitriev, I. *et al.* An adenovirus vector with genetically modified fibers demonstrates expanded tropism via utilization of a coxsackievirus and adenovirus receptor-independent cell entry mechanism. *J Virol* **72**, 9706–13 (1998).

54. Strong, J. E., Coffey, M. C., Tang, D., Sabinin, P. & Lee, P. W. The molecular basis of viral oncolysis: usurpation of the Ras signaling pathway by reovirus. *EMBO J* **17**, 3351–62 (1998).

55. Mansour, M., Palese, P. & Zamarin, D. Oncolytic specificity of Newcastle disease virus is mediated by selectivity for apoptosis-resistant cells. *J Virol* **85**, 6015–23 (2011).

56. Meurs, E. *et al.* Molecular cloning and characterization of the human double-stranded RNA-activated protein kinase induced by interferon. *Cell* **62**, 379–90 (1990).

57. Clemens, M. J. Targets and mechanisms for the regulation of translation in malignant transformation. *Oncogene* **23**, 3180–8 (2004).

58. Jhawar, S. R. *et al.* Oncolytic viruses-natural and genetically engineered cancer immunotherapies. *Front Oncol* **7** (2017).

59. DeWeese, T. L. *et al.* A phase I trial of CV706, a replication-competent, PSA selective oncolytic adenovirus, for the treatment of locally recurrent prostate cancer following radiation therapy. *Cancer Res* **61**, 7464–72 (2001).

60. Chang, J. *et al.* A Phase I study of KH901, a conditionally replicating granulocyte-macrophage colony-stimulating factor: armed oncolytic adenovirus for the treatment of head and neck cancers. *Cancer Biol Ther* **8**, 676–82 (2009).

61. Koeneman, K. S. *et al.* Osteocalcin-directed gene therapy for prostate-cancer bone metastasis. *World J Urol* **18**, 102–10 (2000).

62. Kohlhapp, F. J., Zloza, A. & Kaufman, H. L. Talimogene laherparepvec (T-VEC) as cancer immunotherapy. *Drugs Today (Barc)* **51**, 549–58 (2015).

63. Li, J.-L. *et al.* A phase I trial of intratumoral administration of recombinant oncolytic adenovirus overexpressing HSP70 in advanced solid tumor patients. *Gene Ther* **16**, 376–82 (2009).

64. Pearl, T. M., Markert, J. M., Cassady, K. A. & Ghonime, M. G. Oncolytic Virus-Based Cytokine Expression to Improve Immune Activity in Brain and Solid Tumors. *Mol Ther Oncolytics* **13**, 14–21 (2019).

65. Zhang, N. *et al.* Construction of an IL12 and CXCL11 armed oncolytic herpes simplex virus using the CRISPR/Cas9 system for colon cancer treatment. *Virus Res* **323**, 198979 (2022).

66. Nakao, S. *et al.* Intratumoral expression of IL-7 and IL-12 using an oncolytic virus increases systemic sensitivity to immune checkpoint blockade. *Sci Transl Med* **12**, (2020).

67. Chen, T. *et al.* IL-21 arming potentiates the anti-tumor activity of an oncolytic vaccinia virus in monotherapy and combination therapy. *J Immunother Cancer* **9**, (2021).

68. Kowalsky, S. J. *et al.* Superagonist IL-15-Armed Oncolytic Virus Elicits Potent Antitumor Immunity and Therapy That Are Enhanced with PD-1 Blockade. *Mol Ther* **26**, 2476–2486 (2018).

69. de la Nava, D., Selvi, K. M. & Alonso, M. M. Immunovirotherapy for Pediatric Solid Tumors: A Promising Treatment That is Becoming a Reality. *Front Immunol* **13**, 866892 (2022).

70. Cao, G.-D. *et al.* The Oncolytic Virus in Cancer Diagnosis and Treatment. *Front Oncol* **10**, 1786 (2020).

71. Kennedy, B. E., Sadek, M. & Gujar, S. A. Targeted Metabolic Reprogramming to Improve the Efficacy of Oncolytic Virus Therapy. *Mol Ther* **28**, 1417–1421 (2020).

72. Ahmed, A. & Tait, S. W. G. Targeting immunogenic cell death in cancer. *Mol Oncol* **14**, 2994–3006 (2020).

73. Lynch, J. P., Fishbein, M. & Echavarria, M. Adenovirus. *Semin Respir Crit Care Med* **32**, 494–511 (2011).

74. Lynch, J. P. & Kajon, A. E. Adenovirus: Epidemiology, Global Spread of Novel Serotypes, and Advances in Treatment and Prevention. *Semin Respir Crit Care Med* **37**, 586–602 (2016).

75. Kulanayake, S. & Tikoo, S. K. Adenovirus Core Proteins: Structure and Function. *Viruses* **13**, (2021).

76. Saha, B., Wong, C. M. & Parks, R. J. The adenovirus genome contributes to the structural stability of the virion. *Viruses* **6**, 3563–3583 (2014).

77. Lichtenstein, D. L., Toth, K., Doronin, K., Tollefson, A. E. & Wold, W. S. M. Functions and mechanisms of action of the adenovirus E3 proteins. *Int Rev Immunol* **23**, 75–111 (2004).

78. Russell, W. C. Adenoviruses: Update on structure and function. *J Gen Virol* **90**, 1–20 (2009).

79. Garcia-Moure, M., Martinez-Vélez, N., Patiño-García, A. & Alonso, M. M. Oncolytic adenoviruses as a therapeutic approach for osteosarcoma: A new hope. *J Bone Oncol* **9**, 41–47 (2017).

80. Bergelson, J. M. *et al.* Isolation of a common receptor for Coxsackie B viruses and adenoviruses 2 and 5. *Science* **275**, 1320–3 (1997).

81. Wickham, T. J., Mathias, P., Cheresh, D. A. & Nemerow, G. R. Integrins alpha v beta 3 and alpha v beta 5 promote adenovirus internalization but not virus attachment. *Cell* **73**, 309–19 (1993).

82. Leopold, P. L. *et al.* Fluorescent virions: dynamic tracking of the pathway of adenoviral gene transfer vectors in living cells. *Hum Gene Ther* **9**, 367–78 (1998).

83. Wiethoff, C. M., Wodrich, H., Gerace, L. & Nemerow, G. R. Adenovirus protein VI mediates membrane disruption following capsid disassembly. *J Virol* **79**, 1992–2000 (2005).

84. Strunze, S. *et al.* Kinesin-1-mediated capsid disassembly and disruption of the nuclear pore complex promote virus infection. *Cell Host Microbe* **10**, 210–23 (2011).

85. Farley, D. C., Brown, J. L. & Leppard, K. N. Activation of the early-late switch in adenovirus type 5 major late transcription unit expression by L4 gene products. *J Virol* **78**, 1782–91 (2004).

86. Bett, A. J., Prevec, L. & Graham, F. L. Packaging capacity and stability of human adenovirus type 5 vectors. *J Virol* **67**, 5911–21 (1993).

87. Fueyo, J. *et al.* A mutant oncolytic adenovirus targeting the Rb pathway produces anti-glioma effect in vivo. *Oncogene* **19**, 2–12 (2000).

88. Anders, M. *et al.* Loss of the coxsackie and adenovirus receptor contributes to gastric cancer progression. *Br J Cancer* **100**, 352–9 (2009).

89. Kim, M. *et al.* The coxsackievirus and adenovirus receptor acts as a tumour suppressor in malignant glioma cells. *Br J Cancer* **88**, 1411–6 (2003).

90. Fueyo, J. *et al.* Preclinical characterization of the antiglioma activity of a tropism-enhanced adenovirus targeted to the retinoblastoma pathway. *J Natl Cancer Inst* **95**, 652–660 (2003).

91. Jiang, H. *et al.* Delta-24-RGD oncolytic adenovirus elicits anti-glioma immunity in an immunocompetent mouse model. *PLoS One* **9**, (2014).

92. Lang, F. F. *et al.* Phase I study of DNX-2401 (delta-24-RGD) oncolytic adenovirus: replication and immunotherapeutic effects in recurrent malignant glioma. *Journal of Clinical Oncology* **36**, 1419–1427 (2018).

93. Martínez-Vélez, N. *et al.* The oncolytic virus Delta-24-RGD elicits an antitumor effect in pediatric glioma and DIPG mouse models. *Nat Commun* **10**, (2019).

94. Martinez-Velez, N. *et al.* Delta-24-RGD combined with radiotherapy exerts a potent antitumor effect in diffuse intrinsic pontine glioma and pediatric high grade glioma models. *Acta Neuropathol Commun* **7**, 64 (2019).

95. Garcia-Moure, M. *et al.* Delta-24-RGD, an oncolytic adenovirus, increases survival and promotes proinflammatory immune landscape remodeling in models of AT/RT and CNS-PNET. *Clin Cancer Res* **27**, 1807–1820 (2021).

96. Puigdelloses, M. *et al.* CD137 and PD-L1 targeting with immunovirotherapy induces a potent and durable antitumor immune response in glioblastoma models. *J Immunother Cancer* **9**, (2021).

97. Laspidea, V. *et al.* Exploiting 4-1BB immune checkpoint to enhance the efficacy of oncolytic virotherapy for diffuse intrinsic pontine gliomas. *JCI Insight* **7**, e154812 (2022).

98. Yonezawa, A., Dutt, S., Chester, C., Kim, J. & Kohrt, H. E. Boosting cancer immunotherapy with anti-CD137 antibody therapy. *Clin Cancer Res* **21**, 3113–3120 (2015).

99. Etxeberria, I., Glez-Vaz, J., Teijeira, Á. & Melero, I. New emerging targets in cancer immunotherapy: CD137/4-1BB costimulatory axis. *ESMO open* **4**, e000733 (2020).

100. Wang, C., Lin, G. H. Y., McPherson, A. J. & Watts, T. H. Immune regulation by 4-1BB and 4-1BBL: Complexities and challenges. *Immunol Rev* **229**, 192–215 (2009).

101. Chester, C., Sanmamed, M. F., Wang, J. & Melero, I. Immunotherapy targeting 4-1BB: Mechanistic rationale, clinical results, and future strategies. *Blood* **131**, 49–57 (2018).

102. Hinner, M. J. *et al.* Tumor-localized costimulatory T-cell engagement by the 4-1BB/HER2 bispecific antibody-anticalin fusion PRS-343. *Clin Cancer Res* **25**, 5878–5889 (2019).

103. Hangiu, O. *et al.* Tumor targeted 4-1BB agonist antibody-albumin fusions with high affinity to FcRn induce anti-tumor immunity without toxicity. *iScience* **25**, (2022).

104. Claus, C. *et al.* Tumor-targeted 4-1BB agonists for combination with T cell bispecific antibodies as off-the-shelf therapy. *Sci Transl Med* **11**, (2019).

105. Gaspar, M. *et al.* CD137/OX40 bispecific antibody induces potent antitumor activity that is dependent on target coengagement. *Cancer Immunol Res* **18**, 781–793 (2020).

106. Geuijen, C. *et al.* A human CD137×PD-L1 bispecific antibody promotes anti-tumor immunity via context-dependent T cell costimulation and checkpoint blockade. *Nat Commun* **12**, (2021).

107. Etxeberria, I. *et al.* Antitumor efficacy and reduced toxicity using an anti-CD137 Probody therapeutic. *Proc Natl Acad Sci USA* **118**, e2025930118 (2021).

108. Jiang, H. *et al.* Oncolytic adenovirus and tumor-targeting immune modulatory therapy improve autologous cancer vaccination. *Cancer Res* **77**, 3894–3907 (2017).

109. Croft, M. Control of Immunity by the TNFR-related molecule OX40 (CD134). *Annu Rev Immunol* **28**, 57–78 (2010).

110. Willoughby, J., Griffiths, J., Tews, I. & Cragg, M. S. OX40: Structure and function – What questions remain? *Mol Immunol* **83**, 13–22 (2017).

111. Jiang, H. *et al.* Localized treatment with oncolytic adenovirus delta-24-RGDOX induces systemic immunity against disseminated subcutaneous and intracranial melanomas. *Clin Cancer Res* **25**, 6801–6814 (2019).

112. Nguyen, T. T. *et al.* Reshaping the tumor microenvironment with oncolytic viruses, positive regulation of the immune synapse, and blockade of the immunosuppressive oncometabolic circuitry. *J Immunother Cancer* **10**, e004935 (2022).

113. Workman, C. J., Szymczak-Workman, A. L., Collison, L. W., Pillai, M. R. & Vignali, D. A. A. The development and function of regulatory T cells. *Cell Mol Life Sci* **66**, 2603–2622 (2009).

114. Vignali, D. A. A., Collison, L. W. & Workman, C. J. How regulatory T cells work. *Nat Rev Immunol* **8**, 523–532 (2008).

115. Jordan, M. S. *et al.* Thymic selection of CD4+CD25+ regulatory T cells induced by an agonist self-peptide. *Nat Immunol* **2**, 301–306 (2001).

116. Hawrylowicz, C. M. & O'Garra, A. Potential role of interleukin-10-secreting regulatory T cells in allergy and asthma. *Nat Rev Immunol* **5**, 271–83 (2005).

117. Joetham, A. *et al.* Naturally occurring lung CD4(+)CD25(+) T cell regulation of airway allergic responses depends on IL-10 induction of TGF-beta. *J Immunol* **178**, 1433–42 (2007).

118. Grossman, W. J. *et al.* Differential expression of granzymes A and B in human cytotoxic lymphocyte subsets and T regulatory cells. *Blood* **104**, 2840–8 (2004).

119. Cao, X. *et al.* Granzyme B and perforin are important for regulatory T cell-mediated suppression of tumor clearance. *Immunity* **27**, 635–46 (2007).

120. Thornton, A. M. & Shevach, E. M. CD4+CD25+ immunoregulatory T cells suppress polyclonal T cell activation in vitro by inhibiting interleukin 2 production. *J Exp Med* **188**, 287–96 (1998).

121. de la Rosa, M., Rutz, S., Dorninger, H. & Scheffold, A. Interleukin-2 is essential for CD4+CD25+ regulatory T cell function. *Eur J Immunol* **34**, 2480–8 (2004).

122. Deaglio, S. *et al.* Adenosine generation catalyzed by CD39 and CD73 expressed on regulatory T cells mediates immune suppression. *J Exp Med* **204**, 1257–65 (2007).

123. Borsellino, G. *et al.* Expression of ectonucleotidase CD39 by Foxp3+ Treg cells: hydrolysis of extracellular ATP and immune suppression. *Blood* **110**, 1225–32 (2007).

124. Fallarino, F. *et al.* Modulation of tryptophan catabolism by regulatory T cells. *Nat Immunol* **4**, 1206–12 (2003).

125. Mellor, A. L. & Munn, D. H. IDO expression by dendritic cells: tolerance and tryptophan catabolism. *Nat Rev Immunol* **4**, 762–74 (2004).

126. Nishikawa, H. & Koyama, S. Mechanisms of regulatory T cell infiltration in tumors: Implications for innovative immune precision therapies. *J Immunother Cancer* **9**, (2021).

127. Buck, M. D., Sowell, R. T., Kaech, S. M. & Pearce, E. L. Metabolic Instruction of Immunity. *Cell* **169**, 570–586 (2017).

128. Watson, M. J. *et al.* Metabolic support of tumour-infiltrating regulatory T cells by lactic acid. *Nature* **591**, 645–651 (2021).

129. Simpson, T. R. *et al.* Fc-dependent depletion of tumor-infiltrating regulatory T cells co-defines the efficacy of anti-CTLA-4 therapy against melanoma. *J Exp Med* **210**, 1695–710 (2013).

130. Solomon, I. *et al.* CD25-Treg-depleting antibodies preserving IL-2 signaling on effector T cells enhance effector activation and antitumor immunity. *Nat Cancer* **1**, 1153–1166 (2020).

131. Revenko, A. *et al.* Direct targeting of FOXP3 in Tregs with AZD8701, a novel antisense oligonucleotide to relieve immunosuppression in cancer. *J Immunother Cancer* **10**, (2022).

132. Kumar, P., Bhattacharya, P. & Prabhakar, B. S. A comprehensive review on the role of co-signaling receptors and Treg homeostasis in autoimmunity and tumor immunity. *J Autoimmun* **95**, 77–99 (2018).

133. Hinterbrandner, M. *et al.* Tnfrsf4-expressing regulatory T cells promote immune escape of chronic myeloid leukemia stem cells. *JCI Insight* **6**, (2021).

134. Takeda, I. *et al.* Distinct Roles for the OX40-OX40 Ligand Interaction in Regulatory and Nonregulatory T Cells. *J Immunol* **172**, 3580–3589 (2004).

135. So, T., Lee, S.-W. & Croft, M. Immune Regulation and Control of Regulatory T cells by OX40 and 4-1BB. *Cytokine Growth Factor Rev* **19**, 253–262 (2008).

136. Halvorson, K. G. *et al.* A high-throughput in Vitro drug screen in a genetically engineered mouse model of diffuse intrinsic pontine glioma identifies BMS-754807 as a promising therapeutic agent. *PLoS One* **10**, (2015).

137. Barton, K. L. *et al.* PD-0332991, a CDK4/6 Inhibitor, Significantly Prolongs Survival in a Genetically Engineered Mouse Model of Brainstem Glioma. *PLoS One* **8**, 1–7 (2013).

138. Lal, S. *et al.* An implantable guide-screw system for brain tumor studies in small animals. *J Neurosurg* **92**, 326–33 (2000).

139. Marigil, M. *et al.* Development of a DIPG orthotopic model in mice using an implantable guide-screw system. *PLoS One* **12**, 1–10 (2017).

140. Abengozar-Muela, M. *et al.* Diverse immune environments in human lung tuberculosis granulomas assessed by quantitative multiplexed immunofluorescence. *Mod Pathol* **33**, 2507–2519 (2020).

141. Martinez-Valbuena, I. *et al.* Amylin as a potential link between type 2 diabetes and alzheimer disease. *Ann Neurol* **86**, 539–551 (2019).

142. Gentleman, R. C. *et al.* Bioconductor: open software development for computational biology and bioinformatics. *Genome Biol* **5**, R80 (2004).

143. Canouil, M. *et al.* NACHO: an R package for quality control of NanoString nCounter data. *Bioinformatics* **36**, 970–971 (2020).

144. Ritchie, M. E. *et al.* limma powers differential expression analyses for RNA-sequencing and microarray studies. *Nucleic Acids Res* **43**, e47 (2015).

145. Yu, G., Wang, L.-G., Han, Y. & He, Q.-Y. clusterProfiler: an R package for comparing biological themes among gene clusters. *OMICS* **16**, 284–7 (2012).

146. Rotte, A. Combination of CTLA-4 and PD-1 blockers for treatment of cancer. *J Exp Clin Cancer Res* **38**, 255 (2019).

147. Boutros, C. *et al.* Safety profiles of anti-CTLA-4 and anti-PD-1 antibodies alone and in combination. *Nat Rev Clin Oncol* **13**, 473–86 (2016).

148. Gujar, S., Pol, J. G. & Kroemer, G. Heating it up: Oncolytic viruses make tumors ‘hot’ and suitable for checkpoint blockade immunotherapies. *Oncoimmunology* **7**, (2018).

149. Michael I. Chastkofsky, Katarzyna C. Pituch, Hiroaki Katagi, Markella Zannikou, Liliana Ilut, Ting Xiao, Yu Han, Adam M. Sonabend, David T. Curiel, Erin R.

Bonner, Javad Nazarian, Craig M. Horbinski, Charles D. James, Amanda M. Saratsis, Rintaro Hashizume, I. V. B. Mesenchymal Stem Cells Successfully Deliver Oncolytic Virotherapy to Diffuse Intrinsic Pontine Glioma. *J Obstet Gynaecol (Lahore)* **27**, 1766–1777 (2021).

150. Cockle, J. v. *et al.* Oncolytic Herpes Simplex Virus Inhibits Pediatric Brain Tumor Migration and Invasion. *Mol Ther Oncolytics* **5**, 75–86 (2017).

151. Patel, S. K. *et al.* Generation of diffuse intrinsic pontine glioma mouse models by brainstem-targeted in utero electroporation. *Neuro Oncol* **22**, 381–392 (2020).

152. bin Yu, Yan Zhou, Hao Wu, Zhen Wang, Yang Zhan, Xiao Feng, Ranshen Geng, Yongge Wu, W. K. and X. Y. Seroprevalence of Neutralizing Antibodies to Human Adenovirus Type 5 in Healthy Adults in China. *J Med Virol* **84**, 1408–1414 (2012).

153. Tyler, M. A. *et al.* Neural stem cells target intracranial glioma to deliver an oncolytic adenovirus in vivo. *Gene Ther* **16**, 262–278 (2009).

154. Yong, R. L. *et al.* Human Bone Marrow-Derived Mesenchymal Stem Cells for Intravascular Delivery of Oncolytic Adenovirus Delta-24-RGD to Human Gliomas. *Cancer Res* **69**, 8932–8940 (2009).

155. Shin, D. H. *et al.* Current strategies to circumvent the antiviral immunity to optimize cancer virotherapy. *J Immunother Cancer* **9**, 1–10 (2021).

156. Martínez-Vélez, N. *et al.* The oncolytic virus Delta-24-RGD elicits an antitumor effect in pediatric glioma and DIPG mouse models. *Nat Commun* **10**, 2235 (2019).

157. Mellman, I., Coukos, G. & Dranoff, G. Cancer immunotherapy comes of age. *Nature* **480**, 480–489 (2011).

158. Morvan, M. G. & Lanier, L. L. NK cells and cancer: You can teach innate cells new tricks. *Nat Rev Cancer* **16**, 7-19 (2016).

159. Chiossone, L., Dumas, P. Y., Vienne, M. & Vivier, E. Natural killer cells and other innate lymphoid cells in cancer. *Nat Rev Immunol* **18**, 671-688 (2018).

160. Ross, J. L. *et al.* Platelet-derived growth factor beta is a potent inflammatory driver in paediatric high-grade glioma. *Brain* **144**, 53-69 (2021).

161. Wilcox, R. A. *et al.* Provision of antigen and CD137 signaling breaks immunological ignorance, promoting regression of poorly immunogenic tumors. *J Clin Invest* **109**, 651-659 (2002).

162. Williams, J. B. *et al.* The EGR2 targets LAG-3 and 4-1BB describe and regulate dysfunctional antigen-specific CD8+ T cells in the tumor microenvironment. *J Exp Med* **214**, 381-400 (2017).

163. Weigelin, B. *et al.* Focusing and sustaining the antitumor CTL effector killer response by agonist anti-CD137 mAb. *Proc Natl Acad Sci U S A* 112, 7551-6 (2015).

164. Leem, G. *et al.* 4-1BB co-stimulation further enhances anti-PD-1-mediated reinvigoration of exhausted CD39+CD8 T cells from primary and metastatic sites of epithelial ovarian cancers. *J Immunother Cancer* **8**, (2020).

165. Hinterberger, M. *et al.* Intratumoral virotherapy with 4-1BBL armed modified vaccinia Ankara eradicates solid tumors and promotes protective immune memory. *J Immunother Cancer* **9**, (2021).

166. Weinberg, A. D. *et al.* Engagement of the OX-40 Receptor In Vivo Enhances Antitumor Immunity. *The Journal of Immunology* **164**, 2160–2169 (2000).

167. Redmond, W. L., Linch, S. N. & Kasiewicz, M. J. Combined targeting of costimulatory (OX40) and coinhibitory (CTLA-4) pathways elicits potent effector T cells capable of driving robust antitumor immunity. *Cancer Immunol Res* **2**, 142–153 (2014).

168. Ma, Y. *et al.* Combination of PD-1 Inhibitor and OX40 Agonist Induces Tumor Rejection and Immune Memory in Mouse Models of Pancreatic Cancer. *Gastroenterology* **159**, 306-319.e12 (2020).

169. Han, M. G. *et al.* Combination of OX40 Co-Stimulation, Radiotherapy, and PD-1 Inhibition in a Syngeneic Murine Triple-Negative Breast Cancer Model. *Cancers (Basel)* **14**, 2692 (2022).

170. Jakeman, P. G., Hills, T. E., Fisher, K. D. & Seymour, L. W. Macrophages and their interactions with oncolytic viruses. *Curr Opin Pharmacol* **24**, 23–29 (2015).

171. Alvarez-Breckenridge, C., Kaur, B. & Chiocca, E. A. Pharmacologic and chemical adjuvants in tumor virotherapy. *Chem Rev* **109**, 3125–40 (2009).

172. Fulci, G. *et al.* Depletion of peripheral macrophages and brain microglia increases brain tumor titers of oncolytic viruses. *Cancer Res* **67**, 9398–406 (2007).

173. Shashkova, E. v, Doronin, K., Senac, J. S. & Barry, M. A. Macrophage depletion combined with anticoagulant therapy increases therapeutic window of systemic treatment with oncolytic adenovirus. *Cancer Res* **68**, 5896–904 (2008).

174. Blitz, S. E. *et al.* Tumor-Associated Macrophages/Microglia in Glioblastoma Oncolytic Virotherapy: A Double-Edged Sword. *Int J Mol Sci* **23**, 1808 (2022).

175. Saha, D., Martuza, R. L. & Rabkin, S. D. Macrophage Polarization Contributes to Glioblastoma Eradication by Combination Immunovirotherapy and Immune Checkpoint Blockade. *Cancer Cell* **32**, 253-267.e5 (2017).

176. van den Bossche, W. B. L. *et al.* Oncolytic virotherapy in glioblastoma patients induces a tumor macrophage phenotypic shift leading to an altered glioblastoma microenvironment. *J Neurooncol* **20**, 1494–1504 (2018).

177. Geletneky, K. *et al.* Oncolytic H-1 Parvovirus Shows Safety and Signs of Immunogenic Activity in a First Phase I/IIa Glioblastoma Trial. *Mol Ther* **25**, 2620–2634 (2017).

178. Kober, C. *et al.* Microglia and astrocytes attenuate the replication of the oncolytic vaccinia virus LIVP 1.1.1 in murine GL261 gliomas by acting as vaccinia virus traps. *J Transl Med* **13**, 216 (2015).

179. Delwar, Z. M., Kuo, Y., Wen, Y. H., Rennie, P. S. & Jia, W. Oncolytic virotherapy blockade by microglia and macrophages requires STAT1/3. *Cancer Res* **78**, 718–730 (2018).

180. Freeman, Z. T. *et al.* A conserved intratumoral regulatory T cell signature identifies 4-1BB as a pan-cancer target. *J Clin Invest* **130**, 1405–1416 (2020).

181. Sun, Y. *et al.* Administration of agonistic anti-4-1BB monoclonal antibody leads to the amelioration of experimental autoimmune encephalomyelitis. *J Immunol* **168**, 1457–65 (2002).

182. Houot, R. *et al.* Therapeutic effect of CD137 immunomodulation in lymphoma and its enhancement by Treg depletion. *Blood* **114**, 3431–3438 (2009).

183. Timperi, E. *et al.* Regulatory T cells with multiple suppressive and potentially pro-tumor activities accumulate in human colorectal cancer. *Oncoimmunology* **5**, (2016).

184. Ruby, C. E. *et al.* Cutting Edge: OX40 Agonists Can Drive Regulatory T Cell Expansion if the Cytokine Milieu Is Right. *J Immunol* **183**, 4853–4857 (2009).

185. Polesso, F., Sarker, M., Weinberg, A. D., Murray, S. E. & Moran, A. E. OX40 Agonist Tumor Immunotherapy Does Not Impact Regulatory T Cell Suppressive Function. *J Immunol* **203**, 2011–2019 (2019).

186. Hinterbrandner, M. *et al.* Tnfrsf4-expressing regulatory T cells promote immune escape of chronic myeloid leukemia stem cells. *JCI Insight* **6**, (2021).

187. Griseri, T., Asquith, M., Thompson, C. & Powrie, F. OX40 is required for regulatory T cell-mediated control of colitis. *J Exp Med* **207**, 699–709 (2010).

188. Kumar, P., Bhattacharya, P. & Prabhakar, B. S. A comprehensive review on the role of co-signaling receptors and Treg homeostasis in autoimmunity and tumor immunity. *J Autoimmun* **95**, 77–99 (2018).

189. Buchan, S. L. *et al.* Antibodies to Costimulatory Receptor 4-1BB Enhance Anti-tumor Immunity via T Regulatory Cell Depletion and Promotion of CD8 T Cell Effector Function. *Immunity* **49**, 958-970.e7 (2018).

190. Arce Vargas, F. *et al.* Fc Effector Function Contributes to the Activity of Human Anti-CTLA-4 Antibodies. *Cancer Cell* **33**, 649-663.e4 (2018).

191. Coe, D. *et al.* Depletion of regulatory T cells by anti-GITR mAb as a novel mechanism for cancer immunotherapy. *Cancer Immunol Immunother* **59**, 1367–77 (2010).

192. Ko, K. *et al.* Treatment of advanced tumors with agonistic anti-GITR mAb and its effects on tumor-infiltrating Foxp3+CD25+CD4+ regulatory T cells. *Journal of Experimental Medicine* **202**, 885–891 (2005).

193. Vignali, D. A. A., Collison, L. W. & Workman, C. J. How regulatory T cells work. *Nat Rev Immunol* **8**, 523–532 (2008).

194. Solomon, I. *et al.* CD25-Treg-depleting antibodies preserving IL-2 signaling on effector T cells enhance effector activation and antitumor immunity. *Nat Cancer* **1**, 1153–1166 (2020).

195. Revenko, A. *et al.* Direct targeting of FOXP3 in Tregs with AZD8701, a novel antisense oligonucleotide to relieve immunosuppression in cancer. *J Immunother Cancer* **10**, (2022).

196. Moreno Ayala, M. A. *et al.* Therapeutic blockade of Foxp3 in experimental breast cancer models. *Breast Cancer Res Treat* **166**, 393–405 (2017).

197. Setiawan, M. F. *et al.* FOXP3 Inhibitory Peptide P60 Increases Efficacy of Cytokine-induced Killer Cells Against Renal and Pancreatic Cancer Cells. *Anticancer Res* **39**, 5369–5374 (2019).

198. Redin, E. *et al.* SRC family kinase (SFK) inhibitor dasatinib improves the antitumor activity of anti-PD-1 in NSCLC models by inhibiting Treg cell conversion and proliferation. *J Immunother Cancer* **9**, (2021).

199. Balachandran, V. P. *et al.* Imatinib potentiates antitumor T cell responses in gastrointestinal stromal tumor through the inhibition of Ido. *Nat Med* **17**, 1094–1100 (2011).

200. Larmonier, N. *et al. Imatinib Mesylate Inhibits CD4 CD25 Regulatory T Cell Activity and Enhances Active Immunotherapy against BCR-ABL Tumors 1*. *The Journal of Immunology* **181**, (2008).

201. Oertel, S. *et al.* Human glioblastoma and carcinoma xenograft tumors treated by combined radiation and imatinib (Gleevec®). *Strahlentherapie und Onkologie* **182**, 400–407 (2006).

202. Ito, M. *et al.* Brain regulatory T cells suppress astrogliosis and potentiate neurological recovery. *Nature* **565**, 246–250 (2019).

203. Shi, L. *et al.* Treg cell-derived osteopontin promotes microglia-mediated white matter repair after ischemic stroke. *Immunity* **54**, 1527-1542.e8 (2021).

204. Casanova-Acebes, M. *et al.* Tissue-resident macrophages provide a pro-tumorigenic niche to early NSCLC cells. *Nature* **595**, 578–584 (2021).

205. Proto, J. D. *et al.* Regulatory T Cells Promote Macrophage Efferocytosis during Inflammation Resolution. *Immunity* **49**, 666-677.e6 (2018).

Annex

JCI insight

Exploiting 4-1BB immune checkpoint to enhance the efficacy of oncolytic virotherapy for diffuse intrinsic pontine gliomas

Virginia Laspidea, … , Juan Fueyo, Marta M. Alonso

JCI Insight. 2022;7(7):e154812. https://doi.org/10.1172/jci.insight.154812.

Research Article | Immunology | Oncology

Graphical abstract

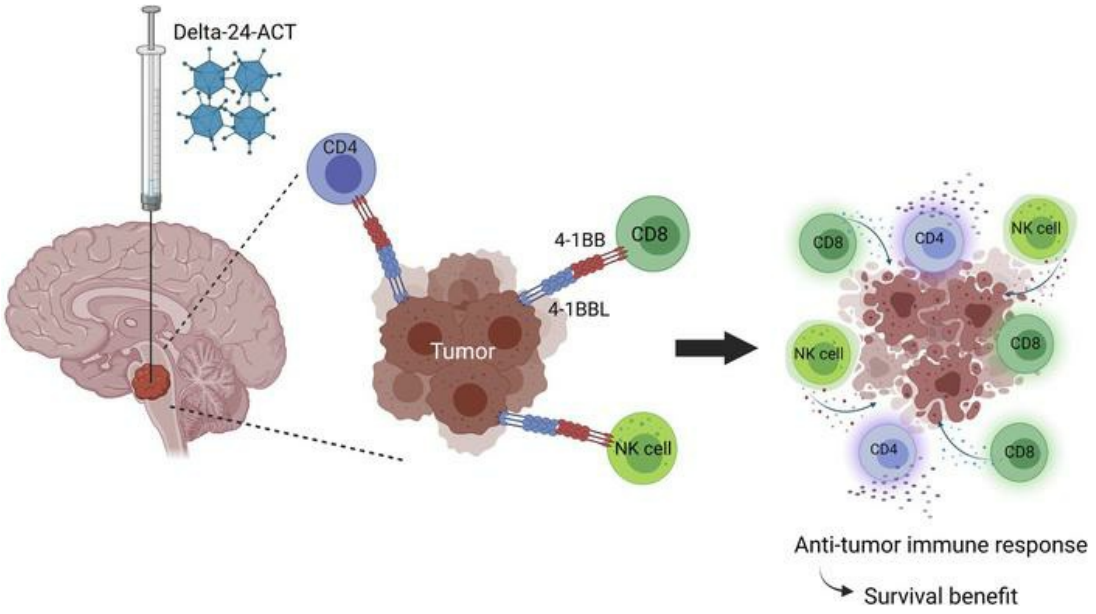

JCI insight

RESEARCH ARTICLE

Exploiting 4-1BB immune checkpoint to enhance the efficacy of oncolytic virotherapy for diffuse intrinsic pontine gliomas

Virginia Laspidea,[1,2,3] Montserrat Puigdelloses,[1,2,3] Sara Labiano,[1,2,3] Lucía Marrodán,[1,2,3] Marc Garcia-Moure,[1,2,3] Marta Zalacain,[1,2,3] Marisol Gonzalez-Huarriz,[1,2,3] Naiara Martínez-Vélez,[1,2,3] Iker Ausejo-Mauleon,[1,2,3] Daniel de la Nava,[1,2,3] Guillermo Herrador-Cañete,[1,2,4] Javier Marco-Sanz,[1,2,3] Elisabeth Guruceaga,[1,5] Carlos E. de Andrea,[1,6] María Villalba,[1,6] Oren Becher,[7,8,9,10] Massimo Squatrito,[11] Verónica Matía,[11] Jaime Gállego Pérez-Larraya,[1,2,12] Ana Patiño-García,[1,2,3] Sumit Gupta,[13] Candelaria Gomez-Manzano,[13] Juan Fueyo,[13] and Marta M. Alonso[1,2,3]

[1]Health Research Institute of Navarra, Pamplona, Navarra, Spain. [2]Solid Tumor Program, Center for the Applied Medical Research, Pamplona, Navarra, Spain. [3]Department of Pediatrics, Navarra University Clinic, Pamplona, Spain. [4]Gene Therapy and Regulation of Gene Expression Program, Center for the Applied Medical Research, Pamplona, Navarra, Spain. [5]Bioinformatics Platform, El Centro de Investigación Médica Aplicada (CIMA), University of Navarra, Pamplona, Spain. [6]Department of Pathology, Navarra University Clinic, Pamplona, Spain. [7]Department of Pediatrics, [8]Department of Biochemistry and Molecular Genetics, and [9]Lurie Comprehensive Cancer Center, Northwestern University, Chicago, Illinois, USA. [10]Division of Hematology Oncology and Stem Cell Transplant, Ann & Robert H. Lurie Children's Hospital, Chicago, Illinois, USA. [11]Seve Ballesteros Foundation Brain Tumor Group, Molecular Oncology Programme, Spanish National Cancer Research Center, Madrid, Spain. [12]Department of Neurology, Navarra University Clinic, Pamplona, Spain. [13]Department of Neuro-Oncology, The University of Texas MD Anderson Cancer Center, Houston, Texas, USA.

Diffuse intrinsic pontine gliomas (DIPGs) are aggressive pediatric brain tumors, and patient survival has not changed despite many therapeutic efforts, emphasizing the urgent need for effective treatments. Here, we evaluated the anti-DIPG effect of the oncolytic adenovirus Delta-24-ACT, which was engineered to express the costimulatory ligand 4-1BBL to potentiate the antitumor immune response of the virus. Delta-24-ACT induced the expression of functional 4-1BBL on the membranes of infected DIPG cells, which enhanced the costimulation of $CD8^+$ T lymphocytes. In vivo, Delta-24-ACT treatment of murine DIPG orthotopic tumors significantly improved the survival of treated mice, leading to long-term survivors that developed immunological memory against these tumors. In addition, Delta-24-ACT was safe and caused no local or systemic toxicity. Mechanistic studies showed that Delta-24-ACT modulated the tumor-immune content, not only increasing the number, but also improving the functionality of immune cells. All of these data highlight the safety and potential therapeutic benefit of Delta-24-ACT the treatment of patients with DIPG.

Conflict of interest: CGM and JF report ownership interest (including patent application no. 14/703876) in DNATrix. MMA has a research grant from DNAtrix.

Submitted: September 14, 2021
Accepted: February 25, 2022
Published: April 8, 2022

Reference information: *JCI Insight*. 2022;7(7):e154812. https://doi.org/10.1172/jci.insight.154812.

Introduction

Diffuse intrinsic pontine gliomas (DIPGs) are aggressive pediatric brain stem tumors that most frequently occur in children ranging in age from 6 to 9 years. With a median overall survival of 9–11 months, DIPGs are the main cause of cancer-related death in children (1, 2). In 2016, the WHO reclassified CNS tumors and included DIPG within a new class: H3-K27M mutant diffuse midline glioma (DMG H3-K27M) (3). Approximately 80% of DIPGs contain H3-K27M mutations (usually in histone H3.3 or H3.1), which have been proposed as driver mutations in this malignancy (4). Other relevant mutations include *TP53* (40%–77%), *PDGFR* (13%–36%), and *ACVR1* (20%–32%) (5, 6).

Because of the disseminating nature and localization of the tumor, surgical resection is not an option, and the current standard treatment is radiotherapy, which slightly improves the survival and quality of life of patients with DIPG in the short term. However, less than 10% of patients survive for more than 2 years

after diagnosis (7–9), pointing to the urgent need for effective therapies. DIPGs are immunologically "cold" tumors due to their low mutational burden and extremely low levels of immune infiltration (10). Recent studies demonstrated that the DIPG microenvironment is mainly made up of microglia/macrophages and that T cell infiltration is minimal (10–12). Because T cells constitute an essential part of the antitumor effect in immune therapies (13), strategies geared toward increasing cytotoxic T cell infiltration are desirable to trigger an effective antitumor immune response, and one such strategy is based on the use of oncolytic adenoviruses (14). Oncolytic viruses are tumor-selective biotherapeutic agents that promote antitumor responses via the cytolysis of tumor cells and the induction of tumor-specific immune responses engaging the innate and adaptive arms. We previously demonstrated that the treatment of DIPG and pediatric high-grade glioma human and murine models with the oncolytic virus Delta-24-RGD increased the survival rates; however, not all of our study animals were cured, indicating that therapeutic improvement is possible (15, 16). Moreover, a phase I clinical trial of DNX-2401 (Delta-24-RGD) in patients with glioblastoma demonstrated that the administered virus was safe and improved patient survival by promoting an increase in tumor immune infiltration (17). In this study, we explored the idea of combining the cytotoxic effect of Delta-24-RGD with the activation of the costimulatory immune checkpoint 4-1BB to further boost the immune effect of the virus. The 4-1BB (also known as CD137 and TNFRSF9) protein is a member of the TNF receptor superfamily that is expressed by activated T lymphocytes and NK cells, among other cell types. Its ligand, 4-1BBL (also known as CD137L), is expressed on antigen-presenting cells, such as DCs, macrophages, and B cells (18). The binding of 4-1BB to its ligand promotes T cell activation in both $CD4^+$ and $CD8^+$ lymphocytes (19). The targeting of 4-1BB, especially by agonist monoclonal antibodies, has yielded promising results in solid tumors (20, 21). However, the systemic administration of such antibodies has been associated with liver toxicity (20). Therefore, we genetically modified Delta-24-RGD to express the costimulatory ligand of 4-1BB (4-1BBL), generating a new virus, Delta-24-ACT (22), for the delivery of 4-1BBL directly into the tumor. This virus displayed antitumor effects in murine glioma models and demonstrated a safe profile. In this study, we characterized the oncolytic capacity of Delta-24-ACT and its ability to recruit immune cells in DIPG. Our results showed that Delta-24-ACT produced a functional 4-1BBL that activated immune cell effector and memory functions in preclinical DIPG models and exhibited a therapeutic effect superior to that of parental Delta-24-RGD while maintaining a safe profile.

Results

4-1BBL expressed by Delta-24-ACT costimulates T cells. In this work, we aimed to improve the ability of Delta-24-RGD to generate an effective antitumor immune response in DIPG tumors. To do so, Delta-24-RGD was genetically modified by incorporation of a cassette expressing the murine 4-1BBL in place of the E3 gene to generate a new oncolytic adenovirus, Delta-24-ACT (22) (Supplemental Figure 1A; supplemental material available online with this article; https://doi.org/10.1172/jci.insight.154812DS1). Delta-24-ACT maintains the same genetic modifications as Delta-24-RGD (23), a 24–base pair deletion in E1A and the introduction of RGD-4C in the HI loop fiber. After generation of the virus, we first determined its ability to express the ligand in DIPG murine (NP53 and XFM) and human (SU-DIPG IV and TP54) cell lines after infection. We readily detected 4-1BBL protein (Figure 1A) and mRNA (Supplemental Figure 1B) expression in infected murine and human cell lines in a dose-dependent manner. More importantly, we detected 4-1BBL expression on the membranes of infected cells, which is essential for correct functioning, by immunofluorescence and flow cytometry (Figure 1, B and C, and Supplemental Figure 1C). In fact, 4-1BBL expression was detected in 80% of infected mouse cell membranes at a multiplicity of infection (MOI) of 50, whereas this percentage was reached at an MOI of 10 on the surface of human cell membranes (Figure 1C). Of importance, we also observed a significant increase in the expression of the ligand in mouse DIPG tumors treated with Delta-24-ACT in vivo (Figure 1D). Moreover, functional studies in vitro demonstrated that the 4-1BBL expressed by the virus was functional and capable of stimulating $CD8^+$ lymphocytes. We performed an experiment in which gp100-specific $CD8^+$ T cells from PMEL mice were cocultured with mock-, Delta-24-RGD–, or Delta-24-ACT–infected NP53 cells (that were previously pulsed with the gp100 peptide) for 48 hours. We observed a significant increase in IFN-γ and granzyme B expression in T lymphocytes cocultured with NP53 cells infected with Delta-24-ACT compared with those cocultured in the presence of noninfected or Delta-24-RGD–infected NP53 cells (Figure 1, E and F). In fact, activated $CD8^+$ T lymphocytes cocultured with Delta-24-ACT–infected NP53 cells acquired a more blastic morphology and formed more clusters in vitro (Supplemental Figure 1D).

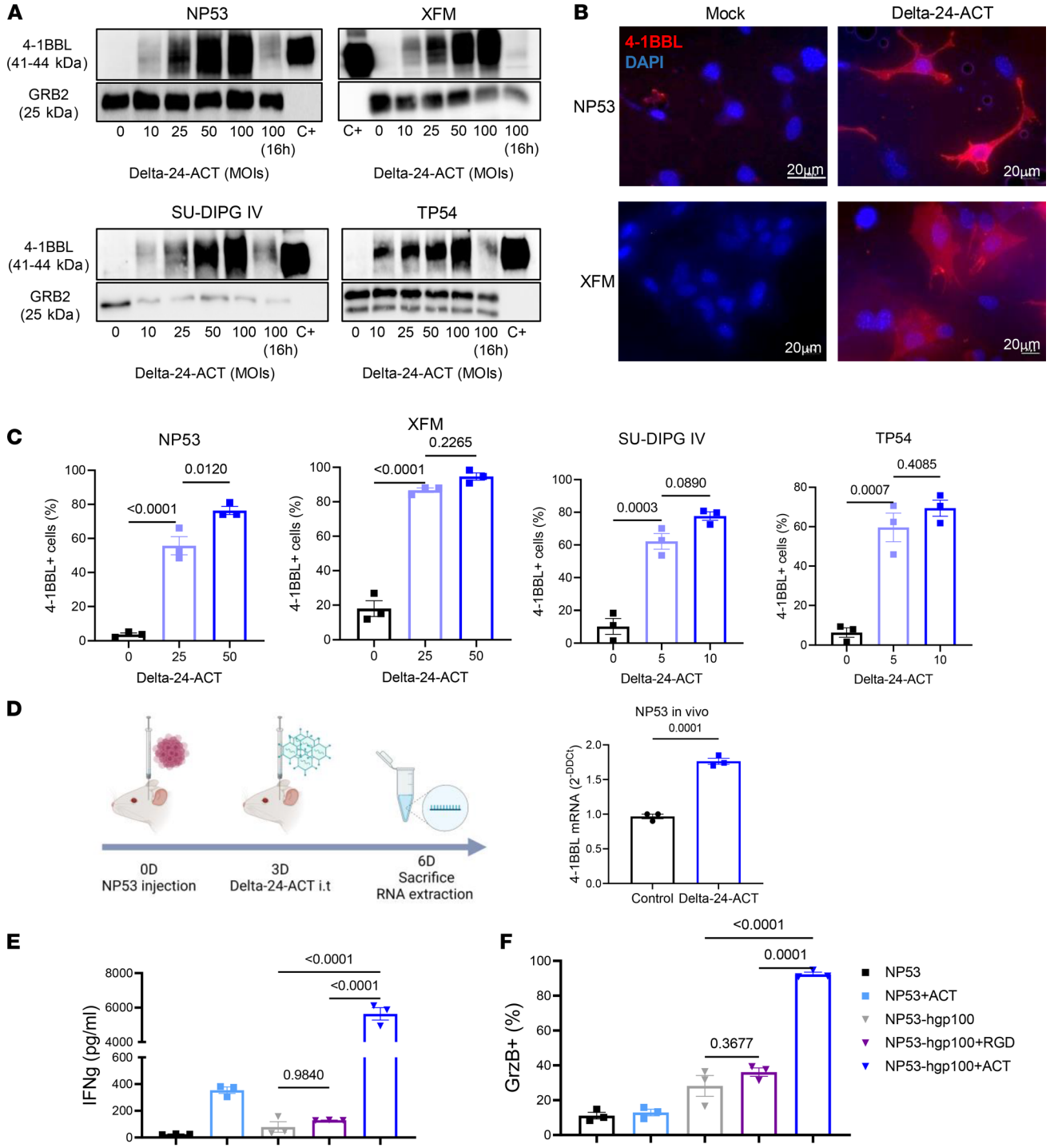

Figure 1. Characterization of Delta-24-ACT functionality in DIPG. (**A**) 4-1BBL protein expression in NP53, XFM, SU-DIPG IV, and TP54 cells infected with Delta-24-ACT at the indicated MOIs, as determined by Western blotting. C+, 4-1BBL recombinant protein. (**B**) Representative immunofluorescence images of 4-1BBL expression in NP53- and XFM-infected cells compared with mock-infected cells. Scale bar: 20 µm. (**C**) 4-1BBL protein expression in the membranes of murine and human cells infected with Delta-24-ACT at the indicated MOIs, as determined by flow cytometry. The percentage of 4-1BBL$^+$ cells is shown. One-way ANOVA was performed (n = 3, each group), and P values are shown above respective bars. Data are shown as the mean ± SEM. (**D**) Schedule of the experiment for the in vivo determination of 4-1BBL expression, and evaluation of 4-1BBL protein expression in NP53 tumors from control- or Delta-24-ACT–treated mice (n = 3), as determined by Q-PCR. Data are shown as the mean ± SEM. (**E**) IFN-γ and (**F**) granzyme B production by CD8$^+$ lymphocytes. CD8$^+$ T cells from PMEL mice were cocultured with NP53 cells infected with Delta-24-RGD, Delta-24-ACT (MOI = 100), or the mock control. CD8$^+$ lymphocytes activated with CD3 and CD28 but not NP53 cells, and CD8$^+$ lymphocytes activated with CD3, CD28, and 4-1BB antibody were used as negative and positive controls for the experiment, respectively. One-way ANOVA was performed (n = 3, each group), and P values are shown above respective bars. Data are shown as the mean ± SEM.

Delta-24-ACT maintains the oncolytic features of Delta-24-RGD and induces immunogenic cell death in vitro. Once we confirmed that 4-1BBL was functional, we next characterized the oncolytic effect of Delta-24-ACT in mouse and human DIPG cell lines. Western blotting was used to analyze E1A expression and adenovirus fiber expression, which are indicative of infection and viral replication, respectively, and we observed dose-dependent changes in viral protein expression in all the cell lines tested (Figure 2A). Next, we tested the cytotoxic effect of Delta-24-ACT 5 days after viral infection (MOIs ranging from 5 to 100) and compared it with that of Delta-24-RGD. We observed that the percentage of viable cells decreased as the viral input increased with both viruses. Delta-24-ACT displayed a half-maximal inhibitory concentration (IC_{50}) ranging from an MOI of 16.1 to an MOI of 0.2; the values were lower in the human DIPG cell lines than in mouse cell lines as a result of effective replication (NP53, 16.1 ± 1.1 PFU/cell; SU-DIPG IV, 6.9 ± 1.1 PFU/cell; XFM, 2.5 ± 1.5 PFU/cell; and TP54, 0.2 ± 1.6 PFU/cell; Figure 2B). Delta-24-RGD showed similar IC_{50} values in vitro, as expected. E1A expression observed by immunohistochemistry in NP53- and XFM-bearing mice treated with Delta-24-ACT 4 days after viral administration (Figure 2C) indicated that the virus can infect tumor cells in vivo.

Immunogenic cell death is accompanied by the exposure and release of damage-associated molecular patterns (DAMPs), which ultimately favor an immune response. Importantly, we observed significant increases in secreted ATP and HMGB1 levels following Delta-24-ACT infection of NP53 and XFM cells (Figure 2, D and E); ATP and HMGB1 are well-described DAMPs (24). Delta-24-ACT infection triggered the translocation of calreticulin to the plasma membrane (Figure 2F), another well-known mechanism that contributes to the immunogenicity of tumor cells by acting as an "eat-me" signal to promote tumor cell phagocytosis by macrophages (25). In summary, Delta-24-ACT was shown to infect murine and human DIPG cell lines, to express functional 4-1BBL, and to exert oncolytic effects leading to the triggering of several DAMPs associated with immunogenic cell death.

Delta-24-ACT exhibits a safe profile in vivo. The administration of an oncolytic virus with the capacity to unleash a potent immune response could result in lethal inflammation of the brain stem. In addition, 4-1BB agonist antibody administration in the clinic has been associated with liver toxicity (20). Thus, we first studied the safety profile of Delta-24-ACT in vivo by either administering different doses of the virus (10^6 and 10^7 PFUs/mouse) or PBS as a control into the pons of 2 tumor-free immunocompetent mouse strains ($NP53^{fl/fl}$ and BALB/c). We assessed whether the virus had any effect in healthy tissue before viral administration into tumor-bearing mice. We weighed the animals every 2–3 days to assess weight variability as a sign of toxicity and observed no significant weight loss at any of the viral concentrations evaluated (Figure 3A and Supplemental Figure 2A). We observed no deaths among any of the $NP53^{fl/fl}$ strain groups (Figure 3B). Among BALB/c mice, there was 1 death each in the PBS and 10^6 PFU groups within the first 7 days of treatment (Supplemental Figure 2B). Evaluation of the brains ruled out lethal inflammation, and we believe that these deaths were due to the procedure itself. The absence of a gross loss of body weight suggested that the viral injection was well tolerated. In a separate experiment, we obtained sera from mice bearing NP53 cells treated with either Delta-24-ACT or PBS (mock control) and measured several parameters, including alanine aminotransferase (ALT), aspartate aminotransferase (AST), and alkaline phosphatase (ALP) levels to monitor hepatic injury and bilirubin and albumin levels to monitor hepatic function. We observed no significant differences between the virus-treated and PBS-treated mice in the measured parameters, except for AST and ALP levels, which were significantly increased in control- (PBS-treated) mice. However, the obtained values were within the range of normal values in mice (AST = 50–100 U/L, ALP = 35–100 U/L) (Figure 3C). To further analyze hepatic toxicity, we conducted anatomopathological analyses of mouse livers 15 days after viral administration to detect histological changes in this organ induced by Delta-24-ACT. Importantly, none of the analyzed livers showed signs of hepatic injury (Figure 3D and Supplemental Figure 2C). Moreover, we did not observe significant weight loss in NP53-bearing mice in the days after the administration of different doses of the virus (10^6 and 10^7 PFU/mouse) or PBS (Figure 3E). These results highlight the safety of Delta-24-ACT and the fact that intratumoral injection of 4-1BBL does not induce hepatic toxicity.

Delta-24-ACT increased survival and promoted immunological memory in orthotopic DIPG models. To evaluate the anti-DIPG effect of Delta-24-ACT in vivo, DIPG tumors were developed by the intracranial injection of NP53 or XFM cells into the pons of immunocompetent mice (26). Three days after cell injections, mice were treated with PBS (control group) or Delta-24-ACT (10^6 PFUs/mouse) and were monitored for survival (Figure 4A). We observed a significant increase in the median survival of mice treated with the virus in

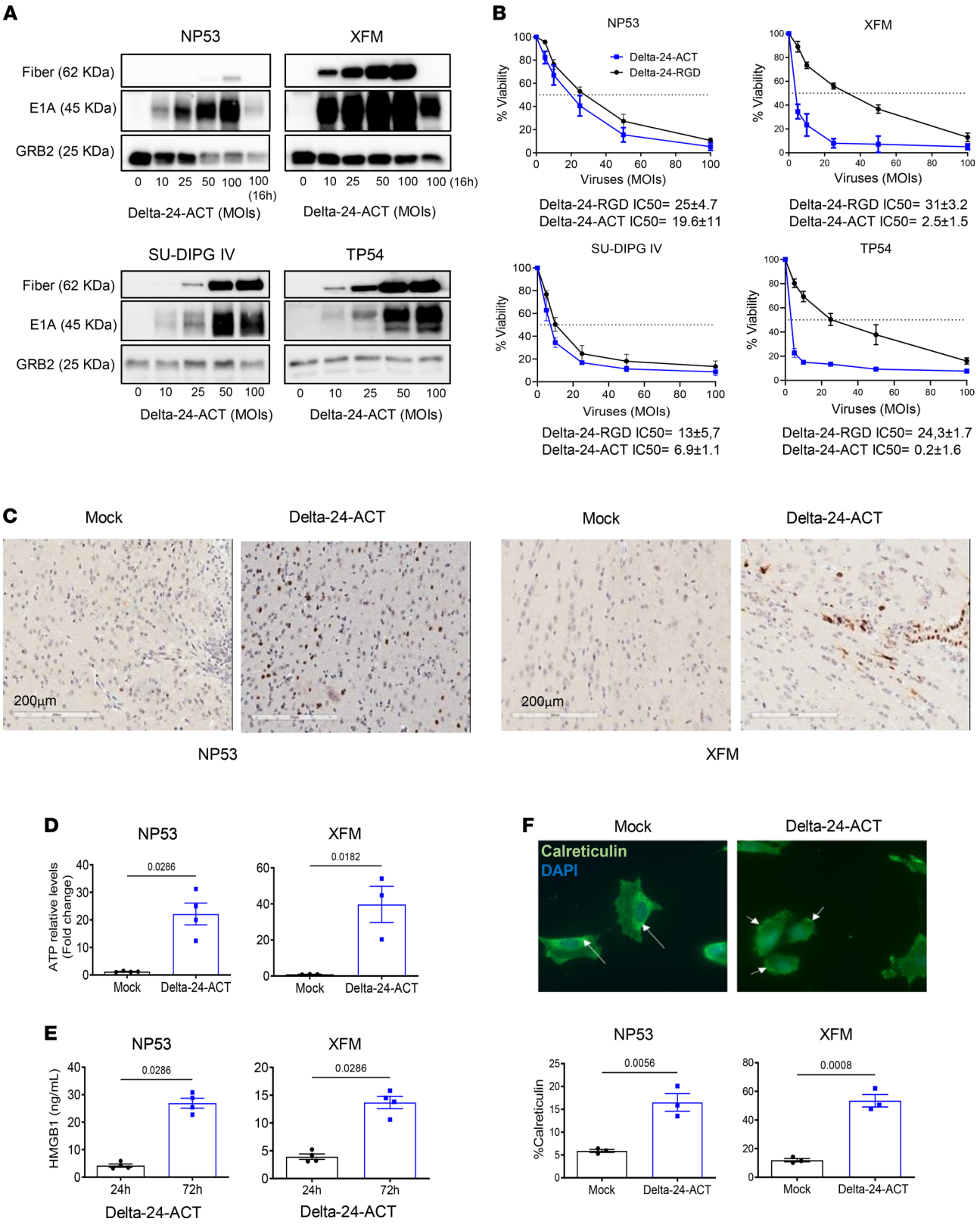

Figure 2. Evaluation of the Delta-24-ACT oncolytic effects in vitro. (**A**) Assessment of viral protein expression (fiber and E1A) in NP53, XFM, SU-DIPG IV, and TP54 cells by Western blotting. Cells were infected with Delta-24-ACT at the indicated MOIs, and whole-cell lysates were collected 48 hours later. GRB2 was used as a protein-loading control. (**B**) Oncolytic effects of Delta-24-ACT on murine and human DIPG cells. To quantify the oncolytic effects of Delta-24-RGD or Delta-24-ACT on cells, they were infected at the indicated MOIs, and viability was evaluated 5 days later by MTS assays. Values indicate the percentages of viable cells in infected cultures compared with noninfected cultures (mean ± SD, *n* = 3 each group). (**C**) Evaluation of the E1A viral protein in vivo. Viral protein expression was evaluated in vivo in mice bearing either XFM or NP53 cells 3 days after mock or Delta-24-ACT treatment.

Representative micrographs are shown. Scale bar: 20 μm. (**D** and **E**) Concentrations of the damage-associated molecular pattern (DAMP) markers ATP and HMGB1 in supernatants obtained from NP53 and XFM cultures at 72 hours after Delta-ACT (n = 4) or mock (n = 4) infection. Data are shown as the mean ± SEM (Mann-Whitney test), and P values are shown above bars. (**F**) Representative fluorescence microscopy images of NP53 cells at 4 hours after infection with Delta-24-ACT or mock infection. Calreticulin (CRT) at the cell surface was detected by immunofluorescence (green) and nuclei (blue; DAPI). Arrows denote the calreticulin location in the cell. Original magnification, ×40. Flow cytometric quantification of membrane calreticulin$^+$ cells after Delta-24-ACT infection. Data are shown as the mean ± SEM (n = 4 each group; Mann-Whitney test), and P values are shown above bars.

comparison to the control groups in both models (log-rank test; $P = 0.014$ for NP53 cells, log-rank test; $P < 0.001$ for XFM cells). The median survival time of the virus-treated mice injected with NP53 cells was 48.5 days, in comparison with 28 days for the controls (Figure 4B). Moreover, Delta-24-ACT treatment showed significantly better efficacy than Delta-24-RGD or radiotherapy (the standard treatment) in the NP53 model (log-rank test; $P = 0.001$ Supplemental Figure 3, A and B). In addition, 25% (2 of 8) of the NP53-bearing mice were long-term survivors (Figure 4B). We also evaluated the antitumor efficacy of Delta-24-ACT in the XFM DIPG model using the same schedule (Figure 4E). The survival time was 30 days for the treated group of mice injected with XFM cells compared with 9 days for the controls. Importantly, 50% (5 of 10) of the XFM-bearing mice were long-term survivors (Figure 4E).

Because DIPGs are known to recur after treatment, and the goal of this project was not only to show local efficacy, but also to achieve protective immunological memory, we performed a rechallenge experiment with long-term survivors of the NP53 experiment. All of the naive mice used as controls (4 of 4) developed tumors, while Delta-24-ACT–treated mice showed 100% protection against rechallenge with NP53 cells (2 of 2; Figure 4C). To demonstrate that the antitumor response observed was due to the immune response, we performed an experiment in immunodeficient (BALB/cA-Rag2$^{-/-}\gamma c^{-/-}$) mice bearing NP53 murine cells, as the replication of the virus is highly attenuated in murine cell lines. Treatment with the virus did not present a survival benefit in this model ($P = 0.622$; Figure 4D). Next, we assessed the antitumor effect of viral treatment in already established XFM tumors, and we postponed viral treatment until 7 days, instead of 3 days, after cell injection (Figure 4F). Delta-24-ACT significantly increased the median survival of treated mice and led to a 30% increase in the long-term survival rate (3 of 10; $P = 0.0093$ Figure 4G). Moreover, 66% of the treated XFM tumor-bearing mice exhibited immunological memory (2 of 3; Figure 4H), and these mice were free of tumors (Figure 4I). Thus, Delta-24-ACT treatment is efficacious against DIPG murine models and induces protective immunological memory against local tumor rechallenge.

Delta-24-ACT triggered a proinflammatory response in DIPG models. To better understand the mechanism underlying the therapeutic effect of Delta-24-ACT, we evaluated the triggered immune response. Thus, we intratumorally injected Delta-24-ACT or PBS (mock group) 3 days after NP53 cell implantation (on day 0). Then, tumor immune infiltrate was analyzed by NanoString and IHC multiplex (on day 15) and flow cytometry at 3, 7 and 10 days after viral administration (Figure 5A). Gene set enrichment analysis of the control- and Delta-24-ACT–treated tumors revealed an increase in positive regulators of the immune response related to the activation and proliferation of lymphocytes (Figure 5B and Supplemental Figure 4, A and B). Similarly, flow cytometry analyses showed an increase over time in immune infiltration between the control- and Delta-24-ACT–treated groups. By day 10 after viral treatment, tumors were highly infiltrated by nearly all the populations tested, except for NK cells (CD45, $P = 0.0038$; CD8$^+$, $P = 0.0056$; CD4$^+$, $P = 0.0039$; Tregs, $P = 0.0015$; F4/80, $P = 0.0019$; B cells, $P = 0.0224$; NK cells, $P = 0.354$; DCs, $P = 0.0226$) (Figure 5C). We analyzed the expression of CD137 in CD8$^+$, CD4$^+$, Tregs (CD4$^+$Foxp3$^+$), and NK cells. On day 7, the 4 tumor-infiltrating populations had higher surface CD137 expression in the Delta-24-ACT–treated tumors than in the controls (Figure 5D) (CD8$^+$, $P = 0.1889$; CD4$^+$, $P = 0.0101$; Tregs, $P = 0.0137$; NK cells, $P < 0.0001$), indicating that they could directly interact with the cells expressing 4-1BBL in a Delta-24-ACT–dependent manner. This upregulation of CD137 expression was lost on day 10 (Supplemental Figure 5A). In addition to CD137, other activation/exhaustion markers, such as GITR, OX40, PD-1, and CD69, were analyzed in CD8$^+$ and CD4$^+$ T cells. We observed significantly upregulated expression of these markers in both populations on day 7 (Figure 5E) but not on day 10 (Supplemental Figure 5B). In addition, we analyzed tumor immune infiltration by immunohistochemistry 15 days after viral administration of NP53-bearing mice and observed a significant increase in the CD8$^+$ subpopulation but no increase in CD4$^+$ cells ($P = 0.0168$ and $P = 0.5744$, respectively). We also observed a significant increase in FOXP3$^+$ Tregs after viral treatment ($P = 0.048$) (Supplemental Figure 5C). In parallel, we used multispectral immunofluorescence to confirm the localization of the CD8$^+$, CD4$^+$, FOXP3$^+$, CD31$^+$, and F4/80$^+$ populations within the tumor 15 days after Delta-24-ACT treatment (Figure 5F and Supplemental Figure 5D).

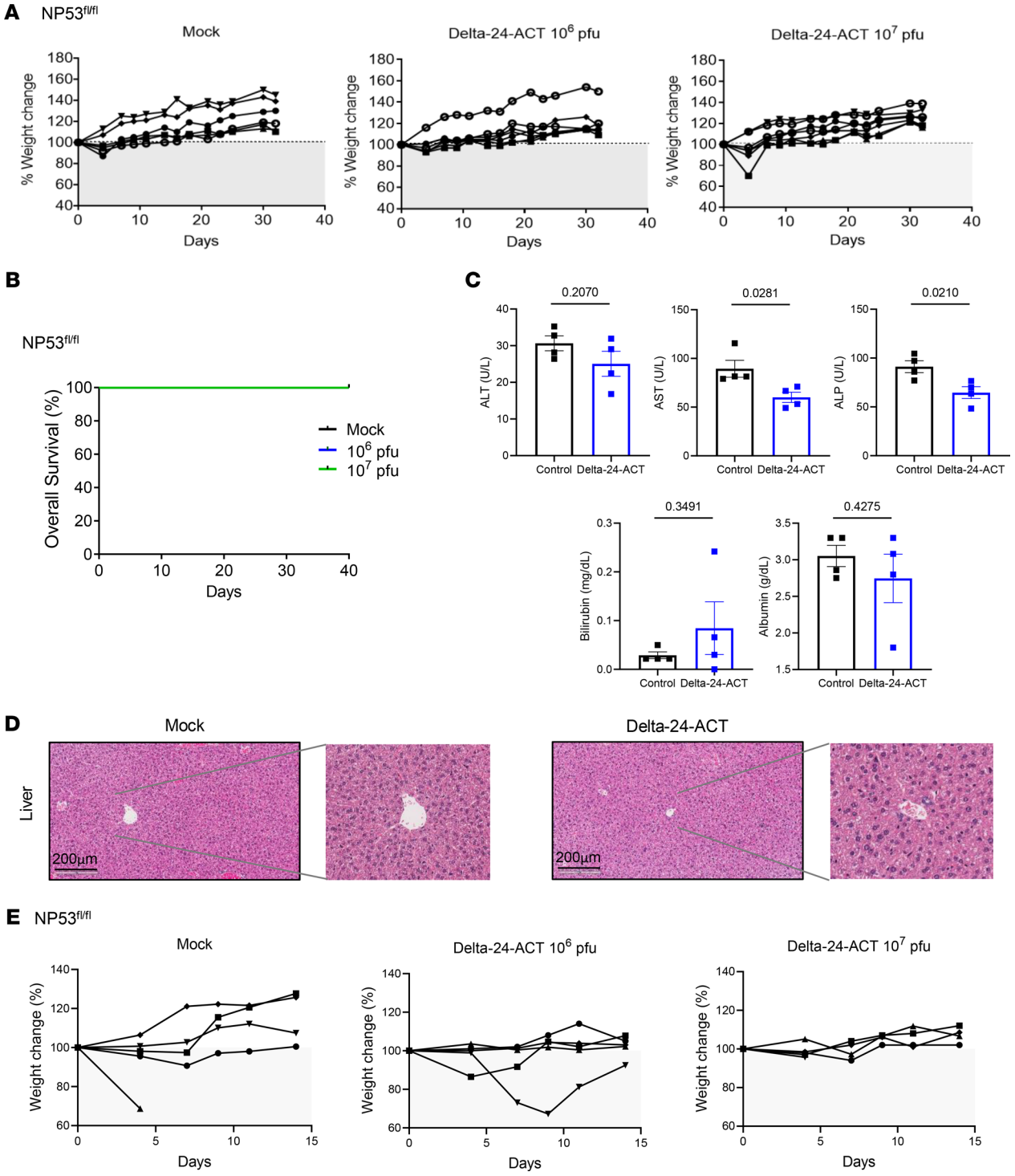

Figure 3. Assessment of Delta-24-ACT toxicity in vivo. (**A**) NP53$^{fl/fl}$ mice were treated intraparenchymally with mock treatment (PBS) (n = 6) or Delta-24-ACT (n = 7) at the indicated doses. Mice from the different groups were weighed every 3–4 days until the end of the treatment (30 days). (**B**) Kaplan-Meier survival plot of NP53$^{fl/}$ mice treated with PBS (control group) and 10^6 PFUs or 10^7 PFUs of Delta-24-ACT in the pons. (**C**) Evaluation of biochemical parameters related to hepatic toxicity after intratumoral injection of Delta-24-ACT. The mice were treated with the mock treatment or virus, and serum samples were collected 3 days later. Several parameters were measured, including alanine aminotransferase (ALT, U/L), aspartate aminotransferase (AST, U/L), and alkaline phosphatase (ALP, U/L) levels, to monitor hepatic injury and bilirubin (mg/dL) and albumin (g/dL) levels to assess hepatic function. Student's t test was performed, and P values are shown above bars. Data are shown as the mean ± SEM. (**D**) Histologic analysis of mouse livers bearing orthotopic DIPGs and treated locally with Delta-24-ACT at 10^8 PFUs. Representative micrographs of H&E staining of mouse livers from the indicated groups of DIPG models. Scale bar: 200 μm. The images show no viral presence in mouse livers and no signs of hepatotoxicity. (**E**) Percentage of weight change in NP53$^{fl/fl}$ mice bearing NP53 tumors treated with 10^6 or 10^7 PFUs/mouse Delta-24-ACT or PBS (as a control).

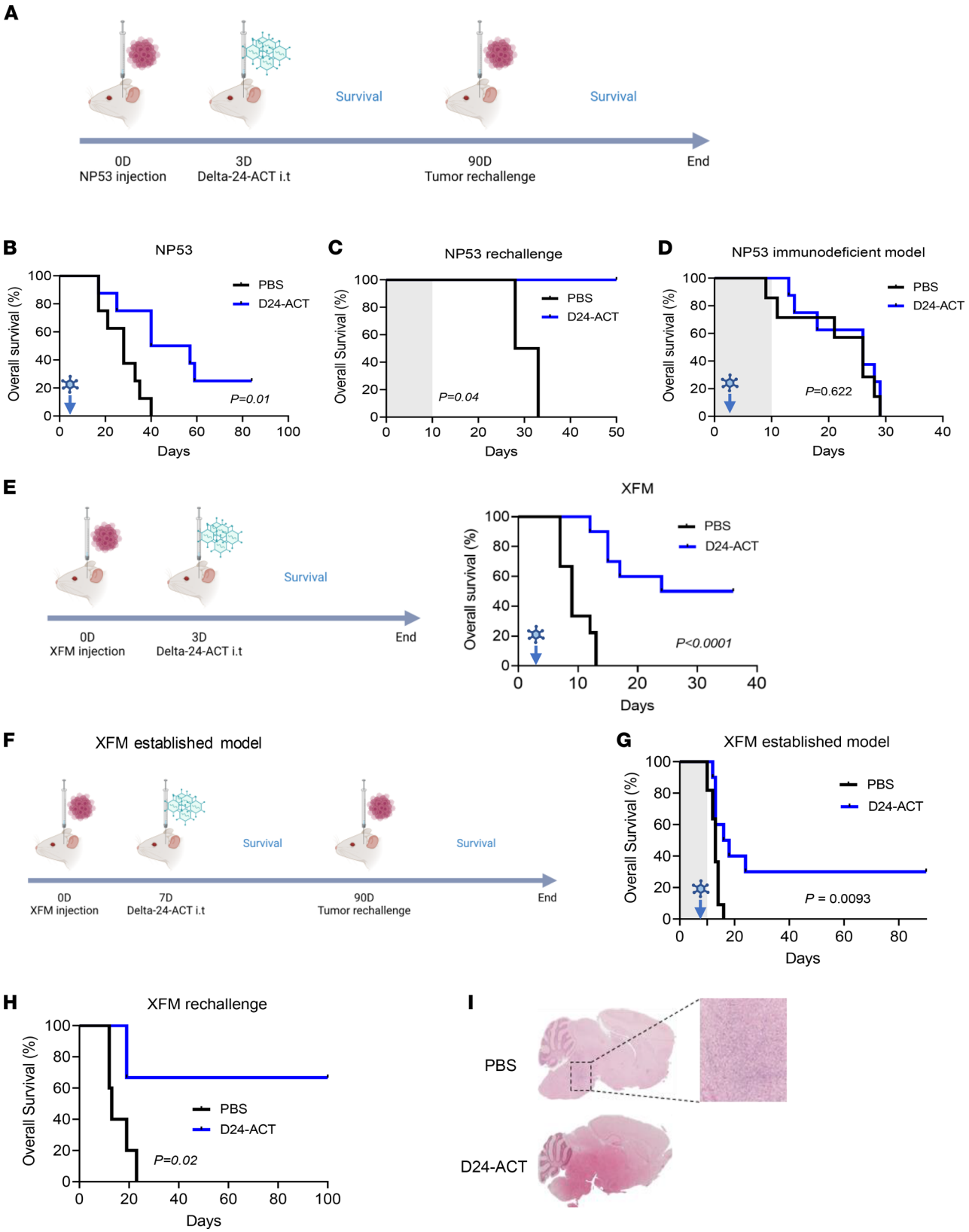

Figure 4. Characterization of the antitumor effect of Delta-24-ACT in DIPG orthotopic models. (**A**) Schedule of survival experiments performed with NP53 cells. (**B**) Kaplan-Meier survival plot of mice bearing NP53 cells treated with 10^6 PFUs of Delta-24-ACT or a mock PBS control 3 days after cell administration (log-rank; $P = 0.01$, $n = 8$ each group). (**C**) The long-term survivors from the Delta-24-ACT–treated group ($n = 2$) were subjected to rechallenge with NP53 and compared with control naive mice ($n = 4$) (log-rank; $P < 0.04$). (**D**) Kaplan-Meier survival plot of immunodeficient mice (BALB/cA-Rag2$^{-/-}\gamma c^{-/-}$) bearing NP53 cells treated with 10^6 PFUs of Delta-24-ACT ($n = 8$) or a mock PBS control ($n = 7$) 3 days after cell administration (log-rank; $P = 0.600$). (**E**) Schedule of survival experiments performed with XFM cells, and Kaplan-Meier survival plot of mice bearing XFM cells that were treated with 10^6 PFUs of

Delta-24-ACT (n = 10) or the mock PBS control 3 days after cell administration (n = 9) (log-rank; $P < 0.0001$). (**F**) Schedule of the survival experiment with the established XFM model; Delta-24-ACT was administered 7 days after cell injection. (**G**) Kaplan-Meier survival plot of mice bearing XFM-established tumors treated with 10^6 PFUs of Delta-24-ACT (n = 10) or a mock PBS control (n = 11) 7 days after cell administration (log-rank; $P = 0.0009$). (**H**) The long-term survivors from the Delta-24-ACT–treated group (n = 3) were subjected to rechallenge with XFM and compared with control naive mice (n = 5) (log-rank; $P = 0.02$). (**I**) Representative micrographs of XFM long-term survivors free of disease versus a naive control (PBS) that presented a tumor. Original magnification, ×4; ×100 (high-magnification image).

We first confirmed that immune cells could infiltrate the tumor, because the labeling was inside the tumor and not in the periphery. Moreover, we observed an increase in T populations in the Delta-24-ACT group, which was significant for Tregs (%$CD8^+$, $P = 0.1067$; $CD4^+$ density, $P = 0.5422$; $Foxp3^+$ density, $P = 0.0419$). We also observed a decrease in the percentages of cells expressing the endothelial cell markers CD31 and F4/80 (which label microglia and macrophages), even though the differences were not significant (Figure 5F and Supplemental Figure 5D). Additionally, examination of long-term survivors from the rechallenge showed animals that were tumor free and lacking any kind of immune infiltration (Supplemental Figure 5E). Finally, we aimed to confirm these results in another DIPG tumor model (XFM), in this case adding Delta-24-RGD. Ten days after viral treatment (Supplemental Figure 5F), tumor-infiltrating lymphocytes (TILs) from XFM tumors were analyzed by flow cytometry. Similar to the results for NP53 tumors, we observed significant increases in the immune infiltrates in the Delta-24-ACT treatment group versus the control group (Supplemental Figure 5G). We observed major differences in the percentage of total immune cells ($CD45^+$); this was due to the increase in the percentage of T lymphocytes, more specifically, to the $CD8^+$ cytotoxic population. Although the proportions of $CD4^+$ cells and Tregs tended to increase, their levels were not significantly different between the groups. We also did not observe any change in the percentage of NK cells between treatment groups (Supplemental Figure 5G). However, we wanted to see if there were differences in proliferation (Ki67 labeling) in the $CD8^+$, $CD4^+$, and NK populations due to the presence of the ligand (when comparing Delta-24-ACT with Delta-24-RGD and the control) (Supplemental Figure 5H). However, $CD8^+$, $CD4^+$, and NK cells present in Delta-24-ACT–treated tumors displayed significantly increased proliferation compared with Delta-24-RGD–treated or control tumors. Finally, we also observed that $CD8^+$ and $CD4^+$ lymphocytes expressed more PD-1 in the presence of Delta-24-ACT (Supplemental Figure 5H).

In order to elucidate whether genetic makeup could lead to differences in the immune infiltrate and, thus, in responses to the virus, we analyzed the basal tumor microenvironment in a spontaneous isogenic system. This murine DIPG model contains *TP53* and *PDGFR* mutations, and they differ in their histone 3 mutational status: H3-WT, H3-K27M, and H3-G34R. We assessed the percentage of different immune populations by flow cytometry in tumors presenting the above genetic mutations. Of importance, our analyses did not reveal significant differences among the 3 groups, except for in B cells and NKT cells, which were slightly higher in H3 WT group (Supplemental Figure 6, A and B). In addition, the tumor presented abundant microglia and macrophages (Supplemental Figure 6, A and B). In the same line, immunohistochemistry analysis of the brains from H3-WT and H3-K27M showed a nearly absent infiltration in both models (Supplemental Figure 7, A and B). Tumor infiltration, thus, was very similar in all genetic subgroups and comparable to that in the NP53 and XFM models.

In summary, altogether these data indicate that Delta-24-ACT can turn "cold" DIPG tumors into "hot" tumors by increasing the numbers of immune cells and their activation states, providing a solid rationale for the further translation of this virus into the clinic.

Discussion

To date, DIPGs remain incurable. In this work, we built upon our previous preclinical and clinical experience with Delta-24-RGD to engineer a virus with superior efficacy. Our clinical studies on adult gliomas and DIPGs illustrate the use of oncolytic viruses and their efficacy in a subgroup of patients (17, 27, 28). Because we previously observed that treatment of DIPG immunocompetent models with the oncolytic virus Delta-24-RGD (15) resulted in increased TILs, strategies aimed at activating these lymphocytes seemed to be the next logical step. Several positive actionable immune checkpoints exist, including 4-1BB, OX40, CD27, and GITR (29). However, the broad spectrum of 4-1BB targets, including not only CD8 T lymphocytes, but also other important populations, such as NK cells (30, 31), prompted us to take advantage of its immune checkpoint ligands. More importantly, a 4-1BB agonist has been shown to exert antitumor effects in not only immunogenic tumor models, but also nonimmunogenic models; this is very

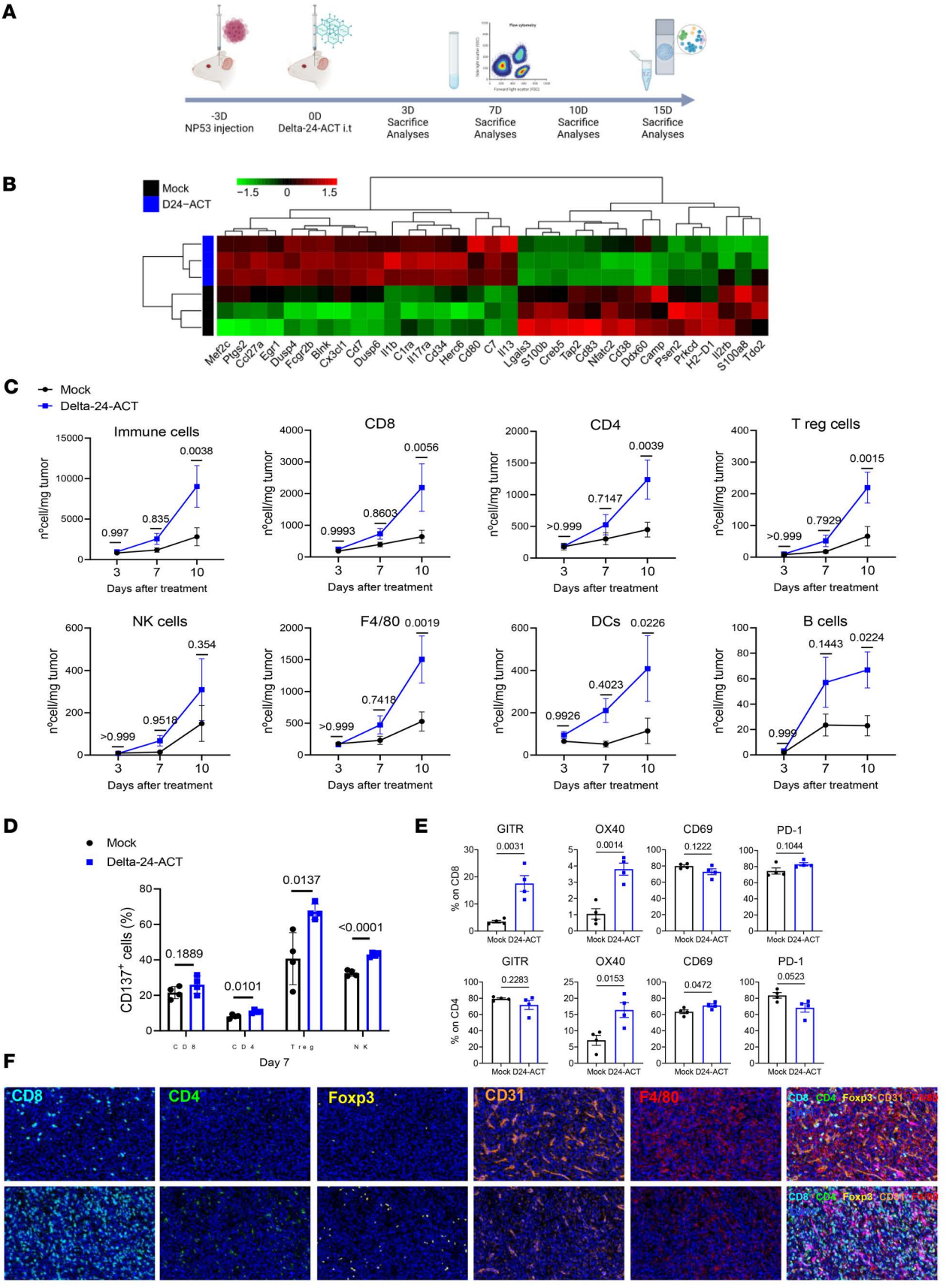
A
-3D
NP53 injection
0D
Delta-24-ACT i.t
3D
Sacrifice
Analyses
7D
Sacrifice
Analyses
10D
Sacrifice
Analyses
15D
Sacrifice
Analyses
B
Mock
D24-ACT
−1.5
0
1.5
Mef2c
Ptgs2
Ccl27a
Egr1
Dusp4
Fcgr2b
Blnk
Cx3cl1
Cd7
Dusp6
Il1b
C1ra
Il17ra
Cd34
Herc6
Cd80
C7
Il13
Lgals3
S100b
Creb5
Tap2
Cd83
Nfatc2
Cd38
Ddx60
Camp
Psen2
Prkcd
H2-D1
Il2rb
S100a8
Tdo2
C
Mock
Delta-24-ACT
Immune cells
CD8
CD4
T reg cells
NK cells
F4/80
DCs
B cells
n°cell/mg tumor
Days after treatment
0.997
0.835
0.0038
0.9993
0.8603
0.0056
>0.999
0.7147
0.0039
>0.999
0.7929
0.0015
>0.999
0.9518
0.354
>0.999
0.7418
0.0019
0.9926
0.4023
0.0226
0.999
0.1443
0.0224
D
Mock
Delta-24-ACT
CD137+ cells (%)
0.1889
0.0101
0.0137
<0.0001
CD8
CD4
Treg
NK
Day 7
E
GITR
OX40
CD69
PD-1
% on CD8
% on CD4
Mock
D24-ACT
0.0031
0.0014
0.1222
0.1044
0.2283
0.0153
0.0472
0.0523
F
Mock
D24-ACT
CD8
CD4
Foxp3
CD31
F4/80

Figure 5. Modulation of the tumor microenvironment by Delta-24-ACT treatment. (**A**) Schedule of mechanistic studies in the NP53 model. NP53 cells were engrafted (day –3), and animals were treated with a mock control or Delta-24-ACT (10^6 PFUs) 3 days later. Animals were sacrificed 3 (3D), 7 (7D) or 10 (10D) days later for flow cytometry and 15 (15D) days later for NanoString and IHC multiplex analyses. (**B**) Representative heatmap of transcriptome profiling using gene set enrichment analysis of murine DIPG tumors from mock-treated and Delta-24-ACT–treated mice (n = 3) using the 770-gene pancancer immunoprofile panel in NanoString. (**C**) Flow cytometry analyses of different immune cell populations in the brains of mice bearing NP53 tumors on the indicated days after treatment with Delta-24-ACT (blue) or PBS (black). Data are shown as number of cells/mg tumor. Two-way ANOVA was performed, and P values are shown above respective bars. (**D**) CD137 expression (percentage) in T cell populations and NK cells 7 days after viral treatment. Multiple comparisons t test was performed (n = 4 each group), and P values are shown above respective bars. Data are shown as the mean ± SEM. (**E**) Flow cytometry analyses of different activation (GITR, OX40, CD69) and exhaustion (PD-1) markers were performed in the $CD8^+$ and $CD4^+$ cell subsets at 7 days after viral administra^{t}ion. Data are shown as the mean ± SEM (n = 4 each group), and P values are shown above respective bars. (**F**) The brains of mice bearing NP53 cells were subjected to multiplexed immunofluorescence analysis to detect the following immune cell markers: CD8 (light blue), CD4 (green), Foxp3 (yellow), CD31 (orange), F4/80 (red), and GFAP (pink). The nuclei were counterstained with DAPI (blue). Representative micrograph are shown (n = 3) Original magnification, ×20.

relevant for DIPGs, because they are nearly devoid of infiltrating lymphocytes and present very few mutations (10–12). One important feature exhibited by 4-1BB agonists in preclinical studies is their capacity to disrupt immunological ignorance (32), which seems very important for tumors such as DIPGs, because their microenvironment is thought to be nonresponsive. In our model, Delta-24-ACT administration led to profound remodeling of the tumor microenvironment, leading to profuse tumor infiltration, which was most likely due to the virus itself and to the presentation of functional T cells due to the 4-1BBL. In fact, preclinical studies on different tumor models showed that 4-1BB agonist treatment resulted in restoration of T cell dysfunctionality in the tumor microenvironment (33) and increased persistence of tumor-specific T cells (34). For example, 4-1BB costimulation further enhanced the anti–PD-1–mediated reinvigoration of exhausted $CD39^+$ $CD8^+$ T cells from the primary and metastatic sites of epithelial ovarian cancers (35). We also observed an increase in Tregs in the NP53 model, probably as a result of the virus treatment, suggesting a potential resistance mechanism to this approach. However, examination of long-term survivors showed no trace of this population. Furthermore, studies will be needed to clarify the role of this cell compartment and the implications for virotherapy. In our study, 4-1BB was efficient at triggering an effective antitumor immune response and, more importantly, at establishing immunological memory. Interestingly, these results were different from those in our study in glioma models, in which this virus was not able to trigger immune memory when long-term survivors were subjected to rechallenge (22). These results suggest a different mechanism of action in DIPG models, which we know present a different microenvironment with less immunosuppression than adult gliomas (10, 11). Unfortunately, although 4-1BB agonists were very effective in preclinical models, clinical trials assessing efficacy were hampered by high toxicity, specifically in the liver (reviewed in ref. 20). However, vectorizing 4-1BBL into a virus could circumvent all the toxicities associated with the systemic administration of 4-1BB agonists while maintaining a safe profile. Supporting this notion, we found no hepatic toxicity. Moreover, an Ankara virus armed with the 4-1BBL as well as tumor-associated antigens, which was administered intratumorally was shown to be effective and safe for eradicating solid tumors (36).

Although oncolytic viruses have been extensively studied in the context of adult brain tumors, there is a paucity of studies that have addressed their suitability and efficacy for pediatric brain tumors and specifically for DIPGs. For example, one study showed that oncolytic herpesvirus 1716 inhibited the migration and invasion of pediatric high-grade glioma and DIPG cells (37); parvovirus H1 also exerted oncolytic effects on these DIPG cell lines in vitro (38). In addition to our study, other preclinical studies have addressed the therapeutic potential of oncolytic viruses; for example, the adenovirus CRAd.S.pK7 showed some degree of antitumor activity when loaded into mesenchymal stem cells (39). We previously demonstrated that Delta-24-RGD was effective at recruiting lymphocytes. More importantly, the virus appeared to be safe and exhibited modest therapeutic efficacy in preclinical models of DIPG (15). Of translational importance, our group began the first human clinical trial for the treatment of naive DIPG with Delta-24-RGD followed by radiotherapy (27). The results of this trial, although not yet published, support the feasibility, safety, and degree of efficacy of this virus in children with this devastating disease (NCT03178032; our unpublished observations). Importantly, another trial evaluating the effect of a virus based on the Delta-24 platform expressing the OX40 ligand for recurrent adult gliomas (DNX-2440; NTC03714334) is currently ongoing at our institution, and 11 patients have thus far been enrolled, with no relevant toxicities.

One limitation of this study is that murine models are not permissive to adenoviral replication (40); consequently, the antitumor effect we observed is hampered by the fact that the virus expresses 4-1BBL

only once due to its inability to replicate in murine cells. Therefore, the effect we observed is somewhat suppressed at the therapeutic and safety levels. Nevertheless, our clinical study of DNX-2440 for recurrent gliomas has shown feasibility and safety, thus far supporting further translation to the clinic.

In summary, we herein provide robust evidence that the intratumoral delivery of Delta-24-ACT is capable of disrupting DIPG microenvironment tolerance by inducing profound proinflammatory changes, leading to the activation of T cells and to the generation of immune memory and, thus, preventing tumor recurrence. The results of this study, along with the excellent safety profile of the Delta-24 platform, provide a strong rationale for exploring this approach in the clinic.

Methods

Further information can be found in Supplemental Methods.

Research design. The objective of this study was to determine the preclinical efficacy of Delta-24-ACT as a therapeutic approach for DIPG. After viral generation, 4-1BBL expression and functionality were assessed by qPCR, Western blotting, immunofluorescence, and flow cytometry assays. Granzyme B and IFN-γ were detected by flow cytometry and ELISA, respectively. MTS and replication assays were used to quantify the antitumor effects of Delta-24-ACT in vitro in DIPG human and murine cell lines. Evaluation of the in vivo antitumor effect and immune response to Delta-24-ACT was performed in immunocompetent mice bearing orthotopic tumors derived from NP53 or XFM murine DIPG cell lines. Histological analysis was performed to assess the localization of both the tumor and virus in vivo and other putative mechanisms involved in responses to viruses. All in vivo experiments were repeated at least 2 times unless mentioned otherwise. Immunophenotyping of the tumor microenvironment was performed via immunohistochemistry, multiplexed immunohistochemistry, and flow cytometry assays.

Cell lines. The murine NP53 and XFM cell lines were provided in-house. Both cell lines were obtained from DIPG tumors generated in genetically modified mice. NP53 cells were generated from a DIPG tumor driven by *PDGF-β* signaling, *p53* loss, and an *H3.3K27M* mutation (41), whereas XFM cells were generated from a tumor induced by PDGF-β signaling and *INK4A* and *ARF* loss (42). Both cell lines were maintained in DMEM supplemented with 10% fetal bovine serum and 1% antibiotics (streptomycin, penicillin).

The SU-DIPG IV cell line was provided by Michelle Monje (Standford University, Standford, California, USA), and TP54 was provided by Marie-Pierre Junier and Hervé Chneiweiss (INSERM Institute, Paris, France). Both human cell lines were maintained as neurospheres in serum-free specialized media. TP54 cells were cultured in medium supplemented with a human neural stem cell proliferation supplement (NeuroCult NS-A Proliferation Kit, 05751, STEMCELL Technologies) and basic fibroblast growth factor and epidermal growth factor (20 ng/mL; MilliporeSigma), while SU-DIPG IV cells were cultured in DMEM/F12 supplemented with B27 (17504-044, Gibco), heparin, and basic fibroblast growth factor and epidermal growth factor (20 ng/mL). The HEK293 (CRL-1573, ATCC) and A549 (CCL-185, ATCC) cell lines were used for viral construction. All cell lines were maintained in a humidified atmosphere at 37°C and 5% CO_2.

Delta-24-ACT construction. Delta-24-ACT was constructed by maintaining the Delta-24-RGD modifications of a 24–base pair deletion and introduction of RGD; however, *m4-1BBL* was incorporated in the E3 locus after removing this gene. Briefly, murine *4-1BBL* was first cloned into a pCDNA3.1 plasmid using the *KpnI* and *XhoI* restriction enzymes (New England Biolabs). Then, *m4-1BBL*, flanked with the cytomegalovirus promoter and bovine growth hormone polyadenylation sequences, was subcloned into the pAB26-RGD plasmid (24) at the *ClaI*/*BamHI* site. Finally, the 4-1BBL expression cassette was introduced into pVK-500C-24, and the Delta-24 plasmid was constructed by homologous recombination with pAB26-m4-1BBL in BJ5183 bacteria. For viral rescue, the obtained plasmid was linearized with *Pac I* and transfected into HEK293 cells with Lipofectamine 2000 (Invitrogen). After confirmation of genetic modifications by PCR and sequencing, Delta-24-ACT was amplified in A549 cells, purified, and stored at –80°C.

Immunoblotting. Cell lysates were obtained by treating the samples with lysis buffer (1X PBS + 1% Triton X-100) together with a protease inhibitor for 30 minutes on ice and centrifuging for 20 minutes at 4°C. The protein amount was assessed using a Bradford colorimetric assay, and 30 μg protein was subjected to sodium dodecyl sulfate-tris-glycine gel electrophoresis and then transferred to nitrocellulose membranes, which were incubated with the following antibodies: E1A (1:1000, Sc-430, Santa Cruz Biotechnology), adenovirus fiber (1:1000, NB600-541, Novus Biologicals), 4-1BBL (1:1000, AF1246, R&D Systems), and GRB2 (1:1000, 610112, BD). Finally, the membranes were developed according to the Amersham enhanced chemiluminescence protocol.

Table 1. Antibodies used for flow cytometry analyses

Antibody	Clone	Dilution	Company	Catalog no.
CD4 FITC	RM4-5	1:800	Biolegend	100510
CD4 BUV496	GK1.5	1:200	Biolegend	612952
CD8a BV510	53-6.7	1:400	Biolegend	100752
CD11b BV510	M1/70	1:400	Biolegend	101263
CD11c PECy7	N418	1:160	Biolegend	117318
CD19 BV421	6D5	1:400	Biolegend	115538
CD45 APC/Fire750	30-F11	1:400	Biolegend	103154
CD69 PECy7	H1.2F3	1:100	Biolegend	104511
CD134 (OX40) PE	OX-86	1:200	Biolegend	119409
CD137 (4-1BB) PE	17B5	1:200	Biolegend	106105
F4/80 APC	BM8	1:200	Biolegend	123116
FOXP3 PE-eFluor610	FJK-16s	1:100	Invitrogen	61-5773-82
GITR PerCP/Cy5.5	DTA-1	1:200	Biolegend	126316
Granzyme B PeCy7	NGZB	1:80	Thermo Fisher Scientific	25-8898-80
IA/IE BV605	M5/114.15.2	1:300	Biolegend	107641
Ki67 FITC	11F6	1:100	Biolegend	151204
Ly6C FITC	HK1.4	1:400	Biolegend	128006
Ly6G PerCP/Cy5.5	1A8	1:400	Biolegend	127616
NK1.1 BV605	PK136	1:100	Biolegend	108710
NKp46 BV605	29A1.4	1:100	Biolegend	137619
PD-1 BV421	29F.1A12	1:160	Biolegend	135218
TCRb BV785	H57-597	1:100	Biolegend	109249

APC, antigen-presenting cell.

NanoString gene expression analysis. RNA was isolated from FFPE tumor sections by dewaxing using deparaffinization solution (QIAGEN). Total RNA was extracted using the RecoverAll Total Nucleic Acid Isolation Kit (Ambion) according to the manufacturer's instructions. RNA purity was assessed on an ND NanoDrop 1000 spectrometer (Thermo Fisher Scientific). For the NanoString platform, 100 ng RNA was used to detect immune gene expression using the nCounterPanCancer Immune Profiling Panel along with custom CodeSet. Counts of the reporter probes were tabulated for each sample by the nCounter Digital Analyzer, and the raw data output was imported into R/Bioconductor (43). First, gene expression data were normalized with the NACHO (44) R package. After quality assessment and outlier detection using R/Bioconductor, a filtering process was performed. Genes without read counts in more than 50% of the samples of all the studied conditions were considered not expressed in the experiment under study. LIMMA (Linear Models for Microarray Data) (45) was used to identify the genes with significant differential expression between experimental conditions. Genes were selected as differentially expressed using a P value cutoff of $P < 0.01$. Further functional and clustering analyses were performed and graphical representations were generated using clusterProfiler (46) and R/Bioconductor. The nanostring data from this study have been submitted to the Gene Expression Omnibus under accession GSE197374.

Flow cytometry. For 4-1BBL expression analysis, 1.5×10^4 cells/well were infected with Delta-24-ACT (MOIs of 25 and 50 for murine cells and 5 and 10 for human cells) and harvested 48 hours later for staining with a PE-coupled anti-4-1BBL antibody (1:200, 107105, Biolegend). Dead cells were removed by Zombie NIR staining (1:1000, 423105, Biolegend), and the remaining samples were then analyzed using the FACSCanto II system (BD Biosciences).

For TIL analysis, brains were collected, and tumor samples were disaggregated to obtain a cell suspension. Briefly, the tumor samples were disaggregated mechanically and then chemically with collagenase and DNase I before being passed through a 40 μm cell strainer. Finally, the obtained suspension was subjected to 30% Percoll treatment to obtain TILs. Cell suspensions were incubated with 100 μL of the antibodies resuspended in PBS 1X + 0.5% FBS + 0.5% EDTA. The antibodies used are listed in Table 1. Dead cells were removed by PromoFluor-840 staining (1:10,000, PK-PF840-3-01, PromoCell), and the remaining samples were then analyzed using CytoFLEX (Beckman Coulter) and FACSDiva software (BD Biosciences).

Immunofluorescence. NP53 and XFM cells (5×10^5) were seeded on glass slides and infected with Delta-24-ACT at an MOI of 50 for 24 hours (1 group was not infected as a control). Forty-eight hours after infection, the cells were fixed with 4% formaldehyde/methanol-free (28906, Thermo Fisher Scientific) and blocked for 1 hour at room temperature (S0809, Dako). Finally, the cells were stained with a PE-coupled anti-4-1BBL antibody (1:200, 107105, Biolegend) for 2 hours at room temperature, and the nuclei were stained with DAPI.

Immunohistochemical analysis. Paraffin-embedded mouse brain sections were first stained with hematoxylin and eosin for tumor analysis. Once tumor status was confirmed, the remaining staining experiments were performed with antibodies against adenovirus rabbit E1A (1:1000; Santa Cruz Biotechnology), CD3 (1:300; clone SP7, NeoMarkers), CD4 (1:1000; EPR19514, ab183685, Abcam), CD8α (1:1000, [D4W2Z], 98941, Cell Signaling), and FoxP3 (1:400; clone JFK-16s, ref 14–5773, eBiosciences, Thermo Fisher Scientific). For immunohistochemical staining, Vectastain ABC kits (Vector Laboratories Inc.) were used according to the manufacturer's instructions. The number of positively stained cells per mm^2 was quantified using the Fiji platform.

Multiplexed immunofluorescence. A multiplex immunolabeling protocol based on tyramide signal amplification (TSA) and Opal fluorophores was developed and validated as previously described (47). Briefly, paraffin-embedded sections of mouse brains were deparaffinized, hydrated, and treated with peroxidase. Then, each section was subjected to sequential rounds of antibody staining, each including heat-induced antigen retrieval at pH 6 and protein blocking with 20% normal goat serum (Dako) in PBS. Finally, the sections were incubated with a primary antibody and secondary antibody HRP conjugate (Dako), followed by TSA visualization with fluorophores Opal 520, Opal 540, Opal 570, Opal 620, Opal 650, and Opal 690 (Akoya Biosciences).

The primary antibodies included CD8 (rabbit monoclonal, 98941, 1:500, Cell Signaling Technology), CD4 (rabbit monoclonal, 25229, 1:400, Cell Signaling Technology), CD31 (rabbit monoclonal, 77699, 1:400, Cell Signaling Technology), FOXP3 (rabbit monoclonal, 12653, 1:600, Cell Signaling Technology), GFAP (rabbit monoclonal, 80788, 1:100, Cell Signaling Technology), and F4/80 (rabbit monoclonal, 70076, 1:400, Cell Signaling Technology). After 6 sequential reactions, nuclei were counterstained with spectral DAPI (Akoya Biosciences), and sections were mounted with Diamond antifade mountant (Life Technologies).

Multiplexed immunofluorescence slides were scanned on a Vectra-Polaris Automated Quantitative Pathology Imaging System (Akoya Biosciences) as previously described (47, 48). The whole tissue present in a single FFPE tissue section was imaged, spectrally unmixed, and exported as a component TIF image tile using Akoya Biosciences Inform software (version 2.4.8). Component TIF image tiles were then imported into the open source digital pathology software QuPath version 0.2.0-m9 and stitched together using the *x-y* coordinates to create a new pyramidal TIF file.

Assessment of $CD8^+$ lymphocyte activation. $CD8^+$ cells from B6. CgThy1a-Tg(TcraTcrb)Rest/J (PMEL) mice were isolated with a $CD8a^+$ T cell isolation kit (130-104-075, Miltenyi Biotec) according to the manufacturer's instructions and seeded with CD3 (clone 145-2C11, 100314 Biolegend) and CD28 (clone 37.51, 102112 Biolegend) antibodies for 24 hours. NP53 cells were infected with Delta-24-RGD, Delta-24-ACT, or a mock control at an MOI of 100 for 48 hours and then incubated with 1 μg/mL hgp100 (RP20344, GenScript) for 2 hours (mock NP53 and NP53-ACT cells without hgp100 served as controls). Finally, $CD8^+$ cells and target cells were cocultured for 48 hours, and the cells and supernatants were then collected. IFN-γ expression was analyzed in the supernatants using a mouse IFN-γ DuoSet ELISA kit (DY485, R&D Systems) according to the manufacturer's instructions. Cells were stained with the intracellular granzyme-B antibody (25-8898-80, Thermo Fisher Scientific) for flow cytometry assessment.

Animal studies. 10^4 NP53 cells were injected into the pons of transgenic mice provided in-house, and 10^3 XFM cells were injected into the pons of female BALB/c mice using a screw-guided system (26). Three days after cell injection, 2 μL PBS or Delta-24-ACT (10^6 PFUs/mouse) was administered intratumorally. Animals that showed obvious symptoms of disease were sacrificed, and survival curves were plotted according to the Kaplan-Meier method.

Serum biochemistry. We obtained serum samples from NP53-bearing mice 3 days after Delta-24-ACT administration (or PBS in the control group), and serum transaminase, ALP, bilirubin, and albumin levels were measured using a Cobas C311 Autoanalyzer (Roche).

Statistics. The in vitro experiments were repeated at least 3 times. Dose-response curves for viral cytotoxicity were obtained by nonlinear regression. Data with normal distributions were assessed by

Shapiro-Wilk tests, and comparisons among groups were performed with 2-tailed nonparametric tests with 95% CIs for nonnormally distributed data sets or parametric tests when normality was confirmed (2-tailed Student's *t* test or 1- or 2-way ANOVA). For the comparison of groups in survival experiments, a log-rank test (Mantel-Cox) was used. GraphPad Prism 8 (Statistical Software for Sciences) was used for the statistical analyses. *P* values less than 0.05 were considered significant.

Study approval. Ethical approval for the animal studies was granted by the Animal Ethical Committee of the University of Navarra under protocol 094-15. All animal studies were performed at the veterinary facilities of the Center for Applied Medical Research in accordance with institutional, regional, and national laws and ethical guidelines for experimental animal care.

Author contributions

VL, MMA, JF, and CGM conceived and designed this study. VL, MP, SL, LM, MGM, MZ, MGH, NMV, IAM, DDLN, GHC, JMS, EG, CEDA, MV, OB, MS, VM, JGPL, APG, SG, CGM, JF, and MMA developed methodology; acquired data (provided animals, acquired and managed patients, provided facilities, etc.); analyzed and interpreted the data (e.g., statistical analysis, biostatistics, and computational analysis); wrote, reviewed, and/or revised the manuscript; and provided administrative, technical, or material support (i.e., reporting or organizing data and constructing databases). MMA, JF, and CGM supervised the study.

Acknowledgments

The performed work was supported by the Departamento de Salud del Gobierno de Navarra (54/2018-APG); a Predoctoral Fellowship from Gobierno de Navarra (to VL and GHC); Instituto de Salud Carlos III y Fondos Feder (PI19/01896 MMA, PI18/00164, to APG); Amigos de la Universidad de Navarra (to MP); Fundación La Caixa/Caja Navarra (to APG and MMA); Fundación El sueño de Vicky, Asociación Pablo Ugarte-FuerzaJulen, Fundación ADEY, and Fundación ACS (to APG and MMA); a Department of Defense Team Science Award undergrant (CA 160525, to MMA, CGM, and JF); AECC/ERA-PermedGAL20732 (to JGPL), and La Marató (to MMA). This project also received funding from the European Research Council under the European Union's Horizon 2020 Research and Innovation Programme (817884 ViroPedTher to MMA) as well as the Chance for Life foundation (to SG).

Address correspondence to: Marta M. Alonso, Lab 2.03 CIMA Building, Pio XII, 55 31008 Pamplona, Navarra, Spain; Phone: 34.948194700 ext. 812026; Email: mmalonso@unav.es.

1. Cooney T, et al. Contemporary survival endpoints: an international diffuse intrinsic pontine glioma registry study. *Neuro Oncol*. 2017;19(9):1279–1280.
2. Hoffman LM, et al. Clinical, radiologic, pathologic, and molecular characteristics of long-term survivors of diffuse intrinsic pontine glioma (DIPG): a collaborative report from the International and European Society for pediatric oncology DIPG registries. *J Clin Oncol*. 2017;36(19):1963–1972.
3. Grasso CS, et al. Functionally defined therapeutic targets in diffuse intrinsic pontine glioma. *Nat Med*. 2015;21(6):555–559.
4. Lowe BR, et al. Histone H3 mutations: an updated view of their role in chromatin deregulation and cancer. *Cancers (Basel)*. 2019;11(5):660.
5. Hoeman CM, et al. ACVR1 R206H cooperates with H3.1K27M in promoting diffuse intrinsic pontine glioma pathogenesis. *Nat Commun*. 2019;10(1):1023.
6. Cordero FJ, et al. Histone H3.3K27M represses p16 to accelerate gliomagenesis in a murine model of DIPG. *Mol Cancer Res*. 2017;15(9):1243–1254.
7. Panditharatna E, et al. Clinicopathology of diffuse intrinsic pontine glioma and its redefined genomic and epigenomic landscape. *Cancer Genet*. 2015;208(7–8):367–373.
8. El-Khouly FE, et al. Diagnostics and treatment of diffuse intrinsic pontine glioma: where do we stand? *J Neurooncol*. 2019;145(1):177–184.
9. Vanan MI, Eisenstat DD. DIPG in children — what can we learn from the past? *Front Oncol*. 2015;5:237.
10. Lieberman NAP, et al. Characterization of the immune microenvironment of diffuse intrinsic pontine glioma: implications for development of immunotherapy. *Neuro Oncol*. 2019;21(1):83–94.
11. Lin GL, et al. Non-inflammatory tumor microenvironment of diffuse intrinsic pontine glioma. *Acta Neuropathol Commun*. 2018;6(1):51.
12. Ross JL, et al. Platelet-derived growth factor beta is a potent inflammatory driver in paediatric high-grade glioma. *Brain*. 2021;144(1):53–69.
13. Chen DS, Mellman I. Elements of cancer immunity and the cancer-immune set point. *Nature*. 2017;541(7637):321–330.
14. Bommareddy PK, et al. Integrating oncolytic viruses in combination cancer immunotherapy. *Nat Rev Immunol*. 2018;18(8):498–513.
15. Martínez-Vélez N, et al. The oncolytic virus Delta-24-RGD elicits an antitumor effect in pediatric glioma and DIPG mouse

models. *Nat Commun*. 2019;10(1):2235.
16. Martinez-Velez N, et al. Delta-24-RGD combined with radiotherapy exerts a potent antitumor effect in diffuse intrinsic pontine glioma and pediatric high grade glioma models. *Acta Neuropathol Commun*. 2019;7(1):64.
17. Lang FF, et al. Phase I study of DNX-2401 (Delta-24-RGD) oncolytic adenovirus: replication and immunotherapeutic effects in recurrent malignant glioma. *J Clin Oncol*. 2018;36(14):1419–1427.
18. Wang C, et al. Immune regulation by 4-1BB and 4-1BBL: complexities and challenges. *Immunol Rev*. 2009;229(1):192–215.
19. Croft M. Co-stimulatory members of the TNFR family: keys to effective T-cell immunity? *Nat Rev Immunol*. 2003;3(8):609–620.
20. Chester C, et al. Immunotherapy targeting 4-1BB: mechanistic rationale, clinical results, and future strategies. *Blood*. 2018;131(1):49–57.
21. Yonezawa A, et al. Boosting cancer immunotherapy with anti-CD137 antibody therapy. *Clin Cancer Res*. 2015;21(14):3113–3120.
22. Puigdelloses M, et al. CD137 and PD-L1 targeting with immunovirotherapy induces a potent and durable antitumor immune response in glioblastoma models. *J Immunother Cancer*. 2021;9(7):e002644.
23. Fueyo J, et al. A mutant oncolytic adenovirus targeting the Rb pathway produces anti-glioma effect in vivo. *Oncogene*. 2000;19(1):2–12.
24. Fueyo J, et al. Preclinical characterization of the antiglioma activity of a tropism-enhanced adenovirus targeted to the retinoblastoma pathway. *J Natl Cancer Inst*. 2003;95(9):652–660.
25. Fucikova J, et al. Detection of immunogenic cell death and its relevance for cancer therapy. *Cell Death Dis*. 2020;11(11):1013.
26. Obeid M, et al. Calreticulin exposure dictates the immunogenicity of cancer cell death. *Nat Med*. 2007;13(1):54–61.
27. Marigil M, et al. Development of a DIPG orthotopic model in mice using an implantable guide-screw system. *PLoS One*. 2017;12(1):e0170501.
28. Tejada S, et al. Phase I trial of DNX-2401 for diffuse intrinsic pontine glioma newly diagnosed in pediatric patients. *Neurosurgery*. 2017;83(5):1050–1056.
29. Tejada S, et al. DNX-2401, an oncolytic virus, for the treatment of newly diagnosed diffuse intrinsic pontine gliomas: a case report. *Front Oncol*. 2018;8:61.
30. Mellman I, et al. Cancer immunotherapy comes of age. *Nature*. 2011;480(7378):480–489.
31. Morvan MG, Lanier LL. NK cells and cancer: you can teach innate cells new tricks. *Nat Rev Cancer*. 2016;16(1):7–19.
32. Chiossone L, et al. Natural killer cells and other innate lymphoid cells in cancer. *Nat Rev Immunol*. 2018; 18(11):671–688.
33. Wilcox RA, et al. Provision of antigen and CD137 signaling breaks immunological ignorance, promoting regression of poorly immunogenic tumors. *J Clin Invest*. 2002;109(5):651–659.
34. Williams JB, et al. The EGR2 targets LAG-3 and 4-1BB describe and regulate dysfunctional antigen-specific CD8+ T cells in the tumor microenvironment. *J Exp Med*. 2017;214(2):381–400.
35. Weigelin B, et al. Focusing and sustaining the antitumor CTL effector killer response by agonist anti-CD137 mAb. *Proc Natl Acad Sci U S A*. 2015;112(24):7551–7556.
36. Leem G, et al. 4-1BB co-stimulation further enhances anti-PD-1-mediated reinvigoration of exhausted CD39^{+} CD8 T cells from primary and metastatic sites of epithelial ovarian cancers. *J Immunother Cancer*. 2020;8(2):e001650.
37. Hinterberger M, et al. Intratumoral virotherapy with 4-1BBL armed modified vaccinia Ankara eradicates solid tumors and promotes protective immune memory. *J Immunother Cancer*. 2021;9(2):e001586.
38. Cockle JV, et al. Oncolytic herpes simplex virus inhibits pediatric brain tumor migration and invasion. *Mol Ther Oncolytics*. 2017;5:75–86.
39. Josupeit R, et al. Pediatric and adult high-grade glioma stem cell culture models are permissive to lytic infection with parvovirus H-1. *Viruses*. 2016;8(5):138.
40. Chastkofsky MI, et al. Mesenchymal stem cells successfully deliver oncolytic virotherapy to diffuse intrinsic pontine glioma. *Clin Cancer Res*. 2020;27(6):1766–1777.
41. Halvorson KG, et al. A high-throughput in vitro drug screen in a genetically engineered mouse model of diffuse intrinsic pontine glioma identifies BMS–754807 as a promising therapeutic agent. *PLoS One*. 2015;10(3):e0118926.
42. Barton KL, et al. PD-0332991, a CDK4/6 inhibitor, significantly prolongs survival in a genetically engineered mouse model of brainstem glioma. *PLoS One*. 2013;8(10):e77639.
43. Gentleman RC, et al. Bioconductor: open software development for computational biology and bioinformatics. *Genome Biol*. 2004;5(10):R80.
44. Canouil M, et al. NACHO: an R package for quality control of NanoString nCounter data. *Bioinformatics*. 2020;36(3):970–971.
45. Ritchie ME, et al. limma powers differential expression analyses for RNA-sequencing and microarray studies. *Nucleic Acids Res*. 2015;43(7):e47.
46. Yu G, et al. clusterProfiler: an R package for comparing biological themes among gene clusters. *OMICS*. 2012;16(5):284–287.
47. Abengozar-Muela M, et al. Diverse immune environments in human lung tuberculosis granulomas assessed by quantitative multiplexed immunofluorescence. *Mod Pathol*. 2020;33(12):2507–2519.
48. Martinez-Valbuena I, et al. Amylin as a potential link between type 2 diabetes and Alzheimer disease. *Ann Neurol*. 2019;86(4):539–551.

Supplementary Materials:

Supplementary material and methods

Cell viability assay

All the cell lines were seeded in 96-well plates (NP53 and XFM at a density of 500 cell/well and SU-DIPG IV and TP54 at $1x10^4$ cell/well). Then, the cells were infected with Delta-24-ACT at MOIs ranging from 5 to 100. Five days after infection, cell viability was assessed using the CellTiter 96® Aqueous One Solution Cell Proliferation Assay (Promega, Fitchburg, WI, USA; G3581) as previously described *(46)*. Viability curves were analyzed using GraphPad Prism 8 (Statistical Software for Sciences) to determine the IC_{50} values of Delta-24-ACT in the tested cell lines (IC_{50} is the viral dose at which 50% of cells are affected, i.e., 50% survival).

qRT-PCR

RNA was extracted with TRIzol at 48 h after cell infection ($1.5x10^4$ cells/well) with Delta-24-ACT at MOIs of 50 and 100. Then, cDNA was obtained from 1 µg of RNA by RT-PCR, and gene expression was analyzed by real-time PCR using Fast SYBR Green PCR Master Mix (Applied Biosystems).The specific primers were as follows:

4-1BBL Fw: 5´CTGTGTTCGCCAAGCTACTG3´ and Rv: 5´GGGACTGTCTACCACCAACT3´; $GAPDH_{mouse}$Fw: 5´GGGAAATTCAACGGCACAGT3´ and Rv: 5´AGATGGTGATGGGCTTCCC3´; and $GAPDH_{human}$Fw: 5´AGCCACATCGCTCAGACAC3´ and Rv: 5´GCCCAATACGACCAAATCC3´.

Measurement of DAMPs

Each cell line was plated at a density of $2x10^5$ cells per well (six-well plates) and was infected with Delta-24-ACT at its corresponding three-day IC_{50}. At 72 h later, the concentrations of the DAMP markers—HMGB1 (ST51011; IBL International), and ATP (ENLITEN® ATP Assay System; FF2000; Promega)—were measured in supernatants of infected and mock-infected cultures.

Immunoblotting

Cell lysates were obtained by treating the samples with lysis buffer (PBS 1X + 1% Triton X-100) together with a protease inhibitor for 30 minutes on ice and centrifuging for 20 minutes at 4°C. The protein amount was assessed using a Bradford colorimetric assay (BCA), and 30 μg of protein were subjected to sodium dodecyl sulfate-tris-glycine gel electrophoresis and then transferred to nitrocellulose membranes, which were incubated with the following antibodies: E1A (1:1000, Sc-430 Santa Cruz Biotechnology), fiber (1:1000, NB600-541 Novus Biologicals), 4-1BBL (1:1000, AF1246 R&D Systems) and GRB2 (1:1000, 610112 BD). Finally, the membranes were developed according to the Amersham enhanced chemiluminescence protocol.

Mice for the isogenic system

All injections were performed in mouse pups aged 0–2 days old among equally distributed sexes for each genotype. *Ntva*;*Ptenfl*/*fl*;*Cdkn2a*−/−mice are in a mixed genetic background while *Ntva*;*Ptenfl*/*fl* mice are in a pure C57BL/6 background (Herting *et al.*, 2017). Mice were housed in a climate-controlled, pathogen-free facility with access to food and water *ad libitum* under a 12-h light/dark cycle. *Ccl2* (#004434) and *Ccl7* (#017638) knockout mice were obtained from the Jackson Laboratory and crossed to C57BL/6 *Ntva*;*Ptenfl*/*fl* mice until homozygous knockout mice were obtained as previously described for the generation of *Ntva*;*Ptenfl*/*fl*;*Ccl2*−/− mice (Tsou *et al.*, 2007;

Chen *et al.*, 2017). *Ccl3* knockout mice were gifted by Dr C. K. Qu, *Ccl8/12*−/− mice were gifted by Dr Sabina Islam, and both were crossed with C57BL/6 *Ntva;Ptenfl/fl* mice until homozygous knockout mice were obtained. Genotyping of all mice was performed using Transnetyx. All experimental procedures were approved by the Institutional Animal Care and Use Committee of Emory University (Protocol #2003253, #201700633) and Icahn School of Medicine at Mount Sinai (Protocol #201900619).

Cell culture and mice injections

DF1 cells (ATCC) were grown at 39°C, expanded to passage 4 and transfected with RCAS-PDGFB-HA, RCAS-shp53-RFP, RCAS-H3.3WT, RCAS-H3.G34R or RCAS-H3.3K27M using a FuGENE® 6 Transfection kit FuGENE 6 Transfection reagent (Promega, Cat. E2691), accordingly to manufacturer's protocol. Cells were cultured with DMEM media (Gibco, 11995-065) supplemented with 1× l-glutamine, 1× penicillin/streptomycin, and 10% fetal bovine serum (FBS) (ATCC). Media containing $2x10^5$ DF1 cells transfected with the different construction was injected in the IV ventricle of 0-2 days old *GFAP-Tva; GFAP-Cre; Rosa26-LSL-Cas9; p53lox/lox* mice using a 30-gauge needle attached to a Hamilton gas-tight syringe (Fisher Scientific,#14-815-250). Mice were closely monitored for signs of tumor development and sacrificed when reaching humane end-point. At this time point, mouse brains were extracted for further analysis.

Immunephenotyping of the isogenic tumors by flow cytometry

After sacrificing, mice were perfused with ice-cold PBS and whole brains obtained for processing. Tumors were digested mechanically and enzymatically with 0.4 mg/ml collagenase (R8757, Merck) and DNAseA (10104159001, Roche) in RPMI + 10% FBS. Erythrocytes were lysed in presence of RBC lysis buffer (00-4333-57, Labclinics) for 2

minutes at room temperature. Then, samples underwent 22% Percoll (17-0891-01, GE Healthcare) gradient separation to obtain TILs.

Cell suspensions were first stained with LIVE/DEAD Fixable Blue Dead Cell Stain (L34962, Life technologies) to differentiate non-viable cells, and then with 100 µl of the antibody mix. The used antibodies are listed in the table below (table 2). For FOXP3 staining cells were fixed in True-Nuclear™ fix reagent (424401, Biolegend) and then permeabilized with True-Nuclear™ permeabilization buffer (424401, Biolegend). Data was acquired using a LRS Fortessa cytometer.

Table 2. List of the antibodies used for the flow cytometry experiment.

ANTIBODY	CLONE	DILUTION	COMPANY	REFERENCE
CD45 PECy7	30-F11	1:400	Invitrogen	25-0451-82
CD3 APC	145-2C11	1:100	BD Pharmingen	553066
NK1.1 BV711	PK136	1:100	Biolegend	108745
B220 BUV661	RA3-6B2	1:100	BD Biosciences	612972
CD11b PerCP-Cy5.5	M1/70	1:100	Invitrogen	45-0112-82
F4/80 APC/Fire750	BM8	1:50	Biolegend	123152
CD204 PE	M204PA	1:200	Invitrogen	12-2046-82
CD4 BV510	RM4-5	1:200	BD Biosciences	563106
CD8 FITC	53-6.7	1:400	Tonbo Biosciences	35-0081
CD25 PerCP-Cy5.5	PC61	1:100	Biolegend	102030
FOXP3 PE	MF-14	1:40	Biolegend	126404

Supplementary Figures:

Supp_ Figure 1

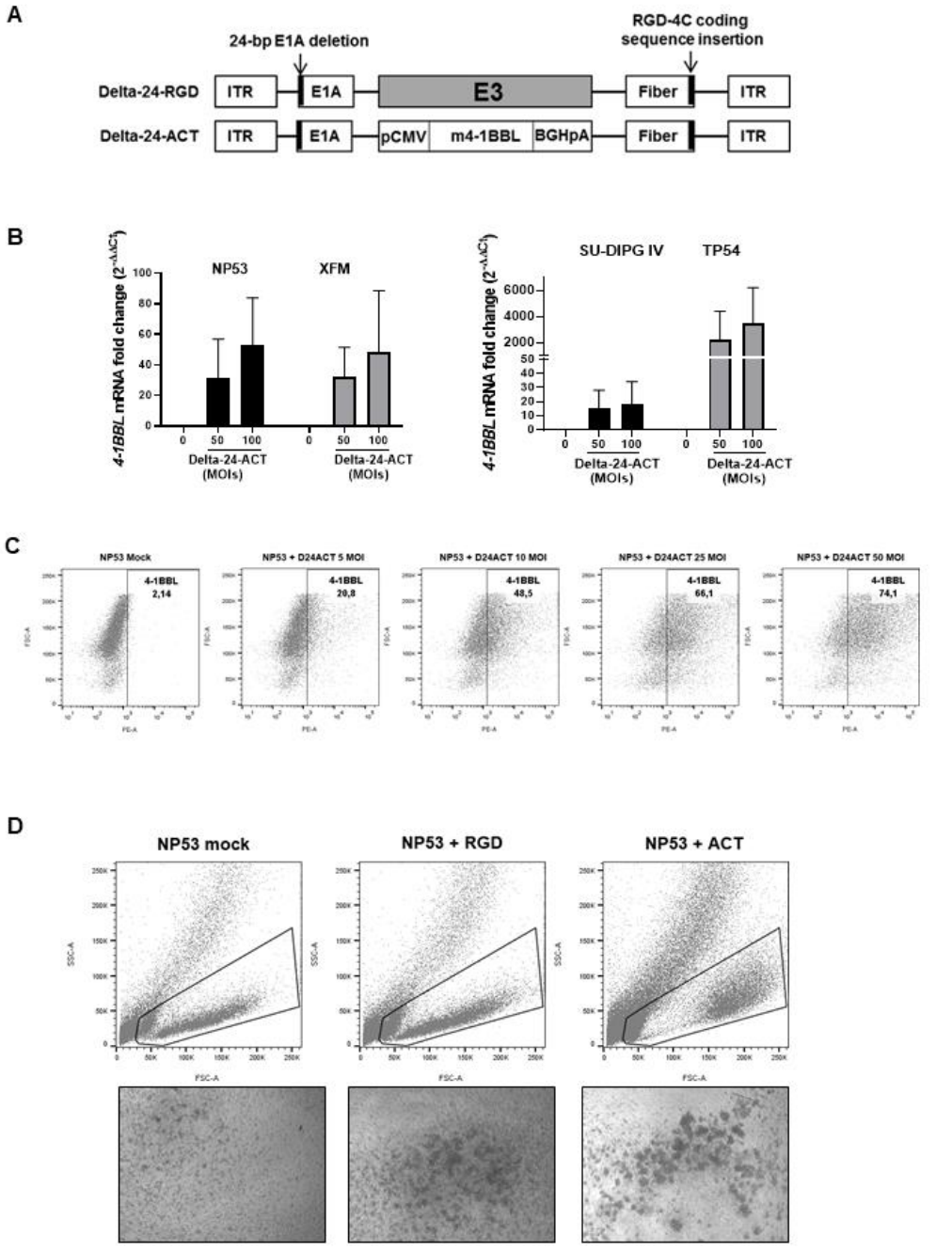

Supplementary figure 1. The 4-1BBL expression in DIPG cells after Delta-24-ACT infection. (A) Schematic representation of the engineered Delta-24-ACT. **(B)** The m4-1BBL expression as determined by qPCR in NP53 and XFM murine cell lines and SU-DIPG IV and TP54 human cell lines after Delta-24-ACT infection at the indicated MOIs. **(C)** Representative images showing the 4-1BBL expression in the membranes of NP53 cells infected with Delta-24-ACT at different MOIs for 48 h as determined by flow cytometry. **(D)** ***Upper panel,*** representative flow cytometry image of $CD8^+$ lymphocytes cocultured with NP53 and NP53 cells infected with Delta-24-RGD or Delta-24-ACT (100 MOI). ***Lower panel,*** representative images of $CD8^+$ clusters acquired on an inverted microscope.

Supp_ Figure 2

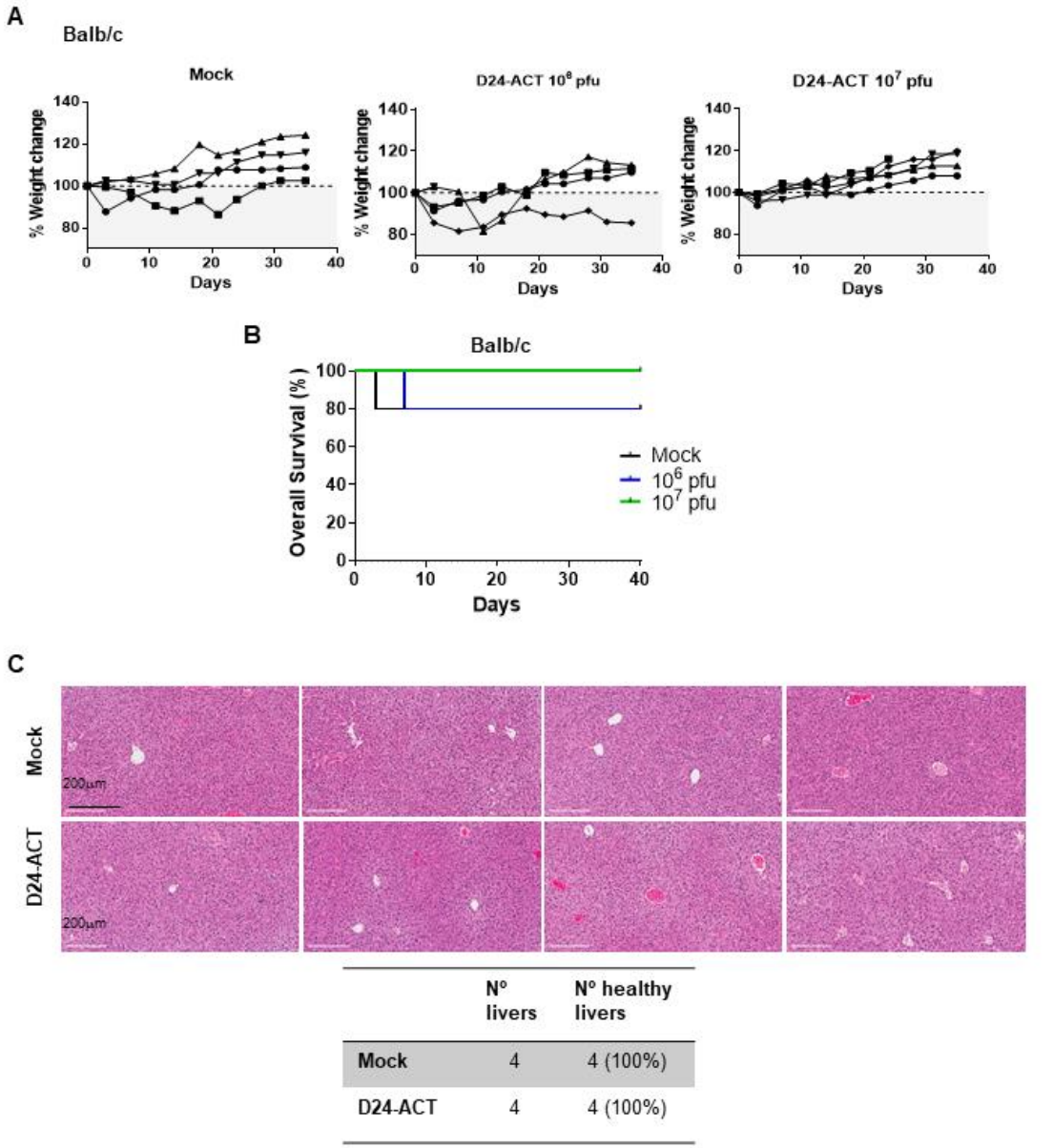

	N° livers	N° healthy livers
Mock	4	4 (100%)
D24-ACT	4	4 (100%)

Supplementary figure 2. Characterization of Delta-24-ACT toxicity in DIPG murine models. (A) Balb/c mice were treated intraparenchymally with mock (PBS) (*n*=5) or Delta-24-ACT (*n*=5) at the indicated doses. Mice from the different groups were weighed every 3-4 days until the end of the treatment (30 days). **(B)** Kaplan-Meier survival plot of Balb/c mice treated with PBS (control group) and 10^6 PFUs or 10^7 PFUs of Delta-24-ACT in the pons. **(C)** Representative histological images of the livers of mice bearing orthotopic DIPGs and treated locally with Delta-24-ACT at 10^8 PFUs. None of the livers analyzed showed hepatic injury.

Supp_ Figure 3

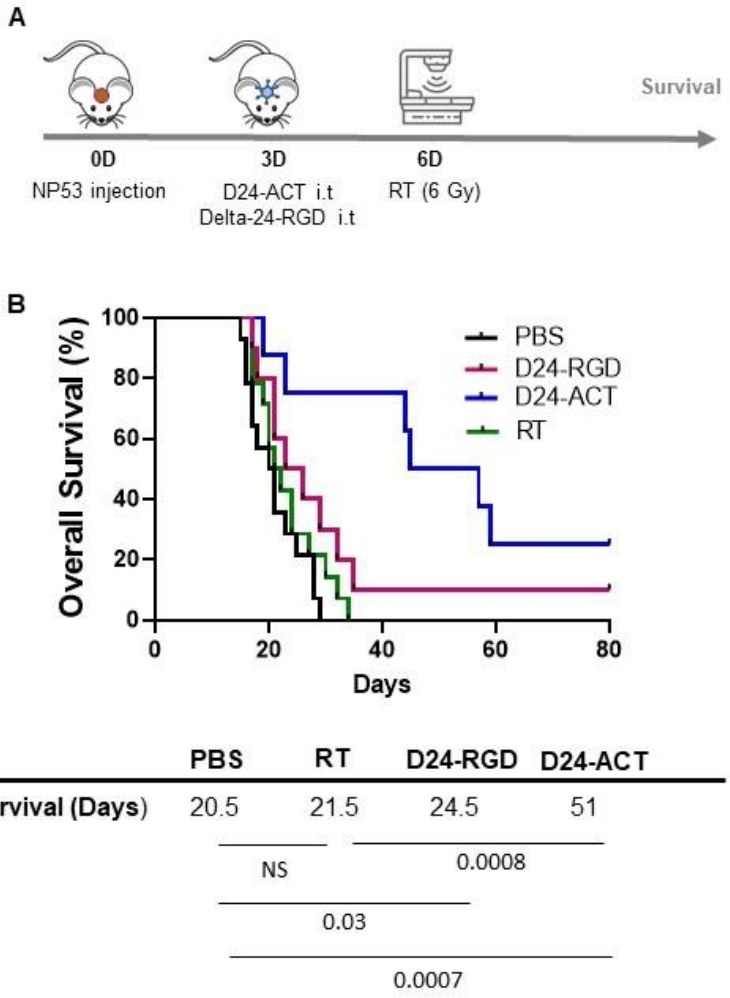

	PBS	RT	D24-RGD	D24-ACT
Median Survival (Days)	20.5	21.5	24.5	51

NS

0.0008

0.03

0.0007

Supplementary figure 3. Characterization of the anti-tumor effect Delta-24-ACT in DIPG murine models. (**A**) Schedule of survival experiments performed with NP53 comparing the effect on survival of viruses Delta-24-RGD and Delta-24-ACT. **(B)** Kaplan-Meier survival plot of mice bearing NP53 cells treated with 10^6 PFUs of Delta-24-RGD or Delta-24-ACT or a mock PBS control (log-rank; *P=0.001*,PBS *n*=14; Delta-24-RGD *n*=10; Delta-24-ACT *n*=8).

Supp_ Figure 4

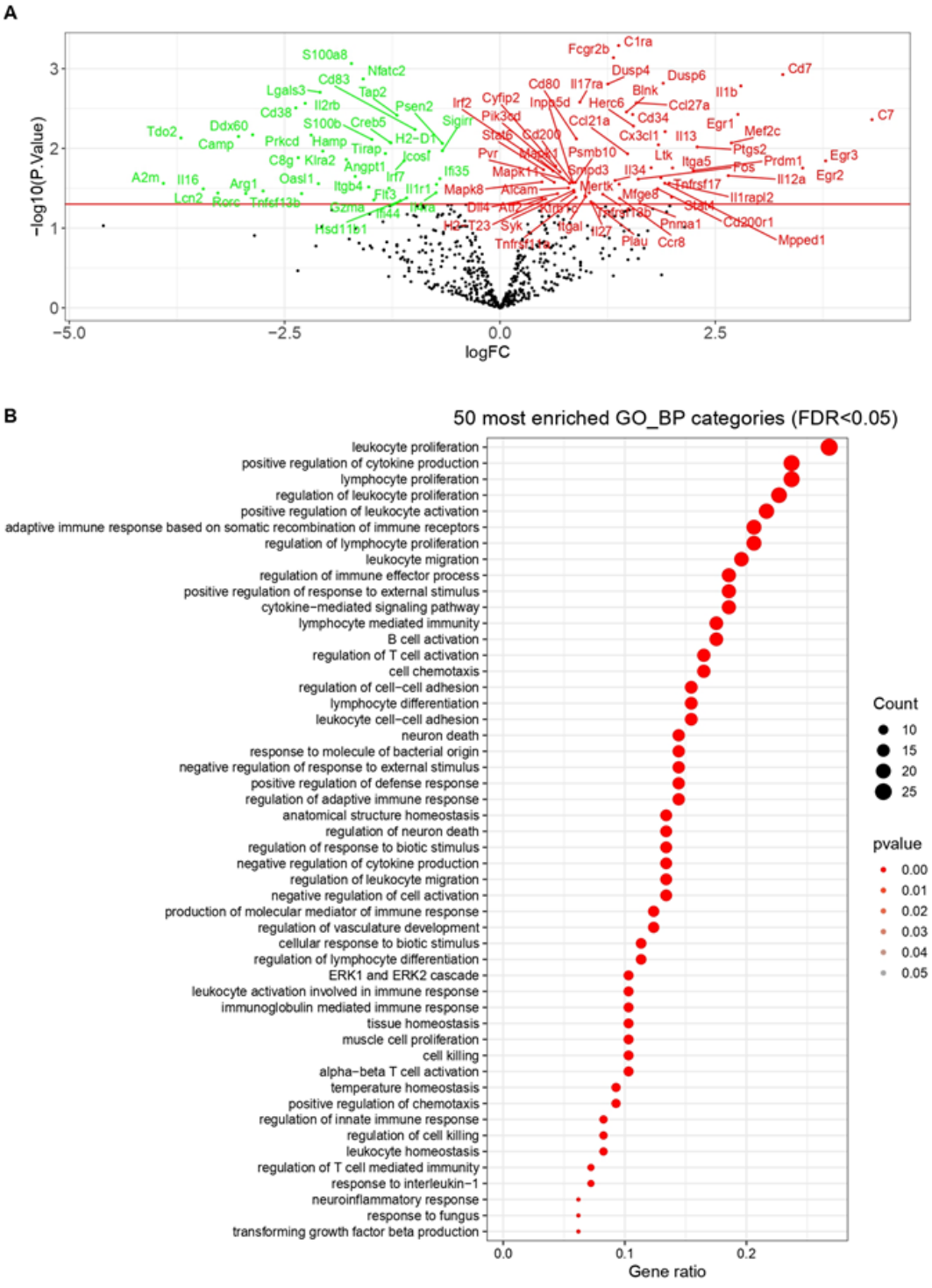

Supplementary figure 4. Evaluation of the tumor microenvironment after Delta-24-ACT treatment in the NP53 orthotopic model. (A) Volcano plot' of statistical significance against fold-change between control-treated and Delta-24-ACT-treated, demonstrating the most significantly differentially expressed genes. **(B)** Graph representing the 50 GO-biological processes enriched in Delta-24-ACT-treated animals versus control-treated.

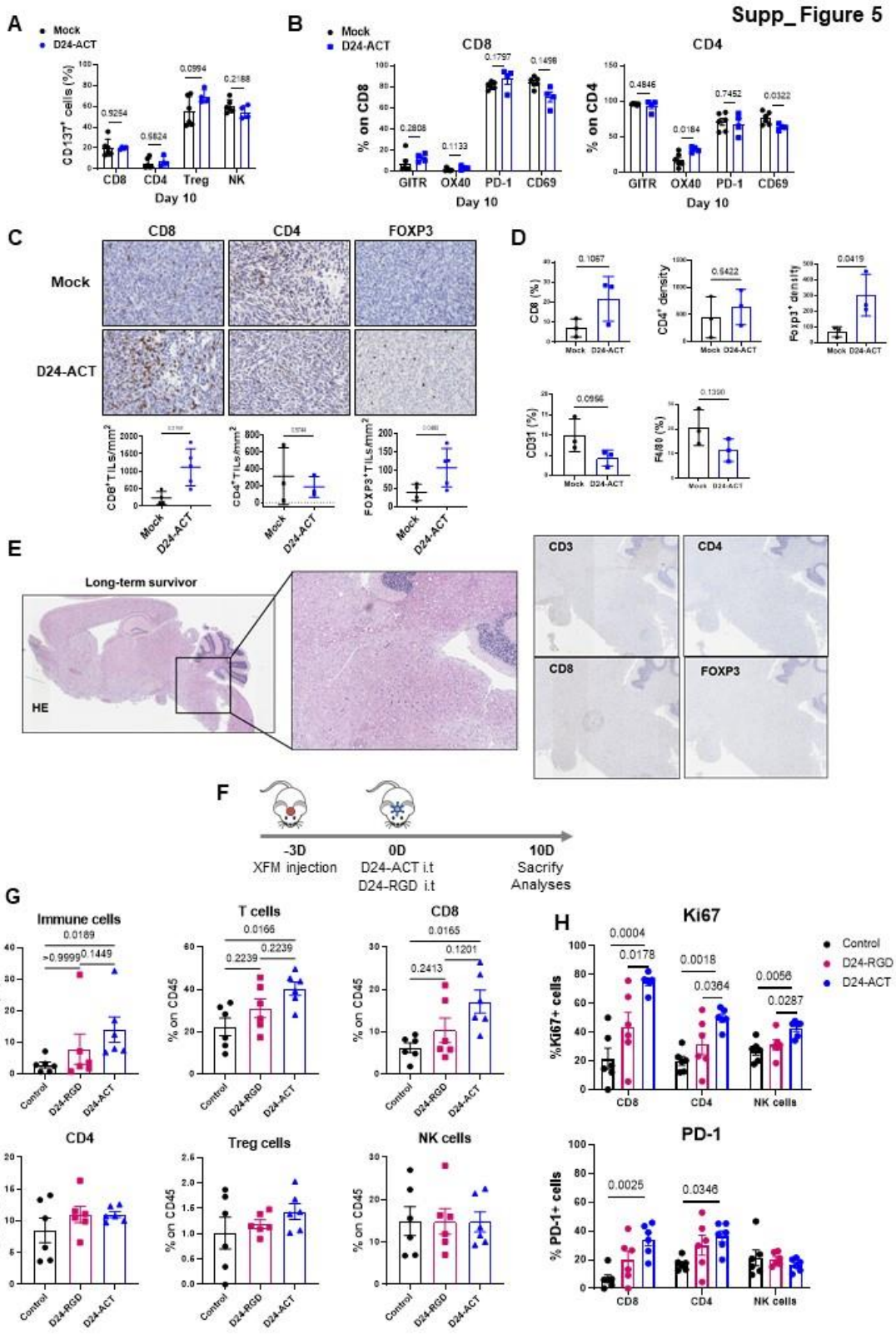

Supplementary figure 5. Modulation of the tumor microenvironment by Delta-24-ACT in the NP53 and XFM orthotopic models. (A) CD137 expression (%) in T cell populations and NK cells 10 days after viral treatment. Multiple t-test was performed (*n*=4/6) **(B)** Flow cytometry analyses of different activation (GITR, OX40, CD69) and exhaustion (PD-1) markers were performed on the $CD4^+$ and $CD8^+$ cell subsets 10 days after viral administration in NP53-bearing mice. The bars indicate the mean ± SD (*n*=6

PBS, *n*=4 D24-ACT) Multiple *t*-test. **(C)** ***Upper panel***, representative images (scale bar, 100 μm) of CD4, CD8, and FOXP3 immunostaining of DIPG tumors from control and Delta-24-ACT-treated mice. ***Lower panel***, quantification of positive $CD4^+$, $CD8^+$, and $FOXP3^+$ cell infiltration per mm^2 of DIPG tumors. Graph showing the quantification of positive cell infiltration at 15 days after cell implantation per mm^2 of tumors treated with either PBS or Delta-24-ACT (*n* =3-5). P values were calculated by the two-tailed Student's t test. **(D)** The brains of mice bearing NP53 cells were subjected to multiplexed immunofluorescence analysis to detectthe following immune cell markers: CD8 (light blue), CD4 (green), Foxp3 (yellow), CD31 (orange), F4/80 (red), and GFAP (pink). Nuclei were counterstained with DAPI (blue). Quantification of the different immune populations at 15 days after treatment (*n*=3). **(E)** Representative micrographs of a NP53 long-term survivor showing H&E and CD3, CD4, CD8, and FOXP3 immunostaining of DIPG tumors from Delta-24-ACT-treated mice subjected to a rechallenge. **(F)** Schedule of mechanistic studies in the XFM model. XFM cells were engrafted (day -3), and the animals were treated with either a mock control, Delta-24-ACT or Delta-24-RGD (10^6 PFUs) three days later. The animals were sacrificedten days (10D) later, and the different immune populations were assessed. **(G)** Flow cytometry analyses of different immune cell populations in the brains of mice bearing XFM tumors 10 days after treatment with Delta-24-ACT (blue), Delta-24-RGD (magenta) or PBS (black). The bars indicate the mean ± SD (*n*=6), One-way ANOVA. **(H)** Flow cytometry analyses of Ki67 proliferation and PD-1 exhaustion markers were performed in the CD8, CD4 and NK cell subsets 10 days after viral administration. The bars indicate the mean ± SD (*n*=6).

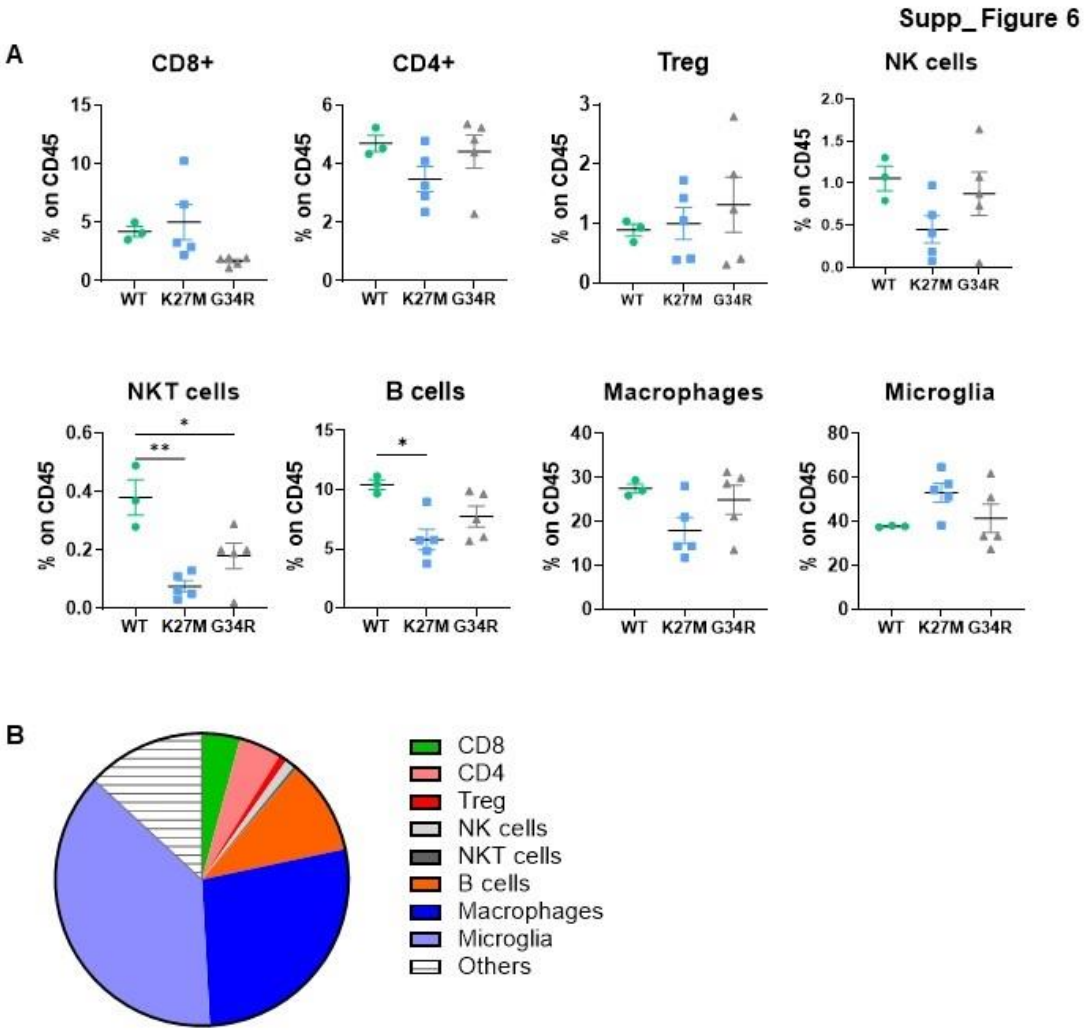

Supplementary Figure 6. Analyses of the composition of TME in an isogenic model. **(A)** Flow cytometry analyses of different immune populations of tumors in an isogenic system. Cells contain TP53 and PDGFR mutations in addition to H3 WT, H3K27M or H3G34R mutations. Data are shown as percentage (%) on CD45+ immune cells. One-way ANOVA was performed (N_{WT}=3, $N_{K27M,G34R}$=5). **(B)** Schematic representation of the proportions of immune cell populations forming the TME. The median percentages of the individuals of H3 WT group are shown.

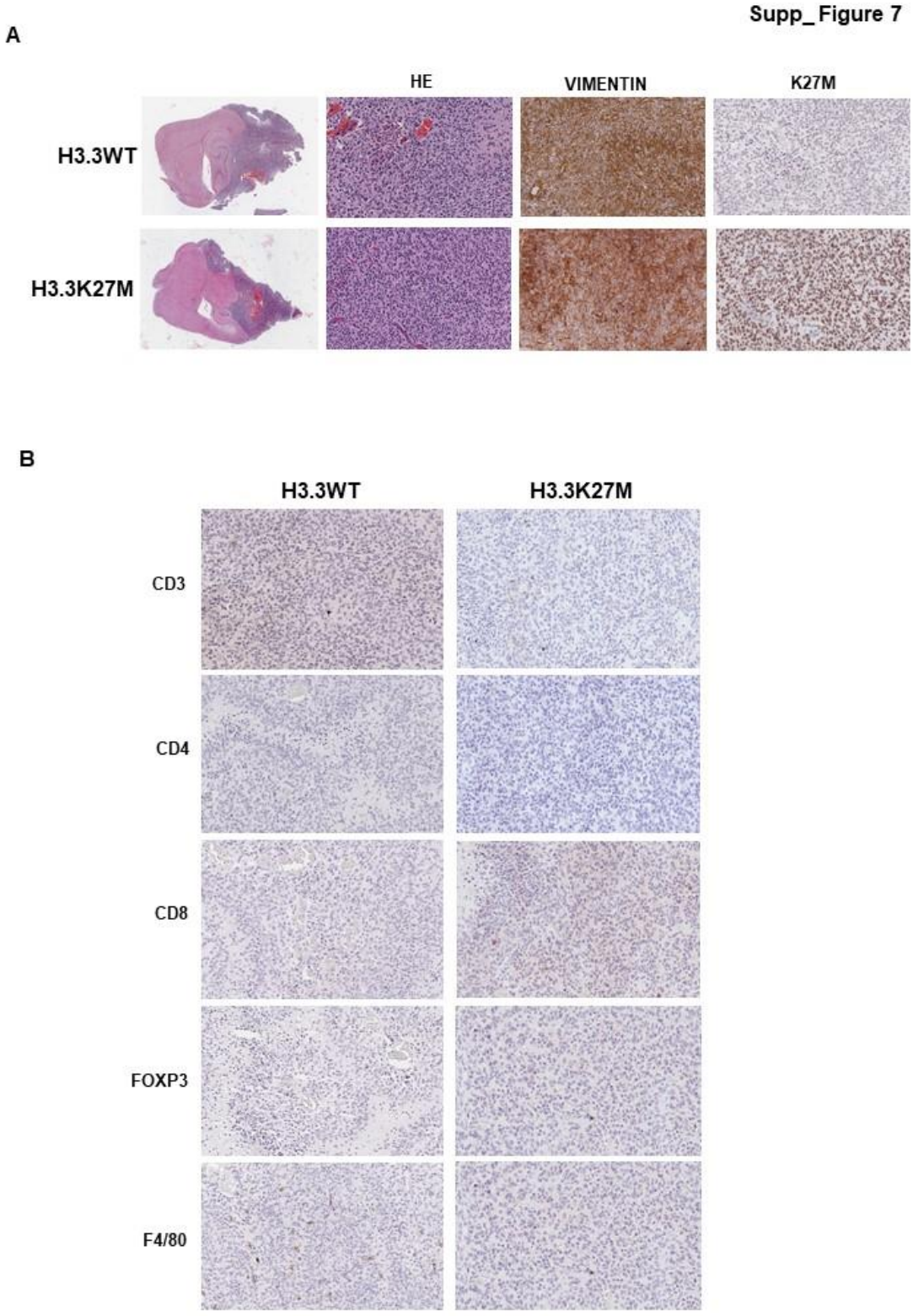

Supplementary Figure 7. Analyses of the composition of TME in an isogenic model. **(A)** Representative micrographs (100 μm) of spontaneous tumors arising from H3 WT or H3K27M transgenic mice. Showing H&E and H3 mutations and vimentin immunostaining. **(B)** Representative micrographs of spontaneous tumors arising from H3 WT or H3K27M transgenic mice. Showing CD3, CD4, CD8, FOXP3 and F4/80 immunostaining.

Local Treatment of a Pediatric Osteosarcoma Model with a 4-1BBL Armed Oncolytic Adenovirus Results in an Antitumor Effect and Leads to Immune Memory

Naiara Martinez-Velez[1,2,3], Virginia Laspidea[1,2,3], Marta Zalacain[1,2,3], Sara Labiano[1,2,3], Marc García-Moure[1,2,3], Montse Puigdelloses[1,2,4], Lucía Marrodan[1,2,3], Marisol Gonzalez-Huarriz[1,2,3], Guillermo Herrador[1,2,3], Daniel de la Nava[1,2,3], Iker Ausejo-Mauleon[1,2,3], Juan Fueyo[5], Candelaria Gomez-Manzano[5], Ana Patiño-García[1,2,3], and Marta M. Alonso[1,2,3]

ABSTRACT

Osteosarcoma is an aggressive bone tumor occurring primarily in pediatric patients. Despite years of intensive research, the outcomes of patients with metastatic disease or those who do not respond to therapy have remained poor and have not changed in the last 30 years. Oncolytic virotherapy is becoming a reality to treat local and metastatic tumors while maintaining a favorable safety profile. Delta-24-ACT is a replicative oncolytic adenovirus engineered to selectively target cancer cells and to potentiate immune responses through expression of the immune costimulatory ligand 4-1BB. This work aimed to assess the antisarcoma effect of Delta-24-ACT. MTS and replication assays were used to quantify the antitumor effects of Delta-24-ACT *in vitro* in osteosarcoma human and murine cell lines. Evaluation of the *in vivo* antitumor effect and immune response to Delta-24-ACT was performed in immunocompetent mice bearing the orthotopic K7M2 cell line. Immunophenotyping of the tumor microenvironment was characterized by immunohistochemistry and flow cytometry. *In vitro*, Delta-24-ACT killed osteosarcoma cells and triggered the production of danger signals. *In vivo*, local treatment with Delta-24-ACT led to antitumor effects against both the primary tumor and spontaneous metastases in a murine osteosarcoma model. Viral treatment was safe, with no noted toxicity. Delta-24-ACT significantly increased the median survival time of treated mice. Collectively, our data identify Delta-24-ACT administration as an effective and safe therapeutic strategy for patients with local and metastatic osteosarcoma. These results support clinical translation of this viral immunotherapy approach.

Introduction

Osteosarcoma is the most common primary bone tumor, affecting mainly children and adolescents, with a second minor peak of incidence at approximately 50 years of age (1). This malignant neoplasm is composed of mesenchymal cells that produce aberrant osteoid and immature bone, developing predominantly near the long bone metaphysis of limbs (2). The mainstay of current osteosarcoma treatment includes surgical resection of local and metastatic disease and pre- and postsurgical combination chemotherapy. The chemotherapy regimen includes a combination of doxorubicin and cisplatin with or without subsequent treatment with high-dose methotrexate and has a patient response rate of 70% (3). However, for patients with metastasis or recurrent disease, curative therapeutic options are limited, and the overall survival rate at 5 years is approximately 20%. This life expectancy is meager, underscoring the need for effective treatments, especially for high-risk populations.

Oncolytic virotherapy is a type of cancer biotherapy that has considered as a valid treatment option. Delta-24-RGD is a conditionally replicative adenovirus engineered to selectively replicate in cancer cells with an aberrant RB pathway (4, 5). In preclinical studies, Delta-24-RGD has shown efficacy in several solid adult (4, 6) and pediatric tumors, including local and metastatic osteosarcoma models (7–9). Clinically, Delta-24-RGD showed good safety and elicited a durable complete response in 20% of patients with recurrent glioblastoma (10). Importantly, the previous clinical trial revealed that intratumoral viral injection instigated an oncolytic effect followed by an inflammatory response potentially responsible for the antitumor effect and subsequent control of the tumor.

To further potentiate the efficacy of this virus, we engineered a new oncolytic virus expressing the immune costimulatory ligand 4-1BB (4-1BBL) to enhance viral antitumor immunity (11). 4-1BB is an inducible receptor promoting the survival and expansion of activated T cells. The interaction of 4-1BBL with 4-1BB enhances the stimulation of $CD4^+$ and $CD8^+$ T cells, causing predominant expansion of $CD8^+$ T cells (12). Signals initiated by 4-1BBL–4-1BB binding promote the $CD8^+$ T-cell costimulation, playing an important role in the differentiation of effector memory responses. Therefore, we hypothesized that the oncolytic adenovirus Delta-24-ACT

[1]Health Research Institute of Navarra (IDISNA), Pamplona, Navarra, Spain. [2]Program in Solid Tumors, Foundation for the Applied Medical Research, Pamplona, Navarra, Spain. [3]Department of Pediatrics, Clínica Universidad de Navarra, Pamplona, Spain. [4]Department of Neurology, Clínica Universidad de Navarra, Pamplona, Spain. [5]Department of NeuroOncology, The University of Texas MD Anderson Cancer Center, Houston, Texas.

Note: Supplementary data for this article are available at Molecular Cancer Therapeutics Online (http://mct.aacrjournals.org/).

N. Martinez-Velez, V. Laspidea, and M. Zalacain contributed equally to this article.

A. Patiño-García and M.M. Alonso contributed equally as the co-senior authors of this article.

Corresponding Authors: Ana Patiño-García, Dept. of Pediatrics, BTBT Lab, University Hospital of Navarra, University of Navarra, Pamplona, Spain. Phone: 349-4825-5400, ext. 4523; E-mail: apatigar@unav.es; and Marta M. Alonso, Phone: 349-4819-4700, ext. 812026; E-mail: mmalonso@unav.es

Mol Cancer Ther 2022;21:471–80

doi: 10.1158/1535-7163.MCT-21-0565

expressing 4-1BBL could trigger an immune response that would lead to a specific antisarcoma effect not only controlling local disease but also resulting in a therapeutic effect on distant untreated lung metastasis.

Materials and Methods

Cell lines and culture conditions

The murine osteosarcoma cell line K7M2 was obtained from the American Type Culture Collection (ATCC cat. No. CRL-2836, RRID: CVCL_V455). The murine osteosarcoma POS-1 and MOS-J cells derived from mouse spontaneous osteosarcoma were provided, respectively, by Drs. Kamijo (13) and Shultz (14) and were cultured in RPMI and DMEM, respectively with 10% FBS and 1% penicillin/streptomycin. The pediatric human osteosarcoma cell line Saos-2 was obtained from ATCC (cat. No. 300331/p651_SaOS-2, RRID: CVCL_0548). 531MII, a primary osteosarcoma cell line, was developed at the Clínica Universidad de Navarra. Cell lines obtained from ATCC were cultured following the manufacturer's instructions. 531MII cells were cultured in minimum essential medium supplemented with 10% FBS and 1% antibiotic. All cells were maintained in a humidified atmosphere with 5% CO_2 at 37°C. Cell lines were routinely tested for *Mycoplasma* (MycoAlert Mycoplasma Detection Kit; Lonza), and human cell lines were authenticated at the CIMA Genomic Core Facility.

Delta-24-ACT construction

Delta-24-ACT was constructed by maintaining the Delta-24-RGD modifications of a 24-base pair deletion and introduction of RGD (15); however, m4-1BBL was incorporated in the E3 locus after removing this gene. Briefly, murine 4-1BBL was first cloned into a pCDNA3.1 plasmid using the *Kpn I* and *Xho I* restriction enzymes (New England Biolabs). Then, m4-1BBL flanked with the cytomegalovirus promoter and bovine growth hormone polyadenylation sequences was subcloned into the pAB26-RGD plasmid at the *Cla I*/*BamH I* site. Finally, the 4-1BBL expression cassette was introduced into pVK-500C-Δ24, and the Delta-24 plasmid was constructed by homologous recombination with pAB26-m4-1BBL in BJ5183 bacteria. For viral rescue, the obtained plasmid was linearized with *Pac I* and transfected into HEK293 cells (cat. No. 300192/p777_HEK293, RRID:CVCL_0045) with Lipofectamine 2000 (Invitrogen). After confirmation of genetic modifications by PCR and sequencing, Delta-24-ACT was amplified in A549 cells (cat. No. 300114/p686_A-549, RRID:CVCL_0023), purified, and stored at −80°C.

Cell viability assay

All cell lines were seeded at a density of 10^3 cells per well in 96-well plates and infected with Delta-24-RGD and Delta-24-ACT at different multiplicity of infections ranging from 0 to 300. Cell viability was assessed 5 days after infection using a CellTiter 96 Aqueous One Solution Cell Proliferation Assay (Promega). The dose–response curves and IC_{50} values were analyzed using GraphPad software (RRID:SCR_002798 v8).

Replication assay

Cells were plated at a density of 5×10^4 and were then infected at an MOI of 10 for human cell lines and 300 for murine cell lines. Seventy-two hours later, the cells and supernatant were collected and subjected to three freeze-thaw cycles. The supernatant was used to infect HEK293 cells, and viral PFUs were determined by the anti-hexon staining method.

Infectivity assay

Cell lines were plated in 96-well plates at a density of 2×10^5 and infected at an MOI of 10 with a nonreplicative virus expressing GFP. After 24 hours, infected cells were harvested, and GFP expression was quantified by flow cytometry.

Immunoblotting

For immunoblotting, samples were subjected to SDS-Tris-Gly gel electrophoresis. Membranes were incubated with antibodies specific for the following molecules: E1A, (1:1,000; Santa Cruz Biotechnology cat. No. sc-430, RRID:AB_630843, Santa Cruz Biotechnology), fiber (1:1,000; Novus cat. No. NB 600–541, RRID:AB_521564, Novus Biological), GRB-2 (1:1,000; BD Biosciences cat. No. 610111, RRID:AB_397517), and LC3 A/B (1:1,000; Cell Signaling Technology cat. No. 4108, RRID:AB_213770).

Immunohistochemical analysis

Paraffin-embedded sections of mouse tibias, lungs, and livers were immunostained following conventional procedures with these antibodies: adenoviral mouse anti-hexon (Chemicon International, Inc.), adenovirus rabbit anti-E1A, (Santa Cruz Biotechnology), anti-CD3 (NeoMarkers), anti-CD4 (Abcam), anti-CD8a (Cell Signaling Technology), anti-FoxP3 (eBioscience, Thermo Fisher Scientific), and anti-vimentin clone V9 (IS30, Dako Denmark A/S). For immunohistochemical staining, Vectastain ABC Kits (Vector Laboratories Inc.) were used according to the manufacturer's instructions.

Measurement of DAMPs

Cell lines were plated and infected with both viruses at MOIs of 25 and 300, and medium was collected 72 hours later. ATP release was assessed with an ENLITEN ATP Assay System (FF2000, Promega). HMGB1 and HSP-90 release into the medium was measured with an HMGB1 ELISA Kit (ST51011, IBL International) and an HSP-90A ELISA kit (ADI-EKS-895, Enzo Life Sciences Inc.).

Calreticulin translocation to the plasma membrane was determined by immunofluorescence staining of 2×10^4 cells infected with Delta-24-ACT at a dose corresponding to the 3-day IC_{50} (or with PBS as a negative control). Four hours postinfection, cells were fixed with 4% methanol-free formaldehyde (28906; Thermo Fisher Scientific) for 15 minutes at 37°C and were then stained with appropriate antibodies.

Flow cytometric analysis

Viral 41BBL expression in osteosarcoma cell lines was determined by flow cytometry. Cells were stained first with a cell death detection antibody in the Zombie-NIR Fixable Viability Kit (423105, BioLegend) following the manufacturer's protocol and then with a PE-conjugated anti–4-1BBL antibody.

Calreticulin cell surface expression was determined by flow cytometry. Cells were stained first with a cell death detection antibody in the Zombie Green Fixable Viability Kit (423111, BioLegend) and then with a fluorophore-conjugated anti-calreticulin antibody (Abcam).

Fluorescence emission was analyzed using a FACSCanto II system with FACSDiva software (RRID:SCR_001456).

To identify immune cell populations, infiltrating immune cells were surface stained with the following antibody panel: anti–CD45-AF700 (BioLegend), anti–Ly6G-PerCP-Cy5.5 (BioLegend), anti–Ly6C-FITC (BioLegend), anti–F4/80-APC (BioLegend), anti–CD8-BV510 (BioLegend), anti–CD11b-BUV395 (BioLegend), and anti–CD4-BUV496 (BioLegend). PromoFLuor840 maleimide (PromoKine) was used as a viability marker. Samples were acquired with a CytoFlex flow

cytometer (Beckman Coulter RRID:SCR_019627) and data analyses were performed using FlowJo v10 (RRID:SCR_008520).

IFNγ and cytokine detection

Splenocytes and tumor-infiltrating lymphocytes (TILs) isolated from treated mice were cocultured with 10,000 K7M2 cells. K7M2 cells were left uninfected or infected with Delta-24-RGD or Delta-24-ACT at an MOI of 100 MOI. Four hours later, K7M2 cells were stimulated with recombinant mouse IFNγ protein and were collected and fixed with 4% formaldehyde 48 hours later. After 72 hours of coculture, supernatants were collected, and IFNγ ELISA (R&D Systems, Inc.) and MACS Plex Mouse Cytokine 10 kits (Miltenyi Biotec, Bergisch Gladbach) were used for analysis following the manufacturers' instructions.

Animal studies

The Ethical Committee of the University of Navarra [Comite Etico de Experimentacion Animal (CEEA)] approved the animal protocols performed in this study (CEEA/022–16). All animal studies were performed at the veterinary facilities of the Center for Applied Medical Research following institutional, regional, and national laws and ethical guidelines for experimental animal care.

To establish osteosarcoma animal models, K7M2 cells were injected into female BALB/c mice through the tibial plateau into the primary spongiosa of the right tibia. PBS or viruses (10^8 pfu/mouse) were administered intratumorally on days 10 and 18 after tumor engraftment. Tumor development and mouse weight were monitored twice weekly during the experiment. The tibia size was measured from the beginning of the experiment, and mice were sacrificed when the tumor volume reached 400 mm^2. Tumor volumes were determined throughout the course of the experiment by measuring the tumors along the two perpendicular diameters with a caliper and calculating the tumor volume with the following formula: volume $= D \times (d)^2 \times 0.5$, where D is the largest diameter and d is the smaller diameter. Animals were sacrificed when the tibial tumor volume reached 430 mm^3 or when they lost more than 20% of their body weight, and we harvested tibias to examine primary bone tumors, lungs to examine metastases, and livers to evaluate safety.

In vivo pulmonary metastasis evaluation

Thorax tomography was performed on mice anesthetized by intraperitoneal injection of ketamine and xylazine. Then, an intratracheal cannula was placed and connected to a flexiVent rodent ventilator (Scireq) set at a rate of 200 breaths/minute and a tidal volume of 10 mL/kg. Animals were maintained on 2% isoflurane inhalation until completely relaxed.

Lung 3D tomographic images were acquired using an X-ray micro-CT system (Quantum-GX, Perkin Elmer) with the following parameters: X-ray source voltage of 90 kVp, current of 88 μA, high-speed scan protocol for a total acquisition time of 14 minutes, and gantry rotation of 360°. Breathing artifacts were denoised using respiratory gating in each acquisition. The three-dimensional tomographic images containing the whole lung had a total of 512 slices with an isotropic voxel size of 72 μm and a resolution of 512 × 512 pixels per slice. Analysis of the lung volume in each sample was carried out using Fiji/ImageJ (RRID:SCR_002285), open-source Java-based image processing software. In brief, lung images were segmented by applying a fixed threshold, and total lung volume was measured over the obtained mask (mm^3). Quantified values were normalized to those of normal, healthy lung parenchyma.

Statistical analysis

The *in vitro* experiments were repeated at least three times. Dose–response curves for viral cytotoxicity were obtained by nonlinear regression. Data with normal distributions were assessed by Shapiro–Wilk tests, and comparisons among groups were performed by two-tailed nonparametric tests with 95% confidence intervals for nonnormally distributed datasets or parametric tests when normality was confirmed (Student t test or one/two-way ANOVA). For comparison of groups in survival experiments, a log-rank test (Mantel–Cox) was used. GraphPad Prism 8 (Statistical Software for Sciences GraphPad Prism) was used for the statistical analyses.

Results

The oncolytic adenovirus Delta-24-ACT is effective against osteosarcoma cells *in vitro*

Delta-24-ACT is a replicative oncolytic adenovirus based on the Delta-24-RGD (4) backbone and modified to encode the mouse 4-1BBL (m4-1BBL; Supplementary Fig. S1A). We showed that the 4-1BBL expressed by the virus was functional and effectively activated T cells *in vitro* and *in vivo* in the context of murine glioma models (15). Human pediatric osteosarcoma cells express receptors (αv3 and αv5 integrins and CAR) necessary for viral entry into cells (16), and Delta-24-ACT utilizes these receptors for recognition and subsequent entry into cells. Thus, we confirmed that Delta-24-ACT was able to infect 531MII and Saos-2 human osteosarcoma cells and K7M2 osteosarcoma cells (Supplementary Fig. S1B). Moreover, K7M2, 531 MII and Saos-2 cells infected with an increasing amount of virus showed dose-dependent expression of 4-1BBL mRNA that was efficiently translated to protein (**Fig. 1A** and **B**; Supplementary Fig. S1C). Importantly, we confirmed that after infection with Delta-24-ACT, 4-1BBL was expressed on the surface of murine (**Fig. 1C** and **D**; Supplementary Fig. S1D) and human osteosarcoma cells (**Fig. 1C**; Supplementary Fig. S1D).

Because viral genome modifications can interfere with effective viral replication, the replication capacity of Delta-24-ACT was quantified and compared with that of Delta-24-RGD in osteosarcoma cell lines after 72 hours of infection. No differences were found between the load of Delta-24-RGD and Delta-24-ACT progeny virions, indicating that insertion of the m4-1BBL expression cassette did not hinder viral replication (**Fig. 1E**; Supplementary Fig. S1E). Finally, the results of cytotoxicity tests showed that both Delta-24-RGD and Delta-24-ACT exerted a potent antitumor effect *in vitro* in all tested osteosarcoma cell lines (**Fig. 1F**; Supplementary Fig. S1F). We observed that both viruses displayed very similar IC_{50}s: Delta-24-RGD proved slightly better although not significant. In K7M2, the IC_{50s} were 27 ± 11.2 and 24 ± 7.9 MOIs for Delta-24-ACT and Delta-24-RGD, respectively. In 531MII were 10.1 ± 3.5 and 7.5 ± 2.4 MOIs for Delta-24-ACT and Delta-24-RGD, respectively. In addition, we confirmed the capability of Delta-24-ACT to replicate and to express m4-1BBL in osteosarcoma tumors *in vivo*. We detected m4-1BBL mRNA and protein expression in osteosarcoma tumors 48 hours after Delta-24-ACT treatment (**Fig. 1G** and **H**). We also observed the presence of viral proteins, specifically E1A and fiber in orthotopic osteosarcoma tumors treated with Delta-24-ACT (**Fig. 1H**). Importantly, the presence of the fiber protein, which is expressed in the late stages of the viral life cycle, suggested viral replication *in vivo*.

In summary, these results demonstrated that the newly generated virus Delta-24-ACT efficiently expressed m4-1BBL in osteosarcoma cells both *in vitro* and *in vivo*, indicating preservation of its replication capacity.

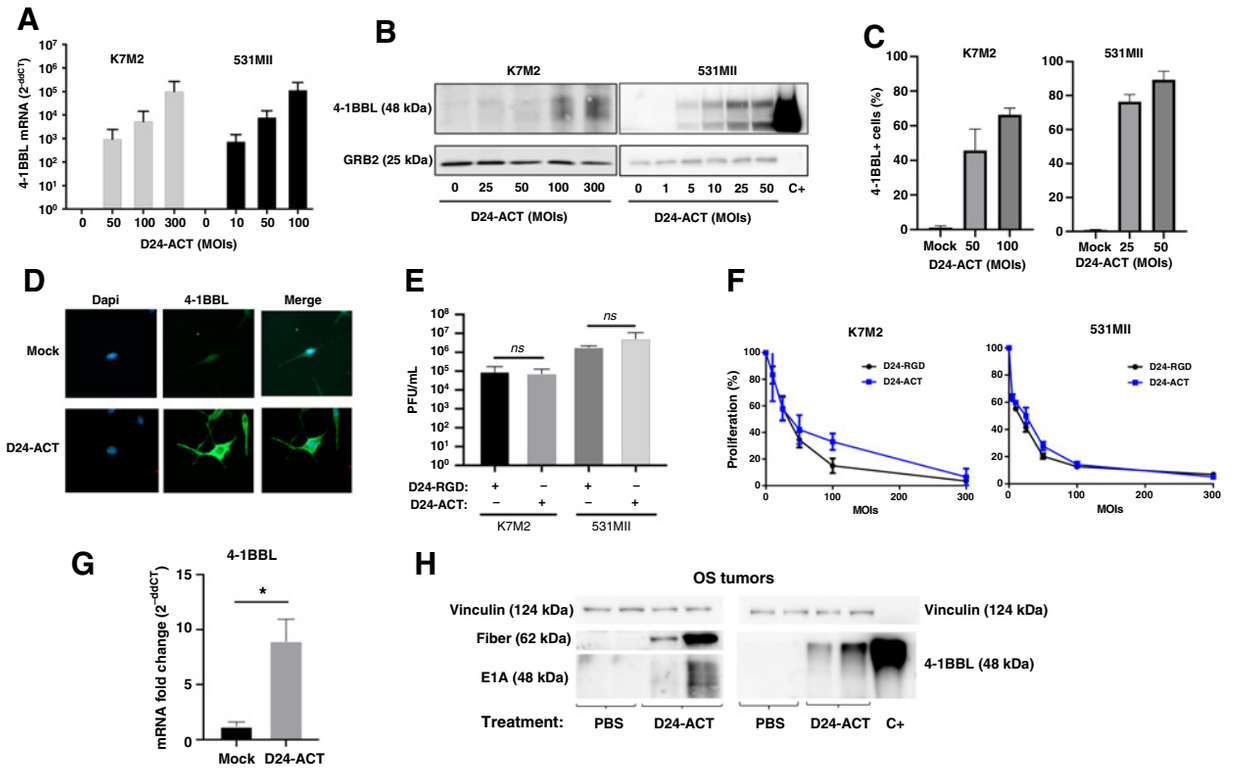

Figure 1.

Characterization of Delta-24-ACT in osteosarcoma cell lines. **A,** Expression of 4-1BBL mRNA after infection with Delta-24-ACT at the indicated MOIs in K7M2 and 531MII cells ($N = 3$). **B,** Assessment of 4-1BBL protein expression by Western blot analysis. Cells were infected with Delta-24-ACT at the indicated MOIs, and 48 hours later, whole-cell lysates were collected. Grb2 was used as the protein loading control, and recombinant 4-1BBL protein was used as the positive control. **C,** Flow cytometric quantification of 4-1BBL expression in the membrane of murine (K7M2) and human (531MII) osteosarcoma cells infected with Delta-24-ACT at the indicated MOIs. **D,** Representative fluorescence micrographs of K7M2 cells 24 hours after infection with Delta-24-ACT or mock infection. 4-1BBL at the cell surface was detected by immunofluorescence (green). Samples were counterstained with DAPI (blue). **E,** Replication of Delta-24-ACT in murine K7M2 and human 531MII osteosarcoma cells. Cells were infected, and Delta-24-ACT replication was determined after 72 hours. The results are expressed as the mean viral titers ± SDs ($N = 3$). **F,** Oncolytic effect of Delta-24-ACT and Delta-24-RGD on murine and human osteosarcoma cells. To quantify the oncolytic effect of the viruses, cells were infected at the indicated MOIs, and five days later, viability was evaluated by MTS assays. The values indicate the percentages of viable cells in infected cultures compared with those in noninfected cultures (mean ± SD). **G,** *In vivo* evaluation of 4-1BBL mRNA expression in orthotopic human osteosarcoma tumors**. H,** Assessment of 4-1BBL, E1A, and fiber expression *in vivo* in orthotopic human osteosarcoma tumors by Western blot analysis. A representative blot is shown.

Delta-24-ACT treatment *in vitro* leads to the production of DAMPs

Autophagy mediates the release of damage-associated molecular patterns (DAMPs) and tumor antigens; therefore, its stimulation has been proposed to be required for immunogenic cell death (ICD; refs. 17–20). Consequently, we assessed whether Delta-24-ACT treatment induces autophagy. We observed an increase in the conversion of LC3I to LC3II and a decrease in the P62/GRB2 ratio in Delta-24-ACT–infected cells compared with Delta-24-RGD–infected cells (Supplementary Fig. S2A). Next, we evaluated whether Delta-24-ACT–induced autophagy led to the release of several DAMPs by evaluating ATP, HMGB1, and HSP-90α release and calreticulin (CRT) exposure in the membrane as hallmarks of ICD. We observed an increase in ATP release in K7M2 ($P = 0.04$) and 531MII ($P = 0.03$) cells 72 hours after treatment with Delta-24-RGD or Delta-24-ACT (**Fig. 1A**). The level of HMGB1 release tended to increase, although nonsignificantly, in both cell lines after viral treatment (Supplementary Fig. S2B). In addition, HSP-90α release, a marker of ICD in human cells, was significantly increased in 531MII cells infected with either Delta-24-ACT or Delta-24-RGD compared with control cells (mock-infected; **Fig. 2B**). Moreover, calreticulin translocation from the endoplasmic reticulum to the cell membrane, forming clusters in K7M2 and 531MII cells after Delta-24-ACT infection, was observed (**Fig. 2C**; Supplementary Fig. S2C). Quantification of calreticulin expression in the membrane of K7MII and 531MII cells showed a significant increase in both cell lines infected with the either virus ($P = 0.002$ and $P = 0.02$ for K7MII cells and 531MII cells, respectively; **Fig. 2D**). In summary, Delta-24-ACT treatment of osteosarcoma cells triggered the production of several DAMPs *in vitro*.

Delta-24-ACT administration significantly stimulates immune infiltration and establishes a proinflammatory microenvironment in murine osteosarcoma tumors

Previously, we showed that Delta-24-RGD treatment triggered an immune response in glioma and DIPG models (7, 10, 21). In fact, viral administration induces the production of DAMPs that attract immune cell populations to the tumor site, eliciting a specific immune response against tumor cells (17). Therefore, BALB/c mice bearing K7M2 murine osteosarcoma cells orthotopically were treated twice with PBS,

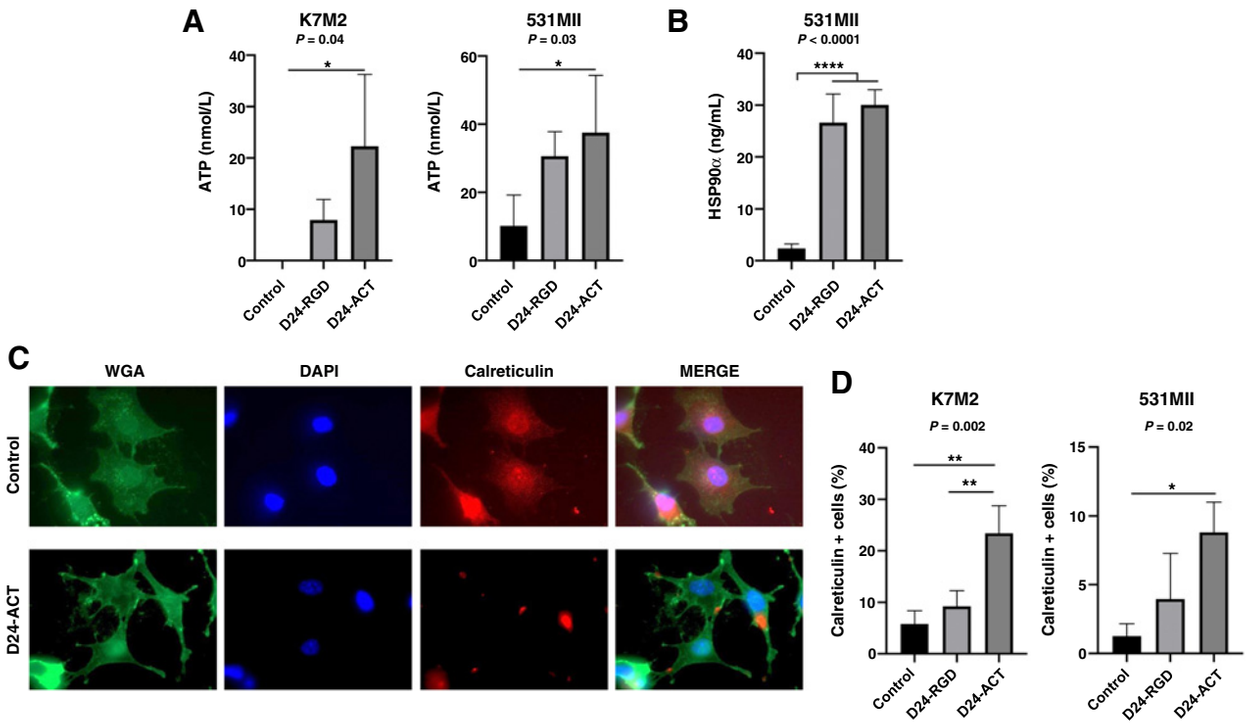

Figure 2.

Delta-24-ACT mediates DAMP release *in vitro*. **A** and **B,** Concentrations of the DAMPs ATP and Hsp90α in supernatants obtained from osteosarcoma cell cultures 72 hours after infection with Delta-24-ACT at the corresponding IC_{50} values for each virus or mock infection. The bar graphs show the mean ± SD values ($n = 3$; ordinary one-way ANOVA with Tukey multiple comparison test). **C,** Representative fluorescence micrographs of K7M2 cells 4 hours after infection with Delta-24-ACT or mock infection. Calreticulin at the cell surface was detected by immunofluorescence (red). Cell membranes (green) and nuclei (blue) were counterstained with wheat germ agglutinin (WGA) and DAPI, respectively. **D,** Flow cytometric quantification of membrane calreticulin + cells after Delta-24-ACT or Delta-24-RGD infection. The bar graphs show the mean ± SD values ($n = 3$; ordinary one-way ANOVA with Tukey multiple comparison test).

Delta-24-RGD, or Delta-24-ACT (days 10 and 18). Anatomopathological studies revealed a significant increase in infiltrating $CD3^+$ and $CD8^+$ cells in tumors treated with Delta-24-ACT compared with those treated with Delta-24-RGD ($P < 0.05$) or PBS ($P < 0.001$). The infiltration density was increased almost twofold in Delta-24-ACT–treated mice compared with Delta-24-RGD–treated mice (**Fig. 3A** and **B**). On the other hand, $CD4^+$ cells were increased in treated tumors, although the difference was not significant (Supplementary Fig. S3A). Quantification of several immune cell populations by flow cytometry at day 7 posttreatment (Supplementary Fig. S3B) confirmed that both viruses significantly increased the number of $CD45^+$, CD3, CD8, CD4, Trg, NK cells, macrophages, and DCs in the tumor (all $P < 0.05$). However, we did not find significant differences among both viruses (**Fig. 3C**). A second experiment confirmed that Delta-24-ACT increased the numbers of $CD3^+$ cells, $CD4^+$ cells, $CD8^+$ cells, and macrophages compared with those in PBS-treated mice ($P = 0.002$, $P = 0.03$, $P = 0.04$, and $P = 0.001$, respectively; **Fig. 3D**). Moreover, $CD4^+$ and $CD8^+$ cells tended to express higher levels of $CD137^+$ (**Fig. 3D**), suggesting that T-cell activation was increased. Quantification of IFNg production in splenocytes isolated from mice in the different treatment groups showed that compared with PBS, both viruses increased significantly the level of this cytokine measured by ELISA ($P = 0.01$ and $P < 0.001$ for Delta-24-RGD and Delta-24-ACT, respectively; **Fig. 3E**). Moreover, splenocytes from Delta-24-ACT–treated mice displayed a more active phenotype than those from Delta-24-RGD ($P = 0.02$). This finding was further confirmed by ELISPOT, which showed that the coculture of K7M2 cells with splenocytes from Delta-24-ACT–treated mice led to a nearly threefold increase in the production of IFNg as compared with the PBS group ($P < 0.0001$; **Fig. 3F**). Delta-24-ACT was also superior to Delta-24-RGD ($P = 0.006$). Moreover, intratumoral injection of Delta-24-ACT led to upregulation of proinflammatory cytokines such as IFNg, GM-CSF, IL5, and IL4 in the tumor. Interestingly, we did not observe any difference in the expression of IL2 or IL12. In addition, virus injection did not induce any changes in protumoral cytokines (Supplementary Fig. S3C).

Collectively, these results showed that Delta-24-ACT increased immune infiltration, inducing a proinflammatory microenvironment.

Delta-24-ACT local administration presents a safe toxicity profile

Because 4-1BB agonists have shown hepatic toxicity in clinical settings (reviewed in refs. 8, 22), we first evaluated the safety of intratumoral administration of Delta-24-ACT. Administration of one or three doses of virus did not affect the weight of the treated animals (**Fig. 4A**). Moreover, quantification of murine hepatic transaminases 48 hours after a single dose and after three doses of Delta-24-ACT revealed no differences in blood alanine aminotransferase (ALT) and aspartate aminotransferase (AST) levels (**Fig. 4B**), suggesting normal hepatic function. Histopathologic analysis confirmed that the livers from virus-treated animals were morphologically normal (**Fig. 4C**), indicating the safety of the virus.

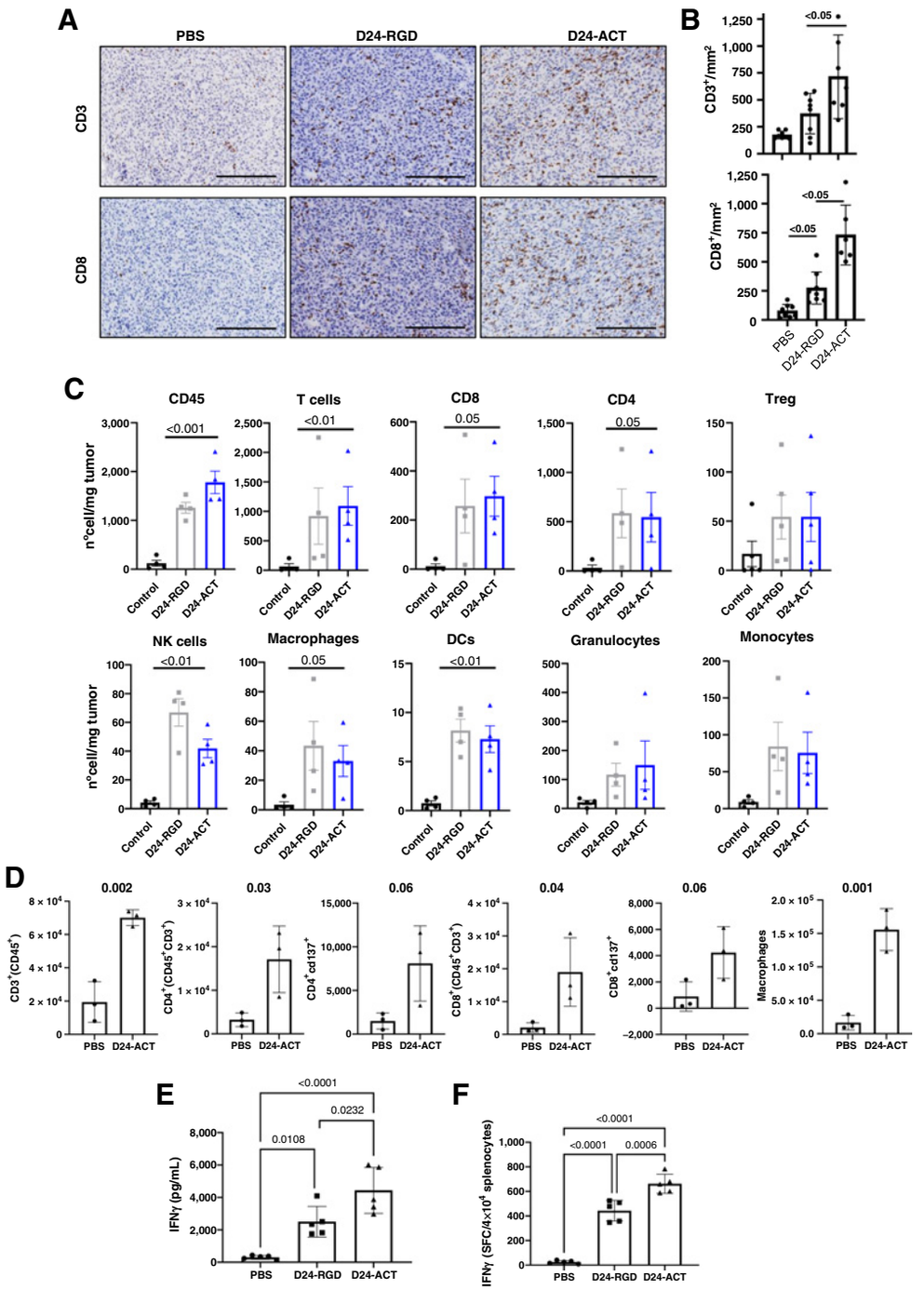

Figure 3.

Administration of Delta-24-ACT results in immune cell infiltration and the production of proinflammatory cytokines. Osteosarcoma tumors were generated by intratibial injection of K7M2 cells, and PBS, Delta-24-RGD, or Delta-24-ACT was administered intratumorally 10 days after cell implantation. Animals were sacrificed on day 17 after cell implantation. **A,** Representative images (scale bar, 100 μm) of CD3 and CD8 immunostaining in osteosarcoma tumors from control mice or virus-treated mice. **B,** Quantification of $CD3^+$ and $CD8^+$ cell infiltration per mm^2 in osteosarcoma tumors ($n = 6–8$). *P* values were calculated using two-tailed Student *t* test. **C,** Flow cytometric analysis of immune cell populations within the TIL population in the tibias of mice bearing intratibial K7M2 tumors and treated with Delta-24-RGD or Delta-24-ACT. The bars indicate the mean ± SD values ($N = 4/5$). **D,** Flow cytometric analysis of immune cell populations within the TIL population in the tibias of mice bearing intratibial K7M2 tumors and treated with Delta-24-ACT. The bars indicate the mean ± SD values ($N = 3$); Mann–Whitney test. **E,** Quantification of IFNγ production by ELISA after 72 hours of coculture of K7M2 cells with splenocytes isolated from mice treated with PBS or the different viruses. The data are presented as the median ± SD values ($n = 5$). One-way ANOVA test was used for comparison between control and treated mice. **F,** Quantification of IFNγ spot-forming cells per 4×10^4 splenocytes isolated from control and Delta-ACT–treated animals and cocultured with tumor cells. *P* values were calculated using one-way ANOVA.

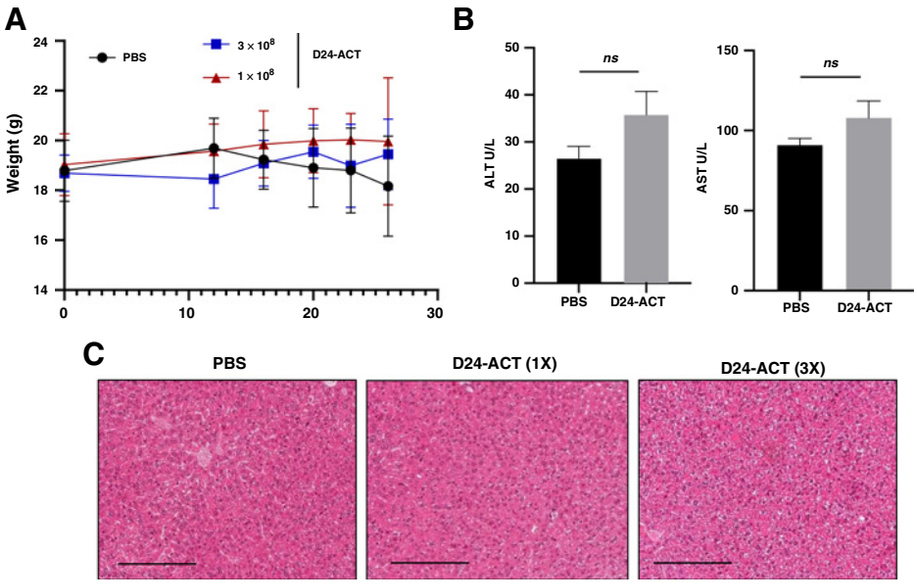

Figure 4.

Administration of Delta-24-ACT presents a safe toxicity profile. **A,** Mice were treated intratibially with mock (PBS) or Delta-24-ACT one or three times at the indicated doses. Mice from the different groups were weighed every 3 to 4 days until the end of the treatment period (25 days). The data are shown as the median ± SD for each group at each time point. **B,** Evaluation of biochemical parameters related to hepatic toxicity after intratumoral injection of Delta-24-ACT. Mice were treated with mock or virus, and serum samples were collected 3 days later. Several parameters, including ALT (U/L) and AST (U/L) levels, were measured to monitor hepatic injury. **C,** Histologic analysis of the livers of mice bearing orthotopic murine osteosarcoma tumors and treated locally with 10^8 PFU Delta-24-ACT one or three times. Representative micrographs of H&E–stained (magnification, 100 μm) livers of mice from the indicated groups are shown. The images show no viral presence in mouse livers and no signs of hepatotoxicity.

Local treatment with Delta-24-ACT increases overall survival in an osteosarcoma murine model

Next, we evaluated the therapeutic effect of the virus. For this study, two local injections were administered on days 10 and 18 (Supplementary Fig. S4A). Mice were weighed until day 40 to rule out toxicity (Supplementary Fig. S4B). Efficacy studies showed that control mice developed visible bone tumors faster than treated mice, and by day 25, all but two control mice exhibited measurable tumors (**Fig. 5A**). Moreover, tumors developed in only four of the 12 tibias in the treated group. The tumor diameters in control mice ranged from 90 to 500 mm^3, whereas the four tumors that developed in the Delta-24-ACT–treated group had volumes between 250 and 450 mm^3 (**Fig. 5A**). Treatment with Delta-24-RGD also delayed tumor growth (Supplementary Fig. S4C). Kaplan–Meier survival curves showed that local administration of Delta-24-ACT led to significantly extended overall survival times, with median survival times of 30 days for PBS-treated mice and 47 days for Delta-24-ACT–treated mice ($P < 0.0001$; **Fig. 5B**). In a second survival study, we compared the efficacy of Delta-24-ACT with Delta-24-RGD and PBS treated mice. We observed that efficacy of Delta-24-ACT was superior to the one exerted by Delta-24-RGD. Kaplan–Meier survival curves showed that local administration of Delta-24-ACT or Delta-24-RGD led to significantly extended overall survival times, with median survival times of 33.5 days for PBS-treated mice, 38 days for Delta-24-RGD ($P < 0.05$) and 60 days for Delta-24-ACT–treated mice ($P = 0.0006$). Both viruses led to the generation of long-term survivors: one (1/10) and four (4/10) for Delta-24-RGD and Delta-24-ACT, respectively (Supplementary Fig. S4D). K7M2 cells are a highly lung metastatic cell line; therefore, we evaluated the potential for lung metastasis. Micro-CT analysis showed that the integrity of the normal lung parenchyma was significantly maintained in mice treated with Delta-24-ACT compared with control mice ($P = 0.05$; **Fig. 5C**), indicating that the viral treatment can control spontaneous lung metastasis. Delta-24-RGD treatment also significantly reduced the number of tumor nodules in the lungs of treated mice (Supplementary Fig. E). Rechallenge of the long-term survivors with K7M2 cells in the contralateral leg showed that 100% of long-term survivors (3/3) were protected against rechallenge through the development of protective immune memory. Moreover, anatomopathological studies showed normal tibias in the animal previously treated with Delta-24-ACT in stark contrast with the tibias of the naïve treated mice (**Fig. 5G**). Lung evaluation also revealed that long-term survivors showed healthier lung parenchyma than naïve counterparts (**Fig. 5H**).

Evaluation of the efficacy of Delta-24-RGD and Delta-24-ACT in immunodeficient model lacking lymphocytes T and B bearing orthotopically K7M2 murine cell line, showed no therapeutic benefit, indicating that the mechanism of action of these viruses is mediated by an efficient antitumoral immune response (**Fig. 5I**; Supplementary Fig. S4F). In summary, these data revealed the efficacy and safety of Delta-24-ACT in a pediatric osteosarcoma murine model.

Discussion

The observation that osteosarcoma tumors exhibit genomic instability and a high mutational burden, associated with an increased presence of neoantigens, suggests that these tumors are amenable to immunotherapy (23). In fact, several immunotherapy-based clinical trials, including trials of immune checkpoint inhibitors, chimeric antigen receptor (CAR) T cells and other immunotherapies (NCT03006848, NCT03628209, NCT04539366, NCT04483778, and

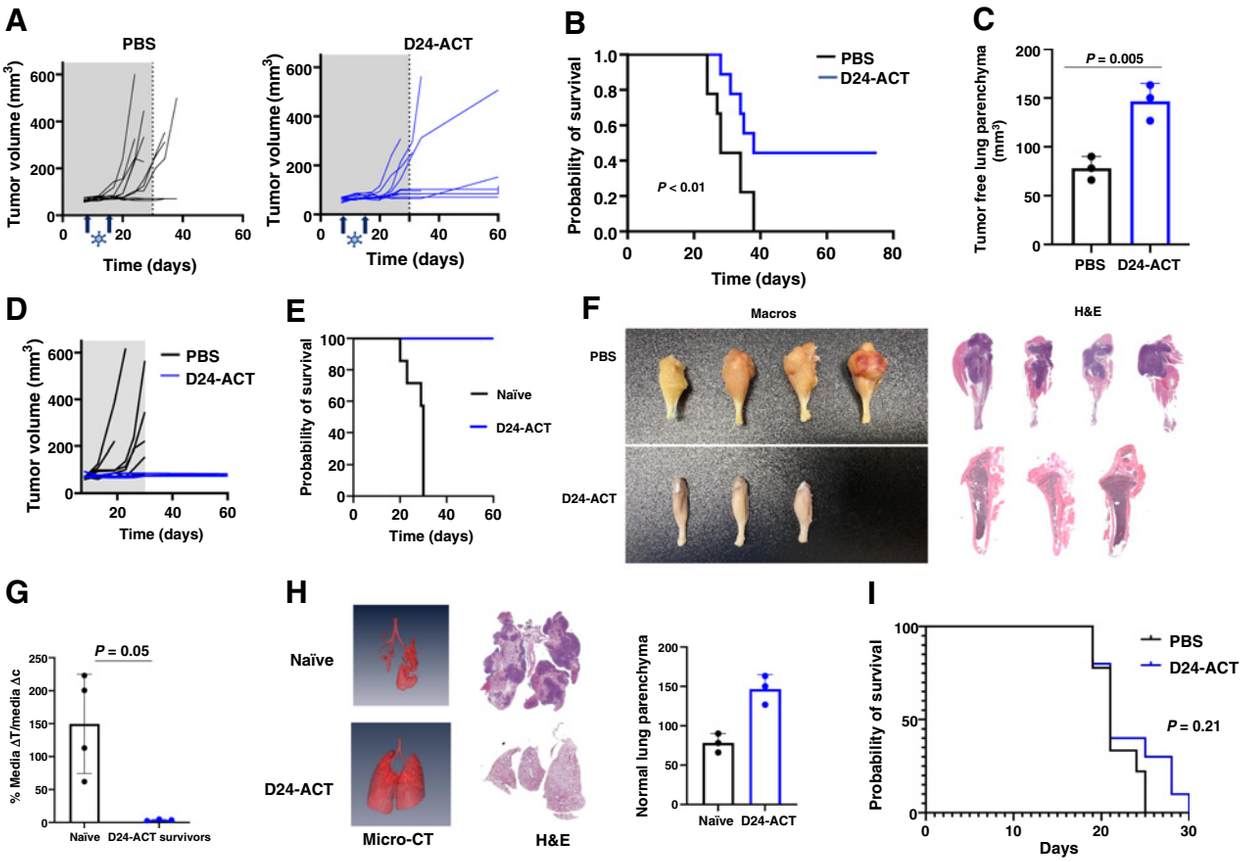

Figure 5.

Administration of Delta-24-ACT results in local and metastatic efficacy effect in a murine osteosarcoma model. **A,** Analyses of tumor burden development in the PBS-treated (control group) and Delta-24-ACT–treated groups. Tumor volume in mouse tibias was measured on different days until the end of the experiment. **B,** Survival curves. The graphs show the overall survival of mice treated with Delta-24-ACT (blue line) or PBS (black line). **C,** Evaluation of lung metastasis using micro-CT. Quantification of the normal lung parenchyma using micro-CT. **D,** The long-term survivors from the Delta-24-ACT–treated group were subjected to rechallenge with K7M2 cells in the contralateral tibia and compared with control untreated mice (naïve). Analyses of tumor burden development in the naïve-treated (control group) and Delta-24-ACT–treated groups. Tumor volume in mouse tibias was measured on different days until the end of the experiment. **E,** Kaplan–Meier survival curves of the long-term survivors from the Delta-24-ACT–treated group subjected to a rechallenge with K7M2 cells in the contralateral tibia and compared with control untreated mice. **F,** Representative macroscopic images and H&E-stained sections of tibias from PBS- or Delta-24-ACT–treated mice. **G,** Differences in tumor growth shown as percentages in comparison with the control groups. **H,** Evaluation of lung metastasis using micro-CT. Representative 3D image reconstruction of the normal lung parenchyma and corresponding histologic macroscopic images of tumors in PBS- and Delta-24-ACT–treated animals (left). Quantification of the normal lung parenchyma using micro-CT (right). **I,** Kaplan–Meier survival curves of Delta-24-ACT (10^7 pfu)-treated and control (PBS)-treated immunodeficient (athymic nude) mice ($n = 11$, both groups) bearing intratibial K7M2 tumors. The *P* value was calculated with the log-rank test.

NCT02470091), are ongoing. However, the published results are modest regarding outcomes in patients with metastatic or refractory osteosarcoma (24, 25). Furthermore, the toxicities induced by some of these agents have hampered their clinical development (26, 27). In this work, we showed that Delta-24-ACT is safe and efficacious in murine osteosarcoma models. Our results are consistent with a plethora of trials that support the inclusion of oncolytic viruses in routine oncology and, most importantly, pediatric oncology (NCT03178032, NTC02444546, NTC03043391, NTC03330197, NTC02031965). Oncolytic viruses have shown good safety profiles and a degree of efficacy (28). These results encourage the combination of these viruses with drugs specifically geared toward targeting aberrancies in pediatric solid tumors. One interesting feature of the virus presented in this work is that the overall survival of the long-term responders (50% of treated mice) developed an effective antiosteosarcoma memory immune response. This capacity of the virus to achieve a "vaccine" effect is of relevance for osteosarcoma therapy because 20% of new cases present with metastasis at diagnosis (29). In this line of thinking, we know that treatment with oncolytic viruses leads to the release of DAMPs and pathogen-associated molecular patterns and ultimately to ICD, which in turn results in tumor antigen release (29). In our system *in vitro*, both viruses led to the release of DAMPs compatible with ICD, and this phenomenon was higher in Delta-24-ACT–treated osteosarcoma cells. Supporting this notion, in an elegant work by Hinterberger and colleagues, where they evaluated the efficacy of a modified Ankara virus (MVA-TAA-4-1BBL) armed with 4-1BBL and administered intratumorally in different tumor models, they observed that the virus triggered profound changes in the tumor microenvironment, including the induction of multiple proinflammatory molecules and ICD (30). However, to clarify the

specific contribution of 4-1BBL to the enhancement of this type of death, further experiments would be needed.

One of the main hurdles of current immunotherapies is the immunosuppressive tumor microenvironment (TME) and the inability to induce a T-cell trafficking to tumor site. Specifically relevant to osteosarcomas is that the presence of malignant osteoid limits immune infiltration into tumor (23). In addition, single-cell RNA sequencing studies of osteosarcoma patient samples have shown that the TME in this type of cancer is highly heterogeneous, with an ample diversity of immune populations with different phenotypes, revealing the complexity of osteosarcoma tumors (30) and suggesting that one strategy does not fit all cancer. We observed that Delta-24-ACT induced T-cell trafficking to osteosarcoma tumors overcoming the immunosuppressive TME. Therefore, the virus could shake the TME and render the tumor more susceptible to other types of immunotherapies such as immune checkpoints. In that line of thinking, an elegant study by Ligon and colleagues uncovered an immune molecular and cellular signature in osteosarcoma pulmonary metastasis that expressed PD-L1, LAG3, and CSF1R and was associated with worse progression-free survival (31). It would be interesting to combine the virus with one or several inhibitors of these molecules and assess the effect on survival.

Besides lymphocytes, we observed a significant upregulation of macrophages in the tumors treated with Delta-24-ACT. Interestingly, this population is prevalent in patients, and their role is complex and context-dependent (32–35). In our work, we did not delve into the phenotype of these cells. In addition, we observed a significant increase in dendritic cells. It is well known that activated APC express high amounts of 4-1BBL. Moreover, it has been shown that immunization with a 4-1BBL lentivirus activates significant numbers of bystander DCs in the draining lymph nodes and leads to more efficacious CD8. In that work, the authors showed that transactivation by 4-1BBL/4-1BB interaction following DC–DC contact could participate in the immune response to infection or vaccination (36). Understanding the potential contribution of APCs to the antisarcoma effect shown by Delta-24-ACT could provide clues to improve this therapy

One limitation of our study is that adenovirus replication is hindered in murine cell lines. The murine osteosarcoma cells used in this work are nonpermissive for adenoviral replication (**Fig. 1**), reducing the adenoviral load and limiting 4-1BBL expression to only a first wave. This constraint probably resulted in milder stimulation of the immune response than that potentially occurring in human counterparts. However, although our study was not ideal, our data showed the efficacy of this virus.

The encouraging results achieved by local administration of Delta-24-ACT, indicating that it can trigger distant tumor remission, underscore the therapeutic potential of this virus and the need for its clinical translation.

Data and materials availability

The data that support the findings of this study are available within the article or Supplementary Information or available from the corresponding author upon request.

Authors' Disclosures

N. Martinez-Velez reports grants from AACR Foundation during the conduct of the study. J. Fueyo reports a patent for Oncolytic adenoviruses pending and licensed to DNAtrix and is a shareholder of DNATrix. C. Gomez-Manzano reports a patent for Oncolytic adenoviruses pending and licensed to DNAtrix and is a shareholder of DNAtrix. M.M. Alonso reports grants from DNAtrix outside the submitted work. No disclosures were reported by the other authors.

Authors' Contributions

N. Martinez-Velez: Conceptualization, methodology, writing–review and editing. **V. Laspidea:** Conceptualization, formal analysis, investigation, methodology, writing–original draft, writing–review and editing. **M. Zalacain:** Conceptualization, investigation, methodology, writing–original draft, writing–review and editing. **S. Labiano:** Investigation, writing–review and editing. **M. Garcia-Moure:** Investigation, writing–review and editing. **M. Puigdelloses:** Investigation, writing–review and editing. **L. Marrodan:** Investigation, writing–review and editing. **M. Gonzalez-Huarriz:** Investigation, writing–review and editing. **G. Herrador:** Investigation, writing–review and editing. **D. de la Nava:** Investigation, writing–review and editing. **I. Ausejo-Mauleon:** Investigation, writing–review and editing. **J. Fueyo:** Formal analysis, methodology, writing–review and editing. **C. Gomez-Manzano:** Formal analysis, methodology, writing–review and editing. **A. Patiño-García:** Conceptualization, resources, funding acquisition, investigation, writing–original draft, writing–review and editing. **M.M. Alonso:** Conceptualization, resources, funding acquisition, investigation, writing–original draft, writing–review and editing.

Acknowledgments

The performed work was supported through the Departamento de Salud del Gobierno de Navarra (54/2018-APG); AACR-AstraZeneca Immuno-oncology Research Fellowship (18-40-12-MART; N. Martinez-Velez); Predoctoral Fellowship from Gobierno de Navarra (V. Laspidea and G. Herrador), Instituto de Salud Carlos III y Fondos Feder (PI19/01896 M.M. Alonso, PI18/00164A. Patiño-García); Amigos de la Universidad de Navarra (to M. Puigdelloses); Fundación La Caixa/Caja Navarra (A. Patiño-García and M.M. Alonso); Fundación El Sueño de Vicky; Asociación Pablo Ugarte-Fuerza Julen, Fundación ADEY, Fundación ACS, (A. Patiño-García and M.M. Alonso); and Department of Defense (DOD) Team Science Award under grant (CA 160525 M.M. Alonso, C. Gomez-Manzano, and J. Fueyo). La Marató (M.M. Alonso). This project also received funding from the European Research Council (ERC) under the European Union's Horizon 2020 Research and Innovation Programme (817884 ViroPedTher to M.M. Alonso).

The costs of publication of this article were defrayed in part by the payment of page charges. This article must therefore be hereby marked *advertisement* in accordance with 18 U.S.C. Section 1734 solely to indicate this fact.

Received June 29, 2021; revised October 26, 2021; accepted December 15, 2021; published first December 29, 2021.

References

1. Mirabello L, Troisi RJ, Savage SA. Osteosarcoma incidence and survival rates from 1973 to 2004: Data from the surveillance, epidemiology, and end results program. Cancer 2009;115:1531–43.
2. Morrow JJ, Khanna C. Osteosarcoma genetics and epigenetics: Emerging biology and candidate therapies. Crit Rev Oncog 2015;20:173–97.
3. Chou AJ, Gorlick R. Chemotherapy resistance in osteosarcoma: current challenges and future directions. Expert Rev Anticancer Ther 2006;6:1075–85.
4. Fueyo J, Alemany R, Gomez-Manzano C, Fuller GN, Khan A, Conrad CA, et al. Preclinical characterization of the antiglioma activity of a tropism-enhanced adenovirus targeted to the retinoblastoma pathway. J Natl Cancer Inst 2003;95:652–60.
5. Suzuki K, Alemany R, Yamamoto M, Curie DT. The presence of the adenovirus E3 region improves the oncolytic potency of conditionally replicative adenoviruses. Clin Cancer Res 2002;8:3348–59.
6. Alonso MM, Gomez-Manzano C, Bekele BN, Yung WKA, Fueyo J. Adenovirus-based strategies overcome temozolomide resistance by silencing the O6-methylguanine-DNA methyltransferase promoter. Cancer Res 2007;67:11499–504.
7. Martínez-Vélez N, Garcia-Moure M, Marigil M, González-Huarriz M, Puigdelloses M, Gallego Pérez-Larraya J, et al. The oncolytic virus Delta-24-RGD elicits an antitumor effect in pediatric glioma and DIPG mouse models. Nat Commun 2019;10:2235.

8. Martinez-Velez N, Xipell E, Jauregui P, Zalacain M, Marrodan L, Zandueta C, et al. The oncolytic adenovirus Δ24-RGD in combination with cisplatin exerts a potent anti-osteosarcoma activity. J Bone Miner Res 2014;29:2287–96.
9. Garcia-Moure M, Gonzalez-Huarriz M, Labiano S, Guruceaga E, Bandres E, Zalacain M, et al. Delta-24-RGD, an oncolytic adenovirus, increases survival and promotes proinflammatory immune landscape remodeling in models of AT/RT and CNS-PNET. Clin Cancer Res 2021;27:1807–20.
10. Lang FF, Conrad C, Gomez-Manzano C, Alfred Yung WK, Sawaya R, Weinberg JS, et al. Phase I study of DNX-2401 (delta-24-RGD) oncolytic adenovirus: replication and immunotherapeutic effects in recurrent malignant glioma. J Clin Oncol 2018; 36:1419–27.
11. Cheuk ATC, Mufti GJ, Guinn BA. Role of 4–1BB:4–1BB ligand in cancer immunotherapy. Cancer Gene Ther 2004;11:215–26.
12. Chester C, Sanmamed MF, Wang J, Melero I. Immunotherapy targeting 4-1BB: Mechanistic rationale, clinical results, and future strategies. Blood 2018; 131:49–57.
13. Kamijo A, Koshino T, Uesugi M, Nitto H, Sai T. Inhibition of lung metastasis of osteosarcoma cell line POS-1 transplanted into mice by thigh ligation. Cancer Lett 2002;188:213–9.
14. Joliat MJ, Umeda S, Lyons BL, Lynes MA, Shultz LD. Establishment and characterization of a new osteogenic cell line (MOS-J) from a spontaneous C57BL/6J mouse osteosarcoma. In Vivo 2002;16:223–8.
15. Puigdelloses M, Garcia-Moure M, Labiano S, Laspidea V, Gonzalez-Huarriz M, Zalacain M, et al. CD137 and PD-L1 targeting with immunovirotherapy induces a potent and durable antitumor immune response in glioblastoma models. J Immunother Cancer 2021;9:e002644.
16. Martínez-Vélez N, Xipell E, Vera B, De La Rocha AA, Zalacain M, Marrodan L, et al. The oncolytic adenovirus VCN-01 as therapeutic approach against pediatric osteosarcoma. Clin Cancer Res 2016;22:2217–25.
17. Kroemer G, Galluzzi L, Kepp O, Zitvogel L. Immunogenic cell death in cancer therapy. Annu Rev Immunol 2013;31:51–72.
18. Garg AD, Nowis D, Golab J, Vandenabeele P, Krysko DV, Agostinis P. Immunogenic cell death, DAMPs and anticancer therapeutics: An emerging amalgamation. Biochim Biophys Acta 2010;1805:53–71.
19. Lin SY, Hsieh SY, Fan YT, Wei WC, Hsiao PW, Tsai DH, et al. Necroptosis promotes autophagy-dependent upregulation of DAMP and results in immunosurveillance. Autophagy 2018;14:778–95.
20. Thorburn J, Horita H, Redzic J, Hansen K, Frankel AE, Thorburn A. Autophagy regulates selective HMGB1 release in tumor cells that are destined to die. Cell Death Differ 2009;16:175–83.
21. Jiang H, Clise-Dwyer K, Ruisaard KE, Fan X, Tian W, Gumin J, et al. Delta-24-RGD oncolytic adenovirus elicits anti-glioma immunity in an immunocompetent mouse model. PLoS One 2014;9:e97407.
22. Sanmamed MF, Pastor F, Rodriguez A, Perez-Gracia JL, Rodriguez-Ruiz ME, Jure-Kunkel M, et al. Agonists of co-stimulation in cancer immunorapy directed against CD137, OX40, GITR, CD27, CD28, and ICOS. Semin Oncol 2015;42: 640–55.
23. Wu CC, Beird HC, Andrew Livingston J, Advani S, Mitra A, Cao S, et al. Immuno-genomic landscape of osteosarcoma. Nat Commun 2020;11:1008.
24. Boye K, Longhi A, Guren T, Lorenz S, Næss S, Pierini M, et al. Pembrolizumab in advanced osteosarcoma: results of a single-arm, open-label, phase 2 trial. Cancer Immunol Immunother 2021;70:2617–24.
25. DeRenzo C, Gottschalk S. Genetically modified T-cell therapy for osteosarcoma: into the roaring 2020s. Adv Exp Med Biol 2020;1257:109–31.
26. Boutros C, Tarhini A, Routier E, Lambotte O, Ladurie FL, Carbonnel F, et al. Safety profiles of anti-CTLA-4 and anti-PD-1 antibodies alone and in combination. Nat Rev Clin Oncol 2016;13:473–86.
27. Gust J, Hay KA, Hanafi LA, Li D, Myerson D, Gonzalez-Cuyar LF, et al. Endothelial activation and blood–brain barrier disruption in neurotoxicity after adoptive immunotherapy with CD19 CAR-T cells. Cancer Discov 2017; 7:1404–19.
28. Martinez-Quintanilla J, Seah I, Chua M, Shah K. Oncolytic viruses: overcoming translational challenges. J Clin Invest 2019;29:1407–18.
29. Moore DD, Luu HH. Osteosarcoma. Cancer Treat Res 2014;162:65–92.
30. Zhou Y, Yang D, Yang Q, Lv X, Huang W, Zhou Z, et al. Single-cell RNA landscape of intratumoral heterogeneity and immunosuppressive microenvironment in advanced osteosarcoma. Nat Commun 2020;11:6322.
31. Ligon JA, Choi W, Cojocaru G, Fu W, Hsiue EH-C, Oke TF, et al. Pathways of immune exclusion in metastatic osteosarcoma are associated with inferior patient outcomes. J Immunother Cancer 2021;9:e001772.
32. Toulmonde M, Penel N, Adam J, Chevreau C, Blay JY, Le Cesne A, et al. Use of PD-1 targeting, macrophage infiltration, and IDO pathway activation in sarcomas a phase 2 clinical trial. JAMA Oncol 2018;4:93–7.
33. Shiraishi D, Fujiwara Y, Horlad H, Saito Y, Iriki T, Tsuboki J, et al. CD163 is required for protumoral activation of macrophages in human and murine sarcoma. Cancer Res 2018;78:3255–66.
34. Buddingh EP, Kuijjer ML, Duim RAJ, Bürger H, Agelopoulos K, Myklebost O, et al. Tumor-infiltrating macrophages are associated with metastasis suppression in high-grade osteosarcoma: a rationale for treatment with macrophage activating agents. Clin Cancer Res 2011;17:2010–19.
35. Heymann MF, Lézot F, Heymann D. The contribution of immune infiltrates and the local microenvironment in the pathogenesis of osteosarcoma. Cell Immunol 2019;343:103711.
36. Macdonald DC, Hotblack A, Akbar S, Britton G, Collins MK. 4–1BB ligand activates bystander dendritic cells to enhance immunization in trans. J Immunol 2014;193:5056–64.

Supplemental Material

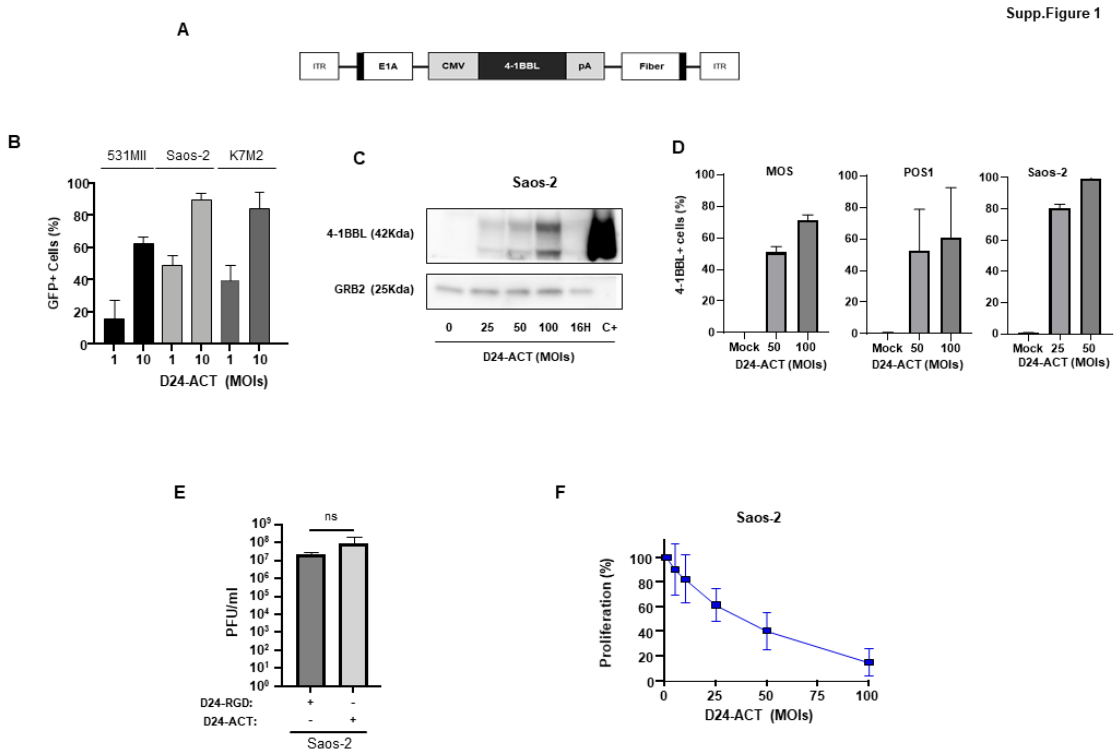

Supplementary Figure 1. Characterization of Delta-24-ACT in osteosarcoma cell lines. A. Schematic representation of engineered Delta-24-ACT. **B.** Quantification of viral infectivity in human (531MII and Saos-2) and murine (K7M2) osteosarcoma cells. Cells were infected with AdGFP-RGD at the indicated MOIs, and GFP expression was measured by flow cytometry 24 h later. The data are presented as the mean numbers of GFP-positive cells ±SDs. **C.** Assessment of 4-1BBL protein expression by western blot analysis. Cells were infected with Delta-24-ACT at the indicated MOIs, and whole-cell lysates were collected 48 h later. Grb2 was used as the protein loading control, and recombinant 4-1BBL protein was used as the positive control. **D.** Flow cytometric quantification of 4-1BBL expression in the membrane of murine (MOS, POS1) and human (and Saos-2) osteosarcoma cells infected with Delta-24-ACT at the indicated MOIs. **E.** Replication of Delta-24-ACT in human Saos-2 osteosarcoma cells. Cells were infected, and Delta-24-ACT replication was determined 72 h later. The results are

expressed as the mean viral titers ± SDs (N = 3). **E.** Oncolytic effect of Delta-24-ACT on human osteosarcoma cells. To quantify the oncolytic effect of Delta-24-ACT, cells were infected at the indicated MOIs, and viability was evaluated by MTS assays five days later. The values indicate the percentages of viable cells in infected cultures compared to those in noninfected cultures (mean ±SD).

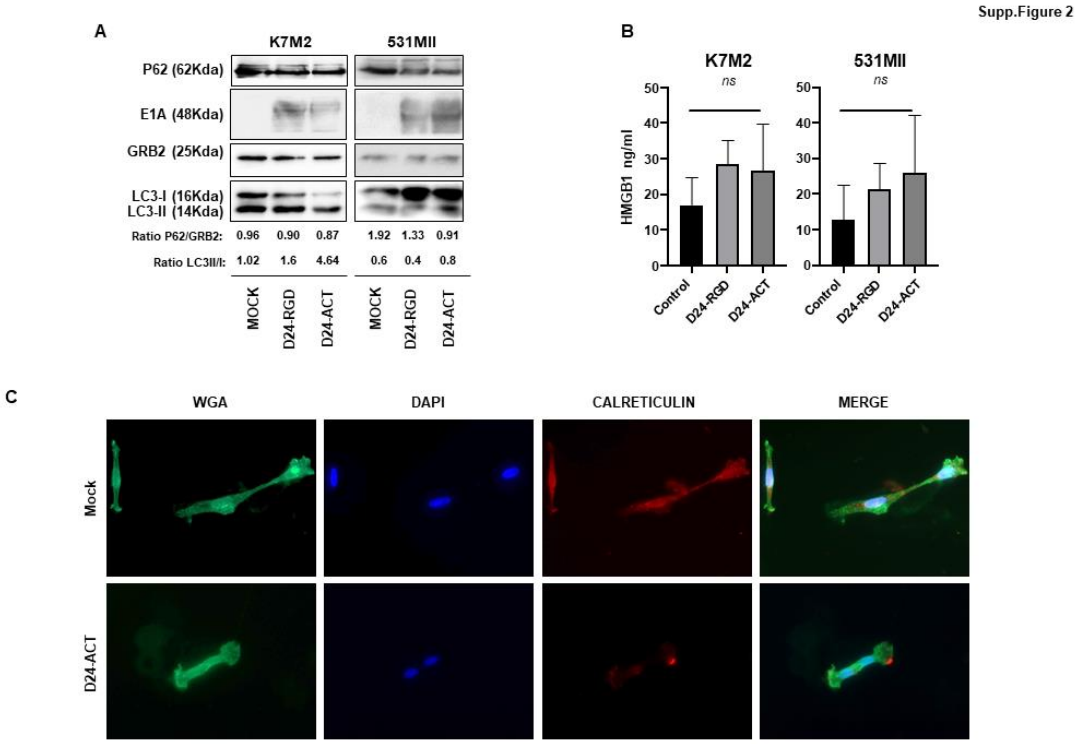

Supplementary Figure 2. Evaluation of DAMPs in Delta-24-ACT-treated cells *in vitro*. A. Evaluation of autophagy-related proteins after Delta-24-ACT treatment in the indicated osteosarcoma cell lines. **B**. Concentrations of the DAMPs HMGB1 in supernatants obtained from osteosarcoma cultures 72 h after infection with Delta-24-ACT at the corresponding IC_{50} values for each virus or after mock infection. The bar graphs show the mean ± SD values (n=3; ordinary one-way ANOVA). **C.** Representative fluorescence micrographs of 531MII cells 4 h after infection with Delta-24-ACT or mock

infection. Calreticulin at the cell surface was detected by immunofluorescence (red). Cell membranes (green) and nuclei (blue) were counterstained with WGA and DAPI, respectively.

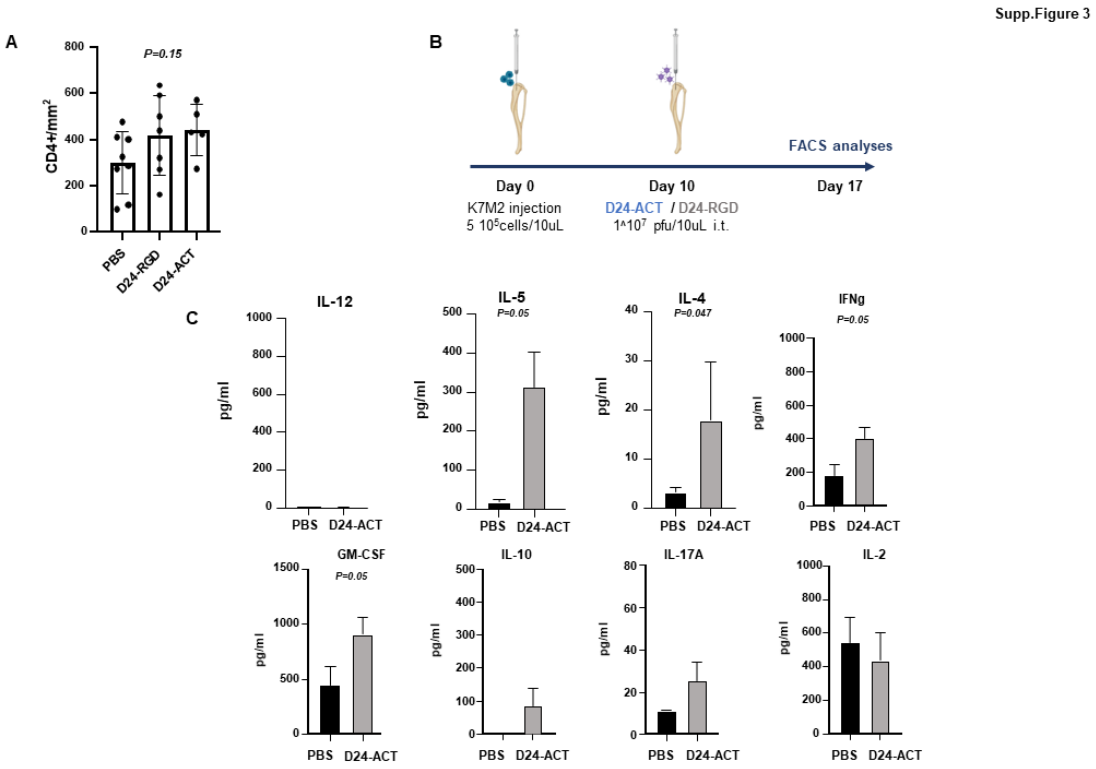

Supplementary Figure 3. Administration of Delta-24-ACT results in immune cell infiltration and the production of proinflammatory cytokines. Osteosarcoma tumors were generated by intratibial administration of K7M2 cells, and PBS, Delta-24-RGD or Delta-24-ACT was administered intratumorally 10 days after cell implantation. Animals were sacrificed on day 21 after cell implantation. **A.** Quantification of CD4+ cell infiltration per mm^2 in osteosarcoma tumors ($n = 6$-8). *P* values was calculated using Student's *t* test. **B.** Treatment scheme for evaluating immune infiltration after treatment with the indicated viruses. Mice were treated intratibially with mock (PBS), Delta-24-RGD or Delta-24-ACT following the schedule indicated in **B. C.** Quantification of the

production of the indicated cytokines by ELISA after K7M2 cells were cocultured for 72 h with splenocytes from mice treated with PBS or Delta-24-ACT. The data are presented as the mean ±SD values ($N = 4$). Two-tailed Student's *t* test was used for comparison between control and treated mice.

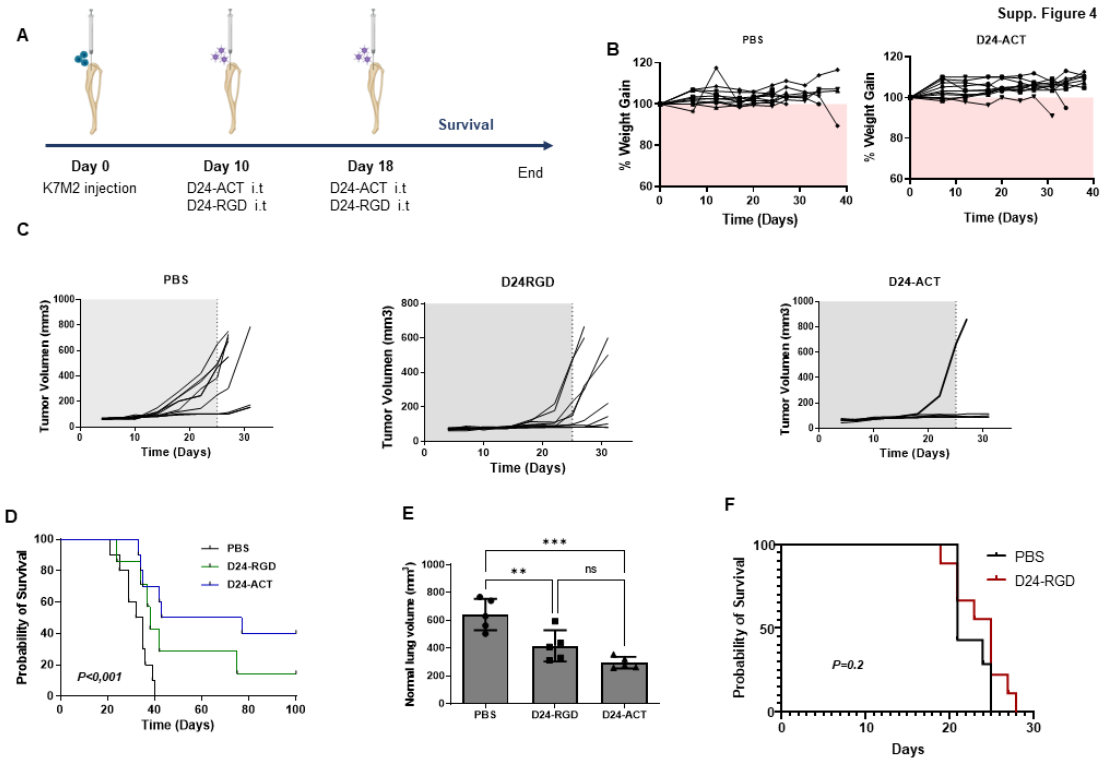

Supplementary Figure 4. **Administration of Delta-24-ACT safely increased overall survival in a murine osteosarcoma model. A.** Treatment scheme for the efficacy evaluation. **B.** Mice were treated intratibially with mock (PBS), Delta-24-RGD or Delta-24-ACT following the schedule indicated in **A**. Mice from the different groups were weighed every 3-4 days until the end of the treatment period (40 days). The data are shown as the median ± SD values for each group at each time point. **C.** Analyses of tumor burden development in the PBS-treated (control group) and Delta-24-RGD-treated groups. Tumor volume in mouse tibias was measured on different days until the end of the experiment. **D.** Survival curves. The graphs show the overall survival of mice treated

with Delta-24-ACT (blue line), Delta-24-RGD (green line) or PBS (black line). **E.** Quantification of lung metastasis using micro-CT after the indicated treatment. **F.** Kaplan-Meier survival curves of Delta-24-RGD (10^7 pfu)-treated and control (PBS)-treated immunodeficient (athymic nude) mice ($N = 10$, both groups) bearing intratibial K7M2 tumors. The *P* value was calculated with the log-rank test.